ALMA MATER STUDIORUM
UNIVERSITÀ DI BOLOGNA

DOTTORATO DI RICERCA IN

ASTROFISICA

Ciclo 37

Settore Concorsuale: 02/C1 - ASTRONOMIA, ASTROFISICA, FISICA DELLA TERRA E DEI PIANETI

Settore Scientifico Disciplinare: FIS/05 - ASTRONOMIA E ASTROFISICA

HIGH-PRECISION STELLAR ASTROPHYSICS: TESTING MODELS OF STELLAR STRUCTURE USING ASTEROSEISMIC, ASTROMETRIC, AND SPECTROSCOPIC CONSTRAINTS

Presentata da: Massimiliano Matteuzzi

Coordinatore Dottorato

Andrea Miglio

Supervisore

Andrea Miglio

Esame finale anno 2025

"It is not his possession of knowledge, of irrefutable truth, that makes the man of science, but his persistent and recklessly critical quest for truth."

-Karl Popper, The Logic of Scientific Discovery

Abstract

Stellar evolutionary models serve as the foundation for much of astrophysical research, including nucleosynthesis, the study of exoplanetary systems, and the formation and evolution of galaxies. However, their internal structures had not been thoroughly tested until recently, thanks to the advent of asteroseismic observations, which now allow for precise inference of stellar interiors.

This PhD thesis investigates the internal structure and evolutionary processes of low-mass core helium burning (CHeB) stars, employing advanced asteroseismic and Bayesian methodologies. The primary aim is to refine our understanding of these stars and assess non-standard evolutionary models that challenge conventional paradigms.

The research begins with the identification of eleven red giant stars in the *Kepler* field, revealing complex oscillation spectra indicative of very low-mass CHeB stars. These stars exhibit a unique seismic signature characterised by a helium core of approximately 0.5 $M_\odot$ and a lighter hydrogen-rich envelope, leading to a higher coupling factor between the internal pressure and gravity mode cavities compared to typical red clump stars. This work demonstrates the potential of asteroseismology to accurately identify anomalously low-mass CHeB stars even in the field, highlighting their role in understanding stellar evolution and mass loss.

While we have improved our methods for detecting these stars, the question of how they form remains unanswered. To tackle this critical gap in knowledge, the analysis presented in this thesis extends to a specific anomalously low-mass CHeB star, KIC4937011, which is a member of the open cluster NGC 6819. This Li-rich star has a mass approximately 1 $M_\odot$ lower than cluster stars in the same evolutionary phase and provides, thus, a unique opportunity to explore the evolutionary pathways that lead to such low-mass configurations. By coupling advanced Bayesian techniques with interacting binary stellar population models, this PhD thesis posits that KIC4937011 is a product of a common-envelope evolution phase where the companion star did not survive, leading to significant mass ejection. This finding not only elucidates the formation scenario of KIC4937011 but also provides crucial insights into the evolution of other stars, including subdwarf B stars and metal-rich RR Lyrae.

Further, this research delves into the asteroseismic signatures associated with structural variations near the convective core of low-mass CHeB stars. By developing semi-analytical

models, the study reveals how structural glitches influence oscillation spectra, offering deeper insights into the internal composition and evolutionary transitions of these stars, paving the way to robust comparisons with high-quality asteroseismic data.

Overall, this thesis contributes significantly to the field of stellar astrophysics by enhancing our understanding of low-mass CHeB stars and their evolutionary histories. It lays the groundwork for future research exploring the complexities of stellar evolution, mass loss mechanisms, and their broader implications for the formation and evolution of the Milky Way.

Contents

List of Figures

List of Tables

Problem statement

Core helium burning (CHeB) phase represents a pivotal stage in the evolution of low- to intermediate-mass stars, marking their transition from the red giant branch (RGB), characterised by an inert and electron-degenerate helium core, to a stable helium-burning phase within a convective core. CHeB stars in the red clump (RC) are particularly valuable for understanding the cosmic distance ladder, mapping Galactic structures, and studying stellar populations (e.g. Girardi 2016).

Recent advancements in asteroseismology, driven by space-based missions such as CoRoT, *Kepler*, K2, and TESS, have significantly enhanced our understanding of the internal structures, properties, and evolutionary phases of red giant stars. The distinct oscillation patterns observed in RC stars compared to RGB stars enable us to differentiate these otherwise spectroscopically similar objects (e.g. Montalbán et al. 2010; Bedding et al. 2011). Additionally, it has been demonstrated that RGB star cores can rotate up to ten times faster than their surfaces (Beck et al. 2012). While models predict significant core spin-up during the RGB phase, observations indicate (e.g. Mosser et al. 2012a; Mosser et al. 2012b) that the core does not spin-up as much as expected. At the end of the RGB phase, a spin-down is observed, which aligns with the expansion of the core (e.g. Mosser et al. 2012a; Mosser et al. 2012b). The detection of oscillations in thousands of field red giant stars has opened new avenues for detailed studies of Milky Way stellar populations (e.g. Miglio et al. 2009). Asteroseismic constraints, combined with photospheric chemical abundances and temperatures, allow for precise measurements of radii and masses (De Ridder et al. 2009; Hekker et al. 2011; Huber et al. 2011; Miglio et al. 2013; Stello et al. 2013; Mosser et al. 2014; Yu et al. 2018; García et al. 2019; Kallinger 2019). This precision has led to robust age determinations (Anders et al. 2016; Casagrande et al. 2016; Pinsonneault et al. 2018; Silva Aguirre et al. 2018; Miglio et al. 2021; Montalbán et al. 2021). Furthermore, it has been possible to estimate the integrated RGB mass loss (e.g. Miglio et al. 2012; Stello et al. 2016; Handberg et al. 2017; Miglio et al. 2021; Tailo et al. 2022; Howell et al. 2022; Howell et al. 2024) and from detailed studies of members of star clusters it has been possible

to find red giants with anomalous masses compared to the average for their evolutionary phases (e.g. Brogaard et al. 2016; Handberg et al. 2017; Brogaard et al. 2018; Brogaard et al. 2021; Miglio et al. 2021), which may indicate interactions with companion stars (see also Li et al. 2022; Bobrick et al. 2024).

Despite these advances, considerable uncertainties persist in the modelling of low-mass CHeB stars and in the identification of non-standard evolutionary paths. One of the main challenges involves accurately modelling the efficiency of mixing processes within these stars. Their internal structure is influenced by the transport of material between convective and radiative core, yet the boundary between these regions and the extent of mixing across this boundary are still not well understood (e.g. Castellani et al. 1971a; Bressan et al. 1986; Straniero et al. 2003; Gabriel et al. 2014; Bossini et al. 2015; Constantino et al. 2015; Bossini et al. 2017; Salaris et al. 2017; Noll et al. 2024). Gaining insight into these mixing processes is essential for constructing precise models of CHeB stars, which has broader implications for astrophysical research, particularly regarding the chemical evolution of galaxies. Moreover, despite potential insights from observations that could assist in distinguishing between different formation scenarios (Brogaard et al. 2018), the evolutionary history of many observed systems with masses that deviate from their expected mass remains uncertain. The limited support from other stars in age determination makes it challenging to identify non-standard evolutionary paths for field stars. An exception to this is the thick disc, which has a well-defined turn-off mass that allows for the tracking of the evolutionary history of these stars (Chiappini et al. 2015; Martig et al. 2015; Izzard et al. 2018; Grisoni et al. 2024).

In light of these critical gaps, the principal objective of this PhD thesis is to accurately characterise the internal structure of CHeB stars and evaluate non-standard evolutionary models through the application of advanced asteroseismic techniques. By meticulously investigating the internal structures of these stars, this study aims to provide essential insights that will refine current models and enhance our understanding of the stellar lifecycle. This exploration is particularly relevant given the significant role that CHeB stars play in stellar evolution and their contributions to the chemical evolution of galaxies.

Structure of the thesis

The principal objective of this thesis is to accurately characterise the internal structure of core helium burning stars and to evaluate non-standard evolutionary models through the application of asteroseismology. To facilitate this investigation, the subsequent chapters

are organised as follows:

- *Chapter 1*: This chapter provides the scientific background essential for understanding the results presented in later sections. It specifically explores the structural characteristics of stellar interiors during the core helium burning phase and illustrates how asteroseismology of solar-like oscillators can serve as a robust methodology for accurately inferring their internal structures;

- *Chapter 2*: This chapter builds upon the findings I published in Matteuzzi et al. (2023). It focuses on the theoretical characterisation of peculiar oscillation spectra observed in core helium burning stars within the *Kepler* field. By employing evolutionary models and theoretical adiabatic oscillation eigenfrequencies, I aim to confirm the very low-mass nature of these stars and their strong coupling between the g-cavity and the p-cavity;

- *Chapter 3*: Expanding on the results I published in Matteuzzi et al. (2024), this chapter examines the formation scenarios for some of the low-mass core helium burning stars introduced in Chapter 2. Notably, it focuses on a star within the old Galactic star cluster NGC6819, KIC4937011, which possesses approximately 1 $M_{\odot}$ less mass than the average of the other stars in the cluster that are in the same evolutionary phase. The findings suggest that this star is the result of a common-envelope evolution phase in which the companion does not survive, offering new insights into the formation of subdwarf B stars and metal-rich RR Lyrae;

- *Chapter 4*: In this chapter, I conduct a detailed analysis of asteroseismic signatures related to structural variations in low-mass core helium burning stars, focusing on the regions near their cores (Matteuzzi et al., to be submitted). I develop semi-analytical models of these stars, calibrated using evolutionary codes. The investigation concentrates on changes in eigenfrequencies and period spacing attributed to density discontinuities, non-differentiable points within the density profile, and bell-shaped glitches in the Brunt-Väisälä frequency;

- *Thesis conclusions*: This last chapter summarises all the results of the thesis work and it contains a brief discussion on possible future developments;

- *Appendix A*: This appendix discusses the physical properties of the complete sample of stars analysed in chapter 2;

- *Appendix B*: This appendix provides details about the grid of stellar models utilised in Chapter 2;
- *Appendix C*: This appendix covers the simulated oscillation spectra of individual modes referenced in Chapter 2;
- *Appendix D*: This appendix discusses the selection of the likelihood function and prior distributions employed in Chapter 3;
- *Appendix E*: This appendix provides Taylor series solutions near the centre of the semi-analytical models explained in Chapter 4;
- *Appendix F*: This appendix shows a set of differential equations to use in Chapter 4 near the surface of barotropic stars to avoid numerical issues;
- *Appendix G*: This appendix presents analytical solutions for the differential equations described in Chapter 4. They are used to test the numerical solver;
- *Appendix H*: This appendix includes a list of published papers, as well as the collaborative work I have engaged in as a co-author on other papers that are not covered elsewhere in this document.

Chapter 1

Scientific background

This chapter introduces my thesis by outlining the research problem, objectives, and significance, as well as its limitations. It also details the methodology used for the analysis presented in subsequent chapters and includes a literature review of key physical processes. Specifically, Section 1.1 examines stars as systems governed by fluid dynamics, with an emphasis on their internal turbulence. Section 1.2 delves into the main heat transport mechanisms occurring within stars. In Section 1.3 I provide an introduction to the core helium burning evolutionary phase and discuss the primary theoretical challenges associated with it. Section 1.4 introduces asteroseismology as a valuable tool for elucidating the internal structure of stars, which is pertinent to the methods deployed in this thesis

1.1 Fluid dynamics in stars

In this section, I introduce the description of the structure and evolution of stars through the lens of fluid dynamics.

Generally, a star can be conceptualised as a collection of moving particles that interact with one another. The average distance a particle travels before experiencing a collision event with another particle is called mean free path (l_{mean}). In stars without electron or neutron degeneracy, it is not necessary to completely solve the quantum field equations to analyse the motion of particles in space and time. This is because their l_{mean} is much higher than their de Broglie wavelength, allowing us to approximate the quantum motion using classical trajectories, as supported by Ehrenfest's theorem (Ehrenfest 1927). Furthermore, upon establishing a characteristic length scale of the system (H_{scale}), we can compute the dimensionless Knudsen number defined as

$$\text{Kn} := \frac{l_{\text{mean}}}{H_{\text{scale}}}. \tag{1.1.1}$$

When Kn $\ll 1$, systems comprised of a finite number of particles can be effectively approximated as a continuous fluid. This situation is applicable to real stars, allowing us to define macroscopic quantities as continuous functions of space ($\vec{x}$) and time (t). Due to the continuum approximation, any infinitesimal fluid element is much smaller than H_{scale}, contains a sufficiently large number of particles to render any statistical fluctuations associated with discreteness negligible, and is significantly larger than l_{mean} (e.g. Landau et al. 1987). From now on H_{scale} can be defined as

$$H_{\text{scale}} \equiv H_Q := \frac{Q(\vec{x},t)}{\|\vec{\nabla}Q(\vec{x},t)\|}, \tag{1.1.2}$$

where $Q(\vec{x},t)$ denotes a macroscopic quantity of the fluid. Useful quantities are the velocity field $[\vec{v}(\vec{x},t)]$, density $[\rho(\vec{x},t)]$ and pressure $[P(\vec{x},t)]$ of the fluid. In fact, as it will become clear later, any other macroscopic quantity (apart from the chemical composition) can be expressed as a function of these five fundamental quantities.

1.1.1 Navier-Stokes equations

The equations that describe the fluid dynamics are known as the Navier-Stokes equations (e.g. Landau et al. 1987). These equations are formulated based on the principles of conservation of mass, momentum, and energy. In the context of a self-gravitating Newtonian fluid with no external forces, no magnetic fields, no bulk viscosity, a constant shear dynamic viscosity (μ) and composed solely of pure hydrogen, the Navier-Stokes equations can be expressed in the Lagrangian tensorial form as

$$\begin{cases} \dfrac{d\rho}{dt} + \rho\partial_i v_i = 0 \\ \rho\dfrac{dv_i}{dt} + \partial_i P + \rho\partial_i\phi - \mu\left[\partial_j\partial_j v_i + \dfrac{\partial_i\partial_j v_j}{3}\right] = 0 \\ \rho T\dfrac{ds}{dt} + \partial_i F_{\text{heat},i} - 2\mu S_{ij}S_{ij} + \rho\Gamma_{\text{net}} = 0 \\ S_{ij} := \dfrac{(\partial_i v_j + \partial_j v_i)}{2} - \dfrac{\delta_{ij}\partial_k v_k}{3} \\ \rho T\dfrac{ds}{dt} = \rho c_P\dfrac{dT}{dt} + \left.\dfrac{\partial\ln\rho}{\partial\ln T}\right|_P\dfrac{dP}{dt} \\ \partial_i\partial_i\phi - 4\pi G\rho = 0. \end{cases} \tag{1.1.3}$$

In this formulation, Φ denotes the gravitational potential of the fluid, T the temperature, c_P the specific heat capacity at constant pressure, s the specific entropy, S_{ij} the deviatoric strain tensor, $\vec{F}_{\text{heat}}$ the heat flux, and Γ_{net} the net cooling function of the fluid. The equation in the last row is the Poisson equation, and it specifies how to relate the gravitational potential to the density of the fluid. Equation 1.1.3 is not a close set of differential equations, because we have at least seven variables $(\rho, \vec{v}, P, \phi, T)$ with six equations. Therefore,

we need at least another equation that can relate these macroscopic quantities to each other, that is, $P(\vec{x},t) \equiv P[\rho(\vec{x},t), T(\vec{x},t)]$. Such an equation is called equation of state (EOS).

1.1.2 Reynolds number

In the field of fluid dynamics, it is advantageous to render the system of equations 1.1.3 dimensionless. This transformation enables the identification of dominant terms within the equations and facilitates the development of meaningful approximations. Specifically, we can achieve a dimensionless form of the second equation of the system by combining μ with the average fluid density ($\langle\rho\rangle$), the average fluid velocity ($\langle v\rangle$) and H_{scale}. This combination yields the dimensionless Reynolds number

$$\text{Re} := \frac{\langle\rho\rangle\langle v\rangle H_{\text{scale}}}{\mu}, \tag{1.1.4}$$

which determines the degree of turbulence of the fluid under study as well as its comparative behaviour with other fluids. It is important to note that as Re increases, the significance of the viscous terms in the Navier-Stokes equations diminishes, thereby suggesting a higher turbulence level in the fluid. In the context of stellar structure and evolution, the Re number reaches extremely high values, such as $\text{Re} = 6 \cdot 10^{12}$ in the convective envelope of the Sun. This large value allows us to neglect the viscous term in equation 1.1.3. As a result, fluid dynamics within stars, especially in their convective regions, exhibit markedly greater turbulence compared to what can be tested in laboratory-scale fluids. This turbulence consists of a spectrum of turbulent eddies of various sizes that propagate throughout the three-dimensional space, even in stars exhibiting spherical symmetry. Therefore, to accurately model this turbulent motion in stars, it is imperative to utilise three-dimensional simulations. However, achieving this requires approximately $\left(\text{Re}^{3/4}\right)^3 \approx 10^{28.8}$ grid points[1] to resolve turbulence down to the Kolmogorov length scale (e.g. Chan et al. 1986), which is a computationally prohibitive requirement (see also Kupka et al. 2017, for a review). Consequently, formulating a complete theory of turbulence within stars poses significant challenges, necessitating the application of alternative approximations (see Section 1.2.2).

1.2 Equations of the stellar structure

In Section 1.1, I demonstrated that stars can be modelled as continuous fluids governed by the Navier-Stokes equations (equation 1.1.3). Nevertheless, further simplification

[1] This estimate is derived from the Re value representative of the Sun.

of these equations is feasible when considering non-rotating, spherical stars at virial equilibrium. In this scenario, the internal velocity becomes negligible (with the exception of the convective zones discussed in Section 1.2.2), and all the internal variables can be expressed solely as functions of time and radius (r). Furthermore, stars are composed of a diverse array of chemical species, with their spatial and temporal distributions being influenced by plasma dynamics (see Section 1.2.2 and 1.3.2) as well as by nuclear reactions (discussed in Section 1.3.3). Therefore, it is crucial to integrate the mass concentrations of these chemical species (X_i) into the system of differential equations that governs stellar structure. This integration enables the formulation of the new set of simplified differential equations

$$\begin{cases} \dfrac{\partial m(r,t)}{\partial r} = 4\pi r^2 \rho(r,t) \\ \dfrac{\partial P(r,t)}{\partial r} = -g(r,t)\rho(r,t) \\ \dfrac{\partial L(r,t)}{\partial r} = 4\pi r^2 \left[\rho\varepsilon_{\text{nuc}} - \rho\varepsilon_\nu - \rho c_P \dfrac{\partial T}{\partial t} - \dfrac{\partial \ln \rho}{\partial \ln T}\bigg|_P \dfrac{\partial P}{\partial t} \right] \\ \dfrac{\partial T(r,t)}{\partial r} = -\dfrac{g(r,t)\rho(r,t)T(r,t)}{P(r,t)} \nabla(r,t) \\ \rho(r,t)\dfrac{\partial X_i(r,t)}{\partial t} = m_i(r,t) \left(\sum_{j=1}^{N} r_{ji} - \sum_{k=1}^{N} r_{ik} \right), \quad i = 1, ..., N \\ \sum_{i=1}^{N} X_i = 1 \quad \text{with} \quad \rho X_i \equiv m_i n_i \\ g(r,t) = \dfrac{Gm(r,t)}{r^2} \end{cases} \tag{1.2.1}$$

for the internal structure of stars, as detailed in the literature (e.g. Kippenhahn et al. 2012). In this formulation, $L(r,t) \equiv L_r(t)$ represents the net energy per second (luminosity) passing outward through a sphere of radius r. This energy rate depends on the specific nuclear reaction rates (ε_{nuc}) adjusted for energy losses due to neutrino emissions (ε_ν), and depends on the specific gravitational energy rate $\left(\varepsilon_{\text{grav}} := -c_P \frac{\partial T}{\partial t} - \frac{1}{\rho}\frac{\partial \ln \rho}{\partial \ln T}\Big|_P \frac{\partial P}{\partial t}\right)$. These rates depend on the pressure, temperature (or any two thermodynamic variables when using an EOS) and the chemical species present in that region. In Section 1.3.3, I will specifically focus on the main nuclear reaction rates occurring in stars undergoing the core helium burning phase (as defined in Section 1.3) and examine the theoretical challenges they present. Ultimately, the temperature gradient $\nabla(r,t) := d\ln T / d\ln P$ in equation 1.2.1 incorporates all heat transfer mechanisms that influence the structure and evolution of stars, namely conduction, radiation, and convection. In sections 1.2.1 and 1.2.2, I will focus on the heat transport through radiation and convection, respectively, while conduction will not be discussed, as it significantly affects only those stellar regions

that contain degenerate matter. This is due to the fact that, in these cases, the mean free path of degenerate particles is considerably larger than that of photons (e.g. Kippenhahn et al. 2012). Conversely, conduction via degenerate electrons is crucial in the evolutionary phase leading up to the onset of core helium burning in low-mass stars, as discussed in Section 1.3.

1.2.1 Radiative heat flux

In equation 1.2.1, I presented the temperature gradient as a general term that includes all the relevant heat transfer mechanisms. This section will investigate the temperature gradient necessary to transport the luminosity L_r via radiative processes.

Within stellar interiors, photons exhibit a notably short mean free path ($l_{\text{mean}} \approx 2\,\text{cm}$ for an average point inside the Sun, as discussed by Kippenhahn et al. 2012) compared to the pressure scale height, due to their continuous absorption and re-emission in an almost random manner[2]. The time taken for a photon to travel from the centre of the star to its surface ($\approx 10\,\text{Myr}$ for the Sun, as discussed by Kippenhahn et al. 2012) significantly exceeds the time that such a photon would require to cover the same distance in vacuum. Therefore, the motion of radiation in stellar interiors can be effectively characterised by Fick's law of diffusion (Fick 1855). This law contains a diffusion coefficient that depends on the speed of light in vacuum (c), the specific heat capacity of the radiation field at constant volume, and the specific absorption coefficient κ_ν at frequency ν, which is often referred to as the opacity coefficient. This coefficient represents the radiative cross section per unit mass at the specified frequency ν. To further simplify the problem, it can be assumed that photons are almost in thermal equilibrium locally, as indicated by the local small temperature fluctuations ($dT/T \approx 10^{-11}$ at a point with $T \approx 10^7$ K in the Sun, see Kippenhahn et al. 2012). Consequently, the radiation field can be treated as black body radiation in these local conditions[3]. Therefore, the temperature gradient required to carry the entire luminosity L_r by radiation in a star in hydrostatic equilibrium can be expresses as

$$\nabla_{\text{rad}}(r,t) = \frac{3\kappa L_r P}{64\pi G\sigma m T^4}, \tag{1.2.2}$$

where σ is the Stefan-Boltzmann constant and κ represents the opacity coefficient averaged

[2]This consideration is not true in the vicinity of stellar surfaces, where we have to solve the full equations of radiative transfer. However, this thesis concentrates on the stellar interiors, rendering the following analysis applicable and relevant.

[3]However, it is important to note that a net heat flux moving from higher-temperature regions to those of lower temperature still remains. Therefore, heat flows from the interior to the exterior parts of stars.

across all frequencies based on Planck radiation, which is typically referred to as Rosseland mean opacity (e.g. Kippenhahn et al. 2012). The function $\kappa = \kappa(T, \rho, \text{chemical elements})$ is quite complex, as it must account for a variety of absorption processes. These processes include bound-bound and bound-free transitions involving ions, atoms, molecules, and dust grains, in addition to free-free absorption and electron scattering from various chemical species. In Section 1.2.1, I provide a summary of the main characteristics of $\kappa(T, \rho)$ for a plasma with solar chemical composition.

From equation 1.2.2, it can be observed that ∇_{rad} increases in regions of strong energy generation, because a localised rise in ε_{nuc} leads to a corresponding increase in L_r, as outlined in equation 1.2.1. Additionally, ∇_{rad} increases in regions with high opacity. Such conditions are frequently found in the cooler outer layers of stars and/or in regions where the mean molecular weight $[\mu(r, t)]$ increases due to the presence of metals[4]. These factors will be further examined in Section 1.3.2. Ultimately, in regions where the actual temperature gradient ∇ is equal to ∇_{rad}, energy transfer occurs predominantly through radiative processes; these areas are in a state of radiative equilibrium and are referred to as radiative regions.

Rosseland mean opacity

In Section 1.2.1, I discussed the complexity of the function $\kappa(T, \rho, \text{chemical elements})$. The development of realistic opacity models that can be computed in real-time within stellar evolutionary codes is indeed highly complex. As such, it is necessary to utilise pre-calculated and tabulated opacity values corresponding to a variety of chemical mixtures, which are expressed as functions of T and ρ. As a result, evolutionary codes can interpolate the most suitable values from opacity tables, significantly reducing calculation time. Examples of such tables applicable for temperatures exceeding approximately 10^4 K are OPAL (Iglesias et al. 1996), the international Opacity Project (OP; Seaton et al. 1994; Badnell et al. 2005) and OPLIB (Colgan et al. 2016). Figure 1.1 provides a summary of the key characteristics of opacity at a fixed chemical composition. In conditions of low density and high temperature, κ remains nearly constant as it is dominated by electron scattering. In contrast, at higher ρ and lower T, free-free, bound-free and bound-bound absorptions become the predominant mechanisms. Lastly, at $T < 10^4$ K the primary factors influencing opacity are atomic recombination, as well as the formation of molecular species and dust particles.

[4]The term metals refers to all chemical elements heavier than helium, encompassing both traditional metals and metalloids.

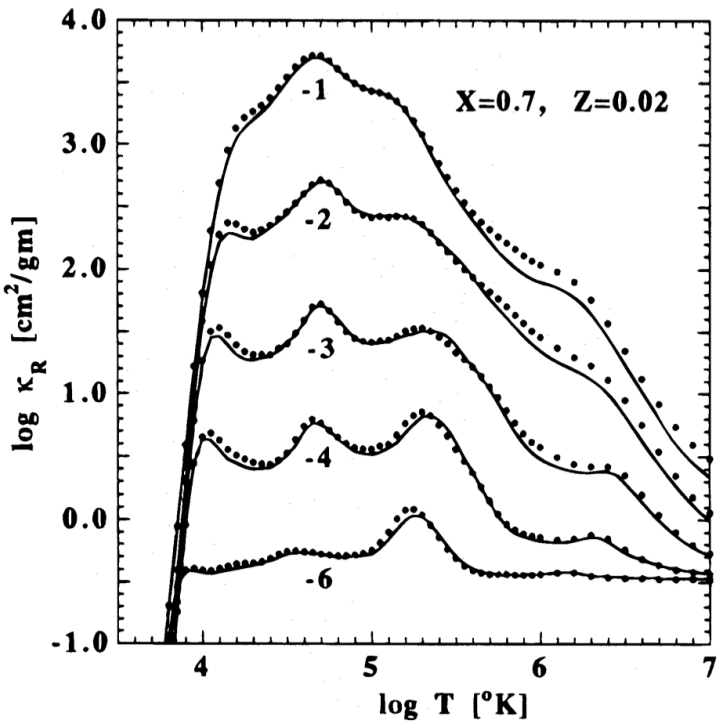

Figure 1.1: Rosseland mean opacity as a function of temperature for various densities, based on the solar mixture presented by Grevesse et al. (1993). The image is sourced from the work of Iglesias et al. (1996).

1.2.2 Convective flux and mixing length theory

In this section, I will provide an overview of the challenges associated with plasma motion in spherically symmetric stars, as well as the conventional approaches used to quantify convective heat flux in one-dimensional evolutionary models.

As outlined in Section 1.1.2, when the motion of plasma inside stars becomes significant, it exhibits no preferential direction of flow and is characterised by a significant degree of turbulence, as indicated by a high Reynolds number. Therefore, even with spherically symmetric stars in hydrostatic equilibrium, it would be necessary to use three-dimensional codes. However, these codes still struggle to accurately simulate long-term convective flows, and are only capable of representing thick convective layers effectively (see also Kupka et al. 2017, for a review on modelling turbulent flows in stars). Therefore, simplifying assumptions and hypotheses about the motion of plasma in stars are needed and cannot be derived self-consistently from the set of equations 1.1.3. One of the most used phenomenological models for local, time-independent convection in stars is the mixing length theory (MLT; e.g. Cox et al. 1968). This model introduces the concept of subsonic flow of fictitious bubbles that are not present in actual convective flows, whether observed in the Sun, Earth's atmosphere, oceans, laboratory experiments of convection, or numerical simulations. De-

spite this limitation, MLT remains popular due to its simplicity and adaptability. The fundamental assumptions underlying this theory include:

- The number of parcels ascending is equal to the number of parcels descending, with all quantities being averaged over a spherical shell, implying the absence of horizontal motion;
- The moving bubbles are in pressure equilibrium with their environment, given that their velocity is significantly lower than the local sound speed;
- Convective regions achieve instantaneous mixing within a single evolutionary time step;
- Each ascending plasma bubble disperses into the surrounding medium after traveling a characteristic distance known as the mixing length (λ_{MLT}). This mixing length serves as a free parameter that can be calibrated against observational data, allowing the predictions to be adjusted accordingly. Consequently, MLT conceptualises a single large-scale eddy of length λ_{MLT} rather than numerous progressively smaller eddies.

Through a comprehensive examination of the dynamics and heat transfer of these bubbles (see for example Kippenhahn et al. 2012), one can derive the system of equations

$$\begin{cases} \Gamma_{\mathrm{conv}} = \dfrac{\nabla - \nabla_{\mathrm{e}}}{\nabla_{\mathrm{e}} - \nabla_{\mathrm{ad}}} \\ U = \dfrac{24\sqrt{2}\sigma T^{2.5} H_p}{\kappa c_p \sqrt{c_p \nabla_{\mathrm{ad}}} \rho^2 \lambda_{\mathrm{MLT}}^2} \\ \nabla_{\mathrm{e}} - \nabla_{\mathrm{ad}} = 2U\sqrt{\nabla - \nabla_{\mathrm{e}}} \\ (\nabla - \nabla_{\mathrm{e}})^{1.5} = \dfrac{8U}{9}\left(\nabla_{\mathrm{rad}} - \nabla\right), \end{cases} \tag{1.2.3}$$

where Γ_{conv} is the efficiency of the convective heat flux, ∇_e signifies the temperature gradient of a plasma parcel that is either ascending or descending within the convective zone and ∇ the temperature gradient of the surroundings. Additionally, the adiabatic temperature gradient (∇_{ad}) is defined as

$$\nabla_{\mathrm{ad}}(r,t) := \frac{P}{\rho c_P T}\left(-\left.\frac{\partial \ln \rho}{\partial \ln T}\right|_P\right). \tag{1.2.4}$$

This gradient describes the temperature profile that the parcel would maintain if it were to move adiabatically. In equation 1.2.3, H_p represents the pressure scale height and λ_{MLT} is conventionally expressed as $\lambda_{\mathrm{MLT}} = \alpha_{\mathrm{MLT}} H_p$, with α_{MLT} being a dimensionless constant

parameter of the model, typically of order unity, used for calibration against empirical data.

Equation 1.2.3 indicates that in regions where $\Gamma_{\rm conv} \approx 0$ (such as in the outermost layers of the Sun), $\nabla \simeq \nabla_{\rm rad}$, which means that the predominant mechanism for heat transfer in these layers is radiation rather than convection[5]. However, it is not always necessary to solve the MLT equations, as the uncertainties associated with this theory diminish when convection is sufficiently effective in heat transport. This is the case for the dense central regions of stars and for throughout much of the convective envelope. For instance, in the Sun, $\Gamma_{\rm conv} \approx 10^{6-9}$ until the outermost layers (Kippenhahn et al. 2012). In such scenarios, equation 1.2.3 indicates that $\nabla \simeq \nabla_{\rm ad}$, which means that each plasma bubble moves almost adiabatically until it reaches the boundary of the convective envelope. Furthermore, regions where ∇ falls between $\nabla_{\rm ad}$ and $\nabla_{\rm rad}$ are termed superadiabatic. High values of $\Gamma_{\rm conv}$ will be relevant for central convection in core helium burning stars, where the primary concern lies in the extent of the convective core rather than the MLT itself (Section 1.3). On the other hand, to gain a more comprehensive understanding of the stellar physics at the surface layers, non-local and time-dependent models of convection are necessary. Such models are essential as convection can induce pulsations, either driving or damping them, and these pulsations may, in turn, influence the convection process (see Houdek et al. 2015, for a review).

Schwarzschild criterion

To understand the foundation of the MLT, it is important to examine the conditions under which plasma motion occurs within stars that are in hydrostatic equilibrium. Notably, small fluctuations resulting from the thermal motion of particles are always present. In regions where these perturbations are dissipated, plasma motion is negligible. Consequently, the material mixing within these layers is minimal, apart from the overshooting regions (see Section 1.3.2), and the convective heat flux is significantly less than the radiative heat flux. These regions are called radiative (see Section 1.2.1). However, in layers where these perturbations grow over time, material mixing takes place, and the convective heat flux may emerge as the predominant mechanism of heat transport.

A fundamental and flexible model used to analyse the conditions under which convection takes place is the Schwarzschild criterion (Schwarzschild 1958), illustrated in figure 1.2. For simplicity, consider a plasma with constant mean molecular weight, but density ρ_1

[5]Nonetheless, a mixing of material still is present within such a convective region.

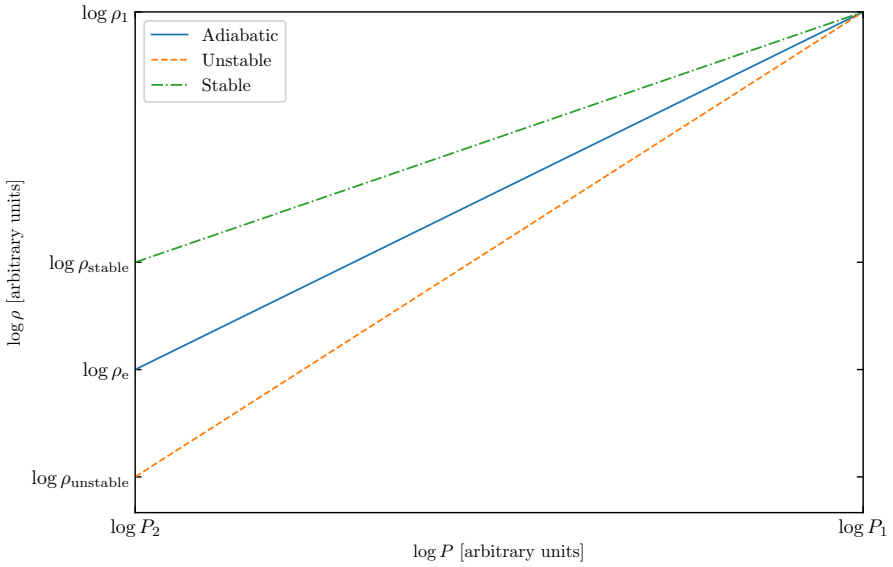

Figure 1.2: Density profiles to summarise the stability criterions for plasma parcels against convection.

and pressure P_1 at position r. We can define ρ_2 and P_2 as the density and pressure, respectively, in the surrounding environment at position $r + dr$. If a fictitious bubble of plasma located at r undergoes a small upward displacement of dr, it has to expand to achieve pressure equilibrium with its surroundings, resulting in new density $\rho_e < \rho_1$. If $\rho_e > \rho_2$, the bubble experiences a net buoyancy force directed downward, causing it to return to its initial position. This motion is characterised by damped oscillations around that position, occurring at a frequency referred to as the Brunt–Väisälä frequency (see Section 1.2.2). In this scenario, the region is stable against convection. Conversely, if $\rho_e < \rho_2$, a net upward buoyancy force is present, which induces convection. If we assume that $\nabla_{\text{e}} = \nabla_{\text{ad}}$ during the upward displacement dr, from equation 1.2.3 we obtain that a layer is unstable for convection where $\nabla_{\text{rad}} \geq \nabla_{\text{ad}}$. In particular, the gradient is superadiabatic where the convection is not efficient (for example in the near-surface convective regions) and adiabatic where the convection is very efficient (Section 1.2.2). On the contrary, regions with $\nabla_{\text{rad}} < \nabla_{\text{ad}}$ are convectively stable and we can use $\nabla = \nabla_{\text{rad}}$.

Ledoux criterion

In the preceding section, I did not account for variations in chemical composition within the star. This section aims to present a generalisation of the Schwarzschild criterion that incorporates gradients in mean molecular weight (∇_μ), known as the Ledoux criterion (Ledoux 1947).

As with the earlier discussion, a summary of this criterion is illustrated in figure 1.2.

The difference respect to the Schwarzschild criterion being a different mean molecular weight of the surrounding environment between position r and $r + dr$. If the fictitious bubble of plasma experiences a small upward displacement without any exchange of matter with its surroundings, then the mean molecular weight of the bubble remains unchanged. The region is considered convectively stable when $\rho_e > \rho_2$, and unstable when $\rho_e > \rho_2$. The revised criterion for instability is expressed as (see e.g. Kippenhahn et al. 2012)

$$\nabla_{\rm rad} \geq \nabla_{\rm ad} - \frac{\chi_\mu}{\chi_T}\nabla_\mu, \tag{1.2.5}$$

where $\chi_\mu := \frac{\partial \ln P}{\partial \ln \mu}\Big|_{\rho,T}$, $\chi_T := \frac{\partial \ln P}{\partial \ln T}\Big|_{\rho,\mu}$ and $\nabla_\mu := \frac{d \ln \mu}{d \ln P}$. Notably, this new criterion aligns with the Schwarzschild criterion in cases where $\nabla_\mu = 0$. From equation 1.2.5 it can be observed that a gradient in composition may stabilise regions that would otherwise be convectively unstable according to the Schwarzschild criterion, or conversely, can lead to instability (see also Salaris et al. 2017, for a review). For instance, a layer constituted of an ideal gas (where $\chi_T = -\chi_\mu = 1$) that is classified as unstable based on the Schwarzschild criterion ($\nabla_{\rm rad} \geq \nabla_{\rm ad}$) can still exhibit stability under the Ledoux criterion ($\nabla_{\rm rad} < \nabla_{\rm ad} + \nabla_\mu$) if $\nabla_\mu > 0$. This observation is essential to understand semiconvective zones in stars undergoing the core helium burning phase (see Section 1.3.2).

In conclusion, it is important to highlight that a comprehensive understanding of the Ledoux criterion can be encapsulated through the examination of the frequency of oscillations around stable positions in radiative zones. This is effectively represented by the squared Brunt–Väisälä frequency

$$N^2 = \frac{g^2\rho}{P}\frac{\chi_T}{\chi_\rho}\left(\nabla_{\rm ad} - \nabla - \frac{\chi_\mu}{\chi_T}\nabla_\mu\right), \tag{1.2.6}$$

where $\chi_\rho := \frac{\partial \ln P}{\partial \ln \rho}\Big|_{T,\mu}$. In this context, regions that exhibit stability according to the Ledoux criterion are characterised by a real value of the Brunt–Väisälä frequency (i.e. $N^2 > 0$), while unstable layers correspond to null or imaginary frequencies (i.e. $N^2 \leq 0$). This frequency will be particularly useful to understand asteroseismology of radiative regions in solar-like oscillators (see Section 1.4).

1.3 Low-mass core helium burning stars

In this section, I explore the core helium burning (CHeB) stage encountered by stars with masses below $\approx 1.8 - 2.2$ $M_\odot$ depending on metallicity [6]. Helium burning in these stars is ignited by a series of helium flashes that eliminate the degeneracy of the helium core

[6] The higher the metallicity, the lower the mass (e.g. Girardi 2016).

formed during the red giant branch phase (Section 1.3.1). For clarity and simplicity, in this section I will primarily focus on evolutionary models computed at solar metallicity ($Z_{\odot} = 0.0134$), utilising solar composition outlined by Asplund et al. (2009), unless otherwise specified. In Section 1.3.2, I will address the uncertainties related to the chemical and thermal stratifications near the boundary of the convective core, emphasising the most commonly used mixing prescriptions. Finally, in Section 1.3.3, I will examine the key issues pertaining to nuclear reaction rates during the CHeB phase.

1.3.1 Helium flashes

Towards the conclusion of the red giant branch (RGB; e.g. Kippenhahn et al. 2012) phase, low-mass stars contain an inert, electron degenerate helium core characterised by quasi-isothermal conditions and non-relativistic behaviour. The internal pressure of this core is primarily generated by degenerate non-relativistic electrons, though there is also a smaller contribution from non-degenerate ions, which will become relevant for the subsequent phases. Consequently, the total pressure within the core can be expressed as

$$P = P_e + P_{\rm ion} = K \left(\frac{\rho}{\mu_e} \right)^{5/3} + \frac{\rho K_B T}{\mu_{\rm ion} m_p}, \tag{1.3.1}$$

where the ions are modelled as an ideal gas for the purposes of this analysis. During the RGB phase, both the temperature and the mass of the helium core progressively increase over time. Numerical calculations indicate that as the core mass grows, the temperature within the core rises, exhibiting spatial variation. This phenomenon can be attributed to two closely related effects. First, the temperature of the surrounding shell increases, contributing to the heating of the core. Additionally, non-stationary processes play a role; as the shell becomes more efficient, it adds more helium to the core. As the mass of the helium core increases, it undergoes contraction, which releases energy. If this contraction occurs rapidly enough, it can heat the transition layer below the shell, raising the temperature of the entire core. Moreover, neutrinos produced within the core interact minimally with the surrounding stellar material, resulting in a cooling effect that modifies the temperature gradient in the core. This causes the peak temperature to shift from the centre to a specific mass value within the core. It is important to note that the primary source of pressure in the core (i.e. degenerate electrons) does not depend on temperature. Therefore, an increase in temperature does not change the pressure $P_e \approx P$ as indicated in equation 1.3.1, meaning the core lacks sufficient pressure to eliminate degeneracy.

When the core temperature is $\approx 10^8$ K, the 3α nuclear reaction (Section 1.3.3) begins in a degenerate environment. Therefore, no work can be done on the environment ($P\,d\rho \approx$

0) and the nuclear energy is directly transformed into internal energy. This situation corresponds to a helium core mass of ≈ 0.47 $M_\odot$ independently on the total mass of the star[7] (e.g. Girardi 2016). At this point, a thermal runway starts with a huge energy production at the location of maximum temperature and lasts seconds. This luminosity is comparable with the total luminosity of a massive disc galaxy (i.e. $\sim 10^{10}$ $L_\odot$) and it does not reach the surface. Instead, it is used by the ions to remove the degeneracy by expanding the core. This corresponds to a helium flash. In models of stellar evolution, we have not just an episode, but at least three or four subflashes that start from the boundary of the helium core to the centre of the star. The final result is a non-degenerate helium core that reaches a thermal equilibrium regulated by the 3α nuclear reaction: the CHeB stage begins. These flashes leave a chemical imprint within the helium core of the star, which is also visible in the Brunt-Väisälä frequency (e.g. Mocák et al. 2011). Key unresolved questions include the frequency and spatial distribution of these flashes, the behaviour of convection during the rapid evolution of the helium flash, and the degree of spherical symmetry and hydrostatic equilibrium during the ignition of helium and the subsequent flashing in a shell. Furthermore, mixing induced by the flashes may take place if the convective shell that forms in the helium-burning region during the flash merges with the outer convective layer. This additional mixing could significantly enhance surface abundances of carbon produced by the 3α reaction, as well as nitrogen generated from proton captures on some of this carbon.

In conclusion, it is important to examine the variations of luminosity of the star during helium flashes. As previously discussed, the mass of the helium core ($M_{\rm core}$) remains constant throughout this process, while its radius ($R_{\rm core}$) experiences an increase. This expansion results in a reduction of the total luminosity, primarily because the hydrogen-burning shell surrounding the helium core serves as the principal energy source, and its luminosity follows the relation (see Kippenhahn et al. 2012)

$$L \approx M_{\rm core}^{7} R_{\rm core}^{-16/3}. \tag{1.3.2}$$

Therefore, at the beginning of the CHeB phase, the star has a lower luminosity than before the first helium flash. In one-dimensional models, this transitional phase generally lasts approximately 2 Myr, which poses challenges for observations in stellar systems. By the time the star stabilises on the horizontal branch, its helium-burning core will have undergone a carbon enrichment of approximately 5% by mass. It is noteworthy that RGB stars with masses less than ≈ 0.5 $M_\odot$ lack sufficient material to develop helium cores with

[7]The higher the metallicity, the slightly lower the helium core mass

a mass ≈ 0.47 $M_\odot$. Consequently, these lower-mass stars are unable to initiate helium fusion in their core and are destined to evolve into helium white dwarfs. However, such an evolution pathway cannot be achieved through single stellar evolution, as it would require a time span exceeding the current age of the Universe.

1.3.2 Mixing prescriptions

At the beginning of the CHeB phase, the central region of the star where nuclear reactions occur becomes convective. This change is induced by the substantial increase in $\nabla_{\rm rad}$ (equation 1.2.2) driven by the energy released by the 3α reaction rate. This rise results in $\nabla_{\rm rad}$ exceeding $\nabla_{\rm ad}$ (Schwarzschild criterion, see Section 1.2.2), establishing the boundary between the convective and radiative cores at the point where $\nabla_{\rm rad} = \nabla_{\rm ad}$. As the CHeB phase progresses, the convective core exhibits increased concentrations of carbon and oxygen owing to ongoing nuclear fusion processes (Section 1.3.3). The augmentation of carbon and oxygen leads to enhanced opacity, since free-free transitions are positively correlated with nuclear charge (e.g. Kippenhahn et al. 2012). It follows from equation 1.2.2 that within the convective core, $\nabla_{\rm rad}$ continues to rise. Therefore, this disparity in chemical composition creates a jump discontinuity in opacity, in $\nabla_{\rm rad}$ (as illustrated in figure 1.3) and in density at the boundary between the radiative and convective core (e.g. Ledoux 1947; Schwarzschild 1958; Castellani et al. 1971b). In stellar evolution codes, employing the Schwarzschild criterion to assess convective stability from the radiative side of the boundary (specifically, if the convective edge is determined based on the limit from the right of $\nabla_{\rm rad}$) can lead to a misinterpretation of the criterion. Such an implementation may result in unstable and non-physical behaviours at the boundary. As shown in the left panel of figure 1.3, the convective core cannot significantly increase in mass under these conditions, and the position of its boundary becomes destabilised by the discontinuity in opacity. This approach is commonly referred to as "bare Schwarzschild" (as explained by e.g. Straniero et al. 2003; Bossini et al. 2015; Salaris et al. 2017), and it establishes a minimum estimate for the extent of the convective core, as well as a lower bound on the lifetime of a CHeB star. In contrast, the correct implementation of the Schwarzschild criterion must be performed from the convective side of the core. Here, the convective boundary is determined based on the limit from the left of $\nabla_{\rm rad}$ (see discussion in e.g. Schwarzschild 1958; Castellani et al. 1971b; Gabriel et al. 2014). The right panel of figure 1.3 illustrates that, under this interpretation, the convective core can grow until a local minimum in $\nabla_{\rm rad}$ meets $\nabla_{\rm ad}$, allowing for a potential splitting of the convective region (see subsection below). To

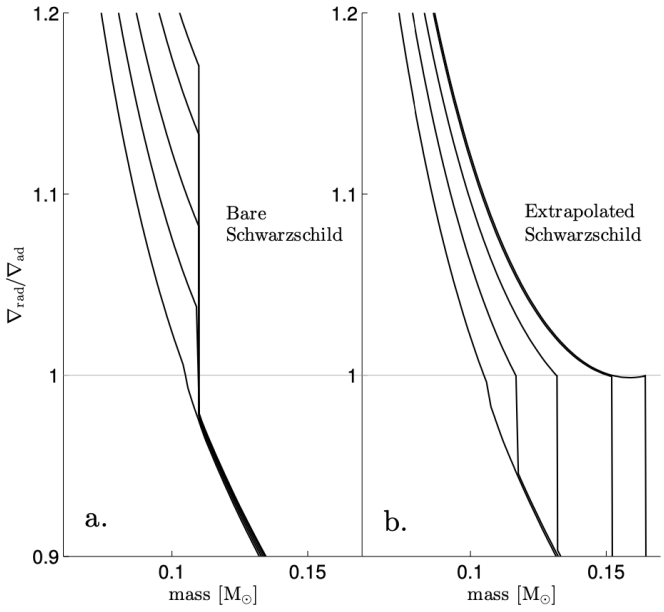

Figure 1.3: The ratios of $\nabla_{\rm rad}$ to $\nabla_{\rm ad}$ are plotted as functions of internal mass at various evolutionary stages during the CHeB phase. The left panel illustrates an erroneous interpretation of the Schwarzschild criterion, leading to an unstable and non-physical behaviour of the convective boundary (referred to as "bare Schwarzschild" mixing prescription, detailed in Section 1.3.2). The right panel depicts the correct interpretation of the Schwarzschild criterion (labelled "extrapolated Schwarzschild", as detailed in Section 1.3.2). Figure adapted from Bossini et al. (2015).

further clarify the limitations of the "bare Schwarzschild" approach, consider the concept of induced overshooting. Each convective element possesses non-zero linear momentum at the boundary where $\nabla_{\rm rad} = \nabla_{\rm ad}$. This momentum facilitates the mixing of carbon and oxygen-rich material from the convective core with the surrounding radiative core. Consequently, as this mixing occurs, $\nabla_{\rm rad}$ increases, inducing convective instability in the previously radiative region. Therefore, even in this scenario, the convective boundary is determined based on the limit from the left of $\nabla_{\rm rad}$.

Semiconvection

During the subsequent evolution, evolutionary stellar models suggest that the growth of the convective core is associated with changes in the physical conditions within the region. These alterations, in conjunction with the accumulation of helium-rich materials, lead to the establishment of a local minimum in $\nabla_{\rm rad}$ within the convective core (see right panel of figure 1.3). Shortly after this local minimum is formed, there is a noticeable decrease in $\nabla_{\rm rad}$ within the convective core, driven by an overall increase in helium-rich materials that results in decreased opacity (see Salaris et al. 2017, for a review). When $Y_c \approx 0.7$ (Castellani et al. 1971a), this minimum in $\nabla_{\rm rad}$ becomes equal to $\nabla_{\rm ad}$. This condition

results in the formation of a convective core characterised by a discontinuity in $\nabla_{\rm rad}$ at its boundary, along with an intermediate region where $\nabla_{\rm rad} = \nabla_{\rm ad}$ holds true. Nevertheless, such a situation may allow for a section of the mixed core near this minimum to exhibit convective stability, thereby presenting a contradiction within our model. Specifically, if instantaneous mixing were to occur throughout the entire convective core, it would produce a reduction in $\nabla_{\rm rad}$ across the mixed region, which would in turn result in a portion of the core near the minimum achieving a state where $\nabla_{\rm rad} < \nabla_{\rm ad}$. To address this issue, one may define the area between $\nabla_{\rm rad} = \nabla_{\rm ad}$ and the outer boundary as a semiconvective region (Castellani et al. 1971a). In this region, a plasma parcel oscillates vertically with increasing amplitude, ascending progressively into the layer. This represents a slow mixing environment, which results in a inhomogeneous chemical composition. In this location, the star exhibits instability with respect to convection according to the Schwarzschild criterion, yet stability according to the Ledoux criterion (see Section 1.2.2). The complexity of this process lies in the fact that any degree of mixing inevitably influences the stratification within the mixed layer (see also the discussion in Gabriel et al. 2014). Nevertheless, each semiconvective layer is mixed to such an extent that $\nabla = \nabla_{\rm ad}$ is achieved in this region if the diffusion coefficient is large enough (Castellani et al. 1971a). Indeed, this is the approach employed by numerical simulations to address semiconvective layers when the main focus is to understand the final structure of the core rather than conduct a detailed study of the physical properties.

Overshooting

One treatment that extends mixing beyond the classical boundary is convective overshooting. As mentioned earlier, each convective element has non-zero linear momentum at the boundary where the radiative gradient equals the adiabatic gradient. It is generally assumed that this overshooting into stable layers does not alter their thermal gradient, thereby maintaining $\nabla = \nabla_{\rm rad}$. Within the framework of the step overshooting formalism introduced by Maeder (1975), it is proposed that the composition is instantaneously homogenised between the convective boundary and the radiative layers situated at a distance $d_{\rm ov} = \alpha_{\rm ov} H_p$ from this boundary. Here, $\alpha_{\rm ov}$ is a constant free parameter (overshooting parameter) that is calibrated against observational data, while H_p represents the pressure scale height at the convective boundary. Nevertheless, this approach is not unique; alternative criteria can also be established, resulting in varying mixing prescriptions within stellar models. For instance, choosing an adiabatic temperature gradient instead of main-

taining a radiative gradient results in a convective overshoot region, a mixing prescription known as penetrative convection (Zahn 1991). Although this method produces comparable results with step overshooting, the Brunt-Väisälä frequencies differ between the two scenarios, leading to discernible variations observable through asteroseismology (see Section 4). Additionally, overshooting regions with intermediate temperature gradients have also been proposed (Christensen-Dalsgaard et al. 2011). Moreover, plasma transport beyond the convective boundary may be a diffusive process, resulting in a slower mixing process that provides different lifetimes of the CHeB phase compared to instantaneous mixing. This mixing prescription is described as diffusive overshooting (Herwig 2000), where the constant free parameter is contained inside the diffusion coefficent. Other evolutionary models adopt modified forms of step overshooting (e.g. Bossini et al. 2015; Constantino et al. 2015; Bossini et al. 2017; Noll et al. 2024). Others avoid the semiconvective region by employing non-local treatments for core overshooting (e.g. Bressan et al. 1986).

1.3.3 Nuclear reaction rates

During the early stages of the CHeB phase, two predominant sources of nuclear energy are present within the star. The 3α reaction serves as the primary mechanism occurring in the convective core, while the CNO cycle is the main energy producer in the hydrogen-burning shell. For $Y_c > 0.7$, the CNO cycle plays a more significant role in energy production than the 3α process. However, as Y_c declines beyond this threshold, the 3α reaction increasingly dominates. Eventually, when $Y_c < 0.2$, the primary source of energy is the nucleosynthesis reaction $^{12}\mathrm{C}(\alpha,\gamma)^{16}\mathrm{O}$ (e.g. Straniero et al. 2003).

The 3α reaction involves two key processes: the fusion of two helium-4 nuclei to form beryllium-8 ($^4\mathrm{He} + {}^4\mathrm{He} \longleftrightarrow {}^8\mathrm{Be}$), followed, in less than 10^{-16} s, by the interaction of beryllium-8 with another helium-4, resulting in the production of carbon-12 in an excited state, which subsequently decays to ground state carbon-12 and a gamma photon ($^8\mathrm{Be} + {}^4\mathrm{He} \longrightarrow {}^{12}\mathrm{C}^* \longrightarrow {}^{12}\mathrm{C} + \gamma$). This sequence of reactions occurs at temperatures of approximately 10^8 K. The reaction rate for helium burning is quite well known within the typical temperature and density ranges encountered by CHeB stars. However, Angulo et al. (1999) estimate a 25% uncertainty in the reaction rate at helium-burning temperatures, and Fynbo et al. (2005) have suggested an uncertainty of approximately 12%. This latter estimate is consistent with other evaluations of the reaction rate, although Kibédi et al. (2020) have presented a value that deviates from the current consensus by roughly 34%. During the dominance of the 3α reaction (approximately 100 Myr, see Girardi 2016),

the luminosity of the star increases slightly. Changes in the 3α reaction rate produce a negligible change in the luminosity of the star at the tip of the red giant branch phase and at the beginning of the CHeB phase, and a small change in CHeB lifetime.

The $^{12}C(\alpha,\gamma)^{16}O$ reaction fuses one carbon-12 nucleus with a helium-4 to form oxygen-16 and a gamma foton ($^{12}C + {}^{4}He \longrightarrow {}^{16}O + \gamma$). From an evolutionary perspective, when this reaction becomes dominant, the helium core becomes more compact. Therefore, the CNO cycle in the hydrogen-burning shell becomes more efficient (equation 1.3.2) and the total luminosity of the star increases. The cross-sections of this reaction have always been uncertain at the temperature of interest for CHeB stars (e.g. Metcalfe et al. 2002; Straniero et al. 2003; Cassisi et al. 2003). Kunz et al. (2002) reported an uncertainty of 35%, Hammer et al. (2005) an uncertainty of 30% and deBoer et al. (2017) estimate an uncertainty of about 20% at central helium-burning temperature. These uncertainties are relevant in determining the chemical profile left at the end of the shell helium-burning phase, but they have a negligible effect on the predicted evolutionary time scale (e.g. Cassisi et al. 2003; Straniero et al. 2003; Bossini et al. 2015; Constantino et al. 2015; Bossini et al. 2017; Tognini et al. 2023; Noll et al. 2024) compared to other sources of uncertainty (as the convective buondary mixing, see Section 1.3.2).

1.4 Asteroseismology of solar-like oscillators

In this section I review the main physical processes involved in the asteroseismology of solar-like oscillators. Unless explicitly stated otherwise, many parts of this section are based on the book by Aerts et al. (2010).

Cepheids, RR Lyrae, Mira, δ Scuti, β Cephei stars are all examples of stars exhibiting pulsations, primarily driven by the κ-mechanism and γ-mechanism. These stars display large observable amplitudes, and it was soon recognised (e.g. Shapley 1914) that these oscillatory motions correlate closely with the dynamical time scale

$$\tau_{\rm dyn} = \sqrt{\frac{R^3}{GM}} \approx 27 \left(\frac{R}{R_\odot}\right)^{1.5} \left(\frac{M_\odot}{M}\right)^{0.5} \text{min.} \tag{1.4.1}$$

Another major driving mechanism for stellar oscillations is stochastic driving. This phenomenon is particularly relevant for stars similar to the Sun, for red giant stars, and, generally for stars possessing a convective envelope. In this case, even if the κ-mechanism is not able to drive the oscillations and the modes are intrinsically stable, it is still possible to observe deviations of the order of μmag in luminosity or cm/s in radial velocity. The chaotic turbulent motion (see Section 1.1.2) within the convective envelope plays a crucial

role in this process. Near the surface of these stars, this turbulent motion occurs at near-sonic speeds (e.g. Kippenhahn et al. 2012), providing an efficient mechanism for exciting the normal eigenmodes of the star to observable amplitudes. Consequently, solar-like oscillations can be understood as damped harmonic oscillations that are externally forced by acoustic noise from this turbulent activity. Each eigenmode possesses a power spectrum $[P(\omega)]$, which can be derived from a Fourier-like transform applied to time series data. This spectrum is characterised by a Lorentzian profile, described by the equation

$$P(\omega) \propto \frac{1}{(\omega - \omega_{\text{peak}})^2 + \eta^2}, \tag{1.4.2}$$

where ω_{peak} denotes the angular frequency of the peak, and η represents the half-width at half maximum (i.e. the linear damping rate of the mode). The amplitudes of these Lorentzian functions are further modulated by a Gaussian envelope (see figure 1.4), with its peak indicating the maximum power. The frequency at this maximum power (ν_{max}) serves as an indicator of the surface gravity of the star once the effective temperature is known. The same figure also allows for the derivation of two significant seismic indicators: the large frequency separation ($\Delta\nu$) and the small frequency separation ($\delta\nu$). $\Delta\nu$ is defined as the difference between two modes of the same angular degree but consecutive radial orders (see definition in Section 1.4.3) and is related to the average density of the star. By combining $\Delta\nu$, ν_{max} and the effective temperature, one can estimate the total mass and radius of the star. Conversely, $\delta\nu$ represents the difference between two modes of consecutive radial order but differing angular degrees, providing insights into the internal properties of stars (see definition in Section 1.4.3). For stars in the CHeB phase, oscillation patterns exhibit increased complexity, which will be discussed in detail in Section 2. In Section 1.4.1, I will outline the methodology for calculating linear oscillations in spherical, non-rotating, non-magnetic stars. Section 1.4.2 will explore an approach to analyse the general behaviour of these oscillations, while Section 1.4.3 will focus on the principal types of oscillations observed in solar-like oscillators.

1.4.1 Adiabatic linear oscillations

Stellar oscillations play a crucial role in our understanding of stellar structure and evolution, providing insights into internal structure and chemical composition. Among the various factors influencing these oscillations, turbulence is a significant yet unresolved issue (see Section 1.1.2). In solar-like oscillators, the computation of oscillation modes must account for various physical effects, particularly nonadiabatic ones that become pronounced near the stellar surface. At this depth, the interplay between oscillations and convection is

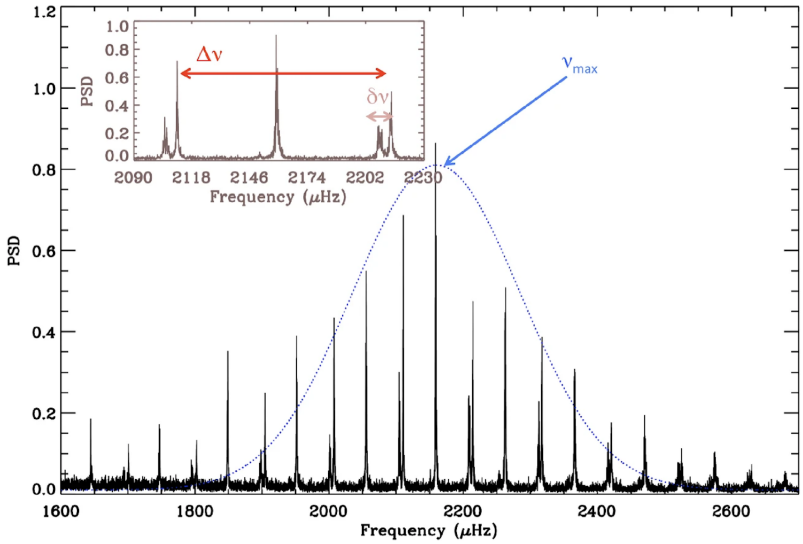

Figure 1.4: Periodogram (in arbitrary units) of the *Kepler* target 16 Cyg A. The Gaussian envelope used to determine the frequency at the maximum power ($\nu_{\max}$) is in blue. The zoom shows the large frequency separation $\Delta\nu$, and the small frequency separation $\delta\nu$. Image took from García et al. (2019).

critical; however, it is often neglected the contribution of convection to the heat flux during perturbation calculations. This introduces a major uncertainty in the calculation of the stability of modes in cool stars with extensive outer convection zones. Furthermore, the improper modelling of the near-surface layers contributes to a general shift of the computed frequencies that depends on their inertia: the near-surface effects (see e.g. Ball et al. 2017). Notably, oscillations occur over exceedingly short timescales, allowing the assumption that the equilibrium state can be regarded as time-independent. The equations governing these oscillations can be derived by considering only the first-order terms in perturbation theory, as the oscillation amplitudes are significantly smaller than the stellar dimensions. Two primary frameworks exist for describing linear perturbations to an equilibrium state Q_0: the Eulerian and the Lagrangian formulations. In the Eulerian approach, the specific spatial location from which perturbations are evaluated remains fixed. Consequently, the Eulerian perturbation of a quantity Q in the position $\vec{x}$ is defined as

$$Q'(\vec{x},t) := Q(\vec{x},t) - Q_0(\vec{x}). \tag{1.4.3}$$

Conversely, the Lagrangian perturbation is determined by tracking the motion of the plasma parcel as it transitions from the equilibrium position $\vec{x}_0$ to a new position $\vec{x} := \vec{x}_0 + \delta\vec{x}$; this is expressed as

$$\delta Q(\vec{x},t) := Q(\vec{x}_0+\delta\vec{x},t) - Q_0(\vec{x}_0) = Q'(\vec{x}_0,t) + \left(\delta\vec{x}\cdot\vec{\nabla}\right) Q_0(\vec{x}_0), \tag{1.4.4}$$

where the quantity $\delta\vec{x}$ represents the Lagrangian displacement[8].

Before I proceed with the analysis of the perturbed quantities, I will start by examining equation 1.2.1, which describes the equilibrium quantities, and establish useful approximations. As previously noted in Section 1.4, I have to disregard the influence of convection on the heat flux while calculating these perturbations. Consequently, I will focus exclusively on the radiative zone of a solar-like star. By incorporating L_r, $\nabla = \nabla_{\rm rad}$ and the definition of $\nabla_{\rm ad}$ into equation 1.2.1, one can derive the equation

$$\frac{\partial \ln T}{\partial t} - \nabla_{\rm ad}\frac{\partial \ln P}{\partial t} = \frac{\varepsilon_{\rm nuc} - \varepsilon_\nu}{c_P T} + \frac{1}{\rho c_P T r^2}\frac{\partial}{\partial r}\left(\frac{16\sigma T^3}{3\kappa\rho} r^2 \frac{\partial T}{\partial r}\right). \tag{1.4.5}$$

The terms on the left-hand side of equation 1.4.5 evolve over different timescales compared to those on the right-hand side. Thus, when considered independently, these terms approximate to

$$\frac{\varepsilon_{\rm nuc} - \varepsilon_\nu}{c_P T} + \frac{16\sigma T^3}{3\kappa\rho^2 c_P H^2_{\rm scale}} \approx \frac{1}{10^7\,\text{years}} \tag{1.4.6}$$

and

$$\frac{\partial \ln T}{\partial t} - \nabla_{\rm ad}\frac{\partial \ln P}{\partial t} \approx \frac{1}{\tau_{\rm dyn}} \approx \frac{1}{27\,\text{min}} \tag{1.4.7}$$

based on typical conditions found within the Sun's interior. Consequently, with a high degree of precision, the complexities associated with the energy equation can be avoided by omitting the heating term until reaching the outer layers of the convective envelope, where this approximation no longer holds. A similar rationale is applicable to linear perturbations, leading to adiabatic linear oscillations. Following this, one can perturb the three-dimensional equations 1.1.3 to obtain

$$\begin{cases} \delta\rho = -\rho_0 \vec{\nabla}\delta\vec{x} \\ \rho_0 \dfrac{\partial^2 \delta\vec{x}}{\partial t^2} = -\vec{\nabla}P' - \rho_0\vec{\nabla}\phi' - \rho'\vec{\nabla}\phi_0 \\ \nabla^2\phi' = 4\pi G\rho' \\ \delta P = \dfrac{\Gamma_{1,0}P_0}{\rho_0}\delta\rho, \end{cases} \tag{1.4.8}$$

where $\Gamma_{1,0} := \left.\frac{\partial \ln P_0}{\partial \ln \rho_0}\right|_{s_0}$ represents the first adiabatic index of the equilibrium model. At this stage, it becomes advantageous to employ spherical coordinates. This allows us to express $\delta\vec{x}$ as $\delta\vec{x} = \xi_r(r,\theta,\phi,t)\vec{e}_r + \vec{\xi}_h(r,\theta,\phi,t)$ leading to the formulation of a new system

[8]It is important to note that at first order, the time derivative of the perturbed quantity Q is connected to the time derivative of the Lagrangian perturbation via the relation $\frac{dQ}{dt} = \frac{\partial \delta Q}{\partial t}$. Therefore, the velocity can be expressed as $\vec{v} = \frac{d\vec{x}}{dt} = \frac{\partial \delta\vec{x}}{\partial t}$.

of equations derived from equations 1.4.8 and 1.4.4

$$\begin{cases} \dfrac{\partial^2}{\partial t^2}\left[\rho' + \dfrac{1}{r^2}\dfrac{\partial}{\partial r}\left(r^2\rho_0\xi_r\right)\right] = \nabla_h^2 P' + \rho_0\nabla_h^2\phi' \\ -\rho_0\dfrac{\partial^2\xi_r}{\partial t^2} = \dfrac{\partial P'}{\partial r} + \rho'\dfrac{d\phi_0}{dr} + \rho_0\dfrac{\partial\phi'}{\partial r} \\ \dfrac{1}{r^2}\dfrac{\partial}{\partial r}\left(r^2\dfrac{\partial\phi'}{\partial r}\right) + \nabla_h^2\phi' = 4\pi G\rho' \\ \rho' = \dfrac{\rho_0}{\Gamma_{1,0}P_0}P' + \rho_0\xi_r\left(\dfrac{1}{\Gamma_{1,0}}\dfrac{d\ln P_0}{dr} - \dfrac{d\ln\rho_0}{dr}\right) \\ \rho_0\dfrac{\partial^2\vec{\xi}_h}{\partial t^2} = -\vec{\nabla}_h P' - \rho_0\vec{\nabla}_h\phi'. \end{cases} \tag{1.4.9}$$

Here, there are four unknowns (ξ_r, ρ', P', ϕ') articulated through four equations, as $\vec{\xi}_h$ is a expressible in terms of P' and ϕ'. Additionally, ∇_h^2 denotes the horizontal Laplace operator, while $\vec{\nabla}_h$ represents the horizontal gradient operator.

Spherical harmonics

Equation 1.4.9 contains derivatives of the four functions ξ_r, ρ', P', ϕ' respect to the angular variables (θ, ϕ) solely through the differential operator ∇_h^2. Consequently, one can isolate the angular dependencies of these four variables by employing spherical harmonics $[Y_\ell^m(\theta,\phi)]$. This approach is advantageous because the functions $Y_\ell^m(\theta,\phi)$ are eigenfunctions of the differential operator ∇_h^2, with corresponding eigenvalues of $-\ell(\ell+1)/r^2$. As a result, within equation 1.4.9, one can derive new differential equations that are independent of the variables θ and ϕ. In summary, the angular component is characterised by the angular degree (ℓ), which is a non-negative integer that defines the number of nodal lines on the surface, and the azimuthal order ($|m| \leq \ell$), an integer that denotes the number of surface nodal lines that align with lines of longitude (see figure 1.5). Furthermore, it has been established that the equilibrium model is nearly static on the timescale of the oscillations. Thus, the temporal dependence presented in equation 1.4.9 can be decoupled from the radial and angular variables, as the time derivatives act exclusively on linear combinations of ρ' and ξ_r. The final result is that the four variables can be expressed as

$$\begin{cases} \xi_r(r,\theta,\phi,t) = \sqrt{4\pi}\,\tilde{\xi}_r(r)Y_\ell^m(\theta,\phi)e^{-i\omega t} \\ \rho'(r,\theta,\phi,t) = \sqrt{4\pi}\,\tilde{\rho}'(r)Y_\ell^m(\theta,\phi)e^{-i\omega t} \\ P'(r,\theta,\phi,t) = \sqrt{4\pi}\,\tilde{P}'(r)Y_\ell^m(\theta,\phi)e^{-i\omega t} \\ \phi'(r,\theta,\phi,t) = \sqrt{4\pi}\,\tilde{\phi}'(r)Y_\ell^m(\theta,\phi)e^{-i\omega t}, \end{cases} \tag{1.4.10}$$

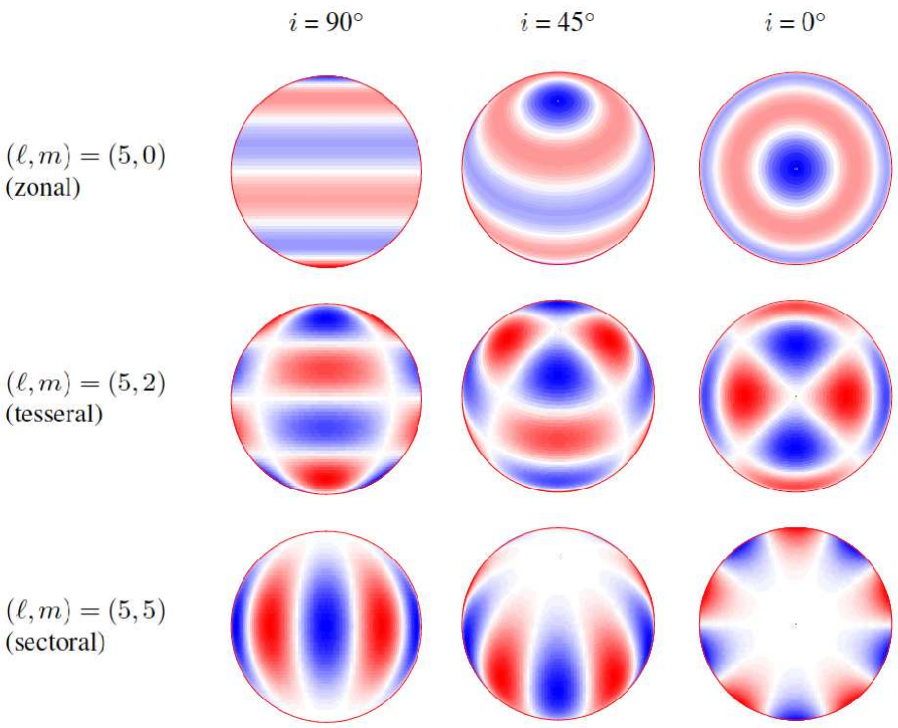

Figure 1.5: Contour plots of the real part of spherical harmonics $Y_\ell^m(\theta, \phi)$. Positive contours are indicated by red lines and negative contours by blue lines. Figure courtesy of K. Uytterhoeven.

leading to a new set of differential equations expressed as

$$\begin{cases} \omega^2 \left[\tilde{\rho'} + \dfrac{1}{r^2} \dfrac{d}{dr} \left(r^2 \rho_0 \tilde{\xi_r} \right) \right] = \dfrac{\ell(\ell+1)}{r^2} (\tilde{P'} + \rho_0 \tilde{\phi'}) \\ \omega^2 \rho_0 \tilde{\xi_r} = \dfrac{d\tilde{P'}}{dr} + \tilde{\rho'} \dfrac{d\phi_0}{dr} + \rho_0 \dfrac{d\tilde{\phi'}}{dr} \\ \dfrac{1}{r^2} \dfrac{d}{dr} \left(r^2 \dfrac{d\tilde{\phi'}}{dr} \right) - \dfrac{\ell(\ell+1)}{r^2} \tilde{\phi'} = 4\pi G \tilde{\rho'} \\ \tilde{\rho'} = \dfrac{\rho_0}{\Gamma_{1,0} P_0} \tilde{P'} + \rho_0 \tilde{\xi_r} \left(\dfrac{1}{\Gamma_{1,0}} \dfrac{d \ln P_0}{dr} - \dfrac{d \ln \rho_0}{dr} \right) \\ \vec{\xi_h} = \sqrt{4\pi}\, \tilde{\xi_h} \left(\dfrac{\partial Y_\ell^m}{\partial \theta} \vec{e}_\theta + \dfrac{1}{\sin\theta} \dfrac{\partial Y_\ell^m}{\partial \phi} \vec{e}_\phi \right) e^{-i\omega t} \\ \tilde{\xi_h} = \dfrac{\tilde{P'} + \rho_0 \tilde{\phi'}}{r \omega^2 \rho_0}, \end{cases} \tag{1.4.11}$$

which is equivalent to a fourth-order differential equation.

Visibility of the modes

In equation 1.4.11, one deals with complex values of ω^2. Nonetheless, it has been demonstrated (e.g. Chandrasekhar 1963; Chandrasekhar 1964) that this system of equations constitutes an eigenvalue problem expressed as $\mathcal{F}(\delta\vec{r}) = \omega^2 \delta\vec{r}$, where $\mathcal{F}$ is a linear operator that is Hermitian for adiabatic oscillations. Consequently, the eigenvalues ω^2 are real, leading to the possibility that ω may either be real or purely imaginary. Therefore,

under the adiabatic approximation, perturbations can present as undamped oscillations or as perturbations that are purely growing or decaying. This implies that the absolute amplitudes of individual eigenmodes cannot be determined solely through adiabatic approximations; since no thermal energy is exchanged, it is not possible to inject or extract energy from the oscillations. Furthermore, this eigenvalue problem is independent of the azimuthal order m; thus, for a fixed ℓ, the values of ω^2 remain the same regardless of the integer m. To derive the perturbed quantities, one can examine the real part of the equations outlined in 1.4.10. As an illustrative example, the perturbed intensity of the star is given by

$$I(\theta, \phi, t) = I_0\sqrt{4\pi}(-1)^m c_{\ell m} P_\ell^m(\cos\theta)\cos(m\phi - \omega t + \delta_0), \tag{1.4.12}$$

where δ_0 denotes an initial phase. Therefore, for the case where $m = 0$, standing waves are observed, while for $m \neq 0$ the behaviour corresponds to traveling waves characterised by an angular speed of ω/m. The period of oscillation for these modes is given by $2\pi/\omega$. A noteworthy consequence of equation 1.4.12 is that modes with $\ell > 3$ remain undetectable in stars regarded as point-like sources. This phenomenon arises because, upon performing an integral average of the perturbed intensity over the stellar surface, it becomes apparent that regions with positive perturbed intensity are counterbalanced by those with negative values for modes with $\ell > 3$. To evaluate the mean square components of the Lagrangian displacement, it is possible to average equation 1.4.10 and equation 1.4.11 over both the surface and time, yielding

$$\begin{cases} \delta r_{\text{rms}}^2 = \langle |\xi_r(r, \theta, \phi, t)|^2 \rangle = \dfrac{|\tilde{\xi}_r(r)|^2}{2} \\ \delta h_{\text{rms}}^2 = \langle \|\vec{\xi}_h r, \theta, \phi, t)\|^2 \rangle = \dfrac{\ell(\ell+1)}{2} |\tilde{\xi}_h(r)|^2. \end{cases} \tag{1.4.13}$$

From this, it follows that oscillation modes with low angular degree exhibit a predominance of radial displacement over horizontal displacement at the surface of the star. Lastly, the time-averaged kinetic energy of each oscillation mode ($\langle E_{\text{kin}} \rangle$) can be derived from equation 1.4.13 and is expressed as

$$\begin{cases} \langle E_{\text{kin}} \rangle = \dfrac{1}{2} \left\langle \displaystyle\int_V \left\| \frac{\partial \delta \vec{r}}{\partial t} \right\|^2 \rho_0 \, dV \right\rangle = \frac{1}{4} \mathcal{E} \omega^2 \\ \mathcal{E} = 4\pi \displaystyle\int_0^R \left[|\tilde{\xi}_r(r)|^2 + \ell(\ell+1)|\tilde{\xi}_h(r)|^2 \right] \rho_0 r^2 \, dr. \end{cases} \tag{1.4.14}$$

Here $\mathcal{E}$ denotes the mode inertia and R the total radius of the star. It is common practice to refer to a normalised version of the mode inertia, defined as

$$E_{\text{norm}} := \frac{4\pi \int_0^R \left[|\tilde{\xi}_r(r)|^2 + \ell(\ell+1)|\tilde{\xi}_h(r)|^2 \right] \rho_0 r^2 \, dr}{M \left[|\tilde{\xi}_r(R)|^2 + \ell(\ell+1)|\tilde{\xi}_h(R)|^2 \right]} \equiv \frac{M_{\text{mode}}}{M}. \tag{1.4.15}$$

This expression represents the ratio of the so-called modal mass ($M_{\rm mode}$) to the total mass (M) of the star. The normalised inertia is a crucial parameter for assessing the detectability of non-radial modes in red giant stars (see also Section 1.4.3). Specifically, the probability of observing a given non-radial mode depends on $1/\sqrt{E_{\rm norm}}$ (e.g. Dupret et al. 2009).

Boundary conditions

The fourth-order differential equation 1.4.11 has to be solved with two regularity conditions in the centre and two boundary conditions at the surface (e.g. Unno et al. 1989). From a Taylor expansion near $r = 0$ it is possible to demonstrate that non-divergent solutions require $\tilde{P}' \in \mathcal{O}(r^\ell)$, $\tilde{\phi}' \in \mathcal{O}(r^\ell)$ and $\tilde{\xi}_r \in \mathcal{O}(r)$ if $\ell = 0$, otherwise $\tilde{\xi}_r \in \mathcal{O}(r^{\ell-1})$. From these considerations, it is possible to obtain the two independent conditions for $r \to 0$

$$\begin{cases} \dfrac{d\tilde{\phi}'}{dr} \to \dfrac{\ell\tilde{\phi}'}{r} \\ \dfrac{d\tilde{P}'}{dr} \to \dfrac{\ell\tilde{P}'}{r} \end{cases} . \tag{1.4.16}$$

One of the two surface condition is obtained by imposing the continuity of $\tilde{\phi}'$ and its derivative at the surface with solution of the Poisson equation in the vacuum. This happens because the density vanishes and the condition is $\frac{d\tilde{\phi}'}{dr} + \frac{\ell+1}{r}\tilde{\phi}' = 0$ at the surface. The other boundary condition at the surface is more complicated to obtain, because the modelling of stellar atmospheres is involved. In this case, a condition is derived when matching the radial displacement solution with the model of the stellar atmosphere. A key factor in this analysis is the critical acoustic frequency ω_a[9], which depends on the sound speed and the pressure scale height (e.g. Christensen-Dalsgaard 2002). When $\omega > \omega_a$, perturbations are only partially reflected by the atmosphere, resulting in the oscillations losing the majority of their energy through the boundary, even if they are adiabatic. On the other hand, when $\omega < \omega_a$, perturbations are fully trapped within the star, making ω_a the minimum frequency for a propagating wave, commonly referred to as the acoustic cut-off frequency (Lamb 1909). To estimate the boundary condition, one can treat the atmosphere as an empty field. In this scenario, no forces act on the boundary, allowing it to move freely. Consequently, one can impose the condition $\delta P = 0$ at the surface, reflecting the fact that pressure remains constant at the perturbed boundary.

[9]For the Sun, this frequency is approximately 5.3 mHz (e.g. Balmforth et al. 1990).

Radial oscillations

The set of differential equations 1.4.11 can be simplified when dealing with radial oscillations ($\ell = 0$), because the direct dependence on $\tilde{\phi}'$ is removed. In this case, the linear perturbations mantain the spherical symmetry of the star and we obtain the linear second-order differential equation

$$\frac{1}{r^3}\frac{d}{dr}\left[r^4\Gamma_{1,0}P_0\frac{d}{dr}\left(\frac{\tilde{\xi}_r}{r}\right)\right] + \frac{\tilde{\xi}_r}{r}\frac{d}{dr}\left[(3\Gamma_{1,0}-4)P_0\right] + \rho_0\omega^2\tilde{\xi}_r = 0 \tag{1.4.17}$$

to solve. From a physical perspective, this result holds because linear adiabatic stellar oscillations can be modelled as a Hamiltonian system (Takata 2006b), and according to Noether's theorem (Noether 1918) it is possible to associate a conserved quantity with a first integral of motion. Specifically, in the case of radial oscillations, this first integral emerges from the solution of the linearised Poisson equation (e.g. Unno et al. 1989). Moreover, in accordance with Lie's theorem (e.g. Hagihara 1970), the order of the canonical equations of the Hamiltonian system is effectively reduced from four to two.

1.4.2 Cowling approximation

In Section 1.4.1, I demonstrated that the fourth-order differential equation 1.4.11 can be simplified to a linear second-order differential equation when considering purely radial oscillation modes. This simplification is also applicable to dipole modes (i.e. $\ell = 1$) as a first integral of motion arises from the conservation of momentum (Takata 2005; Takata 2006a). However, it is important to note that this is not a universal finding; other non-radial oscillation modes (i.e., those with $\ell > 0$) may not have integrals of motion. Consequently, a complete resolution of the fourth-order differential equation 1.4.11 is necessary at least for $\ell > 1$ modes. Nonetheless, Cowling (1941) demonstrated that in short-wavelength (i.e. much smaller than the radius of the star) waves the Eulerian perturbation to the gravitational potential (represented as $\tilde{\phi}'$ of equation 1.4.11) nearly cancels out at each point. This cancellation occurs because it is dependent on the integral of the Eulerian density perturbation (denoted as $\tilde{\rho}'$ in equation 1.4.11), which tends to zero owing to the rapid spatial variation of $\tilde{\rho}'$. As a result, the fourth-order differential equation may be approximated with a more tractable linear second-order equation (see also Unno et al. 1989), a method referred to as the Cowling approximation. Before proceeding, it is useful to introduce two key quantities relevant to mode identification: the squared Brunt-Väisälä (N^2) and Lamb (S_ℓ^2) frequencies. The Brunt-Väisälä frequency was previously defined in equation 1.2.6, but here we shall adopt a complementary definition that excludes the

temperature gradient. These quantities are defined as

$$\begin{cases} N^2 := \dfrac{d\phi}{dr}\left(\dfrac{1}{\Gamma_1}\dfrac{d\ln P}{dr} - \dfrac{d\ln\rho}{dr}\right) \\ S_\ell^2 := \dfrac{\ell(\ell+1)\Gamma_1 P}{\rho r^2} \end{cases} . \tag{1.4.18}$$

I can now substitute equation 1.4.18 into equation 1.4.11, and utilising the Cowling approximation to derive the new set of differential equations

$$\begin{cases} \dfrac{d\tilde{\xi}_r}{dr} = -\left(\dfrac{2}{r} + \dfrac{1}{\Gamma_1}\dfrac{d\ln P}{dr}\right)\tilde{\xi}_r + \dfrac{1}{\Gamma_1 P}\left(\dfrac{S_\ell^2}{\omega^2} - 1\right)\tilde{P}' \\ \dfrac{d\tilde{P}'}{dr} = \rho(\omega^2 - N^2)\tilde{\xi}_r + \dfrac{1}{\Gamma_1}\dfrac{d\ln P}{dr}\tilde{P}' \end{cases} . \tag{1.4.19}$$

In this formulation, the subscript 0 has been omitted from the equilibrium quantities for the sake of simplicity in notation. As it will become clearer in Section 1.4.3, the system of equation 1.4.19 admits non-trivial solutions only for discrete values of the eigenvalues ω^2. These solutions can be associated to an integer number (n) denominated radial order, because it is related to the number of nodes observed in the radial displacement (Eckart et al. 1960; Scuflaire 1974; Osaki 1975, e.g.). This mode integer exhibits a monotonous and continuous increase in relation to the eigenfrequency (Gabriel et al. 1979). Moreover, even if the adiabatic theory cannot tell us the absolute amplitude of each oscillation mode, it can helps us in learning the relative importance of each one compared to the others. For modes of high radial order or high angular degree, the validity of the Cowling approximation has been corroborated through computational studies (e.g. Robe 1968; Christensen-Dalsgaard 1991). However, its efficacy diminishes progressively for modes characterised by low angular degree and low radial order, as the term $\tilde{\phi}'$ becomes significant in these situations.

1.4.3 Asymptotic analysis of stellar oscillations

The Cowling approximation plays a crucial role in the classification of oscillation modes. In fact, through the JWKB method (developed by Jeffreys, Wentzel, Kramers and Brillouin, see e.g. Unno et al. 1989; Gough 2007) characteristic wave solutions can be derived. This methodology is predominantly employed to derive approximate solutions for linear differential equations that exhibit spatially varying coefficients, as exemplified by equation 1.4.19. The resultant solutions are generally expressed as an asymptotic series expansion, a technique commonly referred to as the asymptotic analysis of stellar oscillations (e.g. Shibahashi 1979; Tassoul 1980). As will be elaborated upon later, the Cowling classification distinguishes stationary waves into three main categories (e.g. Deubner et al. 1984; Unno et al. 1989; Gough 1993; Gough 1996): gravity modes (g-modes), acoustic or pressure

modes (p-modes), and the fundamental mode (f-mode), which is associated with surface gravity waves. In this section, I will summarise the main results concerning p-modes and g-modes, along with their interaction in CHeB stars.

To elucidate the primary characteristics of these modes, it is advantageous to define the parameters

$$\begin{cases} b(r) := \dfrac{2}{r} + \dfrac{1}{\Gamma_1}\dfrac{d\ln P}{dr} \\ f(r) := \dfrac{1}{r^2\Gamma_1 P}\left|\dfrac{S_\ell^2}{\omega^2} - 1\right| \\ \hat{\xi}_r := \dfrac{\tilde{\xi}_r}{\sqrt{f(r)}} \\ \tilde{h}(r) := b(r)\dfrac{d\ln f}{dr} - \dfrac{db(r)}{dr} + b^2(r) \\ h(r) := \tilde{h}(r) - \dfrac{1}{2}\dfrac{d^2\ln f}{dr^2} + \dfrac{1}{4}\left(\dfrac{d\ln f}{dr}\right)^2 \\ K(r) := \dfrac{\rho}{\Gamma_1 P\omega^2}\left(S_\ell^2 - \omega^2\right)\left(N^2 - \omega^2\right). \end{cases} \tag{1.4.20}$$

Subsequently, from equation 1.4.19, the second-order differential equation

$$\frac{d^2\hat{\xi}_r}{dr^2} + [K(r) - h(r)]\hat{\xi}_r = 0 \tag{1.4.21}$$

is derived. At this stage, I can assume that the perturbed variables vary much more rapidly than the equilibrium quantities, which is particularly applicable to high radial order oscillations. Therefore, it is possible to neglet all the derivatives of the equilibrium quantities in equation 1.4.21 and seek solutions of the form

$$\begin{cases} \hat{\xi}_r(r) = \dfrac{e^{i\psi(r)}}{\sqrt{|k_r(r)|}} \\ k_r^2(r) = K(r). \end{cases} \tag{1.4.22}$$

Here $\psi(r)$ represents a rapidly varying function, and its derivative corresponds to the local radial wave number $k_r(r)$, which, therefore, is large. Finally, the eigenfunctions are

$$\hat{\xi}_r \propto |K(r)|^{-1/4} \begin{cases} \exp\left(-\displaystyle\int_r^{r_1}\sqrt{|K(x)|}\,dx\right), & K(r) < 0,\ r < r_1 \\ \cos\left(\displaystyle\int_{r_1}^{r}\sqrt{K(x)}\,dx - \dfrac{\pi}{4}\right), & K(r) > 0,\ r_1 \ll r \ll r_2 \\ \exp\left(-\displaystyle\int_{r_2}^{r}\sqrt{|K(x)|}\,dx\right), & K(r) < 0,\ r > r_2, \end{cases} \tag{1.4.23}$$

for which r_1 and r_2 are the points where $K(r) = 0$. These solutions are related to the radial order through the integral

$$\int_{r_1}^{r_2}\sqrt{K(r)}\,dr = (n+\alpha)\,\pi,\ n \in \mathbb{N}, \tag{1.4.24}$$

with α a phase constant. Therefore, where $K(r) < 0$, the oscillations decay exponentially, and where $K(r) > 0$, the oscillations remain undamped. This indicates that each eigenmode is confined within the region designated as the resonance cavity, where $K(r) > 0$, and its frequency is primarily influenced by the structure of the model within this area. The boundaries that delineate these trapping regions occur at $K(r) = 0$, which are referred to as turning points (i.e. r_1 and r_2). It is important to notice that the oscillating part of equation 1.4.23 is applicable only in regions that are sufficiently distant from the turning points. If this condition were not met, it would not have been possible to neglet the derivatives of the equilibrium quantities. In such cases, the eigenfunctions would have been more accurately represented by Airy functions. Finally, there are two principal categories of trapped oscillations that arise for real values of ω:

- $\omega > |N|$ and $\omega > S_\ell$, which we denote as p-modes;
- $\omega < |N|$ and $\omega < S_\ell$, which we denote as g-modes.

A useful method to summarise the classification of eigenmodes and their associated properties is through a propagation diagram. This graph represents S_ℓ^2 and N^2 as functions of either internal radius or mass, as exemplified for a star comparable to the Sun in figure 1.6.

Pressure-modes

Pressure modes are standing sound waves for which the pressure gradient acts as the dominant restoring force, and they can have radial or non-radial spherical harmonic geometries. For radial pressure modes, since there is no angular dependence (i.e. $S_0 = 0$ rad/s), the entire star acts as the resonance cavity. As a result of the definition of $K(r)$ in equation 1.4.20, the eigenfunctions in equation 1.4.23 and the considerations regarding the acoustic cut-off frequency of Section 1.4.1, it is possible to obtain that p-modes are trapped in a region between an inner turning point $[r_t : \omega r_t^2 \rho(r_t) = \ell(\ell+1)\Gamma_1(r_t)P(r_t)]$ and the surface of the star. The propagation diagram of figure 1.6 summarises these results. From the figure it is clear that r_t decreases at decreasing ℓ and increasing ω. Moreover, as a consequence of equation 1.4.24, the higher the radial order, the higher $K(r)$. Therefore, the higher the number of radial nodes of the eigenfunctions and the higher the eigenfrequency. This is why, conventionally, the radial order is designed as a positive integer for p-modes.

When $\omega^2 \gg N^2$ (i.e. high radial order p-modes), $K(r) + \frac{\ell(\ell+1)}{r^2} \approx \omega^2 \frac{\rho}{\Gamma_1 P}$, which is the dispersion relation of an acoustic wave with total wave number $k = \sqrt{K(r) + \frac{\ell(\ell+1)}{r^2}}$.

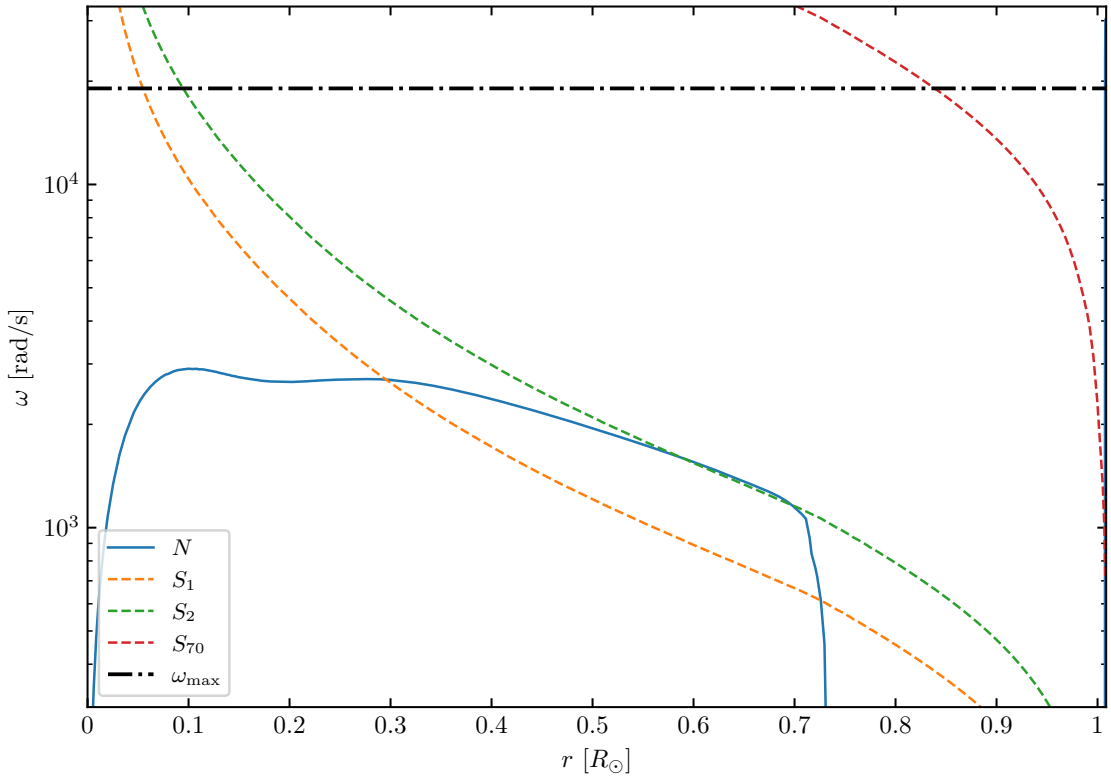

Figure 1.6: Propagation diagram for a star analogous to the Sun, plotted as a function of the internal radius. The solid blue line represents the Brunt-Väisälä frequency, while the two dashed lines depict the Lamb frequency for angular degrees $\ell = 1$ (in orange), $\ell = 2$ (in green) and $\ell = 70$ (in red). The dotted black line illustrates the frequency at which the model exhibits maximum power, which is an indication of the frequency domain of observable solar-like oscillations.

Moreover, it is possible to find an approximate solution for ω with asymptotic expansions of equation 1.4.24 and obtain the asymptotic relation

$$\nu_{n,\ell} = \frac{\omega_{n,\ell}}{2\pi} \approx \left(n + \frac{\ell}{2} + \frac{1}{4} + \alpha\right)\Delta\nu - \left[A\ell(\ell+1) - \delta\right]\frac{\Delta\nu^2}{\nu_{n,\ell}}, \tag{1.4.25}$$

where

$$\Delta\nu := \left(2\int_0^R \frac{dr}{\sqrt{v_{\text{sound}}}}\right)^{-1} \tag{1.4.26}$$

is the asymptotic large frequency separation, δ is a phase constant and

$$A := \frac{1}{4\pi^2\Delta\nu}\left[\frac{v_{\text{sound}}(R)}{R} - \int_0^R \frac{dv_{\text{sound}}}{dr}\frac{dr}{r}\right]. \tag{1.4.27}$$

From equation 1.4.26, it follows that for a fixed ℓ, $\nu_{n,\ell} - \nu_{n-1,\ell} \approx \Delta\nu$. This implies that the eigenfrequencies of consecutive radial order are evenly spaced by the quantity $\Delta\nu$. Additionally, the small frequency separation, defined as $\delta\nu_{n,\ell} := \nu_{n,\ell} - \nu_{n-1,\ell+2}$, is particularly sensitive to the structure of the stellar core. As a result, in main sequence stars, $\delta\nu_{n,\ell}$ serves as a key indicator of age, reflecting changes in the mean molecular weight within the core. Furthermore, it is important to note that high-order p-modes with low angular degree satisfy the condition $K(r) \gg \frac{\ell(\ell+1)}{r^2}$, indicating that their propagation is predominantly radial than horizontal.

Gravity-modes

Gravity modes are standing waves for which the buoyancy acts as the dominant restoring force. They can have only non-radial spherical harmonic geometries, because buoyancy necessitates variations across horizontal surfaces[10]. As a result of the definition of $K(r)$ in equation 1.4.20 and the eigenfunctions in equation 1.4.23, it is possible to obtain that g-modes are trapped in a region between an inner turning point $[r_1 : \omega^2 = N^2(r_1)]$ and an outer turning point $[r_2 : \omega^2 = N^2(r_2)]$. Therefore, it follows that both turning points do not depend on the angular degree, and that g-modes exponentially decay in regions where $N^2 \leq 0$. Consequently, g-modes can be trapped only in the radiative regions of the star. The propagation diagram of figure 1.6 summarises these results. Moreover, also in this case as a consequence of equation 1.4.24, the higher the radial order, the higher $K(r)$. However, the higher the number of radial nodes of the eigenfunctions, the lower the eigenfrequency for g-modes. This is why the radial order is conventionally a negative integer for g-modes.

When $\omega^2 \ll S_\ell^2$ (i.e. high radial order g-modes), $K(r) + \frac{\ell(\ell+1)}{r^2} \approx \frac{\ell(\ell+1)N^2}{\omega^2 r^2}$, which is the dispersion relation of a buoyancy wave with local wave number $k = \sqrt{K(r) + \frac{\ell(\ell+1)}{r^2}}$.

[10] In other words, it does not exist a positive eigenfrequency with $\omega < 0$ rad/s

Moreover, it is possible to find an approximate solution for ω with asymptotic expansions of equation 1.4.24 and obtain the asymptotic relation (Tassoul 1980)

$$\omega_{n,\ell} \approx \frac{\sqrt{\ell(\ell+1)}}{\pi\left(n+\frac{\ell}{2}+\alpha\right)} \int_{r_1}^{r_2} \frac{N}{r}\, dr \tag{1.4.28}$$

from which it is useful to define the quantity

$$\Delta P_{\text{as}} := \frac{2\pi^2}{\sqrt{\ell(\ell+1)}} \left(\int_{r_1}^{r_2} \frac{N}{r}\, dr \right)^{-1} \tag{1.4.29}$$

called asymptotic period spacing. In fact, from equation 1.4.28 and equation 1.4.31, it follows that at a fixed ℓ, eigenperiods (i.e. $P_{n,\ell} = 1/\nu_{n,\ell}$) of consecutive radial order are equally spaced by the quantity ΔP_{as}, that is $P_{n,\ell} - P_{n-1,\ell} \approx \Delta P_{\text{as}}$. Moreover, the higher is ℓ, the lower the period spacing (i.e. $P_{n,\ell} - P_{n-1,\ell}$). Furthermore, it is important to note that high-order g-modes satisfy the condition $K(r) \ll \frac{\ell(\ell+1)}{r^2}$, indicating that their propagation is predominantly horizontal than radial.

Mixed-modes

In red giant stars, the oscillation modes observed are not purely p-modes or g-modes; instead, the oscillation modes exhibit a mixed character, combining the characteristics of both pressure and gravity modes (e.g. Beck et al. 2011). This mixing occurs due to the concurrent increase of N^2 and S_ℓ^2, which facilitates the occurrence of comparable frequencies for both p-modes and g-modes. This behaviour can be summarised in the propagation diagram presented in figure 1.7. Notably, an eigenmode near the frequency of maximum power behaves as a g-mode within the radiative region near the centre of the star, referred to as the g-cavity. In contrast, within the region that extends from the base of the convective envelope to the stellar surface, this same mode manifests as a p-mode, which is termed the p-cavity. Consequently, mixed modes provide valuable information regarding the internal properties of red giant stars while remaining sufficiently detectable. If the modes within the g-cavity possess high radial orders, one can apply the asymptotic expansion of g-modes, as expressed in equation 1.4.28, to those modes with the highest normalised inertia (as defines in equation 1.4.15). These modes predominantly probe the g-cavity than the p-cavity, and exhibit low observable amplitudes. In fact, the observable amplitude for mixed modes near ν_{max} is primarily influenced by $E_{\text{norm}}^{-1/2}$ (e.g. Dupret et al. 2009). Conversely, mixed modes with low inertia show higher observable amplitudes as they are more sensitive to the p-cavity. This p-character leads to deviations from the expected asymptotic period spacing, a phenomenon that will be elaborated upon in Chapter 2. Therefore, mixed modes serve as a powerful tool for differentiating between

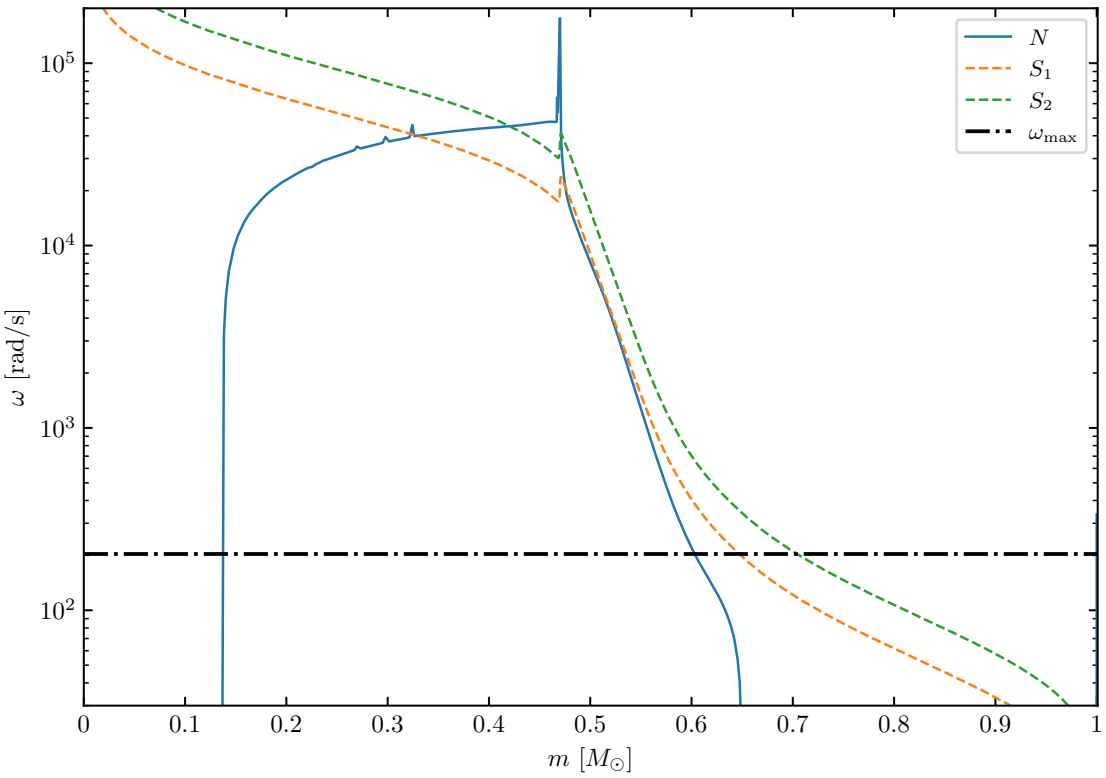

Figure 1.7: Propagation diagram for a star at the beginning of the CHeB stage with one solar mass and solar metallicity, plotted as a function of the internal mass. The solid blue line represents the Brunt-Väisälä frequency, while the two dashed lines depict the Lamb frequency for angular degrees $\ell = 1$ (in orange) and $\ell = 2$ (in green). The dotted black line illustrates the frequency at which the model exhibits maximum power, which is an indication of the frequency domain of observable solar-like oscillations.

low-mass stars on the CHeB phase and those on the red giant branch (e.g. Montalbán et al. 2010; Bedding et al. 2011; Mosser et al. 2011a; Mosser et al. 2012a). Furthermore, data gathered from space missions such as CoRoT and *Kepler* have enabled the assessment of differential rotation in red giants, in addition to enhancing our understanding of core rotation characteristics (Beck et al. 2012; Deheuvels et al. 2014; Deheuvels et al. 2015; Mosser et al. 2018).

The area situated between the two cavities is identified as an evanescent zone, as it satisfies the conditions $\omega > N$ and $\omega < S_\ell$. The dimensions of this zone determine the intensity of the coupling between the g-cavity and the p-cavity. The behaviour of mixed modes can be conceptualised in terms of a wave transmission-reflection problem (see e.g. Roxburgh et al. 2001; Takata 2016b; Pinçon et al. 2022) occurring between resonant cavities. Specifically, an incoming wave from a cavity is partially reflected at the boundary while also being partially transmitted (with phase delays) toward the other cavity situated on the opposite side of the barrier. In the context of adiabatic oscillations, the conservation of wave energy flux also applies, resulting in a transmission coefficient between the two cavities that ranges between 0 and 1. This principle can be similarly applied in the presence of additional g-cavities (Pinçon et al. 2022). The strength of the coupling between two resonant cavities is commonly quantified using the coupling parameter

$$q := \cot(\Phi_g)\tan(\Phi_p), \tag{1.4.30}$$

where Φ_g denotes the total phase of gravity-wave oscillations in the core and Φ_p signifies the acoustic-wave oscillations in the convective envelope (see e.g. Takata 2016a; Takata 2016b). The parameter q is related to the trasmission coefficient ($T_{1,2}$) through the equation

$$q = \frac{1-\sqrt{1-T_{1,2}^2}}{1+\sqrt{1-T_{1,2}^2}}, \tag{1.4.31}$$

and thus varies from 0 (indicating no coupling) to 1 (indicating maximum coupling). In low-mass CHeB stars within the *Kepler* field, typical coupling values are in the range $[0.2-0.45]$ (e.g. Mosser et al. 2017), while in red giant branch stars with comparable luminosities, these values are typically lower (between 0.12 and 0.18, e.g. Mosser et al. 2017). Additionally, the coupling parameter tends to be greater in lower mass stars, suggesting that CHeB stars with the lowest masses generally exhibit the strongest couplings (e.g. van Rossem et al. 2024), a point that will be further discussed in Chapter 2. Finally, it is noteworthy that, from a mathematical perspective, it is feasible to decouple g-modes from p-modes in red giant stars (e.g. Ong et al. 2020). These uncoupled g-modes, referred to as γ-modes, can be

employed to investigate the properties of the g-cavity without the complications introduced by phase lags and the transmission-reflection phenomena. The relevance of γ-modes will be explored in chapters 2 and 4.

Chapter 2

Red horizontal branch stars: An asteroseismic perspective[1]

Robust age estimates of red giant stars are now possible thanks to the precise inference of their mass based on asteroseismic constraints. However, there are cases where such age estimates can be highly precise yet very inaccurate. An example is giants that have undergone mass loss or mass transfer events that have significantly altered their mass. In this context, stars with "apparent" ages significantly higher than the age of the Universe are candidates for stripped stars, or stars that have lost more mass than expected, most likely via interactions with a companion star or because of the poorly understood mass-loss mechanism along the red-giant branch.

In this work, my collaborators and I identify examples of such objects among red giants observed by *Kepler*, both at low ([Fe/H] $\lesssim -0.5$) and solar metallicity. By modelling their structure and pulsation spectra, we find a consistent picture that confirms that they are indeed low-mass objects consisting of a He core of ≈ 0.5 $M_\odot$ and an envelope of $\approx 0.1 - 0.2$ $M_\odot$. Moreover, we find that these stars are characterised by a rather extreme coupling ($q \gtrsim 0.4$) between the pressure-mode and gravity-mode cavities, one that is much higher than the typical value for red clump stars, thus providing a direct seismic signature of their peculiar structure.

The complex pulsation spectra of these objects, if observed with sufficient frequency resolution, hold detailed information about the structural properties of likely products of mass stripping and can hence potentially shed light on their formation mechanism. On the other hand, our tests highlight the difficulties associated with reliably measuring the large frequency separation, especially in shorter datasets, which impacts the reliability of

[1]The work presented in this chapter is based on Matteuzzi et al. (2023).

the inferred masses and ages of low-mass red clump stars with, for example, K2 or TESS data.

2.1 Introduction

It is widely accepted that the large range in colour shown by low-mass stars in the central He-burning phase, called the horizontal branch (HB), is mainly due to variations in the efficiency of the H-burning shell and, hence, due to the mass of the H envelope remaining around a He core of $\simeq 0.5$ $M_{\odot}$ (e.g. Salaris et al. 2006). In a colour-magnitude diagram, low-mass core-He-burning (CHeB) stars appear distributed in both bluer and redder colours than the RR Lyrae instability strip (RRL-IS). Those located between the RR Lyrae and the red clump (RC; e.g. Girardi 2016) are called red horizontal branch (rHB) stars, and they have a H-rich envelope of $\approx 0.1 - 0.2$ $M_{\odot}$ (e.g. Rood et al. 1989; Valcarce et al. 2008; Girardi 2016; Tailo et al. 2020). This HB component has been clearly observed in globular clusters of different metallicities and ages (e.g. Armandroff 1988; Stetson et al. 1989; Catelan 2009; Tailo et al. 2020); however, rHB objects also exist in the field. While their identification is challenging, their census has been considered extremely important for tracing old stellar populations in the Milky Way (e.g. Kaempf et al. 2005; Chen et al. 2010; Chen et al. 2011). Although mainly associated with stars of low to intermediate metallicity, corresponding to the thick disc and halo population, spectroscopic studies (e.g. Afşar et al. 2012; Afşar et al. 2018) have shown that rHB stars are also present in the metal-rich component of the Milky Way. This suggests that the progenitors of these objects have followed a non-standard evolution with significant mass loss or envelope stripping due to binary interactions. Signs of significant mass loss have been revealed in red giants observed by the *Kepler* space telescope (Borucki et al. 2010) in the field and in the open cluster NGC 6819 (e.g. Handberg et al. 2017; Brogaard et al. 2021; Li et al. 2022).

Stellar evolution models predict different structures for rHB and RC stars, with the latter having a similar He core as the former but a larger H envelope. We thus expect their seismic properties to be different. The exquisite precision achieved after 4 years of *Kepler* observations has revealed oscillation spectra of red giants with an increasing level of complexity (see Chaplin et al. 2013, for a review): frequency patterns in red-giant branch (RGB) stars similar to those found in main-sequence stars (universal pattern; Mosser et al. 2011b); spectra of RC stars with "forests" of dipole modes around the nominal acoustic mode, but still with an evident regularity (i.e. Beck et al. 2011); and "outlier" spectra with a larger number of visible modes over the whole frequency domain, which are hypothesised

in this work to belong to rHB stars (see Fig. 2.1).

In this work we identify a small sample of 11 rHB candidates among the red giants in the *Kepler* field. Their global seismic properties and atmospheric parameters suggest that they are low-mass CHeB stars with low, intermediate, or solar metallicity. Combining numerical simulations of stellar structure and evolution and stellar oscillations, we study the consistency between the location of our rHB candidates in the Hertzsprung–Russell diagram (HRD), their theoretically predicted internal structure, and their oscillation spectra. Our rHB sample is presented in Sect. 2.2 and the theoretical models in Sect. 2.3. Section 2.4 discusses the properties of theoretical oscillation spectra of typical rHB and RC stars, as well as the comparison with observations. In Sect. 2.5 we summarise our findings.

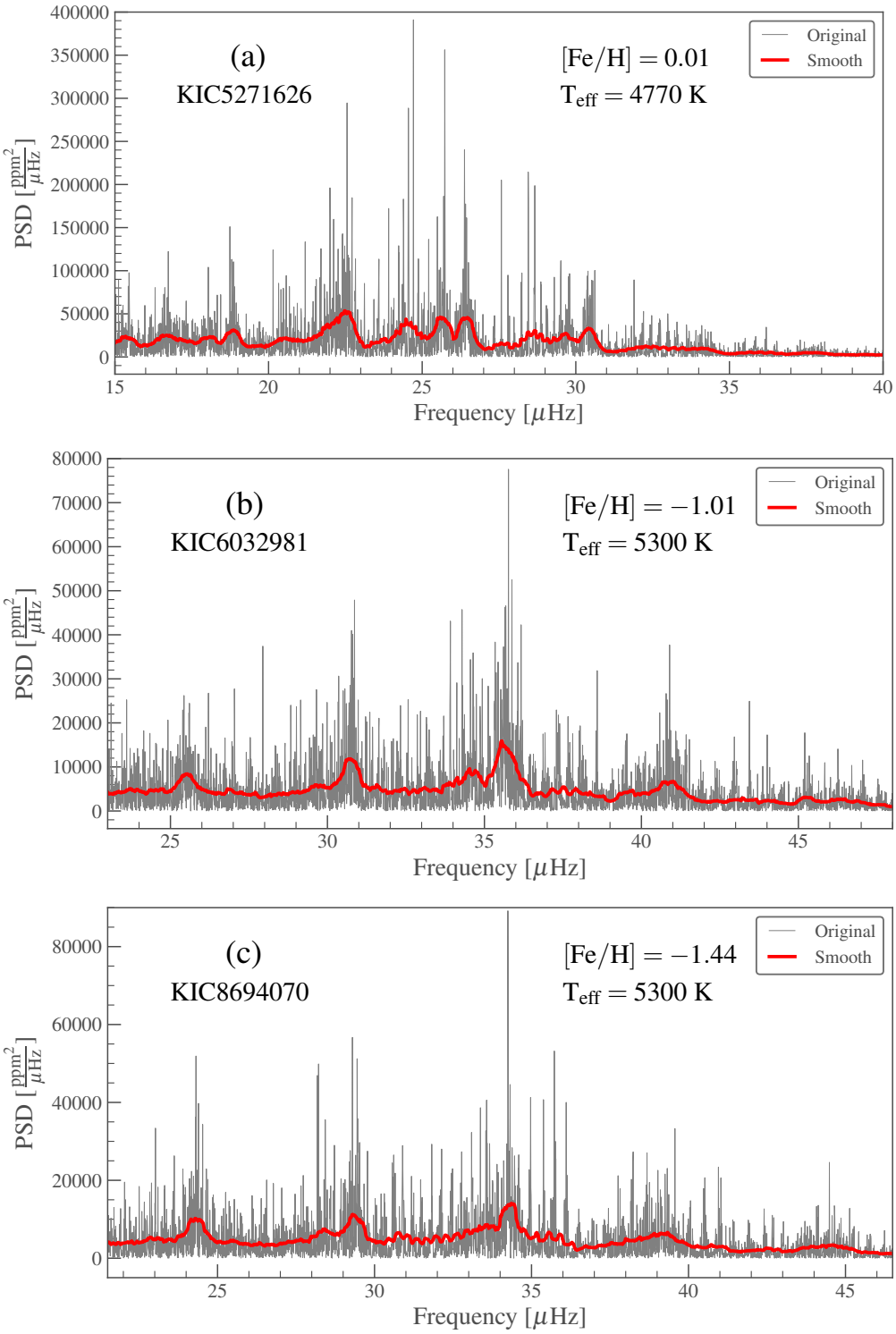

Figure 2.1: PSD for five low-mass red giants (grey lines in the five panels) observed by *Kepler*. Panels (a), (b), and (c) show the three low-mass CHeB stars KIC5271626, KIC6032981, and KIC8694070 (first three rows in Table 2.1 and coloured stars in Fig. 2.2). Panels (d) and (e) show the RC star KIC1161618 and the RGB star KIC2436824, for comparison (see next page). All five panels contain a smoothed PSD (red lines) computed with a box kernel of width 0.5 μHz in panels (a), (b), (c), and (d), and of width 0.1 μHz in panel (e).

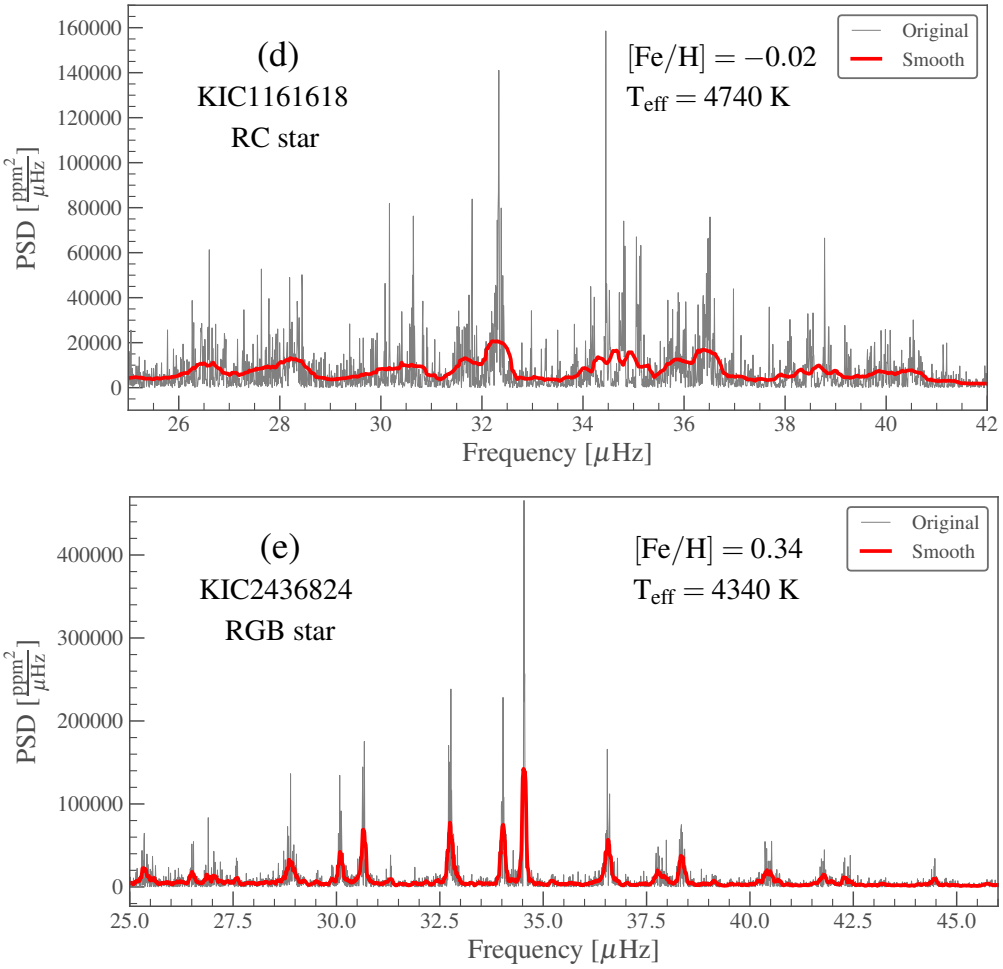

Figure 2.1: *(Continued)*

2.2 Observational data

In addition to KIC4937011, a 0.71 $M_\odot$ CHeB star belonging to the open cluster NGC 6819 (see Handberg et al. 2017) that has a turn-off mass of $\sim 1.6\ M_\odot$, we found 11 red giants in the *Kepler* database[2] with peculiar power spectral densities (PSDs). While their global seismic parameters (mean large frequency separation, $\langle\Delta\nu\rangle$, frequency of maximum power, $\nu_{\rm max}$, and asymptotic period spacing of the dipole modes, $\Delta\Pi_1$) are compatible with low-mass CHeB stars, they have complex oscillation spectra. They have, for instance, an unusually high number of observable dipole mixed modes without the amplitude modulation around the p-like modes that is typically found in low-RGB and RC stars. This fact suggests that all dipole modes also have a significant amplitude in the outer region of the star and, hence, that g and p resonant cavities in these objects are strongly coupled.

[2] https://archive.stsci.edu/missions-and-data/kepler

The ability to transfer the energy of the mode from one cavity to the other, instead of it remaining trapped mainly in one of them, is quantified by the coupling factor, q (e.g. Shibahashi 1979; Takata 2016a). The analysis of *Kepler* light curves provides the seismic parameters mentioned above, as well as the value of q (e.g. Vrard et al. 2016; Mosser et al. 2017; Mosser et al. 2018). Theoretically, the parameter q ranges from 0 (uncoupled) to 1 (completely coupled). All the stars in our sample have $q \gtrsim 0.4$, while the median for RC stars is $\simeq 0.25 - 0.3$ (Vrard et al. 2016; Mosser et al. 2017).

On the other hand, the values of radial mode-linewidths ($\Gamma_0 > 0.2$ μHz) are larger than the third quantile of the full sample of CHeB *Kepler* stars (median value $\Gamma_0 = 0.15$ μHz; Vrard et al. 2018). Both a high q and a high Γ_0 contribute to increasing the complexity of the spectra. Moreover, given the dependence of Γ_0 on the effective temperature, $T_{\rm eff}$ (e.g. Chaplin et al. 2009), the quadrupole modes are more difficult to detect in the hotter metal-poor subsample than in the cooler metal-rich objects.

The seismic properties ($\nu_{\rm max}$, $\langle\Delta\nu\rangle$, $\Delta\Pi_1$, and q) for our sample are reported in Tables 2.1 and A.1, together with the atmospheric parameters ($T_{\rm eff}$ and chemical composition) from APOGEE Data Release (DR) 16 and DR17 (Ahumada et al. 2020; Abdurro'uf et al. 2022). Twenty-five percent (3 out of 12) of the sample are metal-rich ($0 \leq$ [Fe/H] < 0.3) cool ($4600 \leq T_{\rm eff}/K \leq 4800$) stars, and the rest are low- or intermediate-metallicity ($-1.4 <$ [Fe/H] < -0.5) stars with $5200 \leq T_{\rm eff}/K \leq 5600$, that is, they belong to the 'classical' rHB.

Tables 2.1 and A.1 also contain the stellar luminosity derived using *Gaia*-DR3 astrometry data (see Appendix A for details) and an estimate of their mass. The latter can be derived from scaling relations involving atmospheric and global seismic parameters (see e.g. Miglio et al. 2012). Here we use the one combining L, $T_{\rm eff}$, and $\nu_{\rm max}$:

$$\frac{M}{M_\odot} = \left(\frac{T_{\rm eff,\odot}}{T_{\rm eff}}\right)^{3.5} \left(\frac{\nu_{\rm max}}{\nu_{\rm max,\odot}}\right) \left(\frac{L}{L_\odot}\right), \tag{2.2.1}$$

where the solar reference values are $T_{\rm eff,\odot} = 5777$ K and $\nu_{\rm max,\odot} = 3090$ μHz (Huber et al. 2011). The mass uncertainties are calculated in quadrature by considering an uncertainty of at least 50 K in $T_{\rm eff}$ as estimated from an independent analysis of APOGEE spectra (see Appendix A). In Appendix A.1 we also discuss the stellar mass values from a model-based corrected scaling relation involving $T_{\rm eff}$, $\langle\Delta\nu\rangle$, and $\nu_{\rm max}$ (Eq. A.1.1).

We notice that the mass of KIC 4937011 in Table A.1 is that of Handberg et al. (2017), and its value is nevertheless compatible with our results obtained with Eqs. 2.2.1 or A.1.1. All the objects in our sample are then very low-mass stars ($M \lesssim 0.8$ M$_\odot$) with a high

coupling[3] between p-mode and g-mode cavities.

We selected three stars (those in Table 2.1) as representative of low-mass CHeB stars in different metallicity domains. Figure 2.2 shows these stars in an HRD, together with the *Kepler*-APOGEE red giant sample (Miglio et al. 2021, grey dots) and the red edge of the RRL-IS (Marconi et al. 2015, dashed red line). The two metal-poor stars (blue star symbols) are located between the RRL-IS and the RC, as expected for rHB stars, while the metal-rich CHeB star (orange star symbol) appears in the region of the "ensemble" *Kepler*-RC. Its location is nevertheless redder than the RC at solar metallicity, and hence it is indeed a rHB metal-rich star, as also suggested by its mass (see also Handberg et al. 2017) and oscillation spectra. As mentioned above, rHB stars, especially metal-rich ones, must have followed a non-standard evolution to reach their current state within the age of the Universe. They are probably the progeny of strongly interacting binary systems. It has not been possible to confirm that hypothesis using the currently available *Gaia*-DR3 astrometry data (see Halbwachs et al. 2023, for the non-single star processing[4]), but we cannot exclude that they were part of binary systems in the past.

2.3 Simulated data

The aim of this work is not to fit the available observational data, but to analyse the relation between the structures of rHB stars, according to stellar evolution theory, and their oscillation spectra, and to compare the latter with those observed in our sample.

From a grid of models (see Appendix B) we select two sets of parameters that are good representatives of the mass and chemical composition of classical rHB stars ($M = 0.65\ M_\odot$, $[\alpha/\mathrm{Fe}] = 0.2$ and $[\mathrm{Fe/H}] = -1.00$) and metal-rich low-mass CHeB stars ($M = 0.75\ M_\odot$, $[\alpha/\mathrm{Fe}] = 0$ and $[\mathrm{Fe/H}] = 0$). For comparison, we also consider a typical RC star ($M = 1.5\ \mathrm{M}_\odot$ with solar composition). As shown in Fig. 2.2, the parameters selected for our reference models do provide a good representation of the low- to intermediate-metallicity and metal-rich rHB stars in our sample. We also note that without complementary information, such as that provided by asteroseismology, a metal-rich rHB star would be mistaken for a more massive star in the RGB (see also Handberg et al. 2017).

It is generally accepted that, except for the age, the properties of a low-mass star with a He core of $\simeq 0.5\ \mathrm{M}_\odot$ and a H-rich envelope of $\sim 0.1 - 0.2\ \mathrm{M}_\odot$ are largely independent of

[3] We notice that stars in the CHeB stage could have multiple cavities in the inner part due to semi-convection. This could lead to a bias when estimating q from the fit of observations with the asymptotic relation for dipole modes (e.g. Pinçon et al. 2022). This must be considered in future work.

[4] We also checked the non-single star hypothesis using the `fidelity_v2` table.

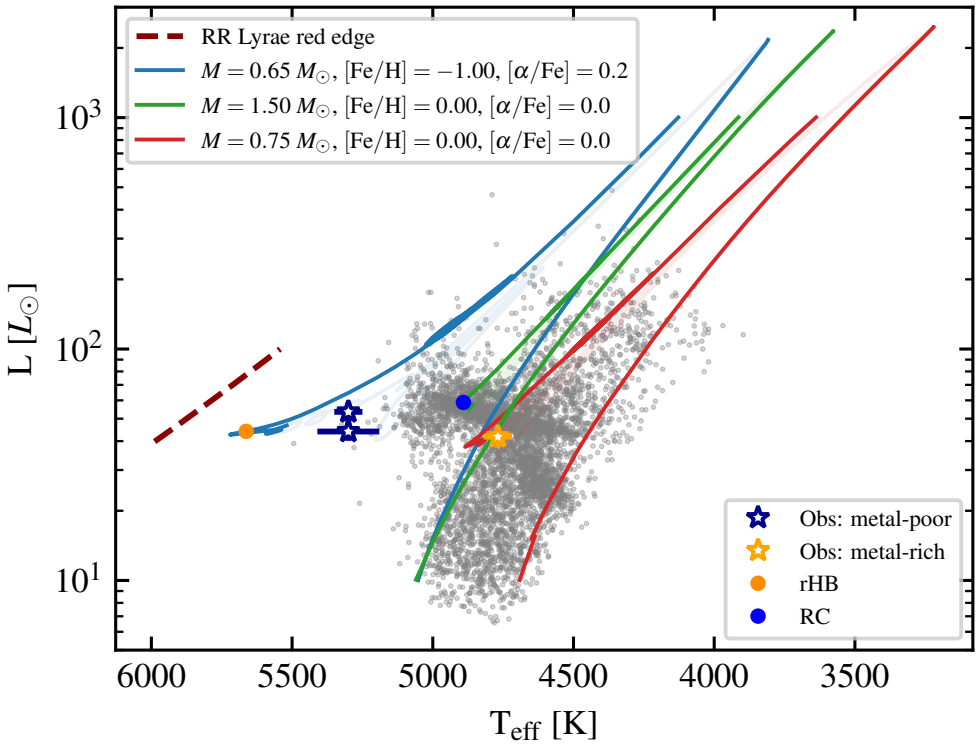

Figure 2.2: HRD of a sample of red giants in the *Kepler* field. The coloured star symbols highlight the location of the first three rHB candidates in Table 2.1, and the grey dots in the background correspond to the *Kepler*-APOGEE sample in Miglio et al. (2021). The blue and red lines represent the theoretical red giant evolutionary tracks (from the RGB phase until the first thermal pulse) of low-mass stars with two different chemical compositions: $M = 0.65\ M_\odot$, [α/Fe] $= 0.2$, [Fe/H] $= -1.00$ (blue) and $M = 0.75\ M_\odot$, [α/Fe] $= 0$, [Fe/H] $= 0$ (red). The green line is the evolutionary track for a 1.5 $M_\odot$ with solar composition, and the dashed red one is the red edge of the RRL-IS for the composition of the blue track (see Marconi et al. 2015). Solid orange and blue circles correspond to our rHB and RC reference models, with a central He mass fraction $Y_c \simeq 0.27$.

Table 2.1: Summary of the seismic and atmospheric properties for three rHB candidates of our sample (Sect. 2.2).

KIC	L [$L_\odot$]	$T_{\rm eff}$ [K]	[Fe/H]	[α/Fe]	$\langle\Delta\nu\rangle$ [μHz]	$\nu_{\rm max}$ [μHz]	q	$\Delta\Pi_1$ [s]	M [$M_\odot$]
5271626*	42 ± 4	4769 ± 9	0.03	0.01	3.91 ± 0.05	25.1 ± 0.5	0.61	291.4 ± 1.7	0.66 ± 0.07
6032981$^+$	44 ± 4	5300 ± 110	-1.01	0.37	5.188 ± 0.017	35.4 ± 0.6	1.15	321 ± 3	0.68 ± 0.08
8694070	53 ± 5	5300 ± 30	-1.44	0.25	5.135 ± 0.018	34.6 ± 0.6	0.7	332 ± 4	0.81 ± 0.09
Mock rHB	44	5663	-1.00	0.2	6.41	42.5	0.65	324	0.65
Mock RC	59	4891	0.00	0.0	4.79	44.1	0.25	313	1.50

Notes. For each *Kepler* ID (KIC) we report: the effective temperature, $T_{\rm eff}$, the [Fe/H], and the [α/Fe] from APOGEE-DR17 or APOGEE-DR16 (one star marked with a plus sign); and the mean large frequency separation, $\langle\Delta\nu\rangle$, and frequency of maximum power, $\nu_{\rm max}$, calculated by us using the code in Davies et al. (2016) or Yu et al. (2018) data (one star marked with an asterisk). The coupling factor, q, and asymptotic period spacing of the dipole modes, $\Delta\Pi_1$, were calculated using the stretched-period method (see e.g. Vrard et al. 2016). The current stellar mass, M, was computed from Eq. 2.2.1. The last two rows show the properties of a simulated rHB and RC star (Sect. 2.3).

whether the star was born with a small mass or whether it originated from a more massive star ($M \lesssim 1.8$ M$_\odot$) that underwent significant mass loss. Therefore, it is justified to use structure models calculated without mass loss such as those in our grid.

In the following we concentrate on a metal-poor model since, as described in Sect. 2.2, we expect metal-poor rHB stars to present more marked differences with respect to the spectra of typical RC stars. We selected structure models with a central He mass fraction $Y_c \sim 0.27$ as representative of the CHeB phase. The structures and oscillation spectra of these reference models will be discussed in Sect. 2.4.

To simulate 4-year-long *Kepler* observations of such objects, we use the code `AADG3` (AsteroFLAG Artificial Dataset Generator, version 3.0.2; Ball et al. 2018, and references therein). Frequencies and normalised inertiae ($E_{\rm norm}$, as outlined in equation 1.4.15 of Section 1.4.1) of radial ($\ell = 0$) and non-radial ($\ell = 1 - 3$) adiabatic oscillation modes were computed using the code `GYRE` (version 6.0.1, Townsend et al. 2013; Townsend et al. 2018; Goldstein et al. 2020). `AADG3` also requires information on mode lifetimes, a quantity that is directly related to non-adiabatic processes and therefore does not result from the `GYRE` computation. `AADG3` uses a relation between Γ_0, ν, $\nu_{\rm max}$, and $T_{\rm eff}$ calibrated on a small sample of main-sequence and RGB spectra. Since the temperatures of our metal-poor rHB stars are outside the domain covered by the calibration sample, and since Γ_0 also depends on the evolutionary state (Vrard et al. 2018), we adopted as values of Γ_0 the ones obtained from peak-bagging radial modes in the spectra of our CHeB sample (using the method described in Davies et al. 2016).

2.4 Discussion

In this section we analyse the structures and oscillation spectra of our reference models (rHB and RC), and we compare the simulated PSD with the observed ones (Sect. 2.4.3).

2.4.1 Propagation diagram

The propagation diagrams of dipole modes for our rHB and RC reference models are shown in the upper panels of Fig. 2.3. In each panel, we show the modified Brunt-Väisälä ($\tilde{N}$) and Lamb ($\tilde{S}$) frequencies (Takata 2006a) as a function of the normalised radius ($x = r/R_{\rm phot}$, with $R_{\rm phot}$ the photospheric radius), as well as the expected frequency domain of the solar-like oscillations.

The $\tilde{N}$ and $\tilde{S}$ profiles define the inner limits of the g and p cavities. For modes with a frequency close to $\nu_{\rm max}$, these limits are defined by the condition $\tilde{S}(x_1) = \nu_{\rm max}$ and

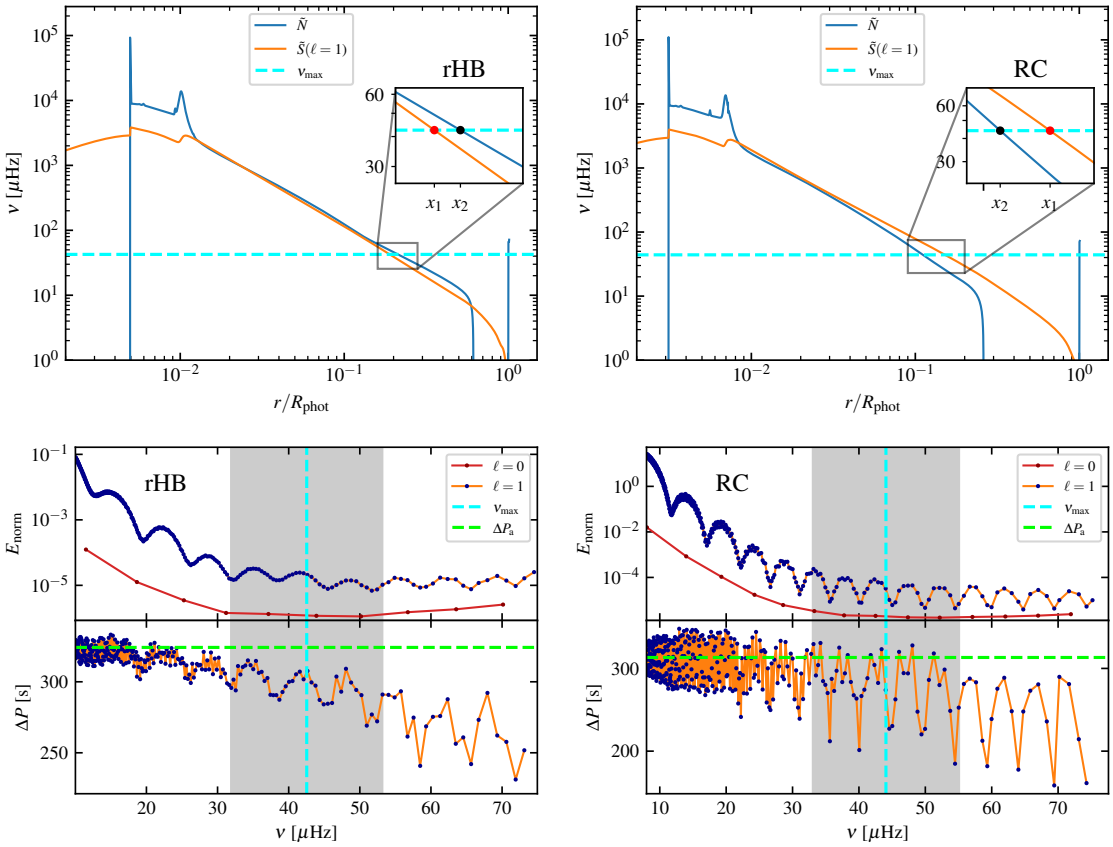

Figure 2.3: Comparison between structure and seismic properties of rHB (left panels) and RC (right panels) reference models (see Sect. 2.3). *Upper panels*: Propagation diagrams of the dipole modes, with blue and orange lines corresponding to the modified Brunt-Väisälä and Lamb frequencies (Takata 2006a), respectively. The grey bands represent the frequency domain of expected solar-like oscillations, and at their centre the dashed cyan lines indicate the ν_{max} values. The insets are zoomed-in views of the evanescent zones, delimited at ν_{max} by the red and black points. Their different extension translates to a different coupling between g and p cavities (see main text). *Lower panels*: Normalised inertia, E_{norm}, and period spacing of the dipole modes, ΔP, as functions of the eigenfrequencies, with the red curve representing, for comparison, the E_{norm} of radial modes. The dashed green line indicates the value of the period spacing from the asymptotic theory of high-order g modes (ΔP_a; Tassoul 1980), and the grey band and the dashed cyan line have the same meaning as in the upper panels.

$\tilde{N}(x_2) = \nu_{\max}$, and in the region between x_1 and x_2 the modes are evanescent.

The extent of the evanescent zone is one of the ingredients that determine the coupling between resonant cavities (Takata 2016a; Pinçon et al. 2020). From the zoomed-in boxes in Fig. 2.3 it appears that this region is smaller in the rHB model than in the RC one, and, therefore, we expect the coupling factor, q, to be larger in the former than in the latter. Indeed, using the structure of our reference models and the strong-coupling approximation[5] for the dipole modes (Takata 2016a; Pinçon et al. 2020), we obtain $q_{\rm rHB} = 0.65$ and $q_{\rm RC} = 0.25$ at $\nu = \nu_{\max}$. We note that these values are consistent, given the typical uncertainties ($\sigma_q \sim 0.2$), with those measured from the observed PSDs (see Tables 2.1 and A.1, Vrard et al. 2016, and Mosser et al. 2017; 2018).

We notice that the value of the coupling factor is also a function of the mode frequency (e.g. Pinçon et al. 2020; Jiang et al. 2020; van Rossem et al. 2024). As shown in Fig. 2.3, the size of the evanescent zone decreases (and thus q increases) with increasing frequency. The value of q varies from 0.56 to 0.74 in the solar-like frequency domain for the rHB model, and from 0.22 to 0.24 for the RC one. In Sect. 2.4.2 we discuss the effect of this variation on the behaviour of the period spacing.

2.4.2 Dipole mode properties

In this section we analyse the properties of the dipole mode spectra computed for our reference models. The bottom panels of Fig. 2.3 show $E_{\rm norm}$ and the period spacing (ΔP, which is the period difference between two consecutive modes of the same angular degree) as a function of the eigenfrequencies.

We recall that $E_{\rm norm}$ is an average of the mode energy, and its value indicates the main region probed by the mode (see Section 1.4.1). Modes that examine central, high-density regions have higher $E_{\rm norm}$ than modes that are preferentially trapped in the outer regions. The inertia of dipole modes of the RC model shows a significant variation between local minima and maxima (ratio up to ≈ 27 in the observable region), corresponding to the p-like and g-like modes, respectively. On the contrary, the inertia in the rHB is almost uniform, with a small contrast between maxima and minima (ratio up to ≈ 3 in the observable region). This indicates that the dipole modes in the rHB are not clearly trapped in any of the resonant cavities, that is, they have an important mixed p–g character. This behaviour is consistent with the coupling factor values derived in the previous section.

[5]The weak-coupling approximation (see e.g. Shibahashi 1979; Unno et al. 1989) does not hold for low-mass CHeB stars (see e.g. Vrard et al. 2016; Mosser et al. 2017; van Rossem et al. 2024).

Since the amplitude of the modes is inversely proportional to the square root of the inertia (see e.g. Dupret et al. 2009), we expect a modulation of the dipole mode amplitudes around the p-like mode in the case of the RC, as observed in some *Kepler* red giants, while many dipole modes with similar amplitudes may be observed in the spectrum of the rHB. This implies an increasing complexity of the oscillation spectra, as shown by the stars in our sample (see Fig. 2.1).

The high value of q also affects the behaviour of the period spacing (see also Mosser et al. 2017). In the bottom part of the lower panels of Fig. 2.3, we plot ΔP as a function of the eigenfrequencies as well as the constant value (dashed green line) predicted by the asymptotic g-mode approximation ($\Delta P_{\rm a}$; Tassoul 1980). In the observable frequency domain, we notice for the rHB model a significant deviation of ΔP from the asymptotic value even for modes with high inertia, as well as a decreasing trend of ΔP with increasing frequency. To show that both effects are a consequence of the high value of q and its frequency dependence, we used the Ong et al. (2020) formalism to separate pure isolated p modes (π modes) from pure isolated g modes (γ modes), that is, pure g modes not affected by the coupling with the acoustic cavity. In Fig. 2.4 we plot the period spacing of dipole γ modes, and, as expected, their average value is consistent with that from the asymptotic approximation of pure high-order g modes. Therefore, the differences in the period spacing of the RC and rHB models are explained by the high coupling for the latter, which causes all dipole modes to have an important acoustic component, thus decreasing the value of ΔP.

2.4.3 Power spectral density

Figure 2.5 shows the simulated PSDs of our reference models together with the inertia of the $\ell = 0, 1, 2, 3$ modes. The contribution of each degree to the PSD is shown in Appendix C.

A comparison between Fig. 2.5 and Fig. 2.1 shows many similarities between the rHB-mock spectrum and the observed ones. These spectra appear noisier than RC ones, with a large number of peaks corresponding to non-radial modes. In particular, there are observable dipole modes in the entire frequency range between two consecutive radial modes, unlike the behaviour in RC and low-RGB stars, where only a few modes around the corresponding p-like mode have observable amplitudes.

We see that the strong coupling also affects the quadrupole modes. Several of them, with frequencies close to those of the p-like modes, are expected to have similar contribu-

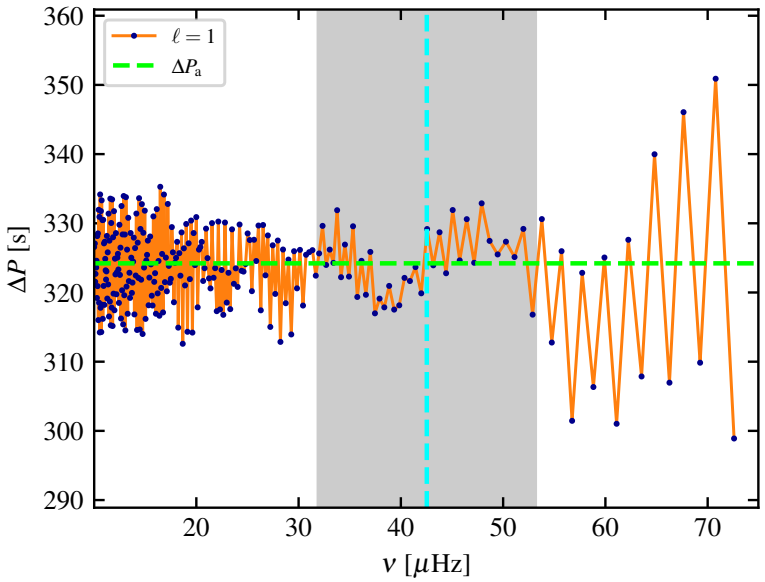

Figure 2.4: Period spacing as a function of the eigenfrequencies of the isolated dipole γ modes (Ong et al. 2020). Other symbols and colours are the same as in Fig. 2.3. The high modulation in the period spacing above the observable frequencies is connected to structural glitches (see e.g. Bossini et al. 2015).

tions to the PSD. Moreover, because of a higher inertia at the local minima with respect to the RC model, quadrupole modes in rHB stars would have lower amplitudes. All that makes it more challenging to detect and characterise $\ell = 2$ modes in CHeB metal-poor stars. Finally, $\ell = 3$ modes have eigenfrequencies close to those of radial modes, and their heights are similar to the background noise. They tend to form a continuum that should be considered during the background analysis (see Appendix C).

2.5 Conclusions

High-quality spectra obtained from the 4-year-long *Kepler* observations of a large number of red giants allowed us to identify a small number of red giants (12) whose oscillation spectra appear to be very noisy or complex with respect to the typical behaviour of oscillation spectra in *Kepler* red giants. Their global seismic parameters are compatible with low-mass stars ($M \lesssim 0.8$ M$_\odot$) in the central He-burning phase, and the fit of the asymptotic relation for the dipole modes (e.g. Vrard et al. 2016) results in coupling factor values $q \gtrsim 0.4$, much higher than the typical value for stars classified as RC ($q \sim 0.25 - 0.30$; e.g. Vrard et al. 2016; Mosser et al. 2017; Mosser et al. 2018). In our sample we find stars with a low to intermediate metallicity (75%) and stars with solar metallicity. Their position in the HRD is compatible with the so-called rHB stars, that is, low-mass objects between the RRL-IS and the RC at the corresponding metallicity. Stellar evolution theory

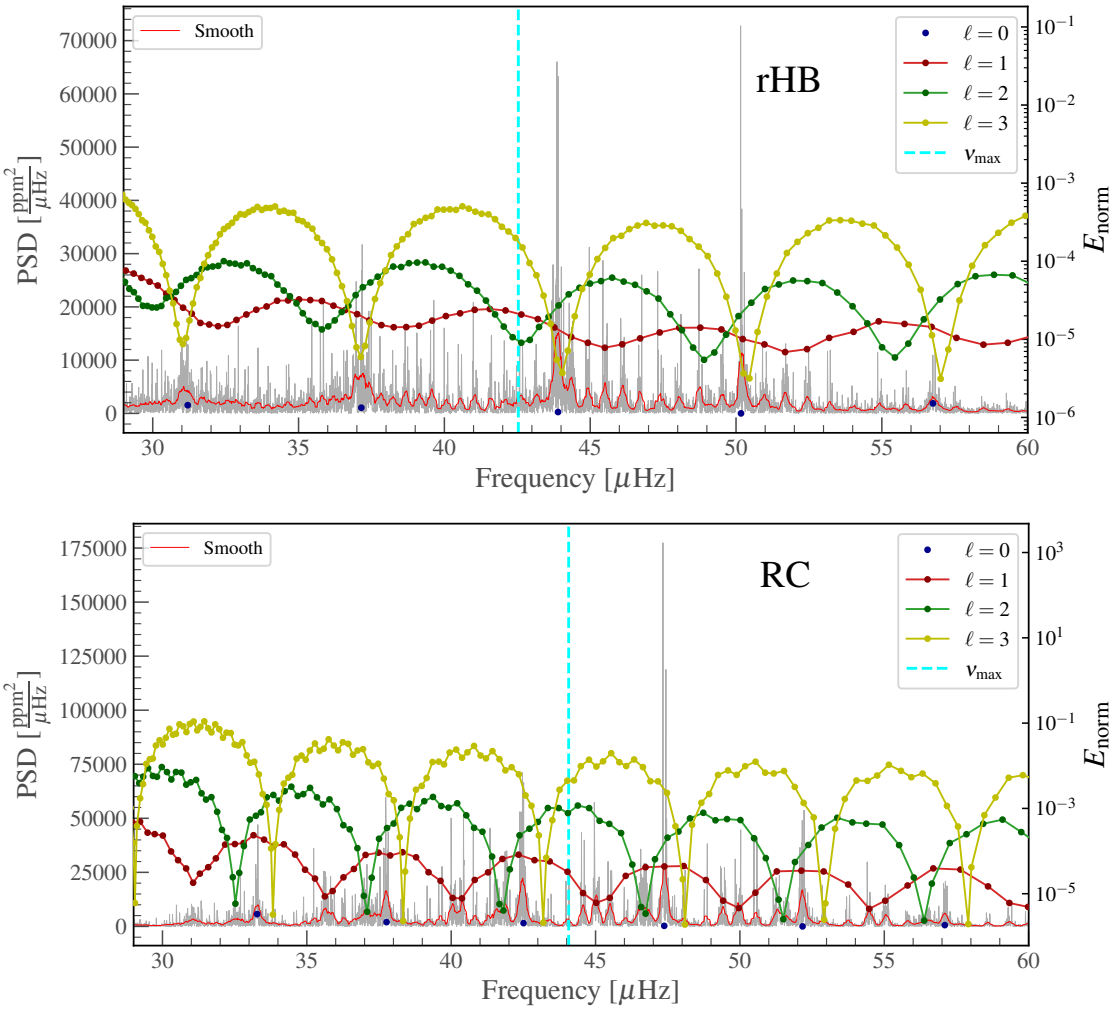

Figure 2.5: Simulated PSD (grey line) as a function of the eigenfrequencies using theoretical $\ell = 0, 1, 2, 3$ modes for rHB (top) and RC (bottom) models. The red line is a smoothed version of the PSD. The vertical dashed cyan lines correspond to ν_{max} values, and coloured dots and lines represent the values of E_{norm} for the $\ell = 0, 1, 2, 3$ modes.

predicts for these stars a structure consisting of a He core of ~ 0.5 $M_\odot$ and an envelope of $\approx 0.1 - 0.2$ $M_\odot$ (e.g. Rood et al. 1989; Valcarce et al. 2008; Gratton et al. 2010; Girardi 2016; Tailo et al. 2020).

In this chapter we have shown that the oscillation spectra we expect for this type of star are entirely consistent with those observed in our sample. These spectra are clearly different from those of the stars that, with a similar He core but a much larger envelope, populate the RC. The main factor determining these differences is the coupling between the inner and outer regions, which reflects very different density profiles inside these stars. A second factor that increases the complexity of these spectra is the higher temperature of the less metallic stars, which decrease the lifetime of the modes. In fact, solar-like oscillations in rHB stars have also been detected in the K2 (Howell et al. 2014) light curves of the globular cluster M4 (e.g. Wallace et al. 2019), where the complexity of the spectra and the reduced observation time (80 days) have made it difficult to extract robust $\langle \Delta\nu \rangle$ values (e.g. Tailo et al. 2022; Howell et al. 2022).

Stars in the rHB stage are well known and easily identified in globular clusters. Here we have also shown the ability of asteroseismology to identify these low-mass CHeB stars in the field and in solar-metallicity environments where, even with high-precision photometry, they would be hardly distinguishable from other stars in RC or RGB phases.

It is clear that 0.7 $M_\odot$ stars, especially those of solar metallicity, must have followed a non-standard evolution during which they lost a large amount of mass (see also Li et al. 2022; Bobrick et al. 2024). This work provides us with a solid framework for the future study of these stars and of the processes that led them to their current mass. Knowledge of this is fundamental for deriving their ages with accuracy, and potentially providing another piece of the puzzle in the sequence between RC and subdwarf B stars or other stripped stars.

Chapter 3

Anomalously low-mass core-He-burning star in NGC 6819 as a post-common-envelope phase product[1]

As discussed in Chapter 2, precise masses of red-giant stars enable a robust inference of their ages, but there are cases where these age estimates are highly precise yet very inaccurate. Examples are core-helium-burning (CHeB) stars that have lost more mass than predicted by standard single-star evolutionary models. Members of star clusters in the *Kepler* database represent a unique opportunity to identify such stars, because they combine exquisite asteroseismic constraints with independent age information (members of a star cluster share similar age and chemical composition). In this work, my collaborators and I focus on the single, metal-rich ($Z \approx Z_{\odot}$), Li-rich, low-mass, CHeB star KIC4937011, which is a member of the open cluster NGC 6819 (turn-off mass of ≈ 1.6 $M_{\odot}$, i.e. age of ≈ 2.4 Gyr). This star has ≈ 1 $M_{\odot}$ less mass than expected for its age and metallicity, which could be explained by binary interactions or mass-loss along the red-giant branch (RGB). To infer formation scenarios for this object, we perform a Bayesian analysis by combining the binary stellar evolutionary framework `binary_c v2.2.3` with the dynamic nested sampling approach contained in the `dynesty v2.1.1` package. We find that this star is likely the result of a common-envelope evolution (CEE) phase during the RGB stage of the primary star in which the low-mass (< 0.71 $M_{\odot}$) main sequence companion

[1]The work presented in this chapter is based on Matteuzzi et al. (2024).

does not survive. The mass of the primary star at the zero-age main sequence is in the range $[1.46, 1.71]$ $M_\odot$, with a log-orbital period in the range $[0.06, 2.4]$ $\log_{10}$(days). During the CEE phase $\approx 1\,M_\odot$ of material is ejected from the system, and the final star reaches the CHeB stage after helium flashes as if it were a single star of mass $\approx 0.7\,M_\odot$, which is what we observe today. Although the proposed scenario is consistent with photometric and spectroscopic observations, a quantitative comparison with detailed stellar evolution calculations is needed to quantify the systematic skewness of radius, luminosity, and effective temperature distributions towards higher values than observations.

3.1 Introduction

The advent of the space mission *Kepler* has made it possible to study in great detail the oscillation spectra of tens of thousands of red-giant stars, and thus, to constrain their internal structures, properties and evolutionary phases. These asteroseismic constraints, coupled with information on photospheric chemical abundances and temperature, have also given us the ability to precisely measure their radii and masses (De Ridder et al. 2009; Hekker et al. 2011; Huber et al. 2011; Miglio et al. 2013; Stello et al. 2013; Mosser et al. 2014; Yu et al. 2018; García et al. 2019; Kallinger 2019).

Precise masses of red-giant stars enable a robust inference of their ages (Anders et al. 2016; Casagrande et al. 2016; Pinsonneault et al. 2018; Silva Aguirre et al. 2018; Miglio et al. 2021; Montalbán et al. 2021), but there are cases in the field and in open star clusters where these estimates are significantly different than the age predicted by standard single-star evolutionary models. For example, some members of open clusters have more mass than the observed average mass for their evolutionary phase (Brogaard et al. 2016; Handberg et al. 2017; Brogaard et al. 2018; Brogaard et al. 2021). This means that such stars appear younger than they actually are, thus, they must have experienced mass transfer or merger events in the past (Izzard et al. 2018). Despite potential insights from observations that could assist in distinguishing between different formation scenarios (Brogaard et al. 2018), the evolutionary history of many observed systems with masses that deviate from their expected mass remains uncertain. The limited support from other stars in age determination makes it challenging to identify non-standard evolutionary paths for field stars. An exception to this is the thick disc, which has a well-defined turn-off mass that allows for the tracking of the evolutionary history of these stars (Chiappini et al. 2015; Martig et al. 2015; Izzard et al. 2018; Grisoni et al. 2024).

While there are observed systems with a significant excess of mass with respect to the

average mass in the cluster for their evolutionary phase, the opposite is true as well. There are red-giant members of open clusters with less mass than the observed average mass for their evolutionary phase (Handberg et al. 2017; Brogaard et al. 2021). Considering their mass and metallicity, they have lost more mass than expected, most likely via interaction with a companion star (Li et al. 2022; Bobrick et al. 2024) or because of mass loss along the red-giant branch (RGB). There are observations of such undermassive stars also in the field (Miglio et al. 2021; Li et al. 2022; Matteuzzi et al. 2023). Some of them are low-mass, core-helium-burning (CHeB) stars located in the colour-magnitude diagram between the RR Lyrae and the red clump (RC), thus are red horizontal branch (rHB) stars. By modelling their structure and pulsation spectra, Matteuzzi et al. (2023) found that these low-mass objects have a helium-core mass of ≈ 0.5 $M_\odot$ and a hydrogen-rich envelope of $\approx 0.1 - 0.2$ $M_\odot$ (see Chapter 2), that is they are stars with a less massive envelope than other stars in the same evolutionary phase and with similar metallicity, but slightly more massive than the RR Lyrae stars with similar metallicity. This means that such undermassive stars are partially stripped, probably as a result of a past binary interaction. Investigating plausible formation scenarios for these stars is critical to better constrain their actual ages and to potentially provide another piece of the puzzle in the sequence between RC stars, metal-rich RR Lyrae and subdwarf B (sdB) stars, or other stripped stars.

In binary stars, mass transfer is possible by direct Roche-lobe overflow (RLOF) or by wind mass loss (see De Marco et al. 2017, for a review). When mass is transferred from red-giant stars and low-mass main sequence (MS) stars on a dynamical time-scale, the companion may be engulfed and a common-envelope evolution begins (CEE; e.g. Paczyński 1976; Ivanova et al. 2013; Röpke et al. 2023). This can happen when mass-transfer is unstable, i.e. the transfer of mass by the donor leads to an increase in mass-transfer rate. Whether the mass-transfer becomes unstable is usually determined based on a critical mass-ratio, $q_{\rm crit}$, between the primary mass and the companion mass and when the system exceeds this mass ratio ($q_1 > q_{\rm crit}$, Hurley et al. 2002) it will undergo unstable mass-transfer followed by a CEE. At this stage drag forces transfer part of the orbital energy to the common envelope (CE), shrinking the orbit and ejecting at least part of the CE (Shima et al. 1985; Kim 2010; MacLeod et al. 2015; Ohlmann et al. 2016; Chamandy et al. 2019; Reichardt et al. 2019; Sand et al. 2020). The consequence of this CE phase is that stars either merge, or end up much closer than before this phase. The easiest way to model the CEE is using the α-formalism (van den Heuvel 1976; Webbink 1984; Livio et al. 1988; de Kool 1990; Han et al. 1994; Dewi et al. 2000; Xu et al. 2010b; Xu et al. 2010a; Ivanova

et al. 2011; Wang et al. 2016), also called the energy formalism. This formalism can be described by the following equation,

$$E_{\rm bind} = \alpha_{\rm ce} \Delta E_{\rm orb}, \tag{3.1.1}$$

where

$$E_{\rm bind} = -\frac{G m_1 m_{1,\rm env}}{\lambda_{\rm ce} R_1} \tag{3.1.2}$$

and

$$\Delta E_{\rm orb} = -\frac{G m_{1,\rm core} m_2}{2 a_{\rm f}} + \frac{G m_1 m_2}{2 a_{\rm i}} \tag{3.1.3}$$

are the binding energy of the envelope of the primary star (the donor star) and the difference in orbital energy after and before the CEE, respectively. $E_{\rm bind}$ depends on the mass (m_1), the envelope mass ($m_{1,\rm env}$), the Roche-lobe radius (R_1) of the primary star, and it also contains a numerical factor $\lambda_{\rm ce}$ to characterise the central concentration of the envelope. $\Delta E_{\rm orb}$ depends also on the core mass of the primary star ($m_{1,\rm core} = m_1 - m_{1,\rm env}$), the mass of the companion star (the accretor star), and the orbital separation before ($a_{\rm i}$) and after ($a_{\rm f}$) the CEE. Finally, $\alpha_{\rm ce}$ indicates the fraction of orbital energy converted into energy used to eject the envelope, thus it is the efficiency of the CE ejection. Unfortunately, there are no direct observations of CEE events with which we can constrain $\lambda_{\rm ce}$ and $\alpha_{\rm ce}$. Nonetheless, observations of post-CEE systems and 3D hydrodynamical simulations suggest that the value of $\alpha_{\rm ce}$ is not universal and depends on many factors such as donor mass, mass ratio and evolutionary stage (Taam et al. 2000; Podsiadlowski et al. 2003; Politano 2004; De Marco et al. 2011; Davis et al. 2012; Iaconi et al. 2019; Belloni et al. 2024). Moreover, many works (Han et al. 1994; Dewi et al. 2000; Dewi et al. 2001; Podsiadlowski et al. 2003; Webbink 2008; Xu et al. 2010b; Xu et al. 2010a; Wong et al. 2014) suggest that $\lambda_{\rm ce}$ varies as the star evolves and significantly deviates from a constant value. However, from an analysis of equations 3.1.1, 3.1.2 and 3.1.3, it is evident that the properties of the post-CEE system do not change when the product $\alpha_{\rm ce} \cdot \lambda_{\rm ce}$ is held constant. Despite our limited understanding of the variables $\lambda_{\rm ce}$ and $\alpha_{\rm ce}$, we can effectively constrain the post-CEE phase by using $\alpha_{\rm ce} \cdot \lambda_{\rm ce}$. Conversely, a better knowledge of the post-CEE phase gives us a constraint on the possible $\alpha_{\rm ce} \cdot \lambda_{\rm ce}$ values.

Members of star clusters observed by the *Kepler* space telescope represent a unique opportunity to constrain formation channels of undermassive stars, because they combine exquisite asteroseismic constraints with age information since members of a star cluster share similar age and chemical composition. In this chapter we focus on the red-giant star KIC4937011, a member of the Galactic star cluster NGC 6819 which has a turn-off mass

of ≈ 1.6 $M_\odot$ (i.e. an age of ≈ 2.4 Gyr, Burkhead 1971; Lindoff 1972; Auner 1974; Rosvick et al. 1998; Kalirai et al. 2001; Basu et al. 2011; Yang et al. 2013; Jeffries et al. 2013; Bedin et al. 2015; Brewer et al. 2016). Based on the scaling relation between the mean large frequency separation and the frequency of maximum power, Handberg et al. (2017) determined that KIC4937011 has a mass of 0.71 ± 0.08 $M_\odot$. This value is consistent, within the errors, with the mass calculated using the scaling relation involving the luminosity and the frequency of maximum power (Matteuzzi et al. 2023). Additionally, analysis of the asymptotic period spacing of the dipole modes indicates that KIC4937011 is currently in the RC phase (Matteuzzi et al. 2023). Based on spectroscopy (Anthony-Twarog et al. 2013; Carlberg et al. 2015; Lee-Brown et al. 2015), we know that it is a single star with near-solar metallicity, a high lithium and oxygen content, and a rotational velocity of 8.3 ± 0.3 km/s (i.e. a higher value than the other red-giant stars in this cluster). This star has ≈ 1 $M_\odot$ less mass than the average mass of RC stars in NGC 6819 (i.e. 1.64 $M_\odot$, Handberg et al. 2017), which could be explained by binary interactions.

The chapter is organised as follows. We briefly describe the observational properties of KIC4937011 in Section 3.2. In Section 3.3 we describe the theoretical framework that permits us to predict the formation channel, and how we simulate binary interactions. In Section 3.4 we present our results, namely the most credible formation channels for this star, which is the consequence of a common-envelope evolution phase in which the companion does not survive. Section 3.5 concludes.

3.2 Observational data

In Section 3.1 we state that KIC4937011 is a RC member of the open cluster NGC 6819 (HRD in Figure 3.1, observational properties in Table 3.2), and this is suggested by its radial velocity (Hole et al. 2009; Anthony-Twarog et al. 2013; Carlberg et al. 2015), CMD position (Anthony-Twarog et al. 2013), and proper-motion (Gaia Collaboration et al. 2016; Gaia Collaboration et al. 2023; Babusiaux et al. 2023). This allows for an independent estimation of the age of KIC4937011 regardless of its mass. In this work we use the age estimate $2.38 \pm 0.05 \pm 0.22$ Gyr[2] based on eclipsing binaries of Brewer et al. (2016), but with an error of 0.27 Gyr[3] (Section 3.3.2). The metallicity of the cluster is similar to solar (Rosvick

[2]These uncertainties are estimates of the random and systematic effects (due to model physics differences and metal content), respectively.

[3]We do not add the two uncertainties in quadrature, because the direct addition is an upper limit of the true uncertainty (Schwarz inequality), which does not depend on any possible correlation between the two.

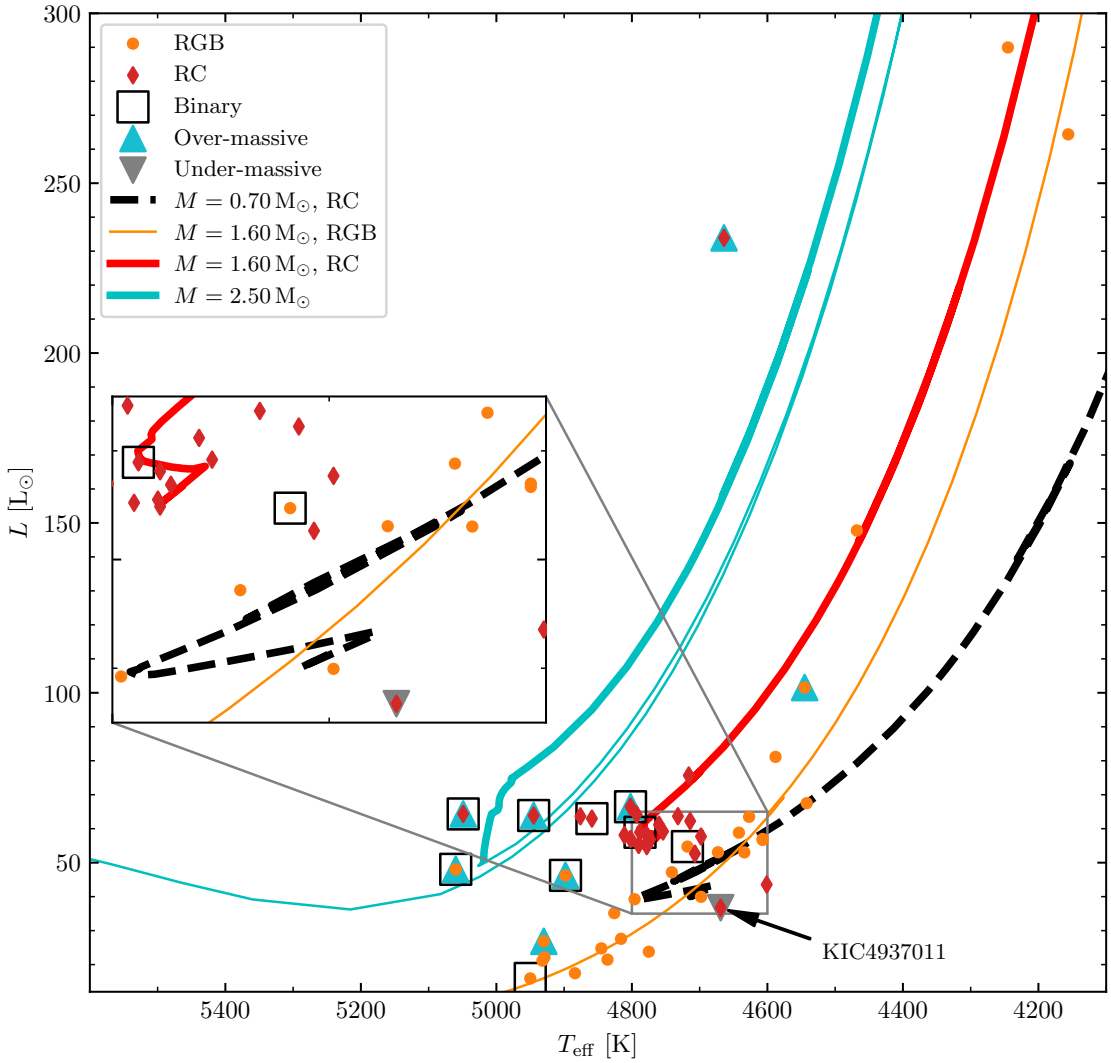

Figure 3.1: HRD of NGC 6819 showing RC and RGB member stars. Apart from standard single stars, some are members of binary systems, some are overmassive stars and one (KIC4937011) is undermassive. The solid lines are evolutionary tracks from the RGB phase until the first thermal pulse in the asymptotic giant branch (AGB) phase for a 1.60 $M_\odot$ and a 2.50 $M_\odot$ star with solar metallicity, while the dotted line represents a 0.70 $M_\odot$ star with solar metallicity from the beginning of the CHeB stage until the first thermal pulse in the AGB phase. KIC4937011 is less bright and hot than other member stars at the same evolutionary stage, and it would be compatible with a 1.60 $M_\odot$ RGB star if we had no information about its evolutionary state and mass. For a full description of the models used in the figure see Handberg et al. (2017).

et al. 1998; Anthony-Twarog et al. 2014; Lee-Brown et al. 2015; Slumstrup et al. 2019), however other works suggest super-solar metallicities ([Fe/H] = 0.09±0.03, Bragaglia et al. 2001). This is in line with the metallicity of KIC4937011, which is approximately solar ([Fe/H] = 0.04, Carlberg et al. 2015; [Fe/H] = −0.05, Lee-Brown et al. 2015). In this work we use a metallicity $Z = 0.02$ for KIC4937011 (Section 3.3.2). The observed $^{12}C/^{14}N$ of KIC4937011 is consistent with its other more massive (i.e. ≈ 1.64 $M_\odot$) counterparts in the RC phase, although the lower the mass, the higher $^{12}C/^{14}N$ should be in a star that evolves in isolation ($^{12}C/^{14}N > 3$ for such a low-mass, metal-rich star, Salaris et al. 2015). Past mass transfer events may provide an explanation for the peculiar $^{12}C/^{14}N$ observed in the envelope of KIC4937011. It is possible that the envelope originates from a star that during its first dredge-up was more massive than the current KIC4937011 (Hekker et al. 2019; Tayar et al. 2023).

Handberg et al. (2017) derive masses in NGC 6819 in the RGB and RC phases using asteroseismic data from *Kepler*, obtaining average masses of 1.61±0.02 $M_\odot$ and 1.64±0.02 $M_\odot$, respectively. This means that the integrated mass loss in the RGB phase in this cluster is compatible with a Reimers' mass loss law (Reimers 1975; Kudritzki et al. 1978) that has an efficiency $\eta_{RGB} = 0.1$. However, KIC4937011 has almost 1 $M_\odot$ less mass than its other counterparts in the RC phase. As a result, an efficiency $\eta_{RGB} > 1$ is required in order to explain the isolated evolution of this star. Such a high efficiency is highly improbable, as it far exceeds the average value measured in NGC 6819. Therefore, it is unlikely that mass loss in the RGB phase through winds alone can account for the mass discrepancy observed in KIC4937011. Indeed, Carlberg et al. (2015) proposed an interaction between a ≈ 1.7 $M_\odot$ red-giant star and a brown dwarf of mass 45 M_{Jup} to explain the enrichment in lithium [$A(Li) = 12 + \log(N_{Li}/N_H) = +2.3$ dex, Anthony-Twarog et al. 2013] and the loss of almost 1 $M_\odot$. However, alternative explanations exist for the observed Li-enrichment in red-giant stars. Some observations suggest that R-stars with similar chemical composition and lithium content may have interacted with a companion star instead of a brown dwarf (Zamora et al. 2006). Another possibility is that lithium-rich RC stars could have been created through the merging of a helium white dwarf (HeWD) star and a RGB star (Zhang et al. 2020). Several mechanisms have been proposed to account for the Li-enrichment in red-giant stars, including planet or brown dwarf engulfment (Ashwell et al. 2005; Aguilera-Gómez et al. 2016b; Aguilera-Gómez et al. 2016a), accretion from an asymptotic giant branch (AGB) star or a nova (José et al. 1998), and the Cameron et al. (1971) mechanism with some extra-mixing (Denissenkov et al. 2004; Guandalini et al. 2009; Denissenkov

2010; Aguilera-Gómez et al. 2023), such as the HeWD-RGB merger mentioned earlier. Therefore, the lithium content alone is not a reliable indicator to discriminate between formation channels. However, considering all available pieces of information, we need to incorporate binary interactions into evolutionary models of KIC4937011.

Carlberg et al. (2015) perform multiple checks of whether the spectroscopic analysis is affected by either a companion to the Li-rich star or an unrelated background object. They find that the radial velocity is constant within $0.1 - 0.2$ km/s in nearly one month of observations. Even when they consider 20 years of observations with other surveys they do not obtain variations in its radial velocity. They also search for a secondary spectrum, but they do not identify any significant secondary peaks. Furthermore, there is no indication of infrared excess, which is observed in other Li-rich red-giant stars (Rebull et al. 2015; Mallick et al. 2022). Even using the currently available Gaia-DR3 astrometry data (non-single star processing in Halbwachs et al. 2023) there is no evidence for companion stars. We also test the non-single star hypothesis using the `fidelity_v2` table (Rybizki et al. 2022) and the `RUWE` value[4]. Together, all this information suggests that KIC4937011 has no companion.

3.3 Bayesian inference of formation scenarios

In this section we describe the Bayesian approach we adopt to infer the most probable formation scenario for KIC4937011. This is done using an evolutionary code for binary stars (Section 3.3.1) coupled with a Monte Carlo (MC) method (Section 3.3.2).

3.3.1 Evolutionary code for binary stars

The software `binary_c v2.2.3`[5] (Izzard et al. 2004; Izzard et al. 2006; Izzard et al. 2009; Izzard et al. 2018; Izzard et al. 2023) makes synthetic populations of single, binary and multiple stars. It is based upon the Binary Star Evolution (`BSE`) code (Hurley et al. 2002), which uses analytic fits to rapidly follow the properties of a system as a function of time (Hurley et al. 2000). In addition, `binary_c v2.2.3` rapidly calculates nucleosynthetic yields from such synthetic populations, adopting first, second, third dredge-up and thermally-pulsing asymptotic giant branch (TPAGB) prescriptions from Izzard et al.

[4]The renormalised unit weight error (`RUWE`) is the square root of the normalised chi-square of the astrometric fit to the along-scan observation. It is expected to be 1.0 for well-behaved solutions of single stars (Gaia Collaboration et al. 2016; Gaia Collaboration et al. 2023).

[5]https://gitlab.com/binary_c/binary_c/-/tree/releases/2.2.3

(2006), which are based on Karakas et al. (2002), and the supernova yields from massive stars from Woosley et al. (1995) and Chieffi et al. (2004). These prescriptions are very useful for globular cluster and Galactic chemical evolution simulations (Izzard et al. 2018; Yates et al. 2024). The physics implemented in the code (De Marco et al. 2017, for a review about relevant physical processes in binary systems) is mainly described in the above cited papers. The code allows for the incorporation of alternative models beyond those utilised in the BSE code, such as different RLOF (Claeys et al. 2014), wind Roche-lobe overflow (WRLOF; Abate et al. 2013; Abate et al. 2015), accretion and thermohaline mixing (Stancliffe et al. 2007; Izzard et al. 2018), supernovae (Boubert et al. 2017b; Boubert et al. 2017a), tides (Siess et al. 2013), rejuvenation (de Mink et al. 2013; Schneider et al. 2014), stellar rotation (de Mink et al. 2013), stellar lifetimes (Schneider et al. 2014), CEE (Wang et al. 2016), and circumbinary discs (Izzard et al. 2023). This algorithm operates about 10^7 times faster than full evolution and nucleosynthesis calculations, which makes it very useful for a Bayesian approach to parameter estimation.

In this work we adopt a Python interface to `binary_c v2.2.3`, `binary_c-python v0.9.6`[6] (Hendriks et al. 2023). We mainly adopt the binary-physics prescriptions of the BSE code, but the model of the properties of the AGB comes from Karakas et al. (2002), the RLOF modelling onto a white dwarf from Claeys et al. (2014), and the critical mass ratios $q_{\rm crit}$ from Table 3.1. We fix to 0.5 the fraction of the recombination energy in the CE that participates in the ejection of the envelope (i.e. $\lambda_{\rm ionisation} = 0.5$ in `binary_c v2.2.3`), and we consider $\alpha_{\rm ce} \cdot \lambda_{\rm ce}$ as a single free parameter of the model. We force a first dredge-up in Hertzsprung gap (HG) and RGB stars that undergo a CEE phase, but not for MS stars, because the dynamical mixing effects owing to the spiral-in process are assumed to completely mix the envelope in red-giant stars (Izzard et al. 2006). Furthermore, we do not include mass loss enhanced by rotation, tides and He flashes; we ignore thermohaline mixing, WRLOF and the lithium abundance change over time.

3.3.2 Monte Carlo simulations

To constrain binary systems that best explain the current state of KIC4937011, we need to efficiently estimate the posterior of a set of parameters for a given model obtained with `binary_c v2.2.3` and `binary_c-python v0.9.6`. We use the dynamic nested sampling approach contained in the `dynesty v2.1.1`[7] package (Speagle 2020).

Initial conditions of all MC simulations are a binary system formed by zero-age main

[6] https://gitlab.com/binary_c/binary_c-python/-/tree/releases/0.9.6/2.2.3

[7] https://github.com/joshspeagle/dynesty/tree/v2.1.1

Table 3.1: Critical mass ratio $q_{\rm crit}$ for stable RLOF for different types of donor stars, in the case of a non-degenerate and a degenerate accretor. The meaning of each acronym is in Hurley et al. (2002).

Donor	Non-deg accretor	Deg accretor
MS with $M \leq 0.718$ M$_\odot$	0.6944	1.0
MS with $M > 0.718$ M$_\odot$	1.6	1.0
HG, HeHG	4.0	4.7619
RGB, EAGB, TPAGB	Hurley et al. (2002)	1.15
CHeB, HeMS	3.0	3.0
HeGB	0.78125	1.15
WD, NS, BH	3.0	0.625

sequence (ZAMS) stars with circular orbits, $Z = 0.02$ and $\eta_{\rm RGB} = 0.1$, where we choose the metallicity and mass loss to be compatible with observations (Section 3.2). Our main results do not change when we allow Z and/or $\eta_{\rm RGB}$ to vary freely within the observational uncertainties. The main difference is that the density distributions become broader and less predictive. We do not consider initially eccentric binaries, because the evolution of close binary populations is almost independent of the initial eccentricity (Hurley et al. 2002).

We use uniform priors for $\alpha_{\rm ce} \cdot \lambda_{\rm ce}$ (Sections 3.1 and 3.3.1), the logarithm[8] of the initial period, $\log P_0$, and the initial mass ratio, $q_{\rm ZAMS} = M_{2,\rm ZAMS}/M_{1,\rm ZAMS}$. For the initial mass of the primary star, $M_{1,\rm ZAMS}$, we employ the probability density distribution of Chabrier (2003)[9]. We calculate the likelihood function given the current evolutionary phase (CHeB), mass ($M_{1,\rm CHeB} = 0.71 \pm 0.08$ M$_\odot$) and age ($t_{\rm age} = 2.38 \pm 0.27$ Gyr) of the star (Sections 3.1, 3.2). For more details on the likelihood used and the intervals chosen for our priors we refer the reader to Appendix D and Table D.1.

In Fig. 3.2 the corner plot showing the age and primary-mass density distributions of our MC simulations at the CHeB stage (see also Table 3.2), compared with the observed values for KIC4937011 (red lines). Our modelling correctly fits, within errors, the observed current age and mass of KIC4937011.

[8] In this chapter we use the notation $\log(x) \equiv \log_{10}(x)$.

[9] We check that uniform priors for $M_{1,\rm ZAMS}$ lead to the same results. However such new priors require more CPU time.

Table 3.2: Medians and credible intervals (CI) of the density distributions explained in Section 3.3.2 and 3.4.1. In the last column the observed values for KIC4937011 with the corresponding references. In Section 3.4.1 we discuss where such narrow CI in chemistry come from.

Parameter	Median	68% CI	99.7% CI	Obs
$t_{\rm age}$ [Gyr]	2.40	[2.18, 2.62]	[1.43, 3.18]	2.38 ± 0.27^{a}
$M_{1,\rm CHeB}$ [$M_\odot$]	0.74	[0.65, 0.83]	[0.50, 0.96]	0.71 ± 0.08^{b}
$\alpha_{\rm ce} \cdot \lambda_{\rm ce}$	14	[6, 23]	[0.5, 47]	...
$\log(P_0/\rm days)$	0.58	[0.36, 1.06]	[0.08, 2.2]	...
$q_{\rm ZAMS}$	0.29	[0.16, 0.37]	[0.05, 0.55]	...
$M_{1,\rm ZAMS}$ [$M_\odot$]	1.69	[1.59, 1.87]	[1.48, 2.62]	...
$M_{2,\rm ZAMS}$ [$M_\odot$]	0.50	[0.29, 0.63]	[0.081, 0.88]	...
$M_{1,\rm He-core}$ [$M_\odot$]	0.48	[0.38, 0.53]	[0.32, 0.60]	...
$R_{1,\rm CHeB}$ [$R_\odot$]	20	[9.6, 28]	[0.2, 50]	9.3 ± 0.5^{b}
$L_{1,\rm CHeB}$ [$L_\odot$]	148	[65, 191]	[40, 376]	37 ± 4^{b}
$T_{\rm eff,1,CHeB}$ [K]	4270	[4074, 5347]	[3588, 27556]	4710 ± 50^{b}
$^{12}C/^{13}C$	90	[32, 90]	[14, 90]	25 ± 5^{d}
$^{12}C/^{14}N$	3.2	[1.4, 3.2]	[0.62, 3.2]	1.4 ± 0.2^{d}
$^{14}N/^{16}O$	0.13	[0.13, 0.23]	[0.13, 0.34]	0.17 ± 0.04^{d}

References. $^{(a)}$ Brewer et al. (2016); $^{(b)}$ Handberg et al. (2017); $^{(b)}$ Matteuzzi et al. (2023); $^{(d)}$ Carlberg et al. (2015)

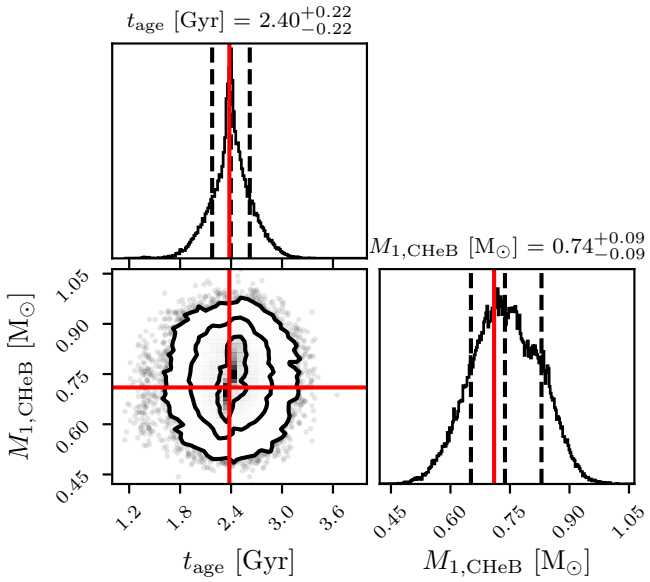

Figure 3.2: Corner plot showing the age and primary mass density distributions at the CHeB stage for our full sample described in Section 3.3.2. The contours are referred to 1, 2, and 3-σ credible regions, respectively. In red the observed values for KIC4937011 (see also Table 3.2). We see that our modelling correctly fits, within errors, the observed current age and mass of KIC4937011. As explained in the Appendix D, we take as the reference time for the CHeB of each MC simulation the age that gives the highest likelihood.

3.4 Results

In this section we present significant results derived from our Monte Carlo simulations (Section 3.4.1), and we discuss the most credible formation channel (Section 3.4.2).

3.4.1 Formation channels constrained by age and mass observations

Figure 3.3 shows the estimated posterior density distributions of Monte Carlo simulations discussed in Section 3.3.2 and presented in Table 3.2. A strong anti-correlation is observed between the product $\alpha_{\rm ce} \cdot \lambda_{\rm ce}$ and log P_0, with a Pearson correlation coefficient of approximately -0.69. There are also weaker anti-correlations between log P_0 and the other parameters. Equation 3.1.1 indicates that as the period increases, so does the orbital radius, while the surface gravity of the CE decreases, requiring a lower $\alpha_{\rm ce}$ for mass ejection. This suggests that certain areas of the log $P_0 - \alpha_{\rm ce} \cdot \lambda_{\rm ce}$ plane can be excluded (Figure 3.3 and Table 3.2), but we are unable to provide stricter constraints on the individual values of log P_0 and $\alpha_{\rm ce} \cdot \lambda_{\rm ce}$. Furthermore, $\alpha_{\rm ce} \cdot \lambda_{\rm ce}$ tends to higher values than suggested by previous studies (Section 2.1). A plausible physical interpretation for this phenomenon relates to recombination energy. Specifically, high $\alpha_{\rm ce} \cdot \lambda_{\rm ce}$ values can be obtained when

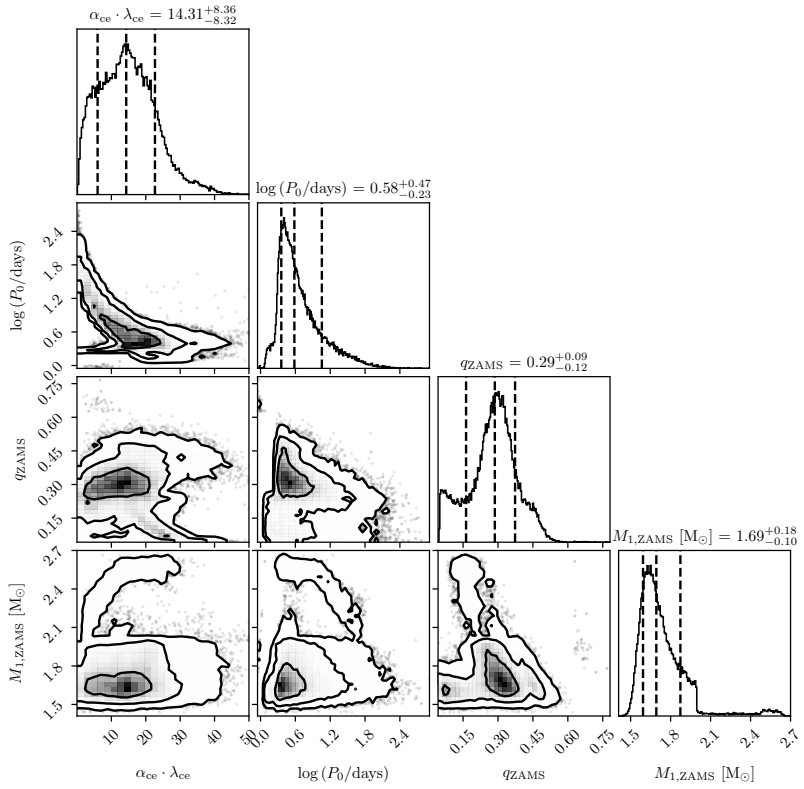

Figure 3.3: Corner plot showing the posterior density distributions of our MC simulations described in Section 3.3.2. The contours are referred to 1, 2, and 3-σ, respectively.

α_{ce} is constrained to values below one, and λ_{ce} is calculated according to the Wang et al. (2016) prescriptions, utilising a high $\lambda_{ionisation}$ value. Nonetheless, we cannot rule out the influence of additional energy sources, including dust formation or nuclear burning, that occur during the CEE phase. They may also contribute to the observed high $\alpha_{ce} \cdot \lambda_{ce}$ values.

Our estimated $M_{1,ZAMS}$ (Figure 3.3 and Table 3.2) is slightly higher than, but still consistent with, the observed average mass of RGB stars in NGC6819 (1.61 ± 0.02 M$_\odot$, Handberg et al. 2017). This implies that a RGB star with a mass of 1.87 M$_\odot$ (i.e. the upper limit of our 68% credible interval for $M_{1,ZAMS}$) would begin the RGB phase about 0.82 Gyr[10] earlier than the current RGB stars in NGC6819. Therefore, any binary interaction and evolution happened between a primary RGB star and a companion should last less than $\approx$ 1 Gyr to be consistent with the observations. Moreover, the q_{ZAMS} posterior distribution lower limit in the 99.7% credible interval is very close to the lower limit of our prior distribution (Table D.1), and probably limits in the prior below 0.08 M$_\odot$ are necessary for the companion mass.

[10]This age difference is calculated using `binary_c v2.2.3` at $Z = 0.02$ and $\eta_{RGB} = 0.1$.

Common-envelope phases create distinct pathways

In this section we summarise the results concerning the number of CEE phases up to the CHeB stage of the primary star for the full sample. Every MC simulation considered (i.e. 65225 simulations) had one CEE phase, with a negligible percentage (0.006%, i.e. 4 out of 65225 simulations) having two. This implies that our modelling predicts KIC4937011 to be a post-common-envelope phase product. The majority of the binary systems (i.e. 99.92%) evolves without mass transfers until the primary star is in the subgiant or in the RGB phase and the companion in the MS phase. At this point an unstable mass transfer begins, leading to a CEE phase, and to the shrinkage of the orbits (Section 3.1). The loss of orbital energy is the reason why the probability of undergoing another CEE phase decreases significantly. Finally, in all our sample of MC simulations the companion star merges with the primary star, leaving as the final product a single CHeB star. This is in line with the observations (Section 3.2).

Primary star physical properties

In Fig. 3.4 and Table 3.2 we present the helium-core mass, radius, luminosity, and effective temperature posterior density distributions of the primary star at the CHeB stage estimated from the MC simulations. In our simulations the primary stars have helium-core masses in the 99.7% credible interval $[0.32, 0.60]$ $M_\odot$. Moreover, from the panel (a) we see that there are three main peaks: at around 0.32 $M_\odot$, 0.47 $M_\odot$ and 0.52 $M_\odot$. The first helium-core mass peak is expected for a secondary clump star, while the second for a RC star (Girardi 2016). However, helium-core masses above ≈ 0.50 $M_\odot$ are expected during the early asymptotic-giant branch (EAGB) stage and not during the CHeB stage. Such high helium-core masses lead to much higher radii ($> 15\,R_\odot$) and luminosities ($> 100\,L_\odot$) than expected of CHeB stars of mass ≈ 0.7 $M_\odot$, and they also lead to effective temperatures well below 4500 K. Moreover, such high luminosities would not be consistent with the observed mixed modes behaviour in KIC4937011. It is worth noting that `binary_c v2.2.3` is based on the Pols et al. (1998) evolutionary models, which predict higher radii, luminosities, and effective temperatures for such low-mass CHeB stars than more recent evolutionary models (Girardi 2016). These systematic effects must be taken into account when comparing with observations (Section 3.4.2).

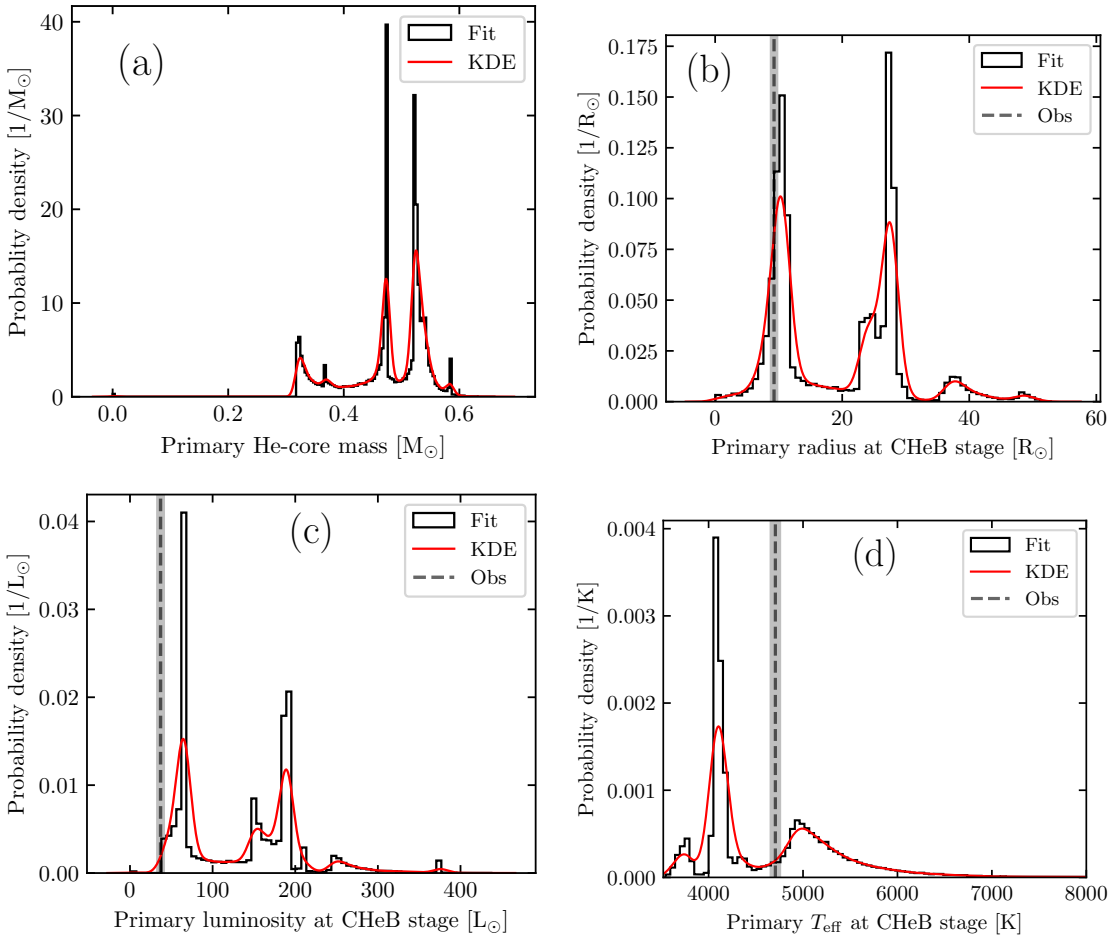

Figure 3.4: Helium-core mass (panel a), radius (panel b), luminosity (panel c) and effective temperature (panel d) posterior density distributions of the primary star during the CHeB stage for the full sample described in Section 3.3.2. We show the histogram (black lines) and the kernel density estimate with a Gaussian kernel (KDE, red lines). The dashed line and the grey area represent the KIC4937011 observations and their 1-σ errors (Table 3.2). Effective temperatures above 8000 K have been omitted from the figure for illustrative purposes only. As explained in the Appendix D, we take as the reference time for the CHeB of each MC simulation the age that gives the highest likelihood.

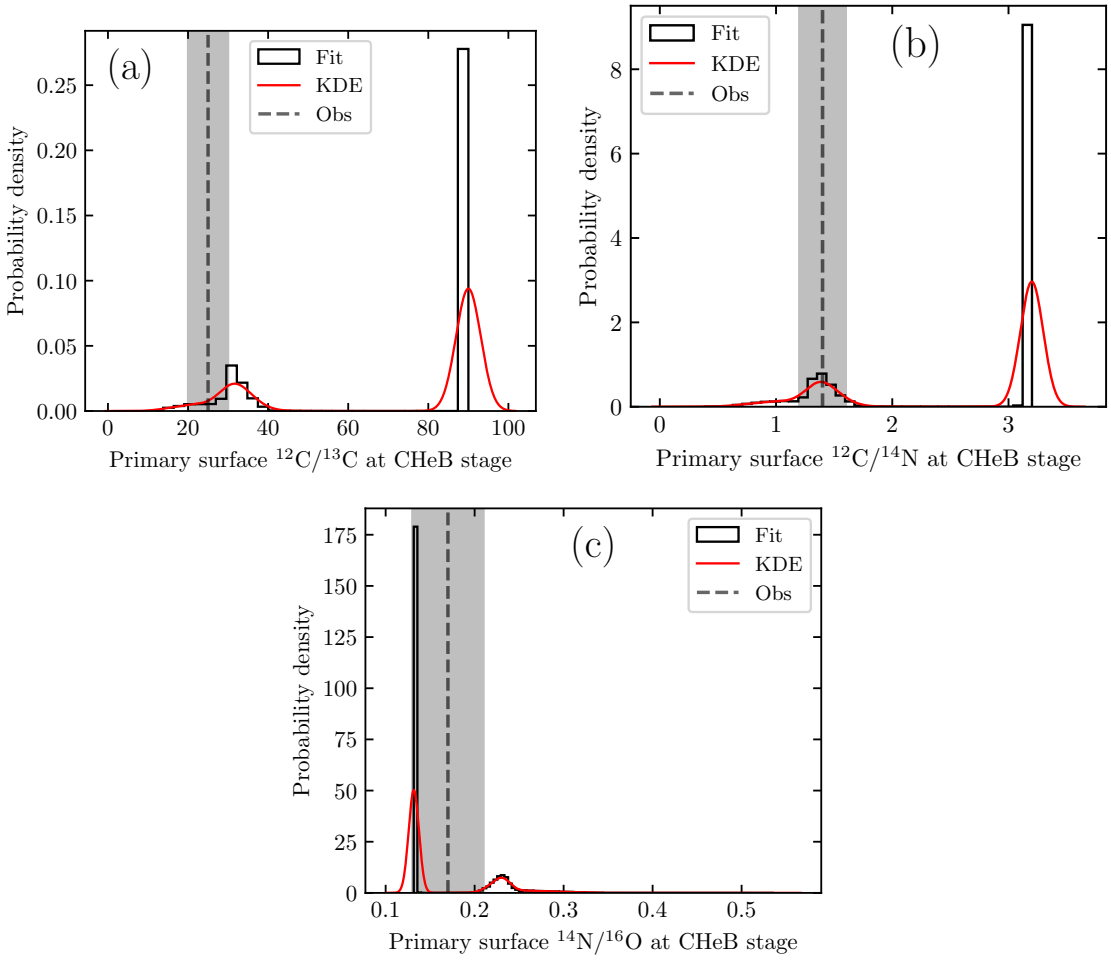

Figure 3.5: Surface $^{12}C/^{13}C$ (panel a), $^{12}C/^{14}N$ (panel b) and $^{14}N/^{16}O$ (panel c) posterior density distributions of the primary star at the CHeB stage for our full sample described in Section 3.3.2. In particular, we have the histogram (black lines) and the kernel density estimation with a Gaussian kernel (KDE, red lines). The dashed line and the grey area represent the observed values of KIC4937011 and their 1-σ errors (also Table 3.2). As explained in the Appendix D, we take as the reference time for the CHeB of each MC simulation the age that gives the highest likelihood.

Dichotomy in the chemical space

In Fig. 3.5 and Table 3.2 the $^{12}C/^{13}C$, $^{12}C/^{14}N$ and $^{14}N/^{16}O$ density distributions of the primary star at the CHeB stage estimated from the MC simulations. A dichotomy is clearly visible in the chemical space, since simulations with the highest $^{12}C/^{13}C$ also have the highest $^{12}C/^{14}N$ and the lowest $^{14}N/^{16}O$. These two peaks are the consequence of two different paths a binary system can follow after the CEE phase. In this section we discuss the channel that produces the highest $^{12}C/^{14}N$ peak, while in Section 3.4.2 we discuss the channel that produces the lowest $^{12}C/^{14}N$ peak.

To explain the peak at $^{12}C/^{13}C \approx 90$, we need a star that contains material in the surface that has not been contaminated by the product of the hydrogen-burning core. Indeed, such a value is not typically observed in CHeB stars, because the first dredge-up has already taken place. As explained in Section 3.4.1, the CEE phase begins when the binary systems are formed by a red-giant primary star and a MS companion. A first dredge-up is forced in HG and RGB stars that undergo a CEE phase, but not for MS stars (Section 3.3.1). In addition, MS stars are assumed to have negligible contamination from companion material, as all such material is ejected from the system soon after the CEE phase. These are the reasons why in our modelling we obtain that 69.51% of the full sample of MC simulations (i.e. 45339 out of 65225 simulations) after the CEE phase are close binaries formed by a HeWD star and a MS star with $M < 0.88$ $M_\odot$[11] that has not been contaminated by the primary star. Such close-binary systems start a stable RLOF from the MS star onto the HeWD star, which eventually formes a single low-mass RGB-like star that later becomes a low-mass CHeB star with a high $^{12}C/^{13}C$. This formation channel explains such a wide distribution of helium-core mass, radius, luminosity, and effective temperature, despite a narrow distribution in chemistry; the envelope comes from the MS star, thus, it depends more on the chosen initial composition than on internal mixing, atomic diffusion or overshooting. We want to highlight that the initial chemical composition of all these MC simulations is taken from Grevesse et al. (1989), thus it is fixed for a fixed metallicity (this explains such narrow bins).

The properties of this formation channel are in good agreement with the literature, because binary systems formed by a HeWD star and a low-mass MS star are thought to be progenitors of low-mass RGB stars and of hot subdwarfs depending on the initial properties of the binary system (Hurley et al. 2002; Shen et al. 2009; Clausen et al. 2011;

[11] Formally this is not the same as the 99.7% credible interval of $M_{2,\mathrm{ZAMS}}$ in Table 3.2, but we checked whether the companion star has not changed much since the ZAMS.

Pyrzas et al. 2012; Nelemans et al. 2016; Zhang et al. 2017; Rui et al. 2024).

3.4.2 Analysis of a more observationally-motivated subsample

In Section 3.4.1 we explain that an interaction between a HeWD and a low-mass MS star can produce a low-mass CHeB star with the same mass and age as KIC4937011, but a higher $^{12}C/^{14}N$. In this section we want to exclude from the analysis all the MC simulations that predict stars much brighter and carbon-enriched than observations suggest, giving us more credible formation channels. Considering Figure 3.4 and 3.5, we decide to exclude stars with luminosity and $^{12}C/^{14}N$ higher than $100\,L_{\odot}$ and 2.5, respectively, because these thresholds are at least 5.5-σ away from the observed values[12]. 13.67% of our full sample of MC simulations (i.e. 8917 out of 65225 simulations) composes this subsample, thus, it is a non-negligible part of the full sample and we have sufficiently high number of MC simulations to calculate statistics[13]. In Fig. 3.6 the corner plot showing the age and

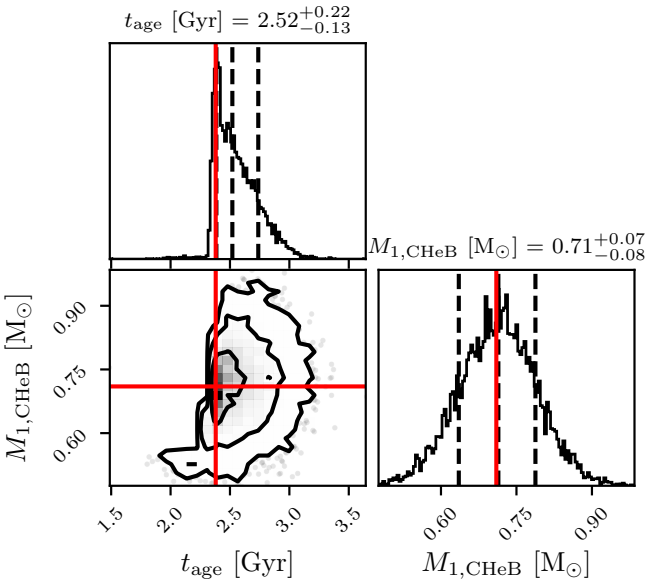

Figure 3.6: Corner plot showing the age and primary mass density distributions at the CHeB stage for the subsample described in Section 3.4.2. The contours are referred to 1, 2, and 3-σ, respectively. In red the observed values for KIC4937011 (Table 3.3). As explained in the Appendix D, we take as the reference time for the CHeB of each MC simulation the age that gives the highest likelihood.

primary mass density distributions for the subsample (see also Table 3.3), compared with

[12]The most credible formation channel remains the same as long as we choose a $^{12}C/^{14}N$ threshold that is still able to separate the two main chemical peaks. The luminosity threshold is necessary in order to exclude stars approaching the beginning of the EAGB.

[13]We check this by randomly sampling one third of our full sample. Even with a reduced number of MC simulations we infer the same results.

Table 3.3: The same as Table 3.2, but for the subsample described in Section 3.4.2.

Parameter	Median	68% CI	99.7% CI	Obs
$t_{\rm age}$ [Gyr]	2.52	[2.39, 2.74]	[1.99, 3.22]	2.38 ± 0.27^{a}
$M_{1,\rm CHeB}$ [$M_\odot$]	0.71	[0.64, 0.79]	[0.50, 0.94]	0.71 ± 0.08^{b}
$\alpha_{\rm ce} \cdot \lambda_{\rm ce}$	14	[6, 24]	[0.4, 43]	...
$\log(P_0/\rm days)$	0.54	[0.26, 1.06]	[0.06, 2.4]	...
$q_{\rm ZAMS}$	0.15	[0.08, 0.30]	[0.05, 0.46]	...
$M_{1,\rm ZAMS}$ [$M_\odot$]	1.58	[1.54, 1.61]	[1.46, 1.71]	...
$M_{2,\rm ZAMS}$ [$M_\odot$]	0.24	[0.12, 0.48]	[0.080, 0.71]	...
$M_{1,\rm He-core}$ [$M_\odot$]	0.4743	[0.4735, 0.4783]	[0.4677, 0.5059]	...
$R_{1,\rm CHeB}$ [$R_\odot$]	9.8	[7.7, 10.9]	[0.38, 13.3]	9.3 ± 0.5^{b}
$L_{1,\rm CHeB}$ [$L_\odot$]	65.5	[65.3, 66]	[64.5, 99.2]	37 ± 4^{c}
$T_{\rm eff,1,CHeB}$ [K]	5269	[5013, 5966]	[4800, 26695]	4710 ± 50^{c}
$^{12}C/^{13}C$	31	[24, 35]	[13, 48]	25 ± 5^{d}
$^{12}C/^{14}N$	1.4	[1.1, 1.5]	[0.6, 2.0]	1.4 ± 0.2^{d}
$^{14}N/^{16}O$	0.23	[0.22, 0.26]	[0.19, 0.33]	0.17 ± 0.04^{d}

References. [(a)] Brewer et al. (2016); [(b)] Handberg et al. (2017); [(b)] Matteuzzi et al. (2023); [(d)] Carlberg et al. (2015)

the observed values for KIC4937011 (red lines). We see that our modelling tends towards higher ages than the full sample, but within the errors the observed current age and mass of KIC4937011 are still correctly fitted.

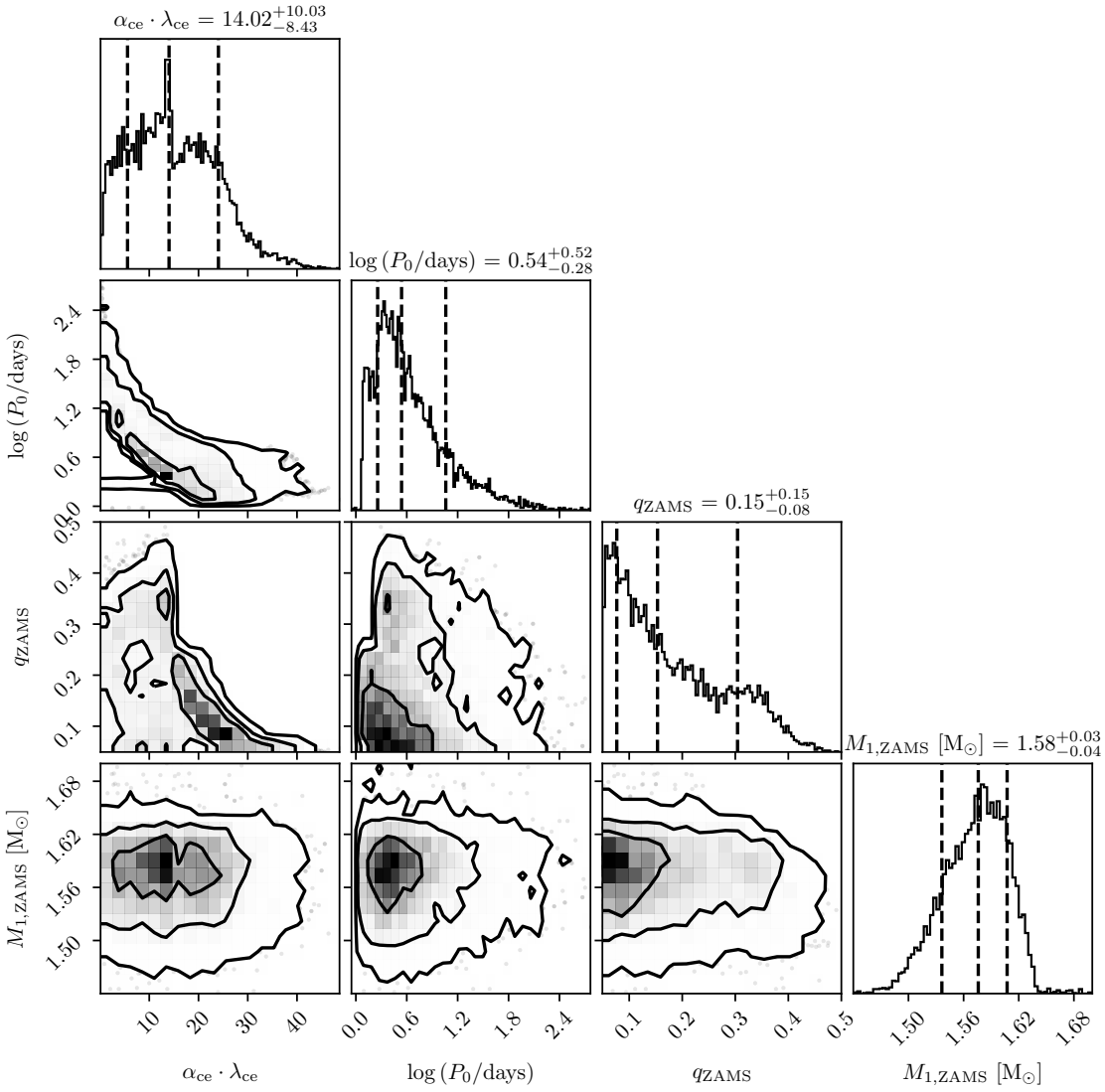

Figure 3.7: Corner plot showing the posterior density distributions of the subsample described in Section 3.4.2. The contours are referred to 1, 2, and 3-σ, respectively.

New posterior density distributions

In Fig. 3.7, 3.8 and 3.9 the estimated posterior density distributions for the subsample (see also Table 3.3). The anti-correlation between $\alpha_{\rm ce} \cdot \lambda_{\rm ce}$ and $\log P_0$ still holds, and both distributions have similar 99.7% credible intervals and medians as the full sample (see Fig. 3.7, Tables 3.2, 3.3). The same conclusion comes for the 99.7% credible interval of $q_{\rm ZAMS}$, but not for its median value. Indeed, this density distribution in the subsample is skewed towards lower values of $q_{\rm ZAMS}$ compared to the full sample (see Tables 3.2, 3.3).

The density distribution of $M_{1,\mathrm{ZAMS}}$ is also skewed towards lower values in the subsample than in the full sample, and it has narrower credible intervals than the full sample (see Tables 3.2, 3.3). However, the $M_{1,\mathrm{ZAMS}}$ distribution in the subsample is still consistent, within the errors, with the observed average mass of RGB stars in NGC6819, suggesting the presence of a fast evolution after the CE phase. We want to highlight that the q_{ZAMS} posterior distribution is also in the subsample very close to the lower limit we put in the prior, suggesting the same conclusions we drew in Section 3.4.1. Finally, as discussed in Section 3.4.1, the high $\alpha_{\mathrm{ce}} \cdot \lambda_{\mathrm{ce}}$ values observed in the subsample can be interpreted as an indication of recombination energy, dust formation, and nuclear burning influencing the CE ejection process.

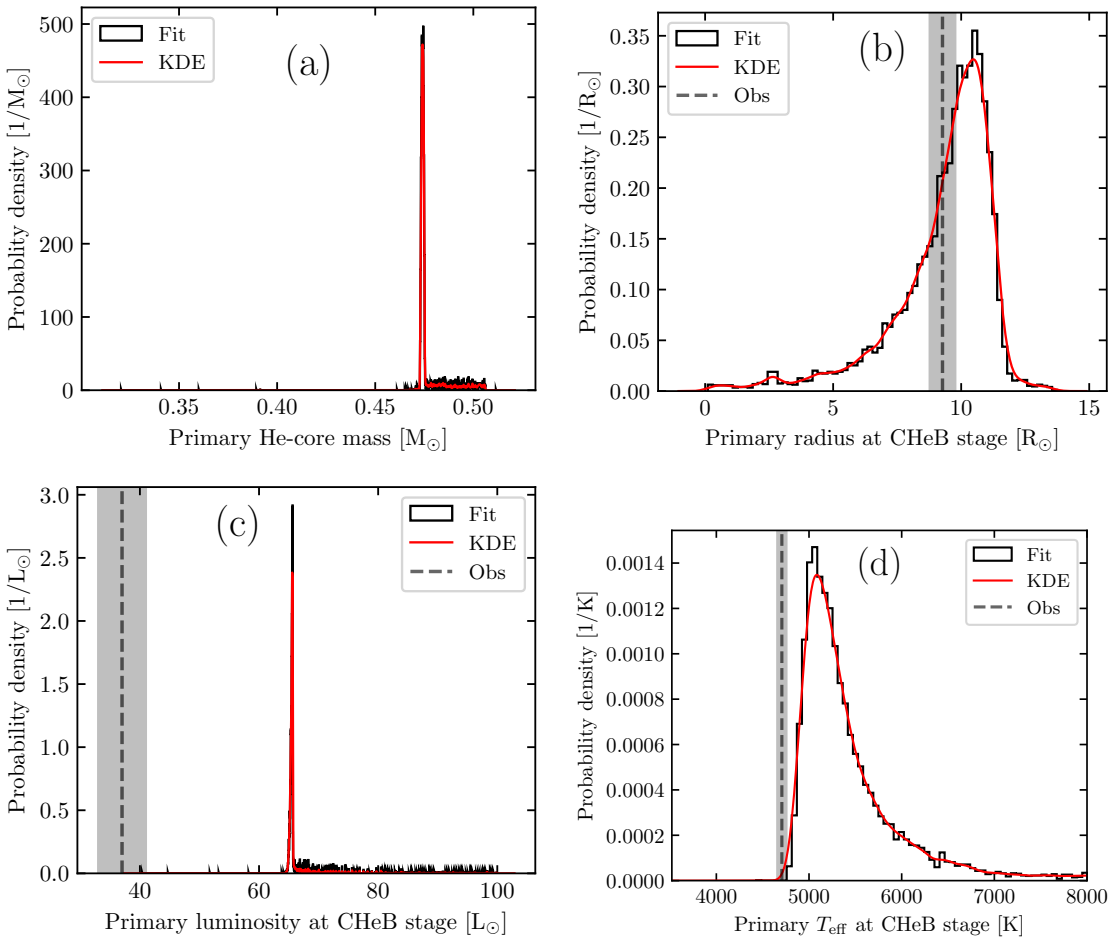

Figure 3.8: Same as Figure 3.4 but for the subsample described in Section 3.4.2 (see aso Table 3.3). Also here effective temperatures above 8000 K have not been included in the figure for illustrative purposes only. As explained in the Appendix D, we take as the reference time for the CHeB of each MC simulation the age that gives the highest likelihood.

The posterior density distributions of helium-core mass, radius, luminosity, and effective temperature are different in the subsample than in the full sample, they have narrower

99.7% credible intervals, and they are more compatible with the observations (see Fig. 3.8, Tables 3.2, 3.3). The helium-core mass distribution is consistent with the theoretical distribution expected for RC stars (Girardi 2016), and it is consistent with the asteroseismic observations of KIC4937011 (Handberg et al. 2017). The radius, luminosity, and effective temperature distributions are a separate case, because they tend to be systematically skewed towards higher values (see Section 3.4.1) than observations and modern evolutionary models (which are more compatible with observations, see Figure 3.1). In fact, even if the median radius is consistent with the observations, within errors, the median luminosity and effective temperature are at least 7-σ away from the observed values. However, these systematic effects do not limit our inference in the formation channel, because they are not used in the likelihood (Appendix D), thus, they are not used to discriminate between models. This is the reason why we decide not to rely on effective temperature, luminosity, and radius to perform a best fit to the observed values in KIC4937011.

Regarding the surface chemical composition distributions (Figure 3.9 and Table 3.3), the $^{12}C/^{13}C$ and $^{12}C/^{14}N$ posterior distributions are consistent, within the errors, with the observed values. The $^{14}N/^{16}O$ posterior distribution tends towards higher values than observations, but with a median of the distribution that is just about 1.2-σ away from the observed value.

KIC4937011's most credible formation channel

In Section 3.4.1 we discuss the dichotomy visible in the $^{12}C/^{14}N$ distribution of the full sample and how the interaction between a HeWD star and a MS star is the main cause of the narrow peak at high $^{12}C/^{14}N$. Even in the subsample (in which we are looking at the lowest values of the $^{12}C/^{14}N$ distribution) nearly all the MC simulations (99.92% of the subsample, i.e. 8910 out of 8917 simulations) share a similar formation scenario (Fig. 3.10). As explained in Section 3.3.2 and visible in Fig. 3.10, we start from two ZAMS stars in a circular orbit. If we consider the 99.7% credible intervals of Table 3.3, we have a mass of the primary star between 1.46 $M_\odot$ and 1.71 $M_\odot$, a mass of the companion below 0.71 $M_\odot$, and an orbital period between 1.15 days and 251 days. Such a close binary starts a RLOF when the primary goes in the RGB phase or in the HG phase. All these MC simulations predict an unstable RLOF and, thus, a CEE phase arises. Very differently to Section 3.4.1 is the post-CEE phase result, because we have not a HeWD with a companion MS star. We have instead a RGB-like star with an evolved helium-core between 0.16 $M_\odot$ and 0.40 $M_\odot$ (99.7% credible intervals, see Figure 3.10) and a smaller envelope than before

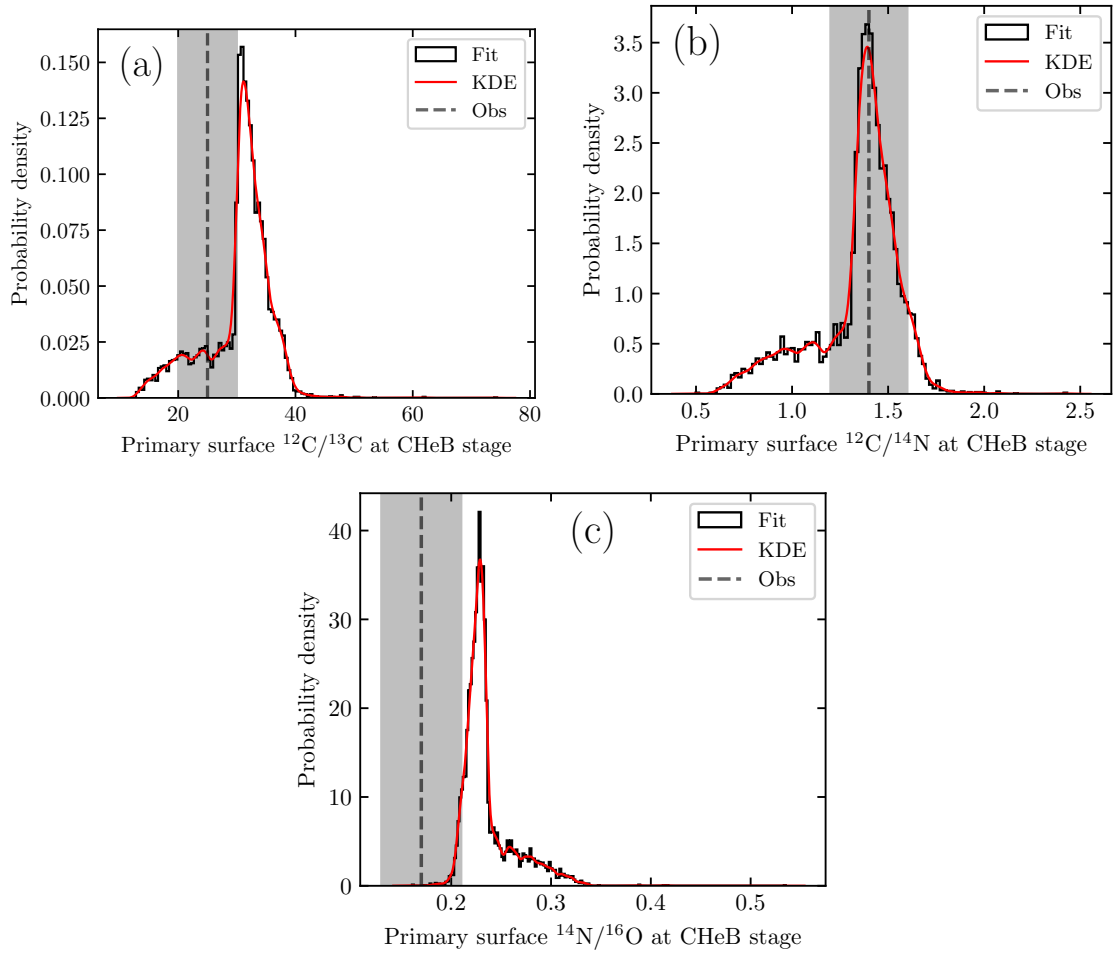

Figure 3.9: Primary star $^{12}C/^{13}C$, $^{12}C/^{14}N$ and $^{14}N/^{16}O$ density distributions at the CHeB stage for the subsample described in Section 3.4.2. In particular, we have the histogram (black lines) and the Kernel Density Estimation with a Gaussian kernel (red lines). The dashed line and the grey area represent the observed values of KIC4937011 and their 1-σ errors (see also Table 3.2). As explained in the Appendix D, we take as the reference time for the CHeB of each MC simulation the age that gives the highest likelihood.

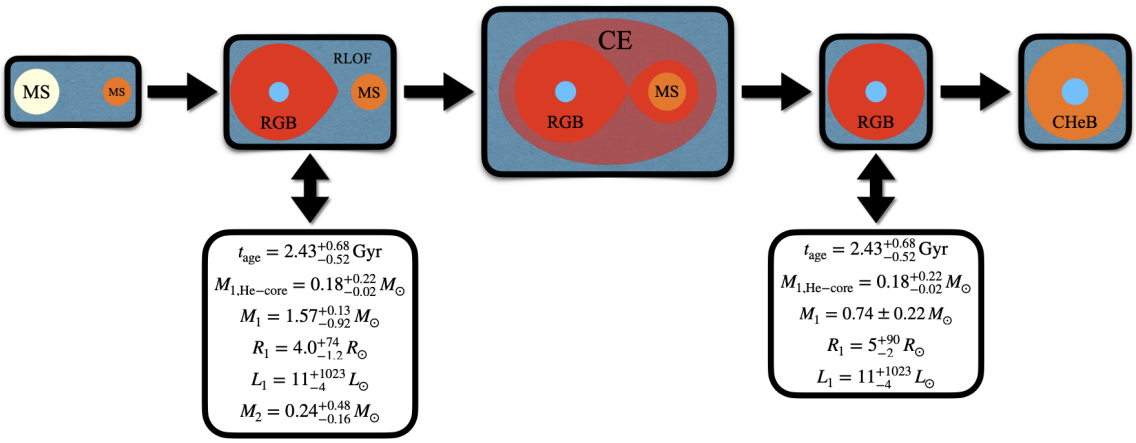

Figure 3.10: Cartoon showing the most credible formation scenario for KIC4937011. Medians and their 99.7% credible intervals just before and after the CE are also shown.

the CEE phase (the 99.7% credible interval for the mass of the star is between 0.52 $M_\odot$ and 0.96 $M_\odot$ after the CEE phase, see Figure 3.10). Indeed, we have a median ejection of $\approx$ 1.1 $M_\odot$ from the system and contemporary the merger of the companion with the helium-core of the primary star. During the CEE phase we have dynamical mixing effects owing to the spiral-in process that completely mix the envelope with material coming from the evolved primary star. After the CEE phase the RGB-like star has an envelope with the low $^{12}C/^{14}N$ value we observe today. Finally, this star reaches the CHeB stage after helium flashes as if it were a single star of mass $\approx$ 0.71 $M_\odot$, consistently with observations. Therefore, this formation channel "naturally" predicts the low $^{12}C/^{14}N$ value compatible with RC star of $\approx$ 1.6 $M_\odot$ (Section 2.2). Moreover, the $R_{1,\mathrm{CHeB}}$, $L_{1,\mathrm{CHeB}}$, and T_{eff} posterior distributions we found after all these binary interactions are compatible with a $\approx$ 0.7 $M_\odot$ CHeB star that evolves in isolation, indicating that our findings are self-consistent within the `binary_c v2.2.3` framework.

However, with this formation channel is difficult to explain the high lithium abundance we observe today in KIC4937011. Insights into this conundrum may be gleaned from studies of red novae, which are thought to be the direct product of a CEE phase with a merger (Tylenda et al. 2006; Pastorello et al. 2019). Some of these red novae are lithium-rich (Kamiński et al. 2023), suggesting the involvement of mechanisms capable of synthesizing and mixing lithium during the CEE phase.

Between the post-CEE phase and the CHeB stage the star evolves in isolation for nearly 150 Myr (maximum a posteriori probability estimate, corresponding to stars with a helium-core mass of about 0.18 $M_\odot$), which is very short compared to the cluster age. We check whether this time and this formation channel are compatible with more state-of-the-art evolutionary codes of single stellar evolution. Using the `MESA v11701` (Modules for Experiments in Stellar Astrophysics; Paxton et al. 2011; Paxton et al. 2019) tool we test the pre-CEE and post-CEE phase conditions. We adopt as a reference solar mixture that from Asplund et al. (2009), and high- and low-temperature radiative opacity tables were computed for the solar specific metal mixture. Envelope convection is described by the mixing length theory Cox et al. (1968); the corresponding α_{MLT} parameter, the same for all the models, is derived from the solar calibration with the same physics. Below the convective envelope, we add a diffusive undershooting (Herwig 2000) with a size parameter $f = 0.02$ (see Khan et al. 2018). Extra mixing over the convective core limit during the CHeB phase is treated following the formalism by Bossini et al. (2017). For the pre-CEE phase we adopt a 1.60 $M_\odot$ star with $Z = 0.022$ and $Y = 0.28$ until it achieves a 0.18 $M_\odot$

helium-core mass in the RGB phase, which takes nearly 2.33 Gyr. For the post-CEE phase we use models with masses between 0.65 $M_\odot$ and 0.80 $M_\odot$ (i.e. a mass range compatible with the 68% credible interval of $M_{1,\mathrm{CHeB}}$ in Table 3.3), and $Z = 0.022$, $Y = 0.28$. We do not include any mass loss in these MESA models. It takes about 500 Myr for a 0.65 $M_\odot$ star to go from a RGB phase with a helium-core mass of 0.18 $M_\odot$ to the CHeB stage, and about 370 Myr for a 0.80 $M_\odot$ star. This means that in MESA models this formation channel would take at least 2.70 - 2.83 Gyr, which is about 1.6-σ away from the observed value. However, if we consider not just a single value of the helium-core mass, but a distribution of values just before the CEE phase, it is also possible in MESA to have a final age consistent with `binary_c v2.2.3`. For example, it takes 2.48 Gyr for a 1.60 $M_\odot$ star in MESA to achieve a helium-core mass of 0.22 $M_\odot$, and other about 150 Myr for a star between 0.65 $M_\odot$ and 0.80 $M_\odot$ to ignite helium in the core.

An example of `binary_c v2.2.3` HRD of a primary star with such a formation channel is in Figure 3.11. This specific simulation begins with a 1.60 $M_\odot$ ZAMS primary star orbiting a 0.25 $M_\odot$ companion in almost 32 days. The CEE begins when the primary star has a helium-core mass of about 0.279 $M_\odot$, and it ends with the ejection of 1.12 $M_\odot$ of material from the system. The post-CEE star begins the CHeB stage at the age of 2.41 Gyr and a mass of 0.70 $M_\odot$.

3.5 Discussion and conclusions

In this chapter we focused on the single metal-rich ($Z \approx Z_\odot$), Li-rich, low-mass, CHeB star KIC4937011, which is a member of the star cluster NGC 6819 (turn-off mass of ≈ 1.6 $M_\odot$, i.e. age of ≈ 2.4 Gyr). This star has ≈ 1 $M_\odot$ less mass than expected for its age and metallicity, thus, it could be the result of a binary interaction or of the poorly understood mass loss mechanism along the red-giant branch. To infer formation scenarios, we adopt a Bayesian approach using the `binary_c v2.2.3` code coupled with the Dynamic Nested Sampling approach contained in the `dynesty v2.1.1` package. The final conclusions are summarised here:

1. This star is the result of a common-envelope evolution phase in which the companion does not survive. All the MC simulations considered have one common envelope phase within the final stage of the CHeB phase of the primary star, and only a negligible fraction of simulations (0.006%) experiences two common envelope phases.

2. Considering a subsample composed by CHeB primary stars with luminosity below

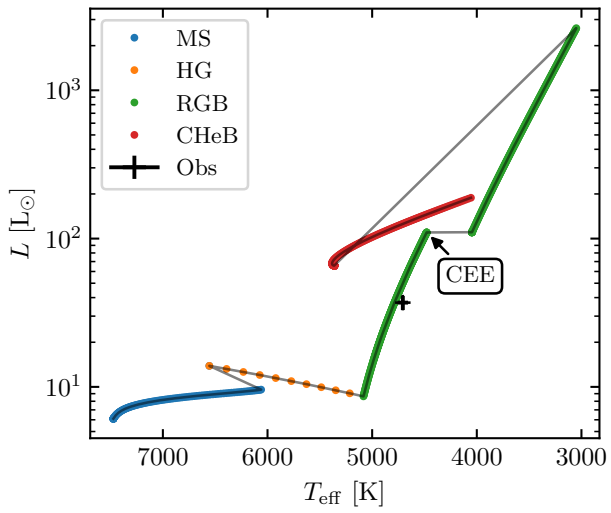

Figure 3.11: HRD of a primary star in the subsample from the ZAMS to the end of the CHeB stage done with `binary_c v2.2.3`. The CEE begins when the primary star has a helium-core mass of about 0.279 $M_\odot$ (arrow in the figure), and it ends with the ejection of 1.12 $M_\odot$ of material from the system. The simulation begins with a 1.60 $M_\odot$ ZAMS primary star orbiting a 0.25 $M_\odot$ companion in almost 32 days. The primary star begins the CHeB stage at the age of 2.41 Gyr and a mass of 0.70 $M_\odot$. In black KIC4937011's observed values (see also Table 3.3).

$100\,L_\odot$ and $^{12}C/^{14}N$ below 2.5, we find that the highest peak in their helium-core mass density distribution is at 0.4743 $M_\odot$. This is in line with the expectations for RC stars, and with the observations of KIC4937011. The $^{12}C/^{13}C$ and $^{12}C/^{14}N$ distributions are consistent, within the errors, with the observations. The $^{14}N/^{16}O$ posterior distribution tends towards higher values than observations, but with a median of the distribution that is just about 1.2-σ away from the observed value. The effective temperatures, luminosities, and radii distributions are systematically higher than observations. This is expected, because for such low-mass stars ($\approx$ 0.7 $M_\odot$) the Pols et al. (1998) evolutionary tracks used in `binary_c v2.2.3` deviates significantly from more modern evolutionary tracks (Girardi 2016). However, these systematic effects do not limit our inference in the formation channel, because they are not used in the likelihood, thus, they are not used to discriminate between models.

3. The most credible formation channel is summarised in Figure 3.10. We start from two ZAMS stars in a circular orbit. In all the MC simulations considered, a RLOF begins when the companion is still in the MS phase, but with a primary star that goes in the RGB phase or in the HG phase. This RLOF is dynamically unstable and, thus, a CEE phase arises. During this CEE phase we have dynamical effects that induce a mixing of the envelope of the primary star with the MS companion,

forming the chemical pattern we observe today. The final effect of this CEE phase is a median ejection of ≈ 1.1 $M_\odot$ of material from the system and contemporary the merger of the companion with the helium-core of the primary star. The post-CEE phase product is an RGB-like star of ≈ 0.71 $M_\odot$ with an evolved He core. Finally, the star reaches the CHeB stage after helium flashes as if it were a single star. This formation channel is consistent with MESA models of single star evolution before and after the CEE phase if we take systematic effects into account.

It is worth mentioning that the same formation channel could form sdB star or metal-rich RR Lyrae (Bobrick et al. 2024), because a non-negligible fraction of low-mass CHeB stars has effective temperatures reaching about 27000 K. This means that this channel potentially provides another piece of the puzzle in the sequence between RC and sdB stars, or other stripped stars.

In future we will analyse other very-low mass CHeB stars in open clusters with the same technique, because a better statistics of such objects is necessary to verify the formation channel as an universal feature. Furthermore, synthetic populations of *Kepler* stars provide valuable insights into the overall probability of such an evolutionary scenario (Mazzi et al., in prep.). We will also improve the posterior distributions by using detailed evolutionary models within the likelihood in order to compute $\lambda_{\rm ce}$ and reduce systematic effects. An analysis of the activity-sensitive He I 10830 Å absorption triplet would also be interesting in order to better study the current mass loss in KIC4937011 and in order to put this star in the wider context of the Li-rich RC stars (Sneden et al. 2022).

Chapter 4

Parametric models of core-helium-burning stars: structural glitches near the core[1].

Understanding the internal structure of core helium burning (CHeB) stars is essential for evaluating transport processes in regions where nuclear reactions occur, developing accurate models of stellar populations, and assessing nucleosynthesis processes that impact the chemical evolution of galaxies. Until recently, detailed insights into the innermost layers of these stars were limited. However, advancements in asteroseismic observations have allowed us to explore their stratification more thoroughly. Despite this progress, the seismic signatures associated with structural variations at the boundary between the convective and radiative core, as well as the chemical composition gradients within the radiative core, have been relatively underexplored in CHeB stars. This chapter aims to fill that gap by investigating how these gradients influence the oscillation modes of low-mass CHeB stars. We specifically focus on mixed dipole modes and uncoupled g-modes as effective probes of stellar interiors. Using semi-analytical models calibrated with the evolutionary codes `BaSTI-IAC`, `CLES`, and `MESA`, we explore the influence of density discontinuities and their associated structural glitches on the period spacings of these oscillation modes. These codes were chosen for their distinct physical prescriptions, allowing us to identify common relevant features for calibration purposes. This approach enables us to control the type of glitch introduced while maintaining a realistic representation of the star. As expected from previous studies, our results indicate that these glitches manifest as distinct periodic components in the period spacings, which can be used to infer the position and amplitude of

[1]The work presented in this chapter is based on Matteuzzi et al., to be submitted.

the structural variations inside CHeB stars. Furthermore, we compare models with smooth transitions to those with sharp discontinuities, highlighting the differences in period spacing and mode trapping, which permits us to infer the sharpness of the glitches. Additionally, we conduct simulations based on four-year-long *Kepler* observations, demonstrating that our models predict oscillation frequencies closely resembling the observed data. Ultimately, our models enable realistic predictions of how each sharp structural variation impacts the observed power spectral density. This alignment not only validates our theoretical approach but also suggests promising directions for interpreting glitches signatures in high-quality asteroseismic data.

4.1 Introduction

Understanding the degree of mixing within the helium core is crucial to refine estimates of CHeB phase lifetimes and improve predictions of stellar internal structures in subsequent evolutionary stages (see Section 1.3). This knowledge plays a key role in developing accurate models of stellar populations and elucidating the chemical evolution of galaxies. Observations of mixed dipole modes in CHeB stars provide a valuable tool for probing their innermost regions (e.g. Montalbán et al. 2010; Bedding et al. 2011; Montalbán et al. 2013; Deheuvels et al. 2016; Deheuvels et al. 2018). These oscillation modes may reveal structural variations that occur at the boundaries of mixed convective regions, areas of element ionisation, or at interfaces between layers with different chemical compositions resulting from nuclear burning. In particular, we expect that CHeB stars exhibit chemical composition gradients at the boundary between convective and radiative core, within the hydrogen-burning shell, and at the base of the convective envelope (see Section 1.3). In low-mass stars with a degenerate helium core, the transition from the RGB to the CHeB phase is expected to involve a succession of off-centre helium flashes (see Section 1.3.1), which induce additional chemical composition gradients within the radiative core. As shown in Figure 4.1 and in equation 1.2.6, these gradients manifest as signatures in the Brunt-Väisälä frequency (N), which determines the behaviour of oscillation modes (see Section 1.4.3). This frequency can also produce deviations in period spacing from the asymptotic value when the characteristic scales of structural variations within the core are comparable to or smaller than the local wavelength of the waves under investigation (see Cunha 2020, for a review). These distinct signatures on the eigenfrequencies are commonly referred to as glitch signatures.

Previous studies have examined near-core mixing conditions through the asymptotic

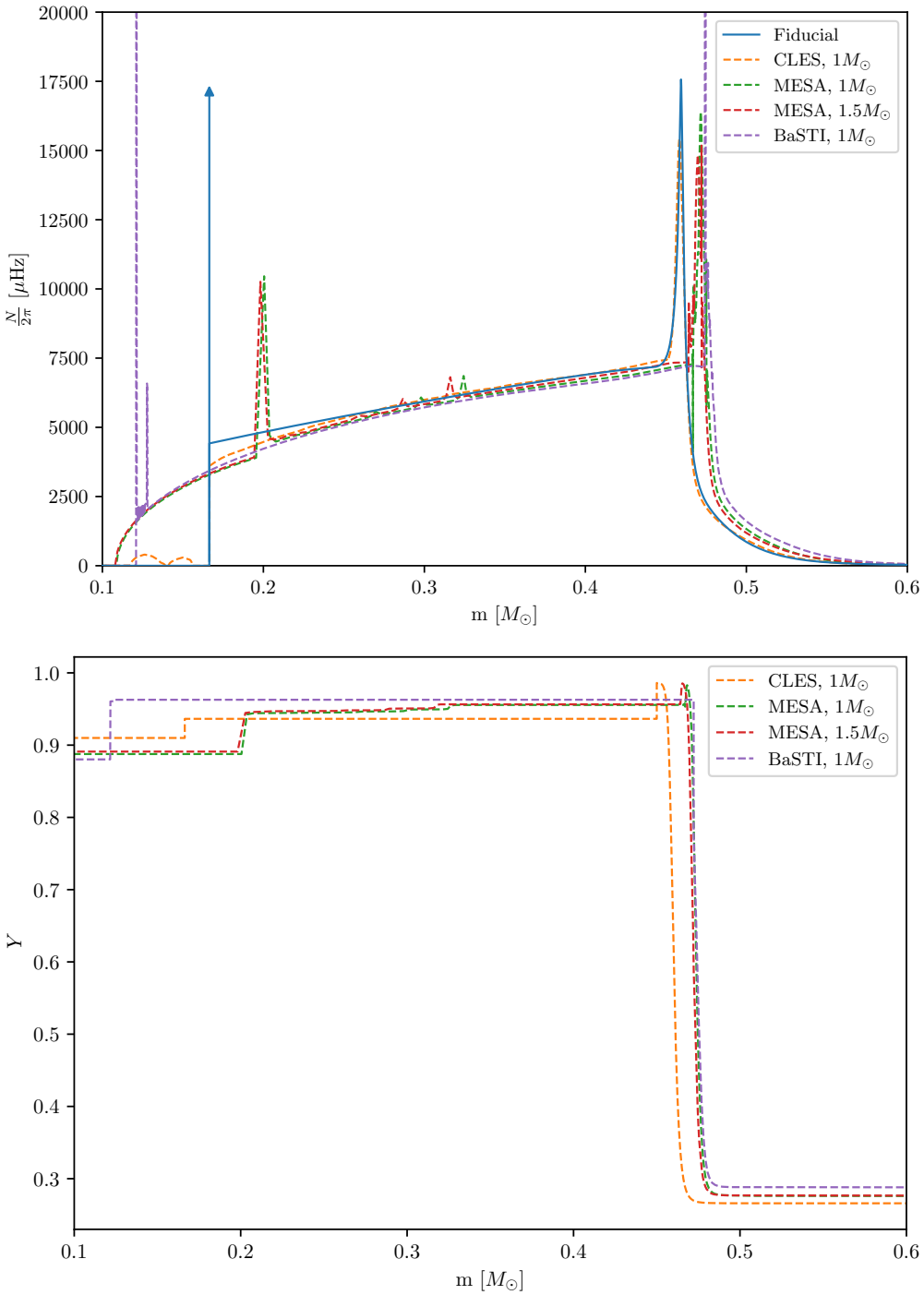

Figure 4.1: Brunt-Väisälä frequencies as a function of internal mass for five different star models at the beginning of the CHeB stage (top panel). The orange, green, red, and violet lines represent models calculated using the evolutionary codes `CLES`, `MESA`, and `BaSTI-IAC`, while the blue line shows the fiducial barotropic model discussed in Section 4.3. All lines, except for the red one, correspond to a 1 $M_\odot$ CHeB star with solar metallicity and a central helium mass fraction of about 0.9. In contrast, the red line depicts a 1.5 $M_\odot$ CHeB star, which has core properties similar to those of lower-mass stars. Notably, these models reveal shared features in their Brunt-Väisälä frequencies, including a convective core, a radiative core, a hydrogen-burning shell, a radiative envelope, and a convective envelope (the last not shown for clarity). In the bottom panel, we show the helium mass fraction as a function of internal mass for four of the five models.

period spacing of dipole modes ΔP_{a} (e.g. Bossini et al. 2015; Constantino et al. 2015; Bossini et al. 2017; Noll et al. 2024), but further insights can be gained by analysing individual eigenfrequencies. Despite extensive observational and theoretical studies on these glitches (e.g. Miglio et al. 2008; Bossini et al. 2015; Cunha et al. 2015; Cunha et al. 2019; Vrard et al. 2022; Hatta 2023; Cunha et al. 2024), the effects of sharp variations in the density profile on eigenfrequencies remain not fully explored. The seismic signature of density discontinuities associated with abrupt composition changes has already been addressed by McDermott (1990), who noted that such jumps can significantly influence the pulsation mode spectrum and stability of non-radially oscillating stars. A density discontinuity can locally contribute to or even become the dominant source of buoyancy. Such a discontinuity is defined as any region where the density changes so rapidly that the density scale height becomes much smaller than the effective wavelength of any oscillation mode of interest. The role of these density discontinuities in the spectrum of gravity modes was also explored by Gabriel et al. (1979), who found that abrupt density changes can lead to mode trapping of g-modes with the proper effective wavelength. If the frequency associated with a density discontinuity is comparable to or larger than the ordinary g-mode frequency, these discontinuities cannot be ignored in computing the g-mode spectrum. Structural glitches give rise to periodic components in the period spacing, allowing for the recovery of information about the location and sharpness of these glitches from their periodicity and amplitude. Therefore, deviations from ΔP_{a} contain information about sharp features in the N frequency, which can be visualised through the normalised buoyancy radius

$$\Phi(r) := \frac{\int_{r_1}^{r} N/y \, dy}{\int_{r_1}^{r_2} N/y \, dy}, \quad N > 0, \quad r_1 \leq r \leq r_2. \tag{4.1.1}$$

This quantity is a monotonically increasing function between the inner turning point r_1 and the outer turning point r_2, effectively serving as a radial coordinate. The coordinate $\Phi(r)$ is particularly valuable for studying the core/envelope symmetry of high-overtone modes, though this symmetry is approximate and can be disrupted by various mechanisms (Montgomery et al. 2003). Within the JWKB approximation (see Section 1.4.3), the kinetic energy density per unit of normalised buoyancy radius is generally constant, except at sharp features such as composition transition zones. This property makes variations in kinetic energy density a clear indicator of mode trapping. Moreover, within the JWKB approximation, the periodic component in the period spacing (P_{glitch}) associated with a structural glitch located at a radius r_{glitch} is related to its normalised buoyancy radius

$[\Phi(r_{\rm glitch})]$ and its periodicity in radial order ($\Delta n_{\rm glitch}$) via the relation:

$$\Delta n_{\rm glitch} \approx 1/\Phi(r_{\rm glitch}) \approx P_{\rm glitch}/\Delta P_{\rm a} \tag{4.1.2}$$

(see e.g. Miglio et al. 2008; Cunha et al. 2015; Cunha et al. 2019; Vrard et al. 2022; Hatta 2023). This equation is particularly useful for interpreting the periodic signals observed in the period spacing of oscillation modes, enabling the extraction of information about the location, amplitude and type of structural glitch. However, studying structural glitches is challenging due to several factors, including complications arising from the growth of the convective core, the lack of a comprehensive mixing theory, the emergence of semiconvective layers (e.g. Castellani et al. 1971a; Straniero et al. 2003), and numerical issues within predictions from evolutionary models. As a result, artificial glitches can arise, making the interpretation of the eigenfrequencies more complicated. To address these challenges, flexible and self-consistent models are essential, particularly for studying low-mass CHeB stars with high coupling factors (Section 2), as they offer deeper insights into their internal structures compared to other RC stars.

The chapter is organised as follows. Section 4.2 describes the theoretical framework for solving the differential equations of stellar structure. Section 4.3 details the semi-analytical model of a 1 $M_\odot$ RC star with solar composition and $Y_c \approx 0.9$, which serves as a reference model for subsequent modifications. Section 4.4 explains how we simulate different levels of mixing between adjacent zones in a self-consistent manner. Results are presented in Section 2.4, and Section 3.5 concludes the chapter.

4.2 Modelling of a realistic star

The structure of a single, spherical, non-rotating, non-magnetic star can be described by the hydrostatic and mass continuity equations (see equation 1.2.1 in Section 1.2). To fully solve these differential equations, it is essential to establish a relation between pressure and density. Furthermore, this relation must include temperature, mass fractions of chemical species, and their corresponding chemical potentials to formulate a complete system of differential equations. In particular, we must incorporate an equation of state (EOS, as discussed in Section 1.2) that connects pressure with these other variables, thereby resulting in a closed system of equations. In this chapter, we will employ a differential representation of an EOS. We start by defining the variable

$$\gamma_{\rm local}(r) := \frac{d\ln P(r)}{d\ln \rho}, \tag{4.2.1}$$

which allows us to derive the differential equation

$$\frac{dP(r)}{dr} = \gamma_{\rm local}(r)\frac{P(r)}{\rho(r)}\frac{d\rho(r)}{dr} \tag{4.2.2}$$

that has to be solved together with the hydrostatic and mass continuity equations. All the information provided by the EOS is encapsulated in equation 4.2.1, which can be seen through a heuristic approach. For simplicity, and without loss of generality, we may consider $\gamma_{\rm local}(r) \equiv \gamma_{\rm local}(T, \rho, \mu)$. By applying the chain rule to equation 4.2.1, we can demonstrate that

$$\gamma_{\rm local}(T, \rho, \mu) = \frac{\chi_\rho}{1 - \chi_T \nabla - \chi_\mu \nabla_\mu}, \tag{4.2.3}$$

where χ_ρ, χ_T, χ_μ, ∇ and ∇_μ are explicitly defined in Section 1.2.2. It is now more evident that $\gamma_{\rm local}$ is predominantly influenced by the thermal and chemical gradients present within the star, and that in adiabatically stratified layers $\gamma_{\rm local} \equiv \Gamma_1$. Moreover, according to equation 4.2.2, a polytropic EOS can be derived (i.e. $P \propto \rho^{\gamma_{\rm local}}$) when $\gamma_{\rm local}$ is treated as a constant. For the purposes of the following discussion, we will denote $\gamma_{\rm local}(r) \equiv \gamma(r)$.

4.2.1 Barotropic CHeB stars

As demonstrated in Section 4.2, a closed set of equations is obtained when we provide the temperature profile and the chemical species. However, stars can be accurately modelled as systems in barotropic equilibrium (i.e. the thermodynamic variables are stratified as the density profile), because $\vec{\nabla}\rho \times \vec{\nabla}P = \vec{0}$ everywhere in self-gravitating spherical stars in hydrostatic equilibrium. Furthermore, the density is a monotonic function of the radius with the exception of a small region near the surface where a density inversion due to hydrogen recombination occurs (e.g. Érgma 1971; Harpaz 1984). This observation leads to the conclusion that, with a high degree of accuracy, $P(r) \equiv P(\rho)$, $T(r) \equiv T(\rho)$, $X_i(r) \equiv X_i(\rho)$ and $\gamma(r) \equiv \gamma(\rho)$. These relations can be incorporated into equation 4.2.2 to derive the differential equation

$$\frac{dP(r)}{dr} = \frac{\gamma(\rho)P(\rho)}{\rho(r)}\frac{d\rho(r)}{dr}. \tag{4.2.4}$$

A general solution of equation 4.2.4 is

$$P(\rho) = P_c \exp\left(\int_{\ln \rho_c}^{\ln \rho} \gamma(t)\, dt\right), \tag{4.2.5}$$

where P_c and ρ_c are the central pressure and density, respectively. Therefore, an a priori knowledge of $\gamma(\rho)$, e.g. from calibrations on evolutionary models, allows us to find the internal structure of the star using the hydrostatic equation, the mass continuity equation, and equation 4.2.4 or 4.2.5.

4.2.2 Differential equations for barotropic stars

From now on we normalise all the quantities respect to reference density (ρ_1) and pressure (P_1) values. As a result, once the dimensionless quantities

$$\begin{cases} \theta := \dfrac{\rho}{\rho_1} \\ \xi := r\sqrt{\dfrac{4\pi G\rho_1^2}{P_1}} \\ \beta := \dfrac{P}{P_1} \\ \psi := m\sqrt{\dfrac{4\pi G^3\rho_1^4}{P_1^3}} \end{cases} \tag{4.2.6}$$

are defined, the hydrostatic equation, the mass continuity equation, equation 4.2.4 and equation 4.2.5 become

$$\begin{cases} \dfrac{d\theta(\xi)}{d\xi} = -\dfrac{\psi(\xi)\theta(\xi)^2}{\gamma(\theta)\beta(\theta)\xi^2} \\ \dfrac{d\psi(\xi)}{d\xi} = \xi^2\theta(\xi) \\ \beta(\theta) = \beta_c \exp\left(\displaystyle\int_{\ln\theta_c}^{\ln\theta} \gamma(t)\,dt\right), \end{cases} \tag{4.2.7}$$

with initial conditions $\theta(\xi = 0) = \theta_c$, $\beta(\xi = 0) = \beta_c$ and $\psi(\xi = 0) = 0$. Therefore, we numerically solve equation 4.2.7 with a Dormand and Prince Runge-Kutta fifth-order method from the centre to the surface and obtain the $\theta(\xi)$ and $\psi(\xi)$ profiles. Finally, with such profiles we a posteriori calculate other variables of interest such as the Brunt-Väisälä frequency

$$N^2(\xi) = 4\pi G\rho_1 \frac{\psi(\xi)^2\theta(\xi)}{\beta(\theta)\xi^4}\left[\frac{1}{\gamma(\theta)} - \frac{1}{\Gamma_1}\right]. \tag{4.2.8}$$

To mitigate numerical issues when solving equation 4.2.7 from the centre, we employ Taylor expansions to approximate the actual solutions near the centre. More details regarding these expansions are provided in Appendix E. We also want to notice that in certain situations it may be more beneficial to solve alternative differential equations rather than equation 4.2.7. In Appendix F, we examine some of these alternative equations, with a specific focus on equations near the stellar surface. In Appendix G, we present analytical solutions to equation 4.2.7 for constant values of $\gamma(r)$, which we utilise to validate our numerical solver.

4.2.3 Discontinuities in the internal profiles

In CHeB stars we expect that certain internal profiles (e.g. ρ) exhibit discontinuities or non-differentiable points. For example, we expect a sharp decrease in density at the

boundary between convective and radiative core due to an abrupt change in the chemical profile (see Section 1.3.2). Therefore, we can establish the jump conditions at a given radial position r_0 by ensuring the continuity of pressure and mass. In fact, in CHeB stars at equilibrium, there are no internal shock waves, and the locations where the internal profiles show discontinuities have zero Lebesgue's measure. For simplicity let us use the notation $\lim_{r\to r_0^-} f(r) := f^-$ and $\lim_{r\to r_0^+} f(r) := f^+$ for an internal profile $f(r)$. Such a profile is continuous when $f^- = f^+ = f(r_0)$. Let us define

$$\Lambda := \frac{\rho^+}{\rho^-} \in \mathbb{R}^+, \tag{4.2.9}$$

because we are mainly interested in jump discontinuities in the density profile. Then, the jump conditions are

$$\begin{cases} \xi^+ = \xi^- \\ \beta^+ = \beta^- \\ \psi^+ = \psi^- \\ \theta^+ = \theta^- \Lambda \\ \left.\dfrac{d\theta}{d\xi}\right|_{r_0^+} = \left.\dfrac{d\theta}{d\xi}\right|_{r_0^-} \Lambda^2 \left(\dfrac{\gamma^-}{\gamma^+}\right) \\ \left.\dfrac{d\psi}{d\xi}\right|_{r_0^+} = \left.\dfrac{d\psi}{d\xi}\right|_{r_0^-} \Lambda \\ (N^2)^+ = (N^2)^- \Lambda \left(\dfrac{\Gamma_1^+ - \gamma^+}{\Gamma_1^- - \gamma^-}\right)\left(\dfrac{\gamma^-}{\gamma^+}\right)\left(\dfrac{\Gamma_1^-}{\Gamma_1^+}\right). \end{cases} \tag{4.2.10}$$

Let us now introduce r_0 as the boundary between two zones with different normalisation constants P_1 and ρ_1. This choice may be useful when equation 4.2.7 creates numerical issues (for example with small θ and β values, see Appendix F). We then define as normalisation constants for the first zone (i.e. for $r \leq r_0^-$) the density and the pressure in the centre of the star (i.e. $P_1 \equiv P_c$ and $\rho_1 \equiv \rho_c$). This simplifies all the equations, because now $\theta_c \equiv 1$ and $\beta_c \equiv 1$. In the second zone (i.e. where $r \geq r_0^+$) it is useful to define as normalisation constants the pressure and the density at the boundary between the two zones. Therefore, we have $P_1 \equiv P(r_0) = P_c \exp\left(\int_0^{\ln\theta^-} \gamma(t)\, dt\right)$ and $\rho_1 \equiv \Lambda\rho^-$. The new jump conditions are

now

$$\begin{cases} \xi^+ = \xi^- \dfrac{\Lambda\theta^-}{\sqrt{\beta^-}} \\ \beta^+ = 1 \\ \psi^+ = \psi^- \dfrac{(\beta^-)^{\frac{3}{2}}}{(\theta^-\Lambda)^2} \\ \theta^+ = 1 \\ \left.\dfrac{d\theta}{d\xi}\right|_{r_0^+} = \left.\dfrac{d\theta}{d\xi}\right|_{r_0^-} \dfrac{\gamma^-}{\gamma^+} \dfrac{\sqrt{\beta^-}}{(\theta^-)^2} \\ \phi^+ = 1 \\ \left.\dfrac{d\phi}{d\xi}\right|_{r_0^+} = (\gamma^+ - 1) \left.\dfrac{d\theta}{d\xi}\right|_{r_0^-} \dfrac{\gamma^-}{\gamma^+} \dfrac{\sqrt{\beta^-}}{(\theta^-)^2}, \end{cases} \tag{4.2.11}$$

where we include the ϕ and $\frac{d\theta}{d\xi}$ variables defined in Appendix F, because useful for Section 4.3.3.

4.3 Fiducial barotropic model

In this section, we derive a fiducial barotropic model for a 1 $M_\odot$ star with solar composition at the onset of the CHeB stage, ensuring it incorporates all the fundamental characteristics of this evolutionary phase. As discussed in Section 4.2.1, knowing $\gamma(\rho)$ allows us to find the internal structure of the star using the hydrostatic equation, the mass continuity equation, and equation 4.2.4 or 4.2.5. However, this information is insufficient on its own; we need detailed evolutionary models for the calibration of $\gamma(\rho)$. For this purpose we employ the evolutionary codes `CLES v21.0` (Code Liégeois d'Évolution Stellaire, Scuflaire et al. 2008a) and `MESA v11701` (Modules for Experiments in Stellar Astrophysics; Paxton et al. 2011; Paxton et al. 2019). In both codes we focused on models that have a mass fraction of helium in the centre of about 0.9 (i.e. $Y_c \approx 0.9$). In particular, both in `CLES v21.0` and in `MESA v11701` we adopt as the reference solar mixture that from Asplund et al. (2009), and high- and low-temperature radiative opacity tables are computed for the solar specific metal mixture. The envelope convection is described by the mixing length theory of Cox et al. (1968); the corresponding $\alpha_{\rm MLT}$ parameter, the same for all the models, is derived from the solar calibration with the same physics. Below the convective envelope, we add a diffusive undershooting (Herwig 2000) with a size parameter $f = 0.02$ (see Khan et al. 2018) in the `MESA v11701` models, while the `CLES v21.0` models incorporated a step undershooting in the form of penetrative convection. Furthermore, additional mixing over the convective core limit during the CHeB phase is treated follow-

ing the formalism by Bossini et al. (2017) in the `MESA v11701` models. In contrast, in the `CLES v21.0` models we adopt a step overshooting of $0.50 H_P$ in the form of penetrative convection, along with prescriptions designed to establish a semiconvective region (more details in Panier et al., in prep.). Unlike `MESA v11701`, `CLES v21.0` begins its simulations from a zero-age horizontal branch, employing a fixed initial helium core mass of 0.45 $M_\odot$. As a result, these models do not undergo helium flashes, but approximately 6% by mass of helium in the core is converted into carbon.

In figure 4.2 we show the $\gamma(r)$ of four different models as a function of density. Two of them are computed with `CLES v21.0` and `MESA v11701`, while another one is a model with $Z = 0.012580$ taken from the `BaSTI-IAC` library[2] explained in Hidalgo et al. (2018). It is clear that they share the same fundamental characteristics of the CHeB phase. We expect a similar situation for models of different masses and/or metallicity; the main difference beeing the location (in density) of such characteristics. Finally, the last $\gamma(r)$ in the figure is a reference barotropic model we derive in Section 4.3.1, 4.3.2 and 4.3.3, which we will call fiducial barotropic model. This model is calibrated on the evolutionary model computed with the code `CLES v21.0`, which we will simply call reference `CLES` model. We decide to divide $\gamma(r)$ of the barotropic model in three different zones: the convective core (Section 4.3.1), the inner radiative region of the star (i.e. the radiative core, the hydrogen-burning shell and the radiative envelope, see Section 4.3.2), and the convective envelope (Section 4.3.3).

It is essential to emphasise that the primary aim of this semi-analytical modelling is to explore the details of the gravity modes spectrum. Therefore, our analysis will concentrate on the characteristics of the stellar radiative regions, while we will simplify the modelling of the convective envelope, as it is less relevant to our investigation.

4.3.1 First zone

The first zone is the convective core of the CHeB star. We model this part by using the same ρ_c and P_c as the reference `CLES` model, but a different Γ_1. We assume a constant Γ_1 equal to $\gamma(\theta)$, i.e. we assume a polytropic EOS in this region. We calibrate the barotropic model to have the same radius and mass at the end of the convective core as the reference `CLES` model by keeping Γ_1 as a free parameter to fit. The results of the calibration are in Table 4.1.

[2] http://basti-iac.oa-abruzzo.inaf.it/astero.html

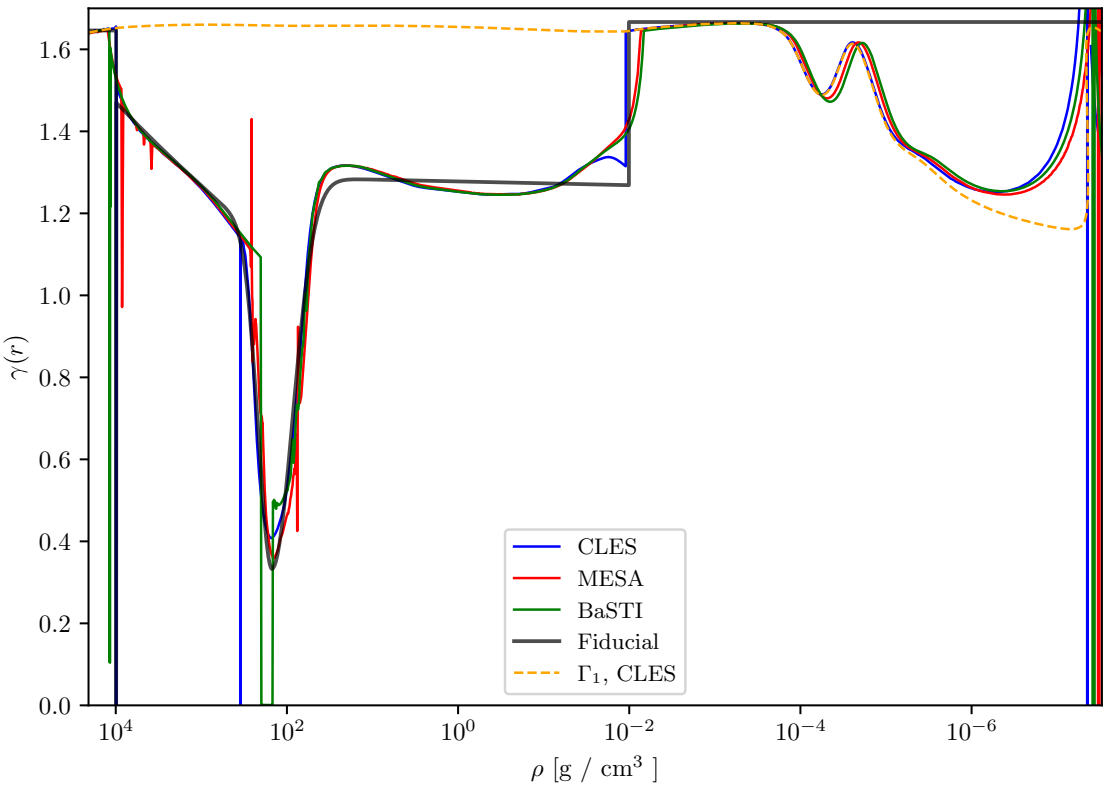

Figure 4.2: Comparison of $\gamma(r)$ as a function of density for four different models of a 1 $M_\odot$ star at the beginning of the CHeB stage ($Y_c \approx 0.9$) with solar metallicity. In blue a model calculated with the tool `CLES v21.0`, in red a model calculated with the code `MESA v11701`, in green a model taken from the `BaSTI-IAC` library, and in black the fiducial barotropic model we present in Section 4.3. In orange we also show the Γ_1 obtained with `CLES v21.0`. All the four models share the fundamental characteristics of the CHeB phase.

Table 4.1: Comparison between the reference `CLES` model and the fiducial barotropic model presented in Section 4.3.

Zone	Γ_1	Radius	Mass	Density	Pressure
First	1.6460	$< 10^{-10}\%$	$< 10^{-10}\%$	0.08%	0.06%
Second, correct BCE	5/3	$< 10^{-10}\%$	$9.3 \cdot 10^{-10}\%$	$1.3 \cdot 10^{-8}\%$	-7.2%
Second, fiducial	5/3	$< 10^{-10}\%$	0.56%	8.2%	7.3%

Notes. This comparison is done by means of the expression $(x_{\mathrm{CLES}} - x_{\mathrm{fiducial}})/x_{\mathrm{CLES}}$, where x is the position, mass, density, and pressure at the boundaries of the zones depending on the column. The second row presents the values achieved when fitting the correct radius and mass at the base of the convective envelope (Section 4.3.2). In contrast, the last row displays the values obtained when aiming for the correct total stellar mass and radius (Section 4.3.2).

4.3.2 Second zone

In the second zone, we simulate the change in chemical composition at the boundary between convective and radiative core with a jump in density identical to the reference `CLES` model (i.e. we adopt the same $\Lambda < 1$). This approach is justified by the fact that $\Lambda \approx \mu^+/\mu^-$ in the perfect gas approximation, because at the boundary between convective and radiative core the pressure and the temperature are continuous functions. In this second zone, we model the star from the base of the radiative core to the base of the convective envelope. In particular, we take

$$\begin{cases} \Gamma_1 = \dfrac{5}{3} \\ 0 \leq \gamma(\rho) < \Gamma_1 \\ \theta := \dfrac{\rho}{\Lambda \rho^-} \\ \beta := \dfrac{P}{P_0} = \exp\left(\displaystyle\int_0^{\ln \theta} \gamma(t)\, dt \right) \end{cases} \tag{4.3.1}$$

with

$$\gamma(\theta) = \begin{cases} A\exp\left[-\dfrac{(\ln\theta - \ln\theta_P)^2}{2\sigma^2}\right] + a\theta^K, \quad \theta_P \leq \theta \leq 1 \\ \\ [A + a\theta_P^K - (a')\theta_P^{K'}]\exp\left[-\dfrac{(\ln\theta - \ln\theta_P)^2}{2(\sigma')^2}\right] + \\ +(a')\theta^{K'}, \quad \theta < \theta_P. \end{cases} \tag{4.3.2}$$

Therefore, we model $\gamma(\theta)$ in this zone with eight parameters (i.e. $[A, \theta_P, \sigma, a, K, \sigma', K', a']$). The normalised pressure is found when applying equation 4.3.2 into $\beta(\theta)$ of equation 4.3.1, that is

$$\ln\beta(\theta) = \begin{cases} A\sqrt{\dfrac{\pi}{2}}\sigma\left[\mathrm{erf}\left(\dfrac{\ln\theta - \ln\theta_P}{\sqrt{2}\sigma}\right) + \mathrm{erf}\left(\dfrac{\ln\theta_P}{\sqrt{2}\sigma}\right)\right] + \\ +\dfrac{a}{K}\left(\theta^K - 1\right), \quad \theta_P \leq \theta \leq 1 \\ \\ A\sqrt{\dfrac{\pi}{2}}\sigma\left[\mathrm{erf}\left(\dfrac{\ln\theta_P}{\sqrt{2}\sigma}\right)\right] + \dfrac{a}{K}\left(\theta_P^K - 1\right) + \\ +[A + a\theta_P^K - (a')\theta_P^{K'}]\sqrt{\dfrac{\pi}{2}}(\sigma')\mathrm{erf}\left(\dfrac{\ln\theta - \ln\theta_P}{\sqrt{2}\sigma'}\right) + \\ +\dfrac{a'}{K'}\left(\theta^{K'} - \theta_P^{K'}\right), \quad \theta < \theta_P. \end{cases} \tag{4.3.3}$$

We find initial guesses of the eight parameters by performing a fit between equation 4.3.2 and the $\gamma(\theta)$ of the reference `CLES` model with a maximum likelihood estimator. Consequently, we modify the values of K' and a' to obtain the same radius and mass at the base of the convective envelope (BCE) as in the reference `CLES` model (see Table 4.1). However, in the final fiducial model we do not keep these values of K' and a', because they would lead to unphysical values of the total stellar mass and radius (Section 4.3.3).

Finally, we want to notice that in the reference `CLES` model there is another drop in density located at the end of the helium core as a signature of the helium-flashes (i.e. the drop in γ of figure 4.2 near $\rho = 100$ g/cm^3). However, in our fiducial barotropic model we exclude such signature, because we will explore better additional jump discontinuities in Section 2.4.

4.3.3 Third zone

In the reference `CLES` model, the density is non-differentiable at the BCE, that is, γ has (with abuse of notation) a "jump discontinuity" at the BCE (see the "jump" in γ as illustrated in figure 4.2 at $\rho = 0.01$ g/cm^3). This characteristic is retained in our barotropic model. Moreover, in contrast to the convective core, the convective envelope (designated

as the third zone in our barotropic model) exhibits low efficiency in convective transport in the near-surface layers, primarily due to their low density values. As a result, these near-surface layers are characterised by a temperature gradient that exceeds the adiabatic temperature gradient, which can be modelled with the mixing length theory (see Section 1.2.2). However, in our barotropic model we adopt a $\gamma(\rho) \equiv \Gamma_1$ (i.e. an adiabatic temperature gradient) everywhere in the convective envelope to simplify subsequent calculations. Additionally, we do not account for helium and hydrogen recombination and we keep a constant $\Gamma_1 = 5/3$ (similarly to the second zone, see Section 4.3.2). Finally, we determine the total stellar mass and radius by solving the Lane-Emden equation F.0.7, with the appropriate jump conditions described in equation 4.2.11, until we reach a density $\rho = 0$.

Due to the simplifications implemented, particularly within the convective envelope, our barotropic model does not yield the same total mass and radius as the reference `CLES` model; instead, it results in a star that is larger and more massive. A correct total radius or a correct total mass can be achieved when $\Gamma_1 > 5/3$ within the convective envelope. However, we decide to retain a more physically plausible value of $\Gamma_1 = 5/3$ and adjust the parameters $[K', a']$[3] to ensure that the barotropic model attains the correct total mass and radius. The change in radius, mass, density and pressure at the BCE resulting from the introduction of the new $[K', a']$ parameters are presented in Table 4.1.

4.4 Smooth transitions in discontinuous density profiles

In real stars, atomic diffusion (e.g. Michaud et al. 1984; Michaud et al. 2010) is expected to smooth gradients in pressure, temperature, concentration and density. It tends to smooth out such gradients when present, as in the case of jump discontinuities in density. Therefore, to make our barotropic model even more realistic, we need a function that smoothly joins two adjacent zones having otherwise a jump discontinuity in density. This must be done in a self-consistent manner and by simulating different levels of mixing between the two zones.

In the fiducial barotropic model of Section 4.3, we have a jump discontinuity in the density at the boundary between convective and radiative core. We can smoothly join these two zones using a sigmoid function $S(P)$ in the $\ln P - \ln \rho$ plane. This means that $\rho \equiv \rho(\rho_I, \rho_R, S)$, where $\rho_I(r)$ is the density profile in the convective core and $\rho_R(r)$ the density profile in the radiative part of the star. In general, the new derivative of the density

[3] We also tested different parameters to reach the correct total mass and radius, but these two are the best compromise.

is

$$\frac{d\ln\rho}{d\ln P} = \frac{\partial\ln\rho}{\partial\ln\rho_I}\frac{d\ln\rho_I}{d\ln P} + \frac{\partial\ln\rho}{\partial\ln\rho_R}\frac{d\ln\rho_R}{d\ln P} + \frac{\partial\ln\rho}{\partial S}\frac{dS}{d\ln P}, \tag{4.4.1}$$

with a convenient choice for $S(P)$ such that it cancels out in the radiative part and becomes one in the convective core. Consequently, a choice for $\rho(\rho_I, \rho_R, S)$ is

$$\ln\rho(P) := \ln\rho_R + (\ln\rho_I - \ln\rho_R)S(P), \tag{4.4.2}$$

which inserted into equation 4.4.1 becomes

$$\frac{d\ln\rho}{d\ln P} = \frac{1-S(P)}{\gamma_R[\rho_R(P)]} + \frac{S(P)}{\Gamma_{1,c}} + (\ln\rho_I - \ln\rho_R)\frac{dS(P)}{d\ln P}. \tag{4.4.3}$$

Finally we obtain that

$$\begin{cases} \dfrac{1}{\gamma(\rho)} = \dfrac{1-S[P(\rho)]}{\gamma_R\{\rho_R[P(\rho)]\}} + \dfrac{S[P(\rho)]}{\Gamma_{1,c}} + \\ +\{\ln\rho_I[P(\rho)] - \ln\rho_R[P(\rho)]\}\dfrac{dS[P(\rho)]}{d\ln P}, \end{cases} \tag{4.4.4}$$

with $P(\rho)$ obtained by inverting equation 4.4.2 numerically. As expected, $\lim_{S\to 0}\gamma = \gamma_R$, $\lim_{S\to 1}\gamma = \Gamma_{1,c}$, and $\lim_{S\to 1/2}\gamma$ has a local minimum whose value depends on the functional form of $S(P)$.

From now on we decide to use the error function as a functional form of $S(P)$:

$$\begin{cases} S(P) := \dfrac{1+\mathrm{erf}[\alpha(\ln P - \ln P_0)]}{2} \\ \dfrac{dS(P)}{d\ln P} = \dfrac{\alpha}{\sqrt{\pi}}\exp\left[-\alpha^2(\ln P - \ln P_0)^2\right], \end{cases} \tag{4.4.5}$$

where $\alpha \geq 0$ is a constant whose increasing value makes the slope of $S(P)$ steeper, and P_0 is the pressure at the boundary between convective and radiative core in the fiducial model of Section 4.3. With such choises, the higher is α, the lower is the amount of mixing between the two consecutive zones. Indeed, for $\alpha \to \infty$ equation 4.4.5 tends to a Heavside function, thus, we tend to the fiducial model of Section 4.3, while for $\alpha = 0$ we have a fixed $S(P) = 1/2$ that corresponds to the maximum mixing. Furthermore, this choice for P_0 results in $\rho_I(P_0) \equiv \rho^-$, $\rho_R(P_0) \equiv \Lambda\rho^-$ and

$$\lim_{P\to P_0}\frac{1}{\gamma} = \frac{1}{2\gamma_R(\Lambda\rho^-)} + \frac{1}{2\Gamma_{1,c}} + \frac{\alpha}{\sqrt{\pi}}\ln\left(\frac{1}{\Lambda}\right). \tag{4.4.6}$$

In summary, in the limit for $\alpha \to \infty$, equation 4.4.4 tends to

$$\lim_{\alpha\to\infty}\gamma(\rho) = \begin{cases} \Gamma_{1,c}, & P > P_0 \\ 0, & P = P_0 \\ \gamma_R(\rho), & P < P_0, \end{cases} \tag{4.4.7}$$

and equation 4.4.2 tends to

$$\lim_{\alpha\to\infty}\rho(P)=\begin{cases}\rho_I(P), & P>P_0\\ \rho_R(P), & P<P_0,\end{cases} \tag{4.4.8}$$

which means that we tend to the fiducial model of Section 4.3 as expected.

To obtain the inverse of $\rho(P)$ we need to evaluate $\ln\rho_I(P)$ and $\ln\rho_R(P)$. From Section 4.3.1 we obtain

$$\ln\rho_I(P)=\ln\rho_c+\frac{\ln P-\ln P_c}{\Gamma_{1,c}}, \tag{4.4.9}$$

but $\ln\rho_R(P)$ does not have an analytical solution. However,

$$\ln P_R(\rho)\approx\ln P_0+\frac{a}{K}\frac{\rho^K-\rho_+^K}{\rho_+^K} \tag{4.4.10}$$

is a very good approximation of the equation 4.3.3 when $\rho\gtrsim 0.24\Lambda\rho^-$. Therefore, the inverse is well approximated by

$$\ln\rho_R(P)\approx\ln(\Lambda\rho^-)+\frac{\ln\left[1+\frac{K}{a}\ln\left(\frac{P}{P_0}\right)\right]}{K} \tag{4.4.11}$$

when $\rho_R\gtrsim 0.24\Lambda\rho^-$. Finally we obtain that

$$\begin{cases}\dfrac{1}{\gamma(\rho)}\approx\dfrac{1-S[P(\rho)]}{a+K[\ln P(\rho)-\ln P_0]}+\dfrac{S[P(\rho)]}{\Gamma_{1,c}}+\\ +\ln\left\{\dfrac{\rho_c}{\Lambda\rho^-}\left[\dfrac{P(\rho)}{P_c}\right]^{\frac{1}{\Gamma_{1,c}}}\left[\dfrac{a}{a+K(\ln P-\ln P_0)}\right]^{\frac{1}{K}}\right\}\dfrac{dS[P(\rho)]}{d\ln P}\\ \\ \ln\rho(P)\approx\ln(\Lambda\rho^-)+\dfrac{\ln\left[1+\frac{K}{a}\ln\left(\frac{P}{P_0}\right)\right]}{K}+\\ +\ln\left\{\dfrac{\rho_c}{\Lambda\rho^-}\left(\dfrac{P}{P_c}\right)^{\frac{1}{\Gamma_{1,c}}}\left[\dfrac{a}{a+K(\ln P-\ln P_0)}\right]^{\frac{1}{K}}\right\}S(P)\end{cases} \tag{4.4.12}$$

when $\rho_R\gtrsim 0.24\Lambda\rho^-$, and from a numerical evaluation of $P(\rho)$ we obtain $\gamma(\rho)$.

For $|\alpha(\ln P-\ln P_0)|>>1$ we have $\gamma\approx\Gamma_{1,c}$ for $\rho\approx\rho^-$, and $\gamma\approx\gamma_R$ for $\rho\approx\rho^+$. Note that to a good approximation

$$\begin{cases}P(\rho=0.24\Lambda\rho^-)\approx P_R(\rho_R=0.24\Lambda\rho^-)\,\text{for}\,\alpha\geq 1.885\\ \gamma(\rho=0.24\Lambda\rho^-)\approx\gamma_R(\rho_R=0.24\Lambda\rho^-)\,\text{for}\,\alpha\geq 2.074,\end{cases} \tag{4.4.13}$$

which means that the approximation in equation 4.4.10, which is valid when $\rho_R\gtrsim 0.24\Lambda\rho^-$, is also valid when $\rho\gtrsim 0.24\Lambda\rho^-$ if $\alpha\geq 2.074$. Moreover, from equation 4.4.13 we derive that $\gamma(\rho\leq\Lambda\rho^-)\approx\gamma_R(\rho_R\leq\Lambda\rho^-)$ and $P(\rho\leq\Lambda\rho^-)\approx P_R(\rho_R\leq\Lambda\rho^-)$ if $\alpha\geq 2.074$. Therefore,

we decide to solve equation 4.4.12 when $\rho > \Lambda\rho^-$, and when $\rho \leq \Lambda\rho^-$ (i.e. until the end of the second zone) we solve

$$\begin{cases} \gamma \approx \gamma_R \\ \\ \ln P \approx \ln P_R = \ln P_1 + \displaystyle\int_{\ln\theta_1}^{\ln\theta} \gamma_R(t)\, dt = \\ = \ln P_1 + A\sqrt{\dfrac{\pi}{2}}\sigma \left[\mathrm{erf}\left(\dfrac{\ln\theta - \ln\theta_P}{\sqrt{2}\sigma}\right) + \mathrm{erf}\left(\dfrac{\ln\theta_P - \ln\theta_1}{\sqrt{2}\sigma}\right)\right] + \\ + \dfrac{a}{K}(\theta^K - \theta_1^K), \end{cases} \tag{4.4.14}$$

where $\theta := \rho/(\Lambda\rho^-)$, $\theta_1 := 0.24$ and $\ln P_1 := \ln P(\theta_1)$, which is found using equation 4.4.12. Finally, we choose Γ_1 such that

$$\Gamma_1 = \begin{cases} \Gamma_{1,c} \quad \text{for} \quad \rho \geq \rho^- \\ \left(\dfrac{5}{3} - \Gamma_{1,c}\right) \dfrac{\ln(\rho) - \ln(\Lambda\rho^-)}{\ln(\Lambda)} + \dfrac{5}{3} \quad \text{for} \quad \Lambda\rho^- < \rho < \rho^- \\ \dfrac{5}{3} \quad \text{for} \quad \rho \leq \Lambda\rho^-. \end{cases} \tag{4.4.15}$$

With this formalism we can explore different behaviours at the boundary betweeen convective and radiative core by varying the parameters Λ and α. In the top panel of figure 4.3, we illustrate four scenarios: one with a jump discontinuity in density (blue lines), another without such a discontinuity (red lines), and two models that share the same Λ as the blue case but differ in α values (orange and green lines). The bottom panel displays the corresponding Brunt-Väisälä frequencies as functions of internal mass, highlighting that a higher α leads to a sharper bell-shaped structure. Furthermore, the same formalism can be applied to smoothly connect two adjacent zones that would otherwise exhibit a jump discontinuity in density within the radiative core. In this context, the primary distinction lies in the fact that $\gamma_I(\rho) \neq \Gamma_{1,c}$, and the validity of the approximation presented in the equations must be verified.

4.5 Results

In this section we explain the main results concerning our fiducial barotropic model (Section 4.5.1) in comparison with different boundaries of the convective core (Section 4.5.2), and different glitches in the radiative core (Section 4.5.3). We compute the adiabatic eigenfrequencies, normalised inertia E_{norm} (as outlined in equation 1.4.15 of Section 1.4.1) and eigenfunctions of radial ($\ell = 0$) and non-radial ($\ell = 1 - 3$) modes using the code `GYRE` (version 6.0.1, Townsend et al. 2013; Townsend et al. 2018; Goldstein et al. 2020), but we

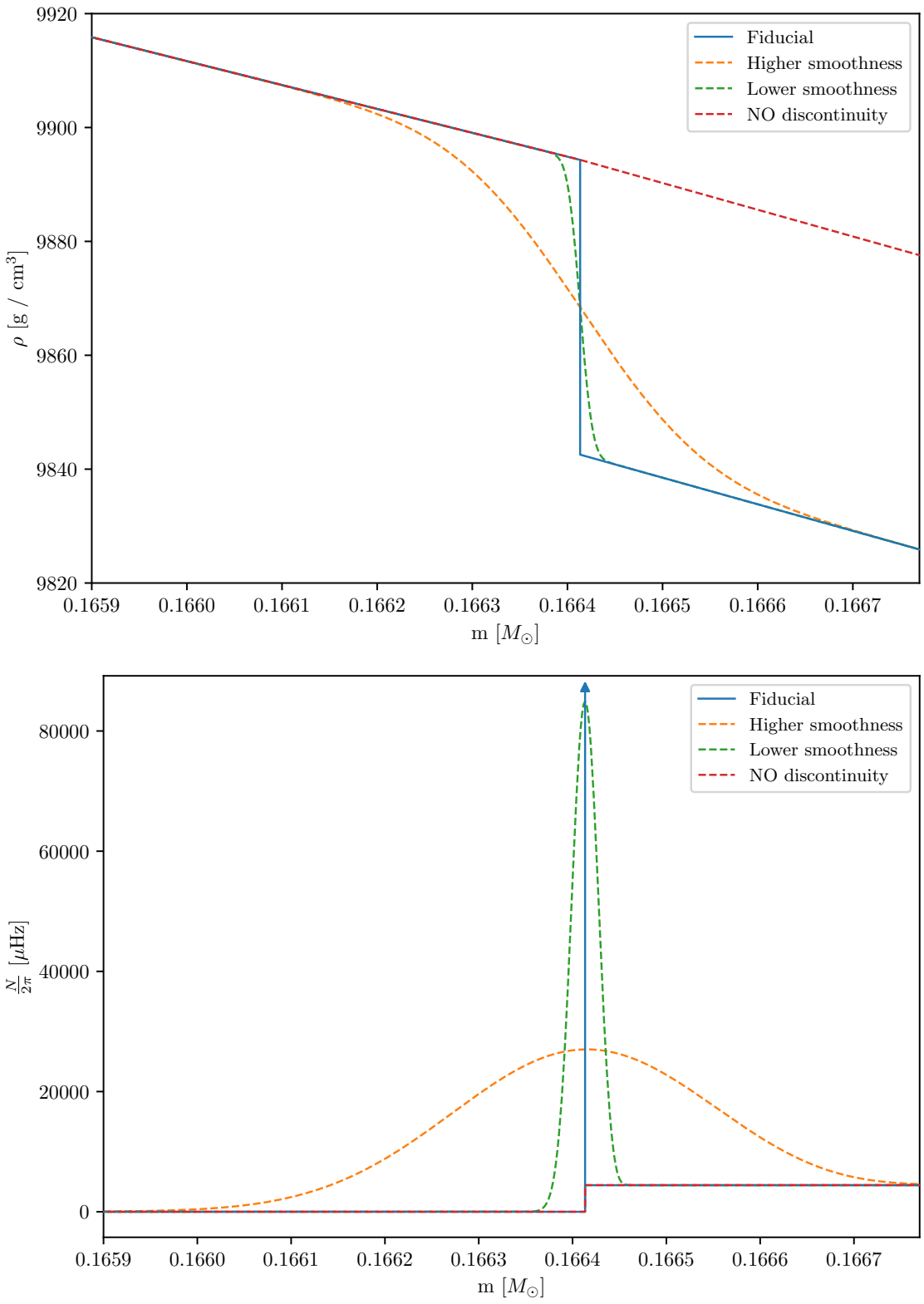

Figure 4.3: Comparison between four different density profiles (top panel) at the boundary between the convective and the radiative core and their corresponding Brunt-Väisälä frequencies (bottom panel) as functions of internal mass. In particular, we compare the fiducial barotropic model (blue) with a model without a jump discontinuity at the boundary (red), and with two models that smoothly join the two cores (orange and green). The orange line incorporates a lower α value than the green line. The blue arrow corresponds to a δ-distribution. The FWHM of the peaks in N presented here are significantly lower than $0.1H_p$.

verify independently the calculations with the tool `LOSC` (Scuflaire et al. 2008b) in the case of the fiducial model. We also simulate 4-year-long *Kepler* observations (lightcurves and power spectral densities) with the code `AADG3` (AsteroFLAG Artificial Dataset Generator, version 3.0.2; Ball et al. 2018, and references therein), with information on mode lifetimes taken from the work of Vrard et al. (2018) on CHeB stars in the *Kepler* field.

4.5.1 Fiducial model

In this section, we highlight the results of the fiducial barotropic model of Section 4.3. In Figure 4.4 we show the Brunt-Väisälä frequency as a function of the internal mass, with a specification for the position of the convective core, the hydrogen-burning shell and the convective envelope (top panel). In the boundary between the convective and radiative core there is a change in Γ_1, a change in $\gamma(\rho)$ and a jump discontinuity in density. This implies that N is a δ-distribution (blue arrow in the figure) at the position corresponding to the boundary. In the BCE, the density profile is non-differentiable due to a "jump" in $\gamma(\rho)$, thus here N has a jump discontinuity.

As discussed at the beginning of Section 4.5, we assess our model by computing adiabatic eigenfrequencies that serve to simulate 4-year-long *Kepler* observations. The corresponding power spectral density (PSD) as a function of frequency is shown in the bottom panel of figure 4.4. This panel includes a cyan dashed line representing the $\nu_{\max}$, derived from the reference `CLES` model, alongside the normalised inertiae as a function of eigenfrequencies for modes with $\ell = 0, 1, 2,$ and 3. As expected (e.g. Montalbán et al. 2010; Mosser et al. 2011b; Mosser et al. 2012a), the radial modes, along with the minima of inertia for the non-radial modes, are evenly spaced in frequency with a $\langle \Delta\nu \rangle \approx 5\mu$Hz. Additionally, a "forest" of dipole mixed modes appears between two consecutive radial modes, a characteristic observed in actual low-mass CHeB stars. We further expect that, in these stars, the period spacing (ΔP) of the observable dipole mixed modes approaches the asymptotic value ($\Delta P_{\rm a}$), which is notably higher than that of RGB stars (e.g. Montalbán et al. 2010; Bedding et al. 2011). Our fiducial model confirms this expectation, as illustrated in the middle panel of figure 4.4. It is apparent that as the frequency decreases, ΔP approaches the asymptotic value of $\Delta P_{\rm a} = 248.34\,$s due to the increasing radial order of the g-modes. Moreover, each minimum in ΔP corresponds to a minimum of inertia, linked to a pressure-dominated mode, and the higher the frequency the lower the ΔP. We also calculate the coupling parameter (q) at $\nu_{\max}$ using the prescriptions of Takata (2016a), yielding $q \approx 0.24$, which aligns with the observational findings (e.g. Vrard et al.

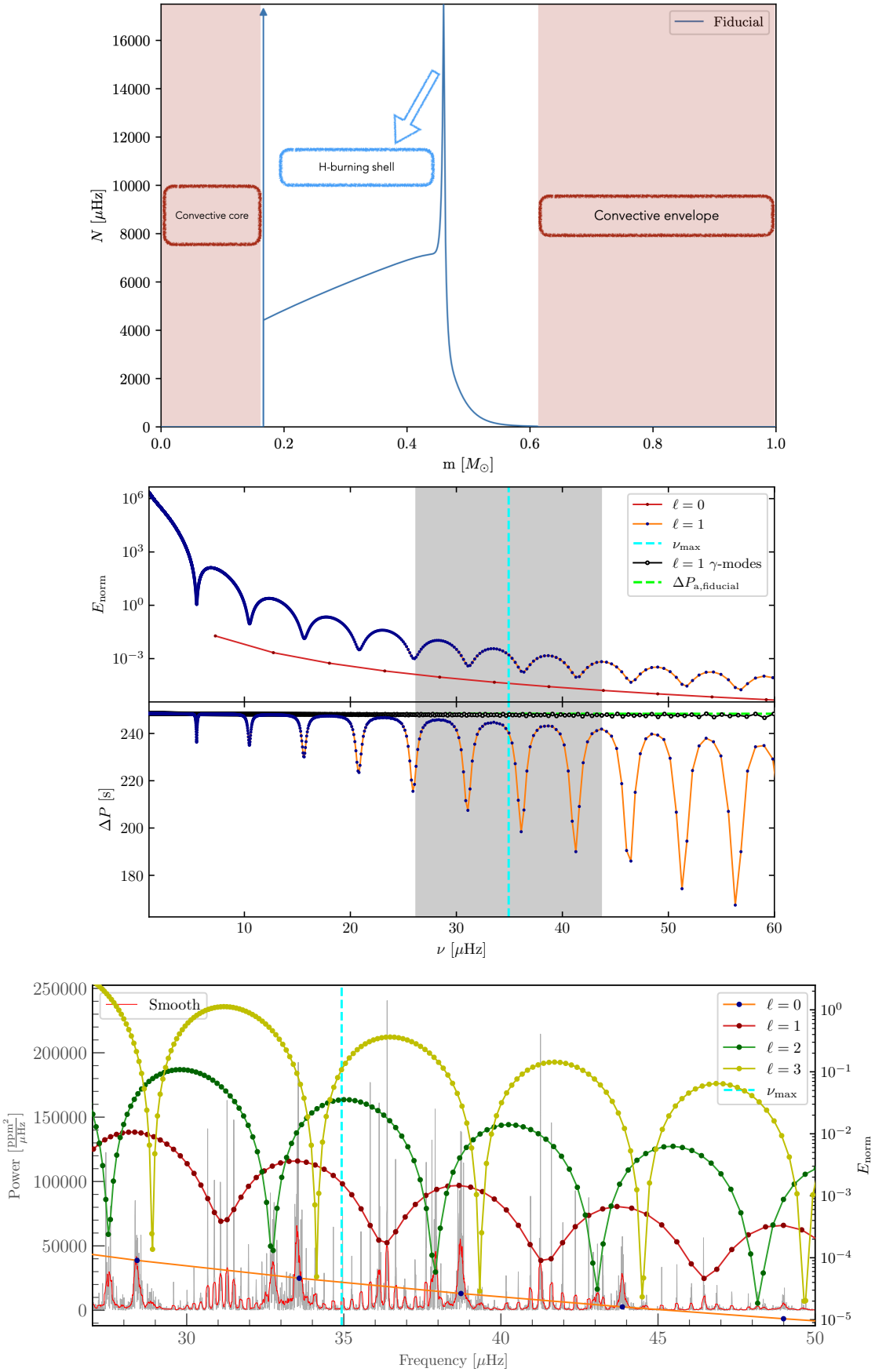

Figure 4.4: This figure displays the Brunt-Väisälä frequency as a function of internal mass (top), normalised inertia and period spacing (middle), and the simulated power spectral density (bottom). The observable region of the spectrum is highlighted in gray, with the cyan dashed line indicating $\nu_{\max}$.

2016; Mosser et al. 2017).

In the hydrogen-burning shell, we observe that the Brunt-Väisälä frequency is non-differentiable at the point where $\theta = \theta_P$, a condition resulting from the specific choice of $\gamma(\rho)$ employed in equation 4.3.2. This non-differentiability has the potential to introduce an artificial glitch in the period spacing of the mixed modes, as noted in previous studies (e.g. Cunha et al. 2015). Therefore, it warrants careful examination. Upon analysing ΔP at frequencies lower than $\nu_{\max}$, we identify a behaviour resembling a small amplitude oscillation centred in $\Delta P_{\rm a}$. The periodicity of this oscillation is approximately 11.6 minutes, while the corresponding periodicity in radial order is $\Delta n \approx 2.80$. These periodicities are consistent with expectations based on equation 4.1.2. However, it is important to note that the Brunt-Väisälä frequency at the normalised buoyancy radius associated with $\Delta n \approx 2.80$ is smooth, which implies that it should not affect the eigenfrequencies with a glitch signature (e.g. Cunha et al. 2015). Notably, this periodicity is accompanied by an alias observed at $\Delta n \approx 1.555$. When this alias is taken into consideration, we find that the associated normalised buoyancy radius is in good agreement with the characteristics of the hydrogen-burning shell, which peaks at $\Phi \approx 0.641$ and has a full width at half maximum (FWHM) of 0.126. Nonetheless, it is crucial to remain aware that this periodicity may also arise from numerical inaccuracies in the computation of the adiabatic frequencies and/or from the presence of the aforementioned non-differentiable point. A way to solve this problem is by a comparison between the local wavelength of the eigenfunctions near the shell and the width of the glitch (or the scale of variation of N, e.g. Cunha et al. 2019), because it shows whether there is a period trapping in the region and what the main source of the trapping is. A simpler way to see buoyancy glitches, and conversely to solve the issue, is to measure the ΔP of the uncoupled g-modes, called γ-modes, through the prescriptions provided by Ong et al. (2020) and included in `GYRE`. As can be seen from the top panel of the figure 4.4 and from figure 4.5, the small amplitude oscillations centred in the asymptotic period spacing $\Delta P_{\rm a}$ are more visible when the modulation caused by the coupling with the p-modes is absent. While the aforementioned periodicity in radial order of these oscillations persists in the γ-modes, we must also account for a newly prominent glitch signature with periodicity $\Delta n \approx 2$, as evidenced by a Fourier transform applied to the period spacing of the oscillation modes. According to equation 4.1.2, we would expect a glitch structure at $\Phi(r_{\rm glitch}) \approx 0.5$. However, the N function is smooth at this location, which means that it cannot generate a glitch signature in the eigenfrequencies. It is now apparent that the glitch at $\Delta n \approx 1.555$ aligns with the non-differentiable point, as at this

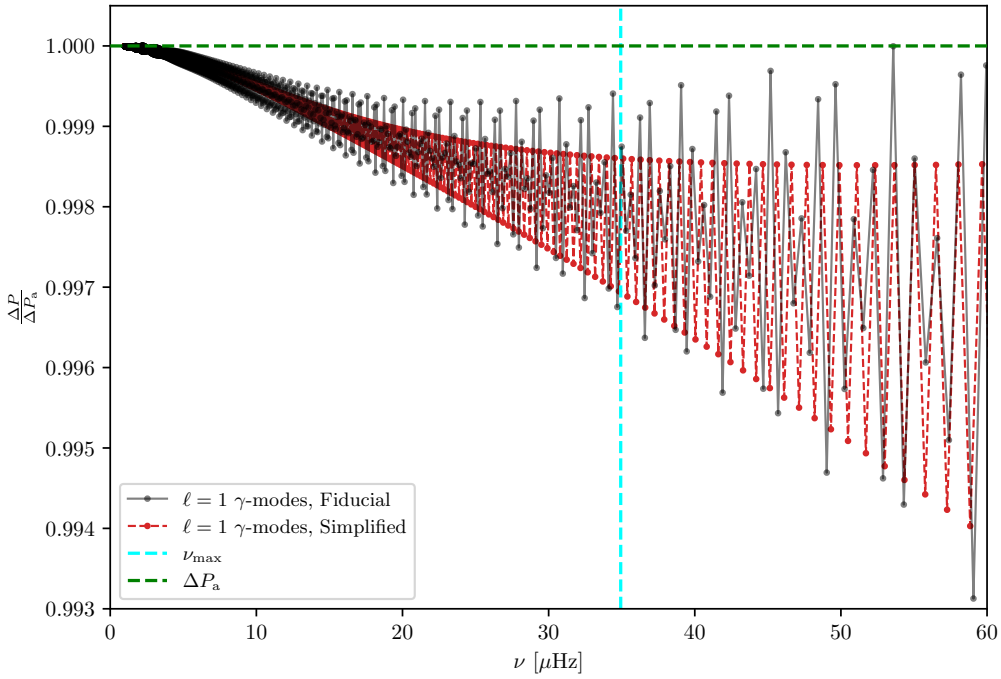

Figure 4.5: Comparison between normalised period spacings for the γ-modes as functions of frequency. The grey area represents the observable region of the spectrum and the cyan line the $\nu_{\max}$. It is clear that the fiducial model (in black) and the simplified model (in red) have similar properties of the g-cavity.

specific location the scale of variation of N is much lower than the local wavelength of the g-modes near $\nu_{\max}$. At this point, we can devise a simplified model that eliminates such non-differentiable point, albeit at the expense of a less realistic g-cavity. In particular, we employ the equations

$$\begin{cases} \gamma(\theta) = A \exp\left[-\dfrac{(\ln\theta - \ln\theta_P)^2}{2\sigma^2}\right] + c, \quad \theta \leq 1 \\ \\ \ln\beta(\theta) = A\sqrt{\dfrac{\pi}{2}}\sigma\left[\operatorname{erf}\left(\dfrac{\ln\theta - \ln\theta_P}{\sqrt{2}\sigma}\right) + \operatorname{erf}\left(\dfrac{\ln\theta_P}{\sqrt{2}\sigma}\right)\right] + \\ +c\ln\theta, \quad \theta \leq 1 \end{cases} \tag{4.5.1}$$

instead of the equations 4.3.2 and 4.3.3, with $c > 0$ a constant chosen in order to have the correct total mass of the star. Figure 4.5 illustrates the normalised period spacings for the γ-modes from both the fiducial model (in black) and the simplified model. The results demonstrate that the observed glitch signature with periodicity $\Delta n \approx 2$ remains intact, and that this oscillation appears to be at least compatible, if not predominant, with the glitch signature originating from the non-differentiable point. To further investigate this, we employed a finer grid when building the barotropic model and utilised different numerical solvers. Despite these modifications, the same glitches in the period spacing were

consistently observed. Therefore, the main deviations from the asymptotic value might arise from numerical inaccuracies in the computation of eigenfrequencies, rather than from the presence of the non-differentiable point. Notably, the peak-to-peak relative difference in the period spacing of the γ-modes is at most 0.2 % (in the high-frequency regime), which is significantly lower than typical observational uncertainties. Consequently, this glitch does not compromise the interpretation of the observed power spectral distributions. Furthermore, it confirms that the other glitches, which will be addressed in subsequent sections, can be examined without concern for interference from this particular glitch, as those will likely be much more significant.

4.5.2 Different boundaries of the convective core

In this section, we explore the impact on frequencies of two different types of boundaries between convective and radiative core. In particular, we discuss the impact of a smooth transition in the density between the two cores, and of a continuous density function that is non-differentiable at the boundary.

Smooth transition

In figure 4.6 we show in the top panel the N profile as a function of the internal mass for a model similar to the fiducial barotropic model, but with a smooth transition in the density profile between the convective and radiative core (Section 4.4). This new model has a N profile (red line) very similar to the fiducial model (blue line), but it contains a bell-shaped structure centred at the boundary instead of a δ-distribution. We expect a value of the asymptotic period spacing of the new model $\Delta P_{\rm a,Smooth}$ lower than the one of the fiducial model $\Delta P_{\rm a,Fiducial}$, because the new model has a slighlty greater g-cavity than the fiducial model and it has higher values of N near the boundary. Moreover, we expect that such bell-shaped structure in the N profile becomes a glitch, which creates a sinusoidal behaviour of ΔP around $\Delta P_{\rm a,Smooth}$ with a decreasing amplitude at increasing frequency, and dips in the period spacing that are evenly spaced in period, with a periodicity compatible with the buoyancy radius of the glitch (Cunha et al. 2019; Cunha et al. 2024).

In the bottom panel we show period spacings of the γ-modes as functions of the eigenperiods for this new model (in red) and the fiducial model (in blue). As expected, there is a very small difference between the two asymptotic period spacings (i.e. $\Delta P_{\rm a,Smooth} \approx \Delta P_{\rm a,Fiducial} - 0.65$ s) and between the γ-modes in the observable region (dashed grey line). Moreover, we observe in the new model a periodicity of approximately 23 hours with a

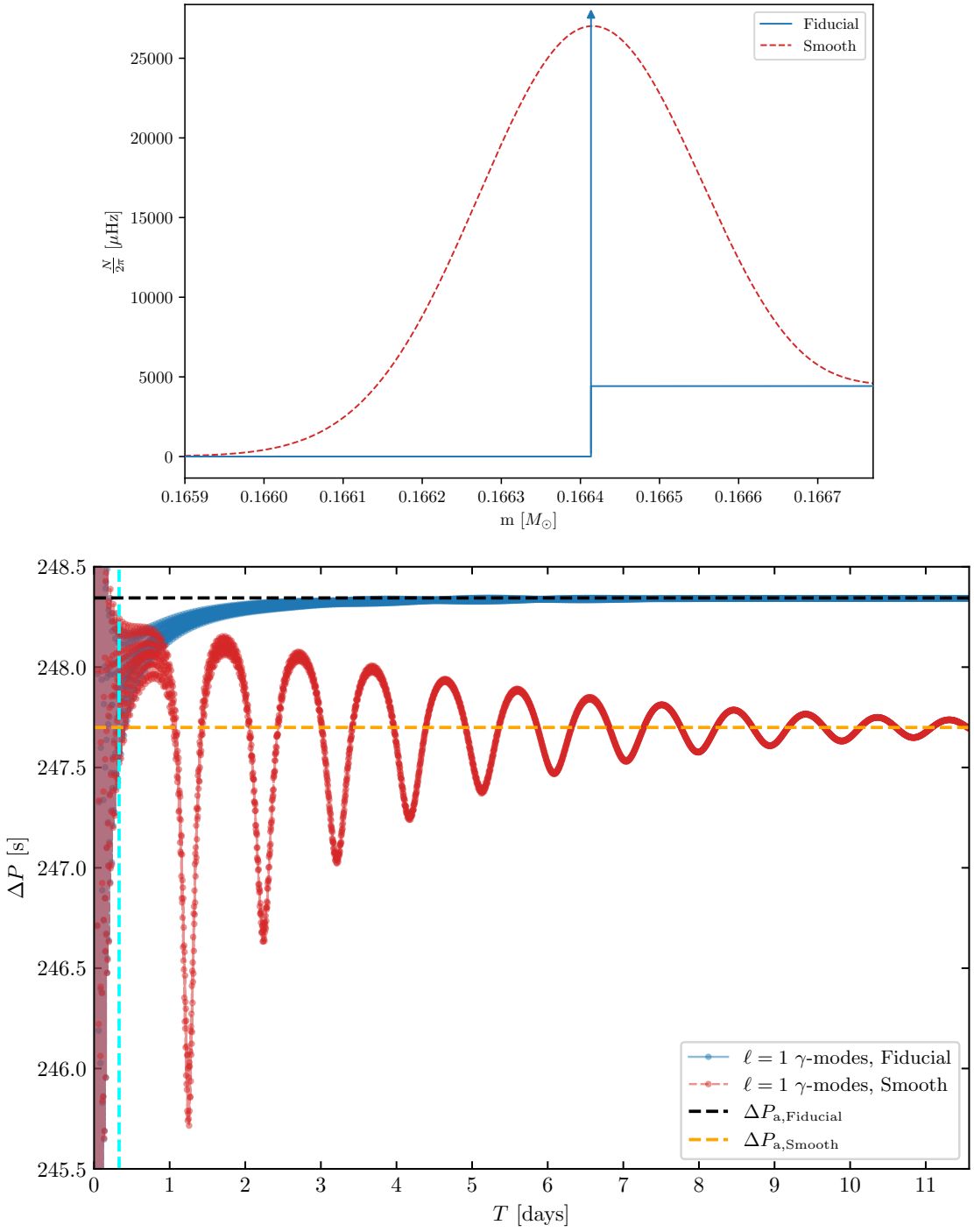

Figure 4.6: Comparison of N profiles as functions of internal mass (top panel) and period spacings of the γ-modes as functions of the eigenperiods (bottom panel). The blue line represents the fiducial model, while the red model features a bell-shaped structure in the N profile at the boundary between the convective and radiative core (see Section 4.4). The periodicity of the glitch corresponds to the location of the bell-shaped structure. The half width at half maximum of the bell-shaped structure presented here is $0.0012 H_P$.

decreasing amplitude at increasing eigenperiods. When expressed in terms of radial orders, this same periodicity corresponds to $\Delta n \approx 334$, which aligns with the expected value derived from applying equation 4.1.2 to the new model. According to the same equation, we also infer that this glitch signature correlates to a structural variation situated at $\Phi(r_{\rm glitch}) \approx 0.0030$. This finding is consistent with the normalised buoyancy radius of the bell-shaped structure in N, which peaks at $\Phi \approx 0.0015$ and possesses a FWHM of 0.0023. Furthermore, within this structure lies a local maximum of the Brunt-Väisälä length scale (H_N) that is significantly lower than the local wavelength of g-modes at $\nu_{\rm max}$. This further supports the compatibility of our findings with the characteristics of the bell-shaped structure. It is important to highlight that within the observable region of the oscillation spectrum, this periodic component would appear too smooth to be identified as a glitch signature. Finally, the small glitch explained in Section 4.5.1 adds to the above glitch, generating relative fluctuations much lower than 1 % around the main behaviour of the period spacing.

No jump discontinuity in density at the boundary of the convective core

In figure 4.7 we show in the top panel the N profile as a function of the internal mass for a model similar to the fiducial barotropic model, but with a continuous density function that is non-differentiable at the boundary between the convective and the radiative core. This new model has a N profile (red line) very similar to the fiducial model (blue line), but it contains a jump discontinuity at the boundary instead of a δ-distribution, and the bell-shaped peak related to the H-burning shell is located at a lower radius than in the fiducial model. Therefore, $\int_{r_1}^{r_2} N/r\, dr$ is higher in the new model and we expect a value of the asymptotic period spacing $\Delta P_{\rm a,NO}$ lower than $\Delta P_{\rm a,Fiducial}$.

In the bottom panel, the period spacings are presented as functions of the eigenfrequencies for both the fiducial model (in blue) and the new model (in red). Although the two asymptotic period spacings differ, the difference is minimal (≈ 0.76 s). Notably, the small glitch discussed in Section 4.5.1 now shows an increased peak-to-peak relative difference in the period spacing of the modes. This could be related to the change of the N profile at the buondary. However, it is important to note that the JWKB approximation used by Cunha et al. (2019) and Cunha et al. (2024) cannot be applied in this context to infer the properties of the glitches. Despite this increased difference, the relative difference remains at most 1 % in the observable region of the spectrum. As a result, it is very difficult to detect such a glitch even with the highest quality data available, especially when analysing

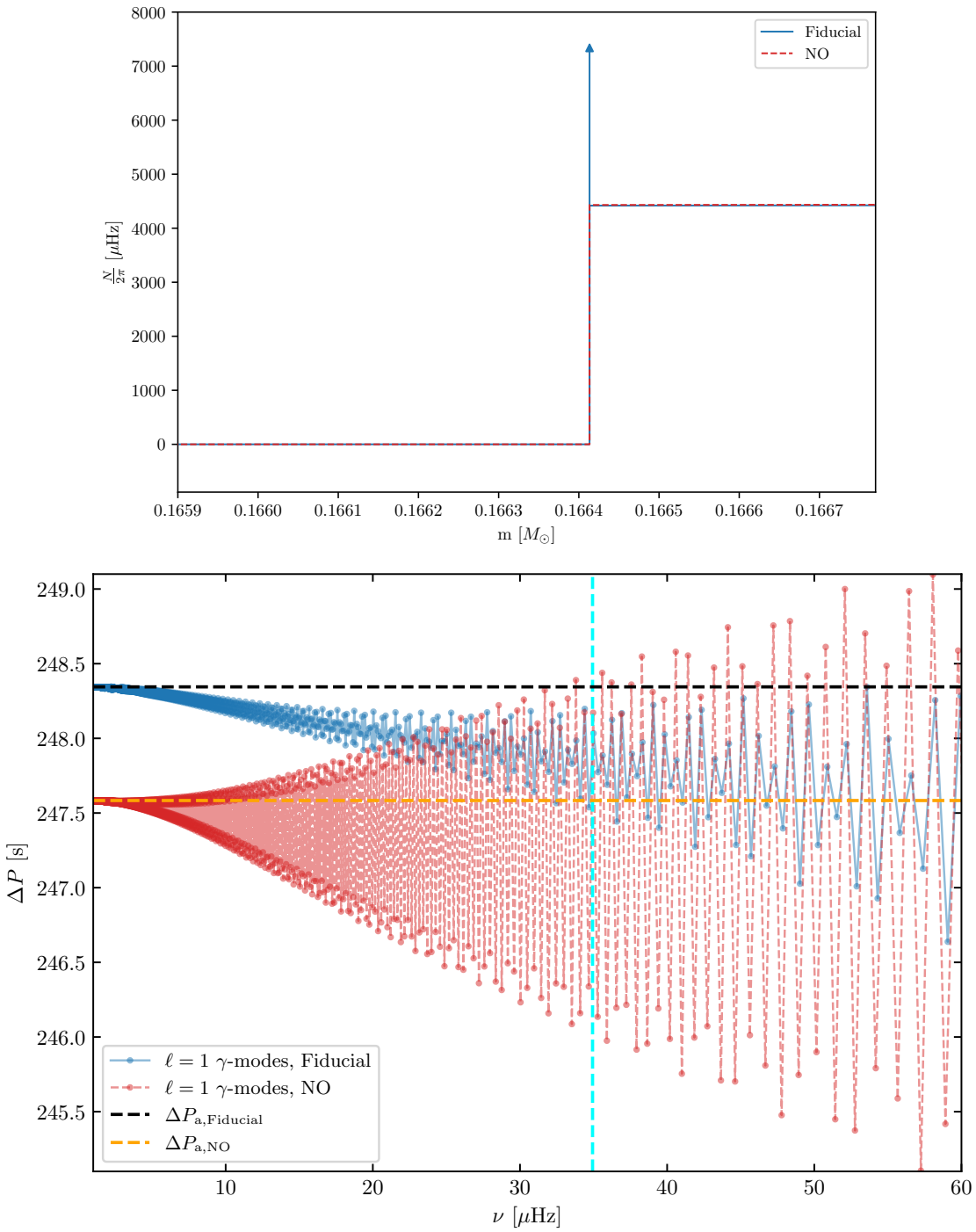

Figure 4.7: Comparison of N profiles as functions of internal mass (top panel) and period spacings of the γ-modes as functions of the eigenfrequencies (bottom panel). The blue line represents the fiducial model, while the red model features a step-like structure in the N profile at the boundary between the convective and radiative core instead of a δ-distribution.

mixed dipole modes.

Nevertheless, it is important to highlight that the glitches discussed in Section 4.5.2 serve as valuable examples for testing purposes. At this stage, we cannot rule out the possibility that signatures of convective boundary mixing may be observed in more evolved CHeB stars, as such glitches at the boundary between the convective and radiative core could potentially be more pronounced in these cases.

4.5.3 Glitches in the radiative core

In this section, we explore the impact on frequencies of two different types of glitches in the radiative core. In Section 4.5.3 we study the impact of a jump discontinuity in density located in a position compatible with a subflash, whereas in Section 4.5.3 we smooth the same discontinuity using the method of Section 4.4.

δ-distribution glitch

In figure 4.8, the top panel displays the N profile as a function of internal mass for a model similar to that presented in Section 4.5.2. This model features a continuous, albeit non-differentiable, density function at the boundary between the convective and radiative core, and it introduces a new jump discontinuity in density that is compatible with a subflash event occurring within the radiative core. The resulting N profile (red line) closely resembles the fiducial model (blue line); however, the red model is characterised by a jump discontinuity at the boundary between the convective and the radiative core rather than a δ-distribution. Moreover, a δ-distribution is observed at the location of the jump discontinuity in density within the radiative core, with the bell-shaped peak associated with the hydrogen-burning shell occurring at a lower radius compared to the fiducial model. Overall, the integral $\int_{r_1}^{x} N/r\,dr$ at a fixed position $x \leq r_2$ in this new model resembles that of the Section 4.5.2 mentioned earlier. However, the jump discontinuity in density within the radiative core leads to a reduction in $\int_{r_1}^{x} N/r\,dr$ for positions above the discontinuity when compared to the other case. This cumulative effect drives the value of the integral $\int_{r_1}^{r_2} N/r\,dr$ below that of the fiducial model. Consequently, we expect a value of the asymptotic period spacing $\Delta P_{\mathrm{a,Discont}}$ higher than $\Delta P_{\mathrm{a,Fiducial}}$. Furthermore, we expect that the δ-distribution in the N profile will manifest as a glitch, resulting in periodic deviations of ΔP relative to $\Delta P_{\mathrm{a,Discont}}$ (e.g. Cunha et al. 2015). These deviations will exhibit a decreasing amplitude with increasing frequency, creating evenly spaced dips in period that align with the periodicity associated with the normalised buoyancy radius

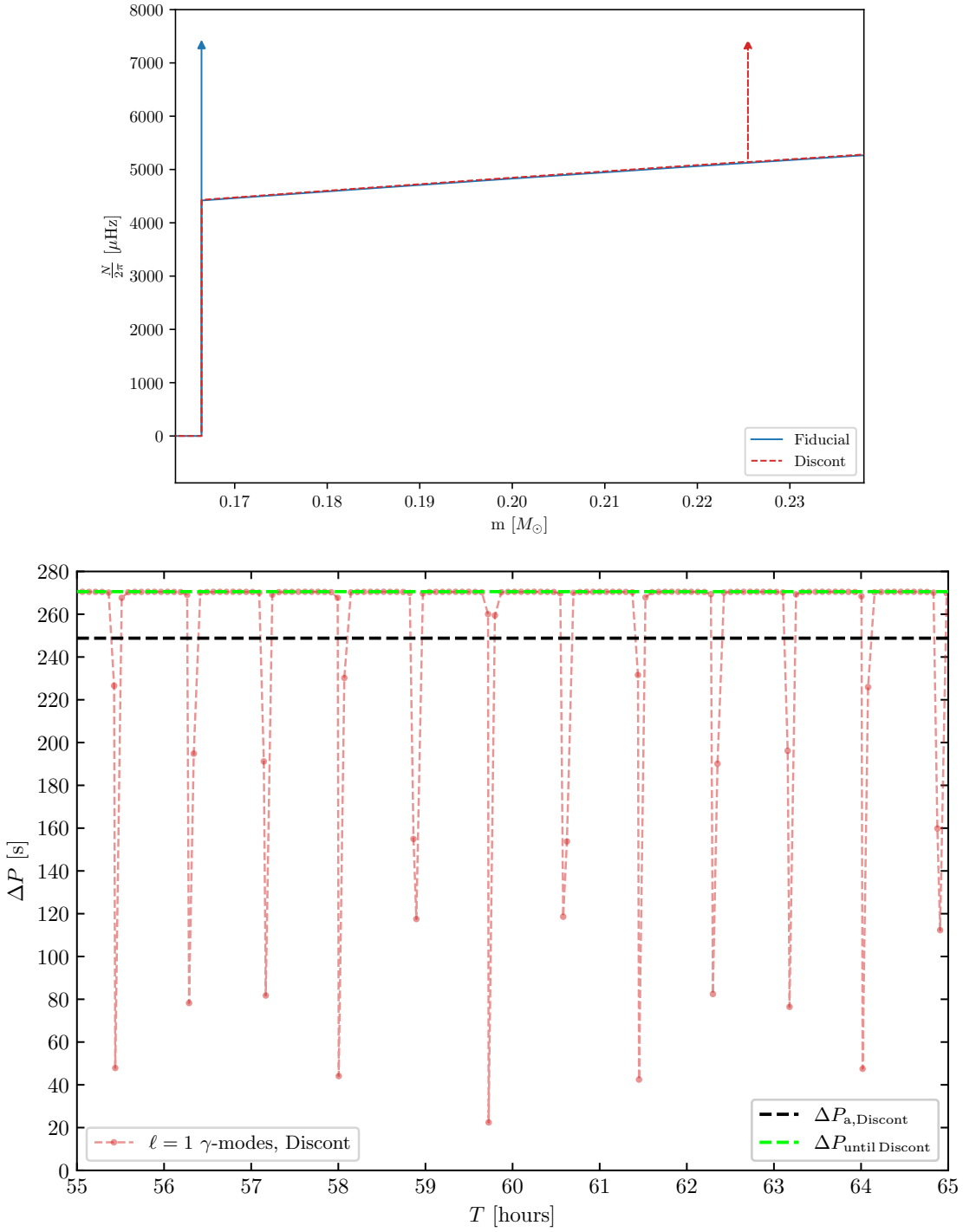

Figure 4.8: This figure presents a comparison of the N profiles as functions of internal mass (top panel) and the period spacings of the γ-modes as functions of the eigenperiods (bottom panel). The blue line represents the fiducial model, while the red model incorporates a δ-distribution glitch in the N profile located within the radiative core. The fiducial model is not displayed in the bottom panel, as it would be indistinguishable from the black line, which represents the ΔP_{a} of the red model. Notably, the periodicity in the bottom panel corresponds to the location of the δ-distribution, and the maximum period spacings measured closely match $\Delta P_{\mathrm{a,until\ Discont}}$. This value reflects the asymptotic ΔP we would obtain if the g-cavity extends from the position of the glitch to the outer boundary.

of the glitch. Additionally, some modes are expected to become trapped as a result of the abrupt change in N.

In the bottom panel, the period spacing of the γ-modes as a function of the eigenperiods for this new model. The fiducial model is not displayed in the bottom panel, as it would be indistinguishable from $\Delta P_{\mathrm{a,Discont}}$, which represents the ΔP_{a} of the red model. As expected, there is a small difference between the two asymptotic period spacings, specifically $\Delta P_{\mathrm{a,Discont}} \approx \Delta P_{\mathrm{a,Fiducial}} + 0.46$ s. Moreover, the period spacing exhibits a periodicity of about 51 minutes; when expressed in terms of radial orders, this periodicity translates to $\Delta n \approx 12.4$, in accordance with the expected value derived from the application of equation 4.1.2 to the model. This analysis also suggests that the glitch signature corresponds to a structural variation situated at $\Phi(r_{\mathrm{glitch}}) \approx 0.080$, which is compatible with the normalised buoyancy radius of the δ-distribution. Notably, the maximum period spacings measured closely match $\Delta P_{\mathrm{a,until\,Discont}}$. This value reflects the asymptotic ΔP we would obtain if the g-cavity extends from the position of the glitch to the outer boundary. It is evident that the inferred ΔP_{a} from observations would resemble $\Delta P_{\mathrm{a,until\,Discont}}$ rather than the true ΔP_{a}, as expected (e.g. Cunha et al. 2015). Finally, the small glitch explained in Section 4.5.1 adds to the above glitch, generating relative fluctuations much lower than 1 % around the main behaviour of the period spacing.

In the top panel of figure 4.9, we compare the period spacing of the γ-modes (in red) with the period spacing of the mixed dipole modes (in blue) in proximity to the observable region of the spectrum. Notably, some minima in the period spacing result from mode trapping rather than the coupling between p-modes and g-modes. This suggests that certain trapped modes may be detectable in actual data. However, not all of these minima show observable amplitudes, as modes with higher inertia tend to have lower amplitudes (e.g. Dupret et al. 2009), leading to decreased detectability even when the period spacing is low. Consequently, the measured ΔP is likely to differ from the true value if some modes are absent. This situation becomes even clearer in the bottom panel of figure 4.9, where we present the PSD (along with the normalised inertiae) for the model featuring a density discontinuity within the radiative core.

Bell-shaped glitch

In the top panel of figure 4.10, we show the N profile as a function of the internal mass for a model similar to the model of Section 4.5.3, but with a smooth transition in density instead of a jump discontinuity. This new model has a N profile (red line) very similar to

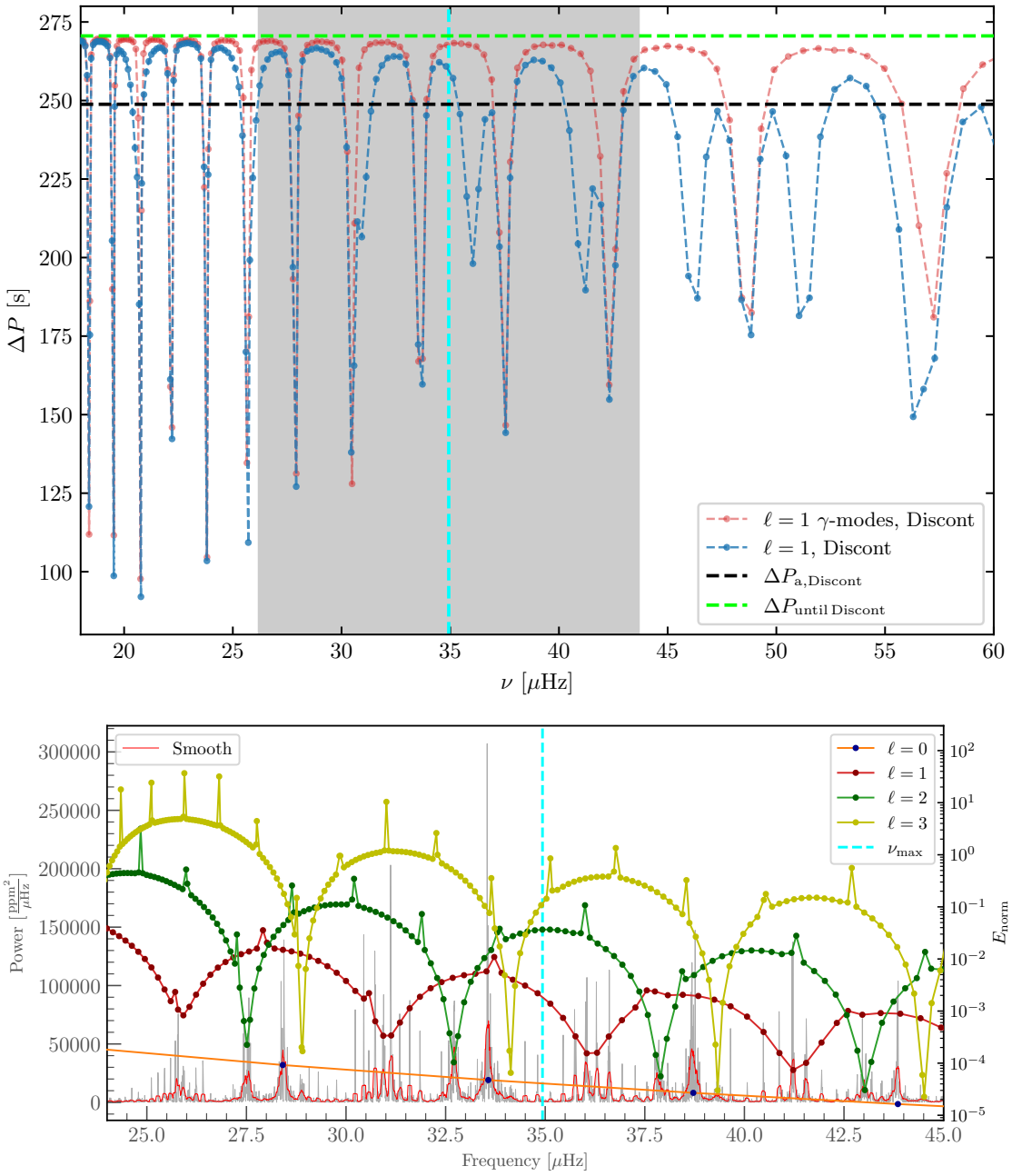

Figure 4.9: This figure displays the period spacing (top panel) as a function of eigenfrequencies. We compare the γ-modes (shown in red) with mixed dipole modes (in blue) in proximity to the observable region of the spectrum, indicated by the grey area with ν_{max} as a cyan line. The black line represents the ΔP_{a} for the red model, while the lime line depicts the expected ΔP_{a} if the g-cavity extends from the glitch location to the outer boundary. Importantly, some minima in the period spacing result from mode trapping rather than the coupling between p-modes and g-modes, and not all of these minima exhibit observable amplitudes. The impact of mode trapping near the density discontinuity on the observed eigenfrequencies is further illustrated in the bottom panel, which presents the corresponding simulated power spectral density.

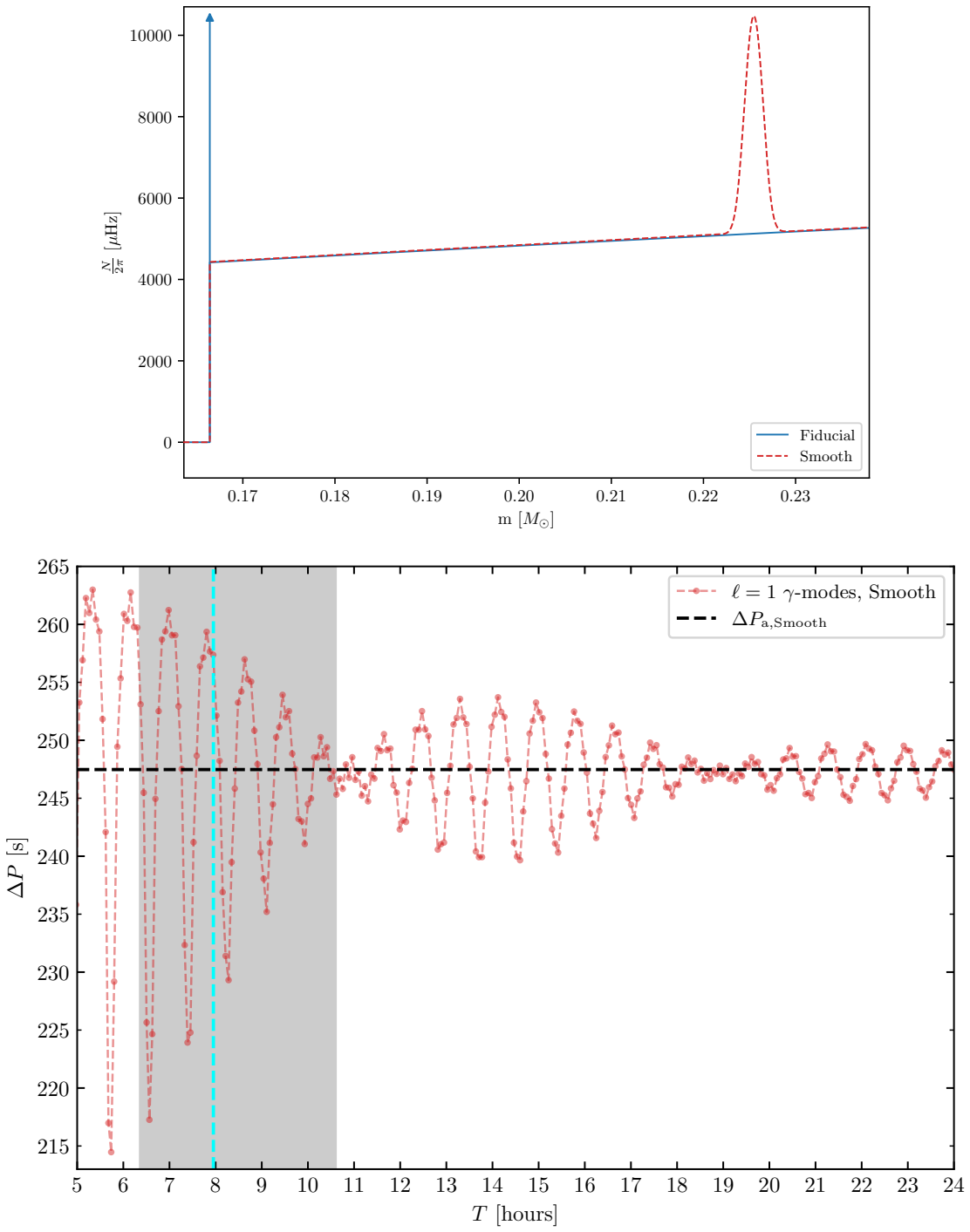

Figure 4.10: Comparison of N profiles as functions of internal mass (top panel) and period spacings of the γ-modes as functions of the eigenperiods (bottom panel). The blue line represents the fiducial model, while the red model features a bell-shaped structure in the N profile within the radiative core. The periodicity of the glitch corresponds to the location of the bell-shaped structure. The observable region of the spectrum is highlighted in gray, with the cyan dashed line indicating ν_{max}. The half width at half maximum of the bell-shaped structure in N presented here is $0.02H_P$.

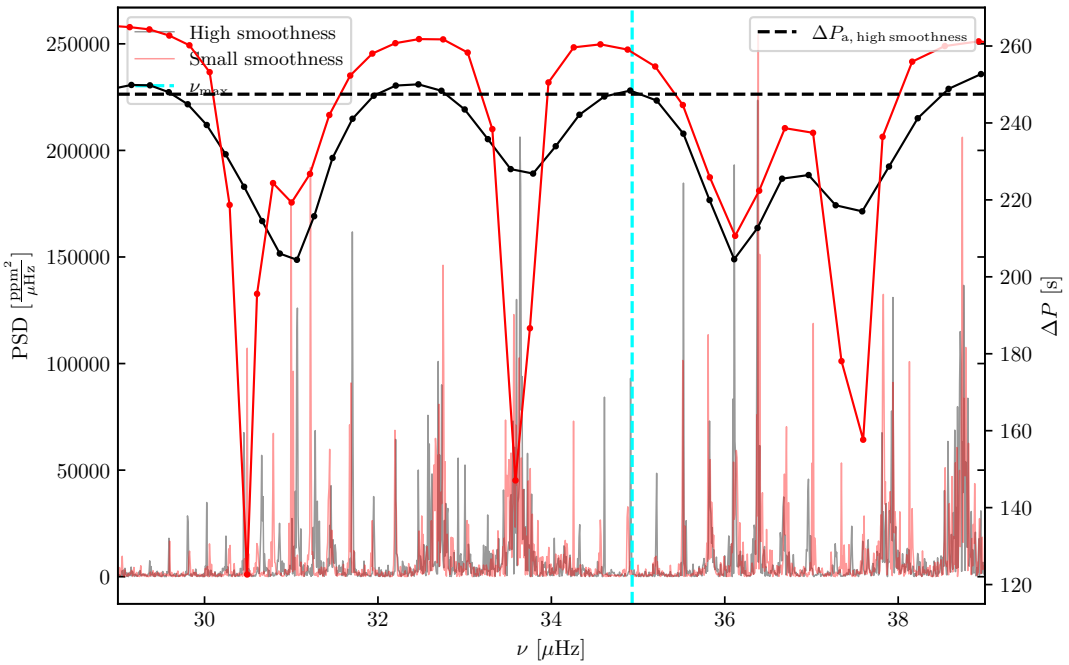

Figure 4.11: This figure displays a comparison of simulated power spectral densities for two differents smoothings in the radiative core along with the corresponding period spacings of the mixed dipole modes. The cyan dashed line indicates $\nu_{\rm max}$, while the black dashed line indicates the asymptotic ΔP for the model with the highest smoothness (i.e. with the lowest α, see Section 4.5.2). Notably, even within the observable region of the spectrum, we observe clear differences in both the period spacing and the detectable modes.

the fiducial model (blue line), but it contains a bell-shaped structure where there is the smooth change in density. This structure increases the integral $\int_{r_1}^{r_2} N/r\, dr$ compared to the fiducial model, thus, we expect a value of the asymptotic period spacing $\Delta P_{\rm a,Discont}$ lower than $\Delta P_{\rm a,Fiducial}$. Moreover, we expect that such bell-shaped structure in the N profile becomes a glitch, because its width is much lower than the local wavelength of the waves (Cunha et al. 2019; Cunha et al. 2024). Therefore, we expect a sinusoidal behaviour of ΔP around $\Delta P_{\rm a,Smooth}$ with a decreasing amplitude at increasing frequency, and dips in the period spacing that are evenly spaced in period, with a periodicity compatible with the normalised buoyancy radius of the glitch. This structure is aligned identically with the glitch discussed in Section 4.5.3, as we have placed the peak of the bell function at a location analogous to the δ-distribution.

In the bottom panel, the period spacing of the γ-modes as a function of the eigenperiods for this new model. The fiducial model is not displayed in the bottom panel, as it would be indistinguishable from $\Delta P_{\rm a,Smooth}$, which represents the $\Delta P_{\rm a}$ of the red model. As expected, there is a small difference between the two asymptotic period spacings, that is $\Delta P_{\rm a,Smooth} \approx \Delta P_{\rm a,Fiducial} - 0.86$ s. The period spacing shows a periodicity of approxi-

mately 51 minutes with a decreasing amplitude at increasing eigenperiods. This periodicity is compatible with the observed $\Delta n \approx 12.4$ and corresponds to a normalised buoyancy radius of 0.081, as described in equation 4.1.2. This indicates consistency with the normalised buoyancy radius of the bell-shaped structure in N, which peaks at $\Phi \approx 0.082$ and possesses a FWHM ≈ 0.011. Within this structure, there exist two local maxima of H_N that are significantly smaller than the local wavelength of the g-modes at $\nu_{\max}$, further reinforcing the alignment of these findings with the characteristics of the bell-shaped structure. However, contrary to the case with the δ-distribution, the period spacing reveals visible beats attributable to the presence of these adjacent maxima in H_N, which can be demonstrated through the application of a Fourier transform on the period spacing data. Finally, the small glitch explained in Section 4.5.1 adds to the above glitch, generating relative fluctuations much lower than 1 % around the main behaviour of the period spacing.

A more detailed characterisation of the detectability of the modes and the ability to differentiate between varying degrees of smoothing of the bell-shape structure is presented in figure 4.11. In this figure, we compare two simulated power spectral densities corresponding to different levels of smoothings, along with the associated period spacing of the mixed dipole modes. Notably, even within the observable region of the spectrum, we observe clear differences in both the period spacing and the detectable modes. This finding highlights promising directions for interpreting glitch signatures in high-quality asteroseismic data, including the possibility to discern the width of the bell-shaped structure in the Brunt-Väisälä frequency.

4.6 Discussion and conclusions

In this chapter, we conducted a theoretical analysis of how structural variations adjacent to the convective core and chemical composition gradients within the radiative core influence the period spacing of mixed dipole modes and γ-modes in low-mass CHeB stars. These variations are also expected to occur within semiconvective layers, within the hydrogen-burning shell, and at the base of the convective envelope. Additionally, in low-mass stars with a degenerate helium core, the transition from RGB to CHeB is characterised by a succession of off-centre helium flashes, which induce chemical composition gradients in the radiative core. To investigate the impact of density discontinuities and associated structural glitches on the period spacings of these oscillation modes, we developed semi-analytical models of low-mass CHeB stars. These models were calibrated using the evolutionary codes `BaSTI-IAC`, `CLES`, and `MESA`. The distinct physical prescriptions of these

codes allowed us to identify common relevant features for calibration while enabling control over the type of structural glitch introduced, all while maintaining a realistic representation of stellar interiors. We first established a fiducial model based on a solar mass CHeB star at solar metallicity with $Y_c \approx 0.9$, featuring a realistic g-cavity. Subsequently, we explored the effects of various discontinuities in density, non-differentiable points within the density profile, and bell-shaped glitches in the Brunt–Väisälä frequency on the adiabatic eigenfrequencies. The key findings from our analysis are summarised as follows:

- Jump discontinuities in the density profile result in distinct glitch signatures in the period spacings of mixed modes. These glitches exhibit periodic behaviours that are closely tied to the normalised buoyancy radius associated with the discontinuities. While certain trapped modes may be observable, their detectability is influenced by their inertia, with higher inertia modes exhibiting lower amplitudes. Consequently, this could lead to discrepancies between measured and true values of ΔP if some modes are missing from observations. Our analysis further highlights that the maximum measured period spacings are in close agreement with $\Delta P_{\rm a}$, indicating that the inferred period spacing from observational data is more likely to reflect this value rather than the true asymptotic value.

- The comparison between models featuring smooth transitions and those with discontinuities highlighted differences in the periodic behaviours. Specifically, this finding suggests that smooth transitions can be just as impactful as sharp discontinuities, leading to the possibility to detect not only position and amplitude of the glitch, but also its sharpness.

- Our simulations of 4-year-long *Kepler* observations reinforced the necessity of incorporating realistic stellar interior models to predict oscillation frequencies accurately. The resulting PSDs and period spacing patterns closely resemble observed data, providing a promising avenue for verifying our theoretical models against real-world observations.

This work establishes a solid foundation for future asteroseismic studies aimed at probing the internal structures of stars. Our models enable realistic predictions of how each sharp structural variation impacts the observed power spectral density. This alignment not only validates our theoretical approach but also suggests promising directions for interpreting glitches signatures in high-quality asteroseismic data. In the future, we aim to leverage this tool to explore glitches arising from varying degrees of jump discontinuities in density

and to study more evolved stellar models, where more pronounced glitches are expected.

Thesis conclusions

The primary aim of this PhD thesis has been to accurately characterise the internal structure of low-mass CHeB stars and evaluate non-standard evolutionary models through the application of advanced asteroseismic and Bayesian techniques. Through a comprehensive investigation, this work has delivered novel insights into the physical processes governing the evolution of these stars, with implications for stellar population studies and the formation history of the Milky Way.

Chapter 2 provided the identification in the *Kepler* field of eleven red giant stars with unusually complex oscillation spectra compared to the average behaviour. The seismic parameters of these stars are compatible with very low-mass ($M \lesssim 0.8$ M$_\odot$) CHeB stars with a helium core of ~ 0.5 M$_\odot$ and a lighter envelope ($0.1-0.2$ M$_\odot$) than typical RC stars in the *Kepler* field. Moreover, they display higher couplings ($q \gtrsim 0.4$) between the g-cavity and the p-cavity than typical RC stars ($q \sim 0.25 - 0.30$). The sample included stars with low to intermediate metallicity (75%) and solar metallicity. In this chapter I have shown that the oscillation spectra we expect for this type of stars are entirely consistent with those observed in our sample. These spectra are clearly different from those of the stars that, with a similar helium core but a much larger envelope, populate the RC. The main factor determining these differences is the coupling between the inner and outer regions, which reflects very different density profiles inside these stars. Here, I have also shown the ability of asteroseismology to identify these low-mass CHeB stars in the field and in solar-metallicity environments where, even with high-precision photometry, they would be hardly distinguishable from other stars in RC or RGB phases. Moreover, I provided cases where, especially those of solar metallicity, the stars must have followed a non-standard evolution during which they lost a large amount of mass. This research establishes a strong foundation for future investigations into these stars and the processes that shaped their current masses. Understanding these factors is crucial for accurately determining their impact in the determination of ages of field stars and may provide another piece of the puzzle in the sequence between RC and subdwarf B stars or other stripped stars.

Chapter 3 continues the analysis of non-standard evolutionary paths by exploring formation scenarios for such low-mass CHeB stars. In particular, I focused my analysis on the CHeB star KIC4937011, which is a Li-rich, low-mass, metal-rich star member of the open cluster NGC 6819. This star has a mass that is approximately 1 $M_\odot$ lower than the other member stars in the same evolutionary stage within the cluster. Using a Bayesian approach, my analysis strongly suggests that this star is the product of a CEE phase where the companion star did not survive. The proposed formation channel involves two ZAMS stars in a circular orbit, with RLOF occurring while the low-mass companion is still on the MS. This leads to a CEE phase with the ejection of about 1.1 $M_\odot$ of material and the merger of the companion with the primary star. The resulting star is a RGB-like star with a smaller hydrogen-rich envelope than the primary star before the CEE phase. Finally, after helium flashes, the degenerate helium core steadly burns helium through the 3α reaction, resulting in the currently observed KIC4937011. While systematic differences were noted between modelled and observed values (e.g., effective temperatures and luminosities), these do not hinder the inference of the formation channel. This formation pathway provides new insights into how mass loss and binary interactions shape the evolution of stars, and this channel may also apply to the formation of sdB stars or metal-rich RR Lyrae, suggesting a connection in the evolutionary pathways of these stars.

Chapter 4 focuses to the detailed internal structure of low-mass CHeB stars, examining the asteroseismic signatures of structural variations near their convective core. By developing semi-analytical models calibrated with advanced evolutionary codes, I was able to investigate the effects of structural glitches on the oscillation spectra of these stars. Structural glitches, such as discontinuities or non-differentiable points in the density profile, leave distinct signatures on the eigenfrequencies of the oscillation modes, providing a window into the internal chemical composition and thermal gradients, convective boundaries, and other key structural features (e.g. amount and position of helium fashes). My analysis demonstrated that these structural glitches offer deep insights into the internal structure, which is particularly promising in very low-mass CHeB stars, where mode trapping and strong coupling between cavities take place. This work establishes a solid foundation for future asteroseismic studies aimed at probing the internal structures of stars. Our models enable realistic predictions of how each sharp structural variation impacts the observed power spectral density. This alignment not only validates our theoretical approach but also suggests promising directions for interpreting glitches signatures in high-quality asteroseismic data. In future, I plan to pursue comparative studies with hydrodynamical simulations,

aiming for a more profound physical understanding of these phenomena. Moreover, I aim to leverage this tool to explore glitches arising from varying degrees of jump discontinuities in density and to study more evolved stellar models, where more pronounced glitches are expected.

The implications of this research extend to multiple areas of astrophysics. By enhancing our understanding of low-mass stellar evolution and the factors that influence it, I can provide new tools to refine stellar population models and to improve age determinations for field stars. Furthermore, this work underscores the importance of binary interactions in the evolutionary histories of stars, suggesting that many seemingly single stars may have undergone significant interactions that shape their current states. Future research directions include expanding the sample of low-mass CHeB stars for more comprehensive statistical analyses and refining models of binary interactions to clarify mass loss mechanisms. Additionally, applying these asteroseismic techniques to other stellar populations may yield further insights into the broader dynamics of stellar evolution. In summary, this research work has made significant contributions to the field of stellar astrophysics, particularly regarding low-mass CHeB stars. By integrating asteroseismology with detailed evolutionary modeling, it lays a solid foundation for future studies aimed at unraveling the complexities of stellar evolution and enhancing our understanding of the Milky Way's formation and evolution.

Appendix A

Physical properties of the full sample

In this appendix we give some details concerning the origin of the physical quantities in Tables 2.1 and A.1. The latter complements the former, providing the properties of the rest of our sample of rHB candidates (see also the HRD of the whole sample in Fig. A.1).

Table A.1: Physical properties for the rest of our sample of rHB candidates.

KIC	L [$L_\odot$]	$T_{\rm eff}$ [K]	[Fe/H]	[α/Fe]	$\langle\Delta\nu\rangle$ [μHz]	$\nu_{\rm max}$ [μHz]	q	$\Delta\Pi_1$ [s]	M [$M_\odot$]
2555126	41 ± 4	5320 ± 20	-0.72	0.26	5.66 ± 0.03	36.4 ± 0.6	0.93	280 ± 20	0.64 ± 0.06
3428926$^+$	36 ± 3	5560 ± 130	-0.50	0.27	6.72 ± 0.02	43.0 ± 0.6	1.15	270 ± 40	0.58 ± 0.07
3626807	50 ± 6	5310 ± 20	-1.16	0.26	5.276 ± 0.011	36.5 ± 0.6	0.69	308 ± 6	0.79 ± 0.10
9335415$^+$	46 ± 4	5580 ± 120	-0.50	0.11	5.808 ± 0.018	34.9 ± 0.5	0.53	240 ± 40	0.59 ± 0.07
9691704	55 ± 7	5230 ± 20	-0.88	0.30	4.802 ± 0.013	32.6 ± 0.5	0.23	334 ± 5	0.83 ± 0.11
11072164	43 ± 4	5215 ± 18	-1.01	0.24	4.761 ± 0.012	32.8 ± 0.5	1.11	300 ± 50	0.65 ± 0.06
11299941*	32 ± 3	4585 ± 7	0.25	0.05	4.08 ± 0.09	28.0 ± 0.8	0.45	300 ± 20	0.64 ± 0.08
12504765$^+$	51 ± 5	5220 ± 130	-1.15	0.33	4.817 ± 0.010	32.4 ± 0.5	0.65	340 ± 20	0.76 ± 0.10
4937011^R	37 ± 4	4707 ± 8	-0.02	0.03	4.08 ± 0.10	28.3 ± 0.4	0.53	224.3 ± 1.4	0.71 ± 0.08

Notes. The table also includes the properties of KIC4937011 (under-massive star in NGC 6819, marked with an R), for which we show the $\langle\Delta\nu\rangle$, $\nu_{\rm max}$, and M from Handberg et al. (2017). See Table 2.1 for a description of the symbols.

The global seismic parameters, $\nu_{\rm max}$ and $\langle\Delta\nu\rangle$, of targets tagged with an asterisk in Tables 2.1 and A.1 are taken from Yu et al. (2018), while those for the NGC 6819 cluster member (KIC 4937011, tagged with ^{R}) are from Handberg et al. (2017). For the rest of the sample, we employ the approach of Davies et al. (2016), and the value of $\langle\Delta\nu\rangle$ is computed using individual frequencies and the weighted fit of the asymptotic relation for radial modes. As discussed in Handberg et al. (2017), this method gives results in good agreement with the values of $\langle\Delta\nu\rangle$ derived by Yu et al. (2018) and allows a forward comparison with model-based values. The asymptotic period spacing of the dipole modes, $\Delta\Pi_1$, and the coupling factor, q, are derived using the stretched-period method (see e.g.

Vrard et al. 2016).

The atmospheric parameters, $T_{\rm eff}$, and chemical composition come from APOGEE-DR17, except for four targets with a `STAR_BAD` flag in that release. For them (marked with a plus symbol in Tables 2.1 and A.1) we adopt the available values in APOGEE-DR16. To check the reliability of these atmospheric parameters and of the quoted uncertainties, we perform an independent analysis for the three stars of Table 2.1. We use `MOOG-synth`[1] with the assumption of local thermodynamic equilibrium and the APOGEE-DR17 linelist (Shetrone et al. 2015; Smith et al. 2021) implemented with lines from the `VALD` database[2] and `MARCS` model atmospheres (Gustafsson et al. 2008). We get results in good agreement with those in APOGEE DR16 and DR17, except for the $T_{\rm eff}$ uncertainties. Even for the best situation in which $\log g$ is fixed to the seismic values (e.g. Valentini et al. 2019), the uncertainty on $T_{\rm eff}$ is $\sigma_{T_{\rm eff}} \sim 50$ K. Therefore, although in Tables 2.1 and A.1 we keep the values from APOGEE, we assume a minimum value of $\sigma_{T_{\rm eff}} = 50$ K when deriving the stellar mass and its uncertainty.

Bolometric luminosities, L, are estimated by combining astrometry data from *Gaia* DR3 (Babusiaux et al. 2023) with 2MASS photometry (Skrutskie et al. 2006) in the K_s band and bolometric correction from Casagrande et al. (2014) and Casagrande et al. (2018). We apply the *Gaia*-DR3 parallax zero-point correction of Lindegren et al. (2021) and estimate reddening and extinction from the three-dimensional maps of Green et al. (2019). The errors in L are calculated with a Markov chain Monte Carlo method and considering the extinction and the value of $M_{\rm bol,\odot}$ to be fixed ($M_{\rm bol,\odot} = 4.75$; Casagrande et al. 2014).

Stellar masses, as described in Sect. 2.2, are estimated using the scaling relation Eq. 2.2.1 and the values of L, $T_{\rm eff}$, and $\nu_{\rm max}$ just described. In the following we present the results obtained with an alternative scaling relation.

A.1 Stellar mass from the scaling relation involving $\langle\Delta\nu\rangle$ and $\nu_{\rm max}$

In order to test the mass estimations made with Eq. 2.2.1 of Sect. 2.2, we employ the model-based corrected scaling relation (see e.g. Kjeldsen et al. 1995; Gai et al. 2011)

$$\frac{M}{M_\odot} = f_{\Delta\nu}^4 \left(\frac{\rm T_{eff}}{\rm T_{eff,\odot}}\right)^{1.5} \left(\frac{\nu_{\rm max}}{\nu_{\rm max,\odot}}\right)^{3} \left(\frac{\langle\Delta\nu\rangle_\odot}{\langle\Delta\nu\rangle}\right)^{4} \tag{A.1.1}$$

[1] https://www.as.utexas.edu/ chris/moog.html

[2] http://vald.astro.uu.se

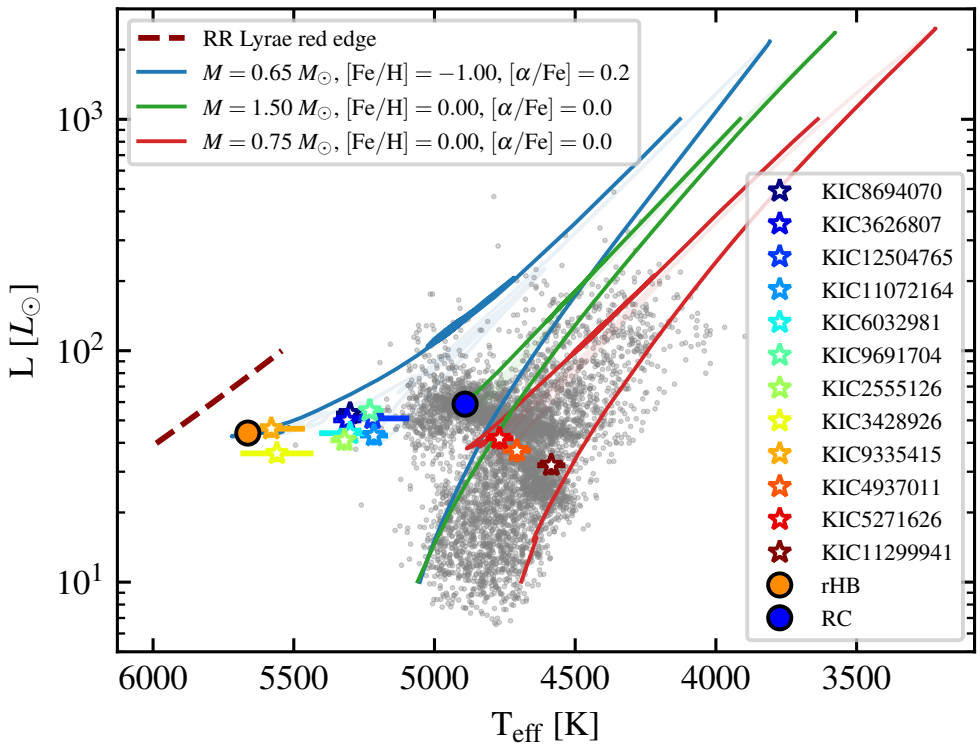

Figure A.1: Same as Fig. 2.2, but including all the CHeB stars in our sample. These stars are colour-coded according to increasing [Fe/H].

for two metal-rich stars (KIC5271626 and KIC4937011) and for two metal-poor stars (KIC6032981 and KIC11072164) of our sample. Here we use the solar reference values of Sect. 2.2 and $\langle\Delta\nu\rangle_\odot = 135.1\ \mu$Hz (Huber et al. 2011). The correction factor, $f_{\Delta\nu}$, on the $\langle\Delta\nu\rangle$ scaling law (Ulrich 1986) is derived with the procedure described in Rodrigues et al. (2017), that is, by using the theoretical radial mode frequencies of stellar models to compute $\langle\Delta\nu\rangle$ from the weighted linear fit of the asymptotic relation (see also Miglio et al. 2021; Tailo et al. 2022). We base the iterative search for the correct $f_{\Delta\nu}$ on evolutionary tracks with the same metallicity (within the errors) as the four stars: solar composition for the metal-rich ones; and [Fe/H] $= -1.00$ with [α/Fe] $= 0.2$ and [α/Fe] $= 0.4$ for the two metal-poor ones (see Appendix B for details on the models). To correct the model-predicted $\langle\Delta\nu\rangle$ for the surface effects, we include the $\langle\Delta\nu\rangle_\odot = 135.3\ \mu$Hz of our solar-calibrated model to the correction factor $f_{\Delta\nu}$ (e.g. White et al. 2011). Finally, we compute the theoretical radial oscillations with the tool `GYRE`. The $f_{\Delta\nu}$ we find are nearly equal to 1.03 and 1.01 for the metal-poor and for the metal-rich stars, respectively. In deriving the masses with Eq. A.1.1, we consider a minimum error of 50 K in $T_{\rm eff}$ (as noted in Appendix A) and an error of 0.01 on $f_{\Delta\nu}$ due to the impossibility of knowing the exact position, at fixed $\nu_{\rm max}$, of our observed stars along the evolutionary tracks. Therefore,

these masses are compatible within the errors with those derived from Eq. 2.2.1. We also note that it is difficult to have a very precise $\langle \Delta\nu \rangle$ estimate for these stars because the radial modes are located in crowded regions (see Appendix C). This leads to systematic errors in the measurement of individual radial modes that can be of the order of 4% by mass.

Appendix B

Grids of stellar models

As mentioned in Sect. 2.3, we choose three sets of stellar parameters to represent a rHB star, a metal-rich low-mass CHeB star, and a RC star. The stellar models at the base of this work belong to a grid of stellar evolutionary models computed with the code `MESA-r11532` (Modules for Experiments in Stellar Astrophysics; Paxton et al. 2011; Paxton et al. 2013; Paxton et al. 2015; Paxton et al. 2016; Paxton et al. 2018; Paxton et al. 2019). In the computation we follow the evolution from the pre-main-sequence phase until the first thermal pulse in the asymptotic giant branch for stellar masses from 0.6 $M_{\odot}$ to 2.00 $M_{\odot}$, with a step of 0.05 $M_{\odot}$. We consider 36 different chemical compositions, with 12 values of [Fe/H] (from -2.5 to 0.25) and three values of alpha-element enhancement: $[\alpha/\mathrm{Fe}] = 0.0$, 0.2, and 0.4. We adopt as a reference solar mixture that from Asplund et al. (2009), and high- and low-temperature radiative opacity tables are computed for these specific metal mixtures, the solar and alpha-enhanced ones. Envelope convection is described by the mixing length theory (Cox et al. 1968); the corresponding α_{MLT} parameter, the same for all the grid, is derived from the solar calibration with the same physics. Below the convective envelope, we add a diffusive undershooting (Herwig 2000) with a size parameter $f = 0.02$ (see Khan et al. 2018). Extra mixing over the convective core limit during the central-He-burning phase is treated following the formalism by Bossini et al. (2017).

Appendix C

Contribution of individual eigenmodes to the PSDs of CHeB stars

In this section we break down the PSDs of our reference models (Fig. 2.5) into the contributions from the modes of different angular degrees. The smoothed PSDs for $\ell = 0, 1, 2, 3$ are shown in Fig. C.1. The smoothing is chosen just for illustration purposes, that is, to resemble a Lorentzian fit of each eigenmode. The modulation around the p-like mode in the dipole modes of the RC star and the higher number of observed mixed modes in the rHB model are evident. Furthermore, the quadrupole modes of the rHB model are less visible than those of the RC model, and its octupole modes resemble a continuous background with small peaks almost coinciding with the radial modes. Finally, we note that the presence, in rHB stars, of $\ell = 1, 2, 3$ modes very close to the radial ones (in some cases almost coinciding; e.g. Fig. C.1) could introduce a non-negligible influence on the analysis of the heights and the linewidths of the $\ell = 0$ modes.

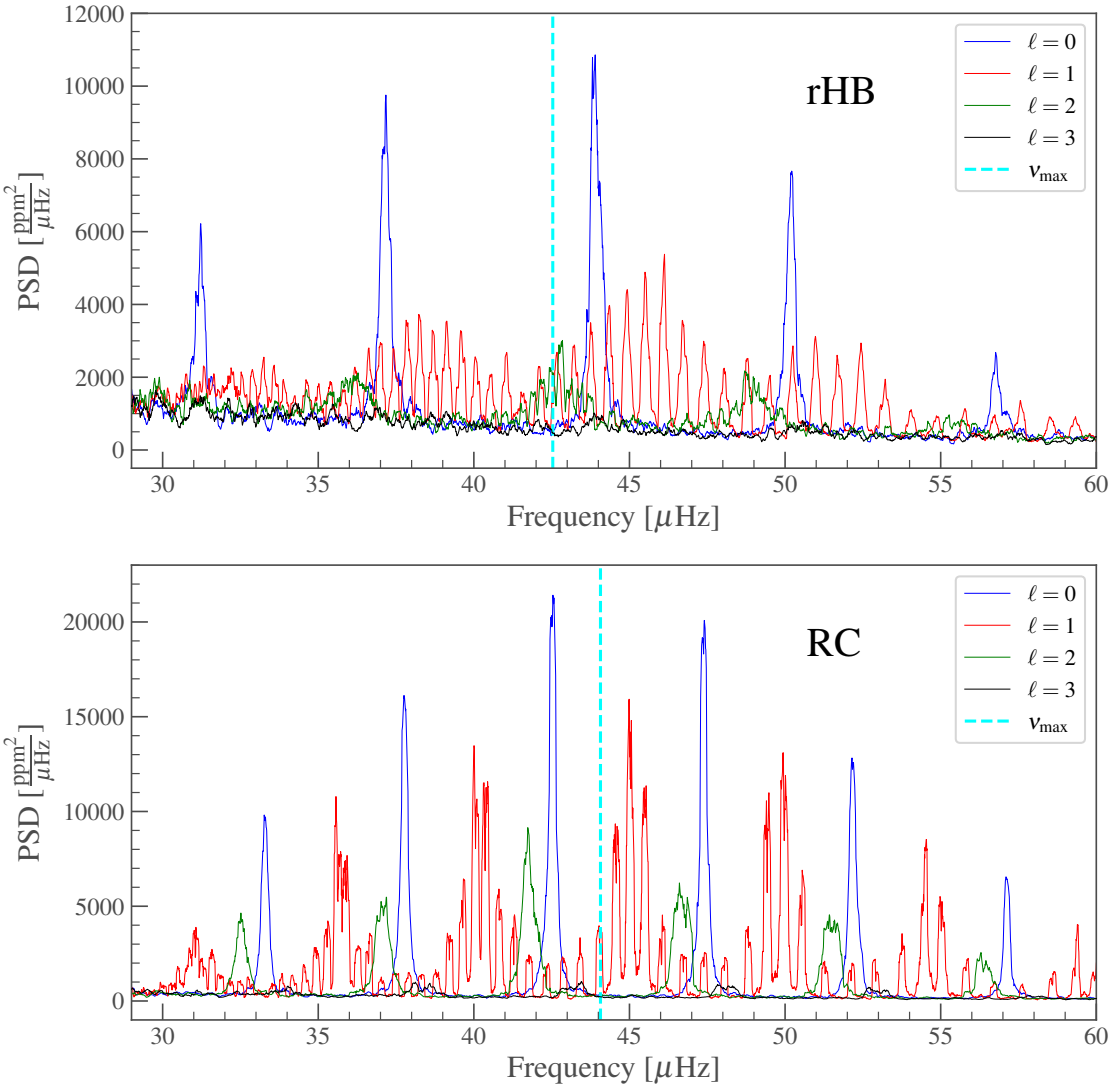

Figure C.1: Smoothed version of the PSDs presented in Sect. 2.4.3. Here we show the individual degrees for the simulated rHB (top) and RC (bottom) stars. The dashed cyan line is the corresponding $\nu_{\max}$.

Appendix D

Likelihood and prior functions

As discussed in Section 3.3.2, we calculate the likelihood function given the current evolutionary phase (CHeB stage), mass ($M_{1,\,\mathrm{obs}} \pm \sigma_{1,\,\mathrm{obs}} = 0.71 \pm 0.08$ $\mathrm{M}_\odot$) and age ($t_{\mathrm{age},\,\mathrm{obs}} \pm \sigma_{\mathrm{age},\,\mathrm{obs}} = 2.38 \pm 0.27$ Gyr) of KIC4937011. We employ the multivariate normal likelihood

$$\mathcal{N}(\mathbf{x}|\boldsymbol{\mu}, \boldsymbol{C}) = \max_{\boldsymbol{t}_{\mathbf{age,\,mod}}} \frac{1}{2\pi\sqrt{|\mathbf{C}|}} \exp\left[-\frac{1}{2}\left(\mathbf{x}-\boldsymbol{\mu}\right)^T \boldsymbol{C}^{-1}\left(\mathbf{x}-\boldsymbol{\mu}\right)\right] \tag{D.0.1}$$

with $\mathbf{x} = [t_{\mathrm{age},\,\mathrm{obs}}; M_{1,\,\mathrm{obs}}]$, $\boldsymbol{\mu} = [\boldsymbol{t}_{\mathbf{age,\,mod}}; \boldsymbol{M}_{\mathbf{1,\,mod}}]$, and $\boldsymbol{C} = \mathrm{diag}(\sigma^2_{\mathrm{age},\,\mathrm{obs}}; \sigma^2_{1,\,\mathrm{obs}})$. It is not possible to univocally associate an age with the CHeB stage, because several ages ($\boldsymbol{t}_{\mathbf{age,\,mod}}$ and the corresponding mass $\boldsymbol{M}_{\mathbf{1,\,mod}}$ are not scalars) correspond to the same evolutionary phase. Therefore, for each evolutionary track we calculate the likelihood corresponding to all ages in the same evolutionary phase and we keep the age that leads to the highest likelihood as a characteristic age to associate at the CHeB stage of that evolutionary track.

In Table D.1 the intervals of the priors. From a comparison with Table 3.2 and 3.3 we can note that three free parameters are well constrained within the intervals. This suggests

Table D.1: Intervals of the priors used in Section 3.3.2. A comparison with Table 3.2 and 3.3 shows that only q_{ZAMS} has a lower bound of the posterior distribution that touches the prior.

Parameter	prior	interval
$\alpha_{\mathrm{ce}} \cdot \lambda_{\mathrm{ce}}$	Uniform	$[0.0, 100.0]$
$\log\left(P_0/\mathrm{days}\right)$	Uniform	$[-10.0, 10.0]$
q_{ZAMS}	Uniform	$[0.08\,\mathrm{M}_\odot/M_{1,\mathrm{ZAMS}}, 1.0]$
$M_{1,\mathrm{ZAMS}}$ $[\mathrm{M}_\odot]$	Chabrier (2003)	$[0.08, \infty)$

that it is not necessary to widen these ranges because we explore the free-parameters space thoroughly. However, q_{ZAMS} has a lower bound of the posterior distribution that touches our chosen prior (see discussion in Section 3.4.1 and 3.4.2).

We also explore the posterior distributions using the same priors and likelihood, but with the Markov Chain Monte Carlo algorithm (MCMC) present in the `emcee` Python package (Foreman-Mackey et al. 2013). We obtain results consistent with Section 3.4.

Appendix E

Taylor series solutions near the centre of barotropic stars

In Section 4.2.2 we discuss the set of differential equations we use to solve the internal structure of a barotropic star knowing the initial conditions. However, we cannot solve the differential equations numerically from the exact centre, because there the term ψ/ξ^2 would lead the Runge-Kutta method to errors. To avoid this problem, we can begin the numerical evaluation of the equations near the centre using Taylor expansions. For simplicity, let us assume for now that $\gamma(\theta) = \gamma_c(\theta/\theta_c)^B$ near the centre of the star. We then obtain

$$\begin{cases} \theta(\xi) = \theta_c - \dfrac{\theta_c^3\xi^2}{6\beta_c\gamma_c} + \dfrac{\theta_c^5\xi^4}{360\beta_c^2\gamma_c^2}\left[13 - 5(B+\gamma_c)\right] + o(\xi^6) \\ \dfrac{d\theta(\xi)}{d\xi} = -\dfrac{\theta_c^3\xi}{3\beta_c\gamma_c} + \dfrac{\theta_c^5\xi^3}{90\beta_c^2\gamma_c^2}\left[13 - 5(B+\gamma_c)\right] + o(\xi^5) \\ \psi(\xi) = \dfrac{\theta_c\xi^3}{3} - \dfrac{\theta_c^3\xi^5}{30\beta_c\gamma_c} + \dfrac{\theta_c^5\xi^7}{2520\beta_c^2\gamma_c^2}\left[13 - 5(B+\gamma_c)\right] + o(\xi^9), \end{cases} \tag{E.0.1}$$

with which we completely solve the numerical issue. Moreover, it can be inferred from equation E.0.1 that, in close proximity to the centre of a barotropic star, $\gamma(r)$ can be regarded as approximately constant. Therefore, very near the centre, the star can be effectively modelled as a polytrope.

Appendix F

Differential equations near the surface of barotropic stars

The set of differential equations we use in Section 4.2.2 creates numerical issues at both the centre of the star (as discussed in Appendix E) and at its surface. The issue observed at the surface arises from the ratio θ^2/β, where both θ and β approach zero. Therefore, it is essential to formulate an alternative set of differential equations that avoids the issue associated with θ^2/β in this region. To achieve this, we introduce a Lane-Emden like variable (ω) defined as

$$\frac{\partial\omega(\theta)}{\partial\theta} := \frac{\beta(\theta)}{\theta^2} \tag{F.0.1}$$

or, equivalently,

$$\omega(\theta) := \omega_c + \int_{\theta_c}^{\theta} \frac{\beta(t)}{t^2}\, dt \ . \tag{F.0.2}$$

The new differential equation we obtain by combining equation 4.2.7 with equation F.0.1 (or equation F.0.2) is

$$\frac{d^2\omega}{d\xi^2} + \left(\frac{d\omega}{d\xi}\right)^2 \frac{1}{\gamma(\omega)}\frac{\partial\gamma(\omega)}{\partial\omega} + \frac{2}{\xi}\frac{d\omega}{d\xi} + \frac{\theta(\omega)}{\gamma(\omega)} = 0, \tag{F.0.3}$$

where the new initial conditions are $\omega(\xi = 0) = \omega_c$ and $\left.\frac{d\omega}{d\xi}\right|_{\xi=0} = 0$. This new equation overcomes the mentioned numerical issue, provided that $\gamma \neq 0$, because as θ approaches zero we do not have to deal with an indeterminate form.

Equation F.0.3 simplifies when $\gamma(\omega)$ is a constant equal to γ_c, because we obtain the Lane-Emden-alike equation

$$\frac{d^2\omega}{d\xi^2} + \frac{2}{\xi}\frac{d\omega}{d\xi} + \frac{\theta(\omega)}{\gamma_c} = 0, \tag{F.0.4}$$

with

$$\beta(\theta) = \beta_c \left(\frac{\theta}{\theta_c}\right)^{\gamma_c}, \tag{F.0.5}$$

and

$$\theta(\omega) = \begin{cases} \left[\dfrac{(\gamma_c - 1)\theta_c^{\gamma_c}}{\beta_c}\omega\right]^{\frac{1}{\gamma_c - 1}} := \phi^{\frac{1}{\gamma_c - 1}}, & \text{for} \quad \gamma_c \neq 1 \\ \theta_c \exp\left(\dfrac{\theta_c}{\beta_c}\omega\right), & \text{for} \quad \gamma_c = 1. \end{cases} \tag{F.0.6}$$

Therefore, equation F.0.4 can be divided into the two differential equations

$$\begin{cases} \dfrac{d^2\phi}{d\xi^2} + \dfrac{2}{\xi}\dfrac{d\phi}{d\xi} + \dfrac{(\gamma_c - 1)\theta_c^{\gamma_c}}{\beta_c \gamma_c}\phi^{\frac{1}{\gamma_c - 1}} = 0, \quad \phi \in [\theta_c^{\gamma_c - 1}, 0], \quad \gamma_c \neq 1 \\ \dfrac{d^2\omega}{d\xi^2} + \dfrac{2}{\xi}\dfrac{d\omega}{d\xi} + \theta_c \exp\left(\dfrac{\theta_c}{\beta_c}\omega\right) = 0, \quad \omega \in [0, -\infty), \quad \gamma_c = 1, \end{cases} \tag{F.0.7}$$

and from $(\phi, \frac{d\phi}{d\xi})$ or $(\omega, \frac{d\omega}{d\xi})$ we can a posteriori evaluate

$$\psi(\xi) = \begin{cases} \dfrac{\beta_c \gamma_c}{(\gamma_c - 1)\theta_c^{\gamma_c}}\left(-\xi^2 \dfrac{d\phi}{d\xi}\right), & \gamma_c \neq 1 \\ -\xi^2 \dfrac{d\omega}{d\xi}, & \gamma_c = 1, \end{cases} \tag{F.0.8}$$

and

$$N^2(\xi) = \begin{cases} 4\pi G \rho_1 \dfrac{\beta_c}{\theta_c^{\gamma_c}\phi(\xi)}\left(\dfrac{\gamma_c}{\gamma_c - 1}\dfrac{d\phi}{d\xi}\right)^2\left(\dfrac{1}{\gamma_c} - \dfrac{1}{\Gamma_1}\right), & \gamma_c \neq 1 \\ 4\pi G \rho_1 \dfrac{\theta_c}{\beta_c}\left(\dfrac{d\omega}{d\xi}\right)^2\left(\dfrac{\Gamma_1 - 1}{\Gamma_1}\right), & \gamma_c = 1. \end{cases} \tag{F.0.9}$$

Appendix G

Numerical solver verification

We validate the numerical solver thanks to known analytical solutions to equation 4.2.7 when $\gamma(\rho) = \gamma_c$ is a constant. One solution is the Plummer sphere (i.e. $\gamma_c = 6/5$), which is

$$\begin{cases} \theta(\xi) = \theta_c \left(1 + \dfrac{\theta_c^2 \xi^2}{18\beta_c}\right)^{-\frac{5}{2}} \\ \beta(\theta) = \beta_c \left(\dfrac{\theta}{\theta_c}\right)^{\frac{6}{5}} = \beta_c \left(1 + \dfrac{\theta_c^2 \xi^2}{18\beta_c}\right)^{-3} \\ \psi(\xi) = \dfrac{\theta_c \xi^3}{3} \left(1 + \dfrac{\theta_c^2 \xi^2}{18\beta_c}\right)^{-\frac{3}{2}}. \end{cases} \tag{G.0.1}$$

Another solution is for $\gamma_c = 2$, which is

$$\begin{cases} \theta(\xi) = \dfrac{\sqrt{2\beta_c}}{\xi} \sin\left(\dfrac{\theta_c \xi}{\sqrt{2\beta_c}}\right) \\ \beta(\theta) = \beta_c \left(\dfrac{\theta}{\theta_c}\right)^2 = \dfrac{2\beta_c^2}{\theta_c^2 \xi^2} \sin^2\left(\dfrac{\theta_c \xi}{\sqrt{2\beta_c}}\right) \\ \psi(\xi) = \dfrac{(2\beta_c)^{\frac{3}{2}}}{\theta_c^2} \left[\sin\left(\dfrac{\theta_c \xi}{\sqrt{2\beta_c}}\right) - \left(\dfrac{\theta_c \xi}{\sqrt{2\beta_c}}\right) \cos\left(\dfrac{\theta_c \xi}{\sqrt{2\beta_c}}\right)\right]. \end{cases} \tag{G.0.2}$$

Appendix H

List of publications and co-authorships

The following publications are the result of work conducted during the PhD, but not presented in this thesis:

- Matteuzzi et al. 2022: *Newcomers and suburbanites can drive the evolution of the size-stellar mass relation of early type galaxies in galaxy clusters*, MNRAS, 513, 3893–3905. At the beginning of my PhD I completed the paper regarding the research done during my master thesis.

- Casali et al. 2023: *Time evolution of Ce as traced by APOGEE using giant stars observed with the Kepler, TESS and K2 missions*, A&A, 677, A60. As a co-author, I helped Giada Casali with the statistical framework of the paper.

- Grisoni et al., 2024: *K2 results for "young" α-rich stars in the Galaxy*, A&A, 683, A111. As a co-author, I helped Valeria Grisoni in developing a statistical framework to start with for the paper, and I helped her in writing the introduction.

- Mucciarelli et al., 2024: *The true nature of HE0057-5959, the most metal-poor Li-rich star*, A&A, 689, A89. As a co-author, I helped Alessio Mucciarelli by analysing the asteroseismic observations of metal-poor Li-rich stars.

- Thomsen et al., submitted to A&A: *Advancing accuracy in age determinations of old-disk stars using an oscillating red giant in an eclipsing binary.* As a co-author, I helped Jeppe S. Thomsen by computing mock observations of power spectral densities of RGB, CHeB and E-AGB stars.

- Casali et al., submitted to MNRAS: *Mapping the Milky Way: Calibrating chemical ages with high-precision Kepler data.* As a co-author, I helped Giada Casali with the observations of red giant stars at the TNG, La Palma.

- Briganti et al., submitted to A&A: *Inferring the efficiency of convective-envelope overshooting in Red Giant Branch stars.* As a co-author, I helped Lorenzo Briganti in developing a statistical framework to start with for the paper.

- Mosser et al., in prep.: *Extra trees in the mixed-mode forest.* As a co-author, I am helping Benoît Mosser by implementing semi-analytical models of low-mass CHeB stars.

- Panier et al., in prep.: *CLES models of core helium burning stars.* As a co-author, I am helping Lucy Panier by implementing semi-analytical models of low-mass CHeB stars.

Bibliography

Abate, C. et al. (Apr. 2013). "Wind Roche-lobe overflow: Application to carbon-enhanced metal-poor stars". In: A&A 552, A26, A26. DOI: 10.1051/0004-6361/201220007. arXiv: 1302.4441 [astro-ph.SR].

Abate, C. et al. (Sept. 2015). "Modelling the observed properties of carbon-enhanced metal-poor stars using binary population synthesis". In: A&A 581, A62, A62. DOI: 10.1051/0004-6361/201526200. arXiv: 1507.04969 [astro-ph.SR].

Abdurro'uf et al. (Apr. 2022). "The Seventeenth Data Release of the Sloan Digital Sky Surveys: Complete Release of MaNGA, MaStar, and APOGEE-2 Data". In: ApJS 259.2, 35, p. 35. DOI: 10.3847/1538-4365/ac4414. arXiv: 2112.02026 [astro-ph.GA].

Aerts, C., J. Christensen-Dalsgaard, and D. W. Kurtz (2010). *Asteroseismology*.

Afşar, M., C. Sneden, and B. -Q. For (July 2012). "Chemical Compositions of Thin-disk, High-metallicity Red Horizontal-branch Field Stars". In: AJ 144.1, 20, p. 20. DOI: 10.1088/0004-6256/144/1/20. arXiv: 1205.3659 [astro-ph.SR].

Afşar, Melike et al. (June 2018). "A Spectroscopic Survey of Field Red Horizontal-branch Stars". In: AJ 155.6, 240, p. 240. DOI: 10.3847/1538-3881/aabe86. arXiv: 1804.04477 [astro-ph.SR].

Aguilera-Gómez, Claudia, Matías I. Jones, and Julio Chanamé (Feb. 2023). "Evidence of extra mixing in field giants as traced by the lithium and carbon isotope ratio". In: A&A 670, A73, A73. DOI: 10.1051/0004-6361/202244518. arXiv: 2207.08905 [astro-ph.SR].

Aguilera-Gómez, Claudia et al. (Dec. 2016a). "On Lithium-rich Red Giants: Engulfment on the Giant Branch of Trumpler 20". In: ApJ 833.2, L24, p. L24. DOI: 10.3847/2041-8213/833/2/L24. arXiv: 1609.07492 [astro-ph.SR].

— (Oct. 2016b). "On Lithium-rich Red Giants. I. Engulfment of Substellar Companions". In: ApJ 829.2, 127, p. 127. DOI: 10.3847/0004-637X/829/2/127. arXiv: 1605.05332 [astro-ph.SR].

Ahumada, Romina et al. (July 2020). "The 16th Data Release of the Sloan Digital Sky Surveys: First Release from the APOGEE-2 Southern Survey and Full Release of eBOSS Spectra". In: ApJS 249.1, 3, p. 3. DOI: 10.3847/1538-4365/ab929e. arXiv: 1912.02905 [astro-ph.GA].

Anders, F. et al. (Sept. 2016). "Galactic Archaeology with CoRoT and APOGEE: Creating mock observations from a chemodynamical model". In: *Astronomische Nachrichten* 337.8-9, p. 926. DOI: 10.1002/asna.201612400. arXiv: 1604.07771 [astro-ph.GA].

Angulo, C. et al. (Aug. 1999). "A compilation of charged-particle induced thermonuclear reaction rates". In: Nucl. Phys. A 656.1, pp. 3–183. DOI: 10.1016/S0375-9474(99)00030-5.

Anthony-Twarog, Barbara J., Constantine P. Deliyannis, and Bruce A. Twarog (Sept. 2014). "A uvbyCaHβ Analysis of the Old Open Cluster, NGC 6819". In: AJ 148.3, 51, p. 51. DOI: 10.1088/0004-6256/148/3/51. arXiv: 1406.4787 [astro-ph.SR].

Anthony-Twarog, Barbara J. et al. (Apr. 2013). "A Lithium-rich Red Giant Below the Clump in the Kepler Cluster, NGC 6819". In: ApJ 767.1, L19, p. L19. DOI: 10.1088/2041-8205/767/1/L19. arXiv: 1303.2984 [astro-ph.SR].

Armandroff, Taft E. (Aug. 1988). "Color-Magnitude Diagrams for Six Metal-Rich, Low-Latitude Globular Clusters". In: AJ 96, p. 588. DOI: 10.1086/114833.

Ashwell, Johanna F. et al. (Oct. 2005). "Beryllium enhancement as evidence for accretion in a lithium-rich F dwarf". In: MNRAS 363.1, pp. L81–L85. DOI: 10.1111/j.1745-3933.2005.00090.x. arXiv: astro-ph/0508125 [astro-ph].

Asplund, Martin et al. (Sept. 2009). "The Chemical Composition of the Sun". In: ARA&A 47.1, pp. 481–522. DOI: 10.1146/annurev.astro.46.060407.145222. arXiv: 0909.0948 [astro-ph.SR].

Auner, G. (Feb. 1974). "Photographic photometry of the Galactic Cluster NGC 6819". In: A&AS 13, p. 143.

Babusiaux, C. et al. (June 2023). "Gaia Data Release 3. Catalogue validation". In: A&A 674, A32, A32. DOI: 10.1051/0004-6361/202243790. arXiv: 2206.05989 [astro-ph.SR].

Badnell, N. R. et al. (June 2005). "Updated opacities from the Opacity Project". In: MNRAS 360.2, pp. 458–464. DOI: 10.1111/j.1365-2966.2005.08991.x. arXiv: astro-ph/0410744 [astro-ph].

Ball, Warrick H. and L. Gizon (Apr. 2017). "Surface-effect corrections for oscillation frequencies of evolved stars". In: A&A 600, A128, A128. DOI: 10.1051/0004-6361/201630260. arXiv: 1702.02570 [astro-ph.SR].

Ball, Warrick H. et al. (Dec. 2018). "A Synthetic Sample of Short-cadence Solar-like Oscillators for TESS". In: ApJS 239.2, 34, p. 34. DOI: 10.3847/1538-4365/aaedbc. arXiv: 1809.09108 [astro-ph.SR].

Balmforth, N. J. and D. O. Gough (Oct. 1990). "Effluent Stellar Pulsation". In: ApJ 362, p. 256. DOI: 10.1086/169262.

Basu, Sarbani et al. (Mar. 2011). "Sounding Open Clusters: Asteroseismic Constraints from Kepler on the Properties of NGC 6791 and NGC 6819". In: ApJ 729.1, L10, p. L10. DOI: 10.1088/2041-8205/729/1/L10. arXiv: 1102.2231 [astro-ph.SR].

Beck, Paul G. et al. (Apr. 2011). "Kepler Detected Gravity-Mode Period Spacings in a Red Giant Star". In: *Science* 332.6026, p. 205. DOI: 10.1126/science.1201939.

Beck, Paul G. et al. (Jan. 2012). "Fast core rotation in red-giant stars as revealed by gravity-dominated mixed modes". In: Nature 481.7379, pp. 55–57. DOI: 10.1038/nature10612. arXiv: 1112.2825 [astro-ph.SR].

Bedding, Timothy R. et al. (Mar. 2011). "Gravity modes as a way to distinguish between hydrogen- and helium-burning red giant stars". In: Nature 471.7340, pp. 608–611. DOI: 10.1038/nature09935. arXiv: 1103.5805 [astro-ph.SR].

Bedin, L. R. et al. (Apr. 2015). "Hubble Space Telescope observations of the Kepler-field cluster NGC 6819 - I. The bottom of the white dwarf cooling sequence". In: MNRAS 448.2, pp. 1779–1788. DOI: 10.1093/mnras/stv069. arXiv: 1501.02953 [astro-ph.SR].

Belloni, Diogo, Matthias R. Schreiber, and Monica Zorotovic (July 2024). "Formation of long-period post-common-envelope binaries. II. Explaining the self-lensing binary KOI 3278". In: A&A 687, A12, A12. DOI: 10.1051/0004-6361/202449320. arXiv: 2401.17510 [astro-ph.SR].

Bobrick, Alexey et al. (Feb. 2024). "RR Lyrae from binary evolution: abundant, young, and metal-rich". In: MNRAS 527.4, pp. 12196–12218. DOI: 10.1093/mnras/stad3996. arXiv: 2208.04332 [astro-ph.SR].

Borucki, William J. et al. (Feb. 2010). "Kepler Planet-Detection Mission: Introduction and First Results". In: *Science* 327.5968, p. 977. DOI: 10.1126/science.1185402.

Bossini, Diego et al. (Nov. 2015). "Uncertainties on near-core mixing in red-clump stars: effects on the period spacing and on the luminosity of the AGB bump". In: MNRAS 453.3, pp. 2290–2301. DOI: 10.1093/mnras/stv1738. arXiv: 1507.07797 [astro-ph.SR].

Bossini, Diego et al. (Aug. 2017). "Kepler red-clump stars in the field and in open clusters: constraints on core mixing". In: MNRAS 469.4, pp. 4718–4725. DOI: 10.1093/mnras/stx1135. arXiv: 1705.03077 [astro-ph.GA].

Boubert, D. et al. (Sept. 2017a). "Binary companions of nearby supernova remnants found with Gaia". In: A&A 606, A14, A14. DOI: 10.1051/0004-6361/201731142. arXiv: 1704.05900 [astro-ph.SR].

Boubert, D. et al. (Aug. 2017b). "Hypervelocity runaways from the Large Magellanic Cloud". In: MNRAS 469.2, pp. 2151–2162. DOI: 10.1093/mnras/stx848. arXiv: 1704.01373 [astro-ph.GA].

Bragaglia, Angela et al. (Jan. 2001). "Metal Abundances of Red Clump Stars in Open Clusters. I. NGC 6819". In: AJ 121.1, pp. 327–336. DOI: 10.1086/318042. arXiv: astro-ph/0009321 [astro-ph].

Bressan, A., G. Bertelli, and C. Chiosi (Jan. 1986). "Evolution of low mass stars with convective overshooting." In: Mem. Soc. Astron. Italiana 57, pp. 411–426.

Brewer, Lauren N. et al. (Mar. 2016). "Determining the Age of the Kepler Open Cluster NGC 6819 With a New Triple System and Other Eclipsing Binary Stars". In: AJ 151.3, 66, p. 66. DOI: 10.3847/0004-6256/151/3/66. arXiv: 1601.04069 [astro-ph.SR].

Brogaard, K. et al. (Sept. 2016). "Testing asteroseismic scaling relations using eclipsing binaries in star clusters and the field". In: *Astronomische Nachrichten* 337.8-9, p. 793. DOI: 10.1002/asna.201612374. arXiv: 1601.01412 [astro-ph.SR].

Brogaard, K. et al. (Dec. 2018). "The blue straggler V106 in NGC 6791: a prototype progenitor of old single giants masquerading as young". In: MNRAS 481.4, pp. 5062–5072. DOI: 10.1093/mnras/sty2504. arXiv: 1809.00705 [astro-ph.SR].

Brogaard, K. et al. (Oct. 2021). "Asteroseismology of overmassive, undermassive, and potential past members of the open cluster NGC 6791". In: MNRAS 507.1, pp. 496–509. DOI: 10.1093/mnras/stab2183. arXiv: 2108.03869 [astro-ph.SR].

Burkhead, M. S. (Apr. 1971). "Photometric observations of the star cluster NGC 6819." In: AJ 76, pp. 251–259. DOI: 10.1086/111113.

Cameron, A. G. W. and W. A. Fowler (Feb. 1971). "Lithium and the s-PROCESS in Red-Giant Stars". In: ApJ 164, p. 111. DOI: 10.1086/150821.

Carlberg, Joleen K. et al. (Mar. 2015). "The Puzzling Li-rich Red Giant Associated with NGC 6819". In: ApJ 802.1, 7, p. 7. DOI: 10.1088/0004-637X/802/1/7. arXiv: 1501.05625 [astro-ph.SR].

Casagrande, L. and Don A. VandenBerg (Oct. 2014). "Synthetic stellar photometry - I. General considerations and new transformations for broad-band systems". In: MNRAS 444.1, pp. 392–419. DOI: 10.1093/mnras/stu1476. arXiv: 1407.6095 [astro-ph.SR].

— (Sept. 2018). "On the use of Gaia magnitudes and new tables of bolometric corrections". In: MNRAS 479.1, pp. L102–L107. DOI: 10.1093/mnrasl/sly104. arXiv: 1806.01953 [astro-ph.SR].

Casagrande, Luca, Victor Silva Aguirre, and Aldo M. Serenelli (Jan. 2016). "Asteroseismology for Galactic archaeology: bridging two fields". In: *IAU Focus Meeting* 29B, pp. 680–685. DOI: 10.1017/S1743921316006347.

Cassisi, Santi, Maurizio Salaris, and Alan W. Irwin (May 2003). "The Initial Helium Content of Galactic Globular Cluster Stars from the R-Parameter: Comparison with the Cosmic Microwave Background Constraint". In: ApJ 588.2, pp. 862–870. DOI: 10.1086/374218. arXiv: astro-ph/0301378 [astro-ph].

Castellani, V., P. Giannone, and A. Renzini (Mar. 1971a). "Induced Semi-Convection in Helium-Burning Horizontal-Branch Stars II". In: Ap&SS 10.3, pp. 355–362. DOI: 10.1007/BF00649680.

— (Feb. 1971b). "Overshooting of Convective Cores in Helium-Burning Horizontal-Branch Stars". In: Ap&SS 10.2, pp. 340–349. DOI: 10.1007/BF00704092.

Catelan, M. (Apr. 2009). "Horizontal branch stars: the interplay between observations and theory, and insights into the formation of the Galaxy". In: Ap&SS 320, pp. 261–309. DOI: 10.1007/s10509-009-9987-8. arXiv: astro-ph/0507464 [astro-ph].

Chabrier, Gilles (July 2003). "Galactic Stellar and Substellar Initial Mass Function". In: PASP 115.809, pp. 763–795. DOI: 10.1086/376392. arXiv: astro-ph/0304382 [astro-ph].

Chamandy, Luke et al. (Dec. 2019). "How drag force evolves in global common envelope simulations". In: MNRAS 490.3, pp. 3727–3739. DOI: 10.1093/mnras/stz2813. arXiv: 1908.06195 [astro-ph.SR].

Chan, K. L. and S. Sofia (Aug. 1986). "Turbulent Compressible Convection in a Deep Atmosphere. III. Tests on the Validity and Limitation of the Numerical Approach". In: ApJ 307, p. 222. DOI: 10.1086/164409.

Chandrasekhar, S. (Oct. 1963). "Letter to the Editor: a General Variational Principle Governing the Radial and the Non-Radial Oscillations of Gaseous Masses." In: ApJ 138, p. 896. DOI: 10.1086/147694.

— (Feb. 1964). "A General Variational Principle Governing the Radial and the Non-Radial Oscillations of Gaseous Masses." In: ApJ 139, p. 664. DOI: 10.1086/147792.

Chaplin, W. J. et al. (June 2009). "Mode lifetimes of stellar oscillations. Implications for asteroseismology". In: A&A 500.2, pp. L21–L24. DOI: 10.1051/0004-6361/200911952. arXiv: 0905.1722 [astro-ph.SR].

Chaplin, William J. and Andrea Miglio (Aug. 2013). "Asteroseismology of Solar-Type and Red-Giant Stars". In: ARA&A 51.1, pp. 353–392. DOI: 10.1146/annurev-astro-082812-140938. arXiv: 1303.1957 [astro-ph.SR].

Chen, Y. Q. et al. (Aug. 2010). "Metallicity and Kinematic Distributions of Red Horizontal-branch Stars from the SDSS Survey". In: AJ 140.2, pp. 500–509. DOI: 10.1088/0004-6256/140/2/500. arXiv: 1110.1789 [astro-ph.SR].

Chen, Y. Q. et al. (Dec. 2011). "The Metallicity Gradient of the Thick Disk Based on Red Horizontal-branch Stars from SDSS DR8". In: AJ 142.6, 184, p. 184. DOI: 10.1088/0004-6256/142/6/184. arXiv: 1110.1782 [astro-ph.SR].

Chiappini, C. et al. (Apr. 2015). "Young [α/Fe]-enhanced stars discovered by CoRoT and APOGEE: What is their origin?" In: A&A 576, L12, p. L12. DOI: 10.1051/0004-6361/201525865. arXiv: 1503.06990 [astro-ph.SR].

Chieffi, Alessandro and Marco Limongi (June 2004). "Explosive Yields of Massive Stars from Z = 0 to Z = Z_{solar}". In: ApJ 608.1, pp. 405–410. DOI: 10.1086/392523. arXiv: astro-ph/0402625 [astro-ph].

Christensen-Dalsgaard, J. (Jan. 1991). "Some aspects of the theory of solar oscillations". In: *Geophysical and Astrophysical Fluid Dynamics* 62.1, pp. 123–152. DOI: 10.1080/03091929108229129.

Christensen-Dalsgaard, J. et al. (June 2011). "A more realistic representation of overshoot at the base of the solar convective envelope as seen by helioseismology". In: MNRAS 414.2, pp. 1158–1174. DOI: 10.1111/j.1365-2966.2011.18460.x. arXiv: 1102.0235 [astro-ph.SR].

Christensen-Dalsgaard, Jørgen (Nov. 2002). "Helioseismology". In: *Reviews of Modern Physics* 74.4, pp. 1073–1129. DOI: 10.1103/RevModPhys.74.1073. arXiv: astro-ph/0207403 [astro-ph].

Claeys, J. S. W. et al. (Mar. 2014). "Theoretical uncertainties of the Type Ia supernova rate". In: A&A 563, A83, A83. DOI: 10.1051/0004-6361/201322714. arXiv: 1401.2895 [astro-ph.SR].

Clausen, Drew and Richard A. Wade (June 2011). "How to Make a Singleton sdB Star via Accelerated Stellar Evolution". In: ApJ 733.2, L42, p. L42. DOI: 10.1088/2041-8205/733/2/L42.

Colgan, J. et al. (Feb. 2016). "A New Generation of Los Alamos Opacity Tables". In: ApJ 817.2, 116, p. 116. DOI: 10.3847/0004-637X/817/2/116. arXiv: 1601.01005 [astro-ph.SR].

Constantino, Thomas et al. (Sept. 2015). "The treatment of mixing in core helium burning models - I. Implications for asteroseismology". In: MNRAS 452.1, pp. 123–145. DOI: 10.1093/mnras/stv1264. arXiv: 1506.01209 [astro-ph.SR].

Cowling, T. G. (Jan. 1941). "The non-radial oscillations of polytropic stars". In: MNRAS 101, p. 367. DOI: 10.1093/mnras/101.8.367.

Cox, J. P. and R. T. Giuli (1968). *Principles of stellar structure.*

Cunha, M. S. et al. (June 2015). "Structural Glitches near the Cores of Red Giants Revealed by Oscillations in g-mode Period Spacings from Stellar Models". In: ApJ 805.2, 127, p. 127. DOI: 10.1088/0004-637X/805/2/127. arXiv: 1503.09085 [astro-ph.SR].

Cunha, M. S. et al. (Nov. 2019). "Analytical modelling of period spacings across the HR diagram". In: MNRAS 490.1, pp. 909–926. DOI: 10.1093/mnras/stz2582. arXiv: 1909.04966 [astro-ph.SR].

Cunha, Margarida S. (Jan. 2020). "Diagnostics from Solar and Stellar Glitches". In: *Dynamics of the Sun and Stars; Honoring the Life and Work of Michael J. Thompson.* Ed. by Mário J. P. F. G. Monteiro et al. Vol. 57. Astrophysics and Space Science Proceedings, pp. 185–196. DOI: 10.1007/978-3-030-55336-4_26. arXiv: 2109.03674 [astro-ph.SR].

Cunha, Margarida S. et al. (July 2024). "Buoyancy glitches in pulsating stars revisited". In: A&A 687, A100, A100. DOI: 10.1051/0004-6361/202348681. arXiv: 2404.12992 [astro-ph.SR].

Davies, G. R. and A. Miglio (Sept. 2016). "Asteroseismology of red giants: From analysing light curves to estimating ages". In: *Astronomische Nachrichten* 337.8-9, p. 774. DOI: 10.1002/asna.201612371. arXiv: 1601.02802 [astro-ph.SR].

Davis, P. J., U. Kolb, and C. Knigge (Jan. 2012). "Is the common envelope ejection efficiency a function of the binary parameters?" In: MNRAS 419.1, pp. 287–303. DOI: 10.1111/j.1365-2966.2011.19690.x. arXiv: 1106.4741 [astro-ph.SR].

de Kool, M. (July 1990). "Common Envelope Evolution and Double Cores of Planetary Nebulae". In: ApJ 358, p. 189. DOI: 10.1086/168974.

De Marco, Orsola and Robert G. Izzard (Jan. 2017). "Dawes Review 6: The Impact of Companions on Stellar Evolution". In: PASA 34, e001, e001. DOI: 10.1017/pasa.2016.52. arXiv: 1611.03542 [astro-ph.SR].

De Marco, Orsola et al. (Mar. 2011). "On the α formalism for the common envelope interaction". In: MNRAS 411.4, pp. 2277–2292. DOI: 10.1111/j.1365-2966.2010.17891.x. arXiv: 1010.4374 [astro-ph.SR].

de Mink, S. E. et al. (Feb. 2013). "The Rotation Rates of Massive Stars: The Role of Binary Interaction through Tides, Mass Transfer, and Mergers". In: ApJ 764.2, 166, p. 166. DOI: 10.1088/0004-637X/764/2/166. arXiv: 1211.3742 [astro-ph.SR].

De Ridder, Joris et al. (May 2009). "Non-radial oscillation modes with long lifetimes in giant stars". In: Nature 459.7245, pp. 398–400. DOI: 10.1038/nature08022.

deBoer, R. J. et al. (July 2017). "The ^{12}C(α ,γ)^{16}O reaction and its implications for stellar helium burning". In: *Reviews of Modern Physics* 89.3, 035007, p. 035007. DOI: 10.1103/RevModPhys.89.035007. arXiv: 1709.03144 [nucl-ex].

Deheuvels, S. and K. Belkacem (Dec. 2018). "Seismic characterization of red giants going through the helium-core flash". In: A&A 620, A43, A43. DOI: 10.1051/0004-6361/201833409. arXiv: 1808.09458 [astro-ph.SR].

Deheuvels, S. et al. (Apr. 2014). "Seismic constraints on the radial dependence of the internal rotation profiles of six Kepler subgiants and young red giants". In: A&A 564, A27, A27. DOI: 10.1051/0004-6361/201322779. arXiv: 1401.3096 [astro-ph.SR].

Deheuvels, S. et al. (Aug. 2015). "Seismic evidence for a weak radial differential rotation in intermediate-mass core helium burning stars". In: A&A 580, A96, A96. DOI: 10.1051/0004-6361/201526449. arXiv: 1506.02704 [astro-ph.SR].

Deheuvels, S. et al. (May 2016). "Measuring the extent of convective cores in low-mass stars using Kepler data: toward a calibration of core overshooting". In: A&A 589, A93, A93. DOI: 10.1051/0004-6361/201527967. arXiv: 1603.02332 [astro-ph.SR].

Denissenkov, Pavel A. (Nov. 2010). "Numerical Simulations of Thermohaline Convection: Implications for Extra-mixing in Low-mass RGB Stars". In: ApJ 723.1, pp. 563–579. DOI: 10.1088/0004-637X/723/1/563. arXiv: 1006.5481 [astro-ph.SR].

Denissenkov, Pavel A. and Falk Herwig (Sept. 2004). "Enhanced Extra Mixing in Low-Mass Red Giants: Lithium Production and Thermal Stability". In: ApJ 612.2, pp. 1081–1091. DOI: 10.1086/422575.

Deubner, Franz-Ludwig and Douglas Gough (Jan. 1984). "Helioseismology: Oscillations as a Diagnostic of the Solar Interior". In: ARA&A 22, pp. 593–619. DOI: 10.1146/annurev.aa.22.090184.003113.

Dewi, J. D. M. and T. M. Tauris (Aug. 2000). "On the energy equation and efficiency parameter of the common envelope evolution". In: A&A 360, pp. 1043–1051. DOI: 10.48550/arXiv.astro-ph/0007034. arXiv: astro-ph/0007034 [astro-ph].

Dewi, Jasinta D. M. and Thomas M. Tauris (Jan. 2001). "On the λ-Parameter of the Common Envelope Evolution". In: *Evolution of Binary and Multiple Star Systems*. Ed. by Ph. Podsiadlowski et al. Vol. 229. Astronomical Society of the Pacific Conference Series, p. 255.

Dupret, M. -A. et al. (Oct. 2009). "Theoretical amplitudes and lifetimes of non-radial solar-like oscillations in red giants". In: A&A 506.1, pp. 57–67. DOI: 10.1051/0004-6361/200911713. arXiv: 0906.3951 [astro-ph.SR].

Eckart, Carl and J. Gillis (1960). "Hydrodynamics of oceans and atmospheres". In: URL: https://api.semanticscholar.org/CorpusID:121134770.

Ehrenfest, P. (July 1927). "Bemerkung über die angenäherte Gültigkeit der klassischen Mechanik innerhalb der Quantenmechanik". In: *Zeitschrift für Physik* 45, pp. 455–457. DOI: 10.1007/BF01329203.

Érgma, É. (Aug. 1971). "Density Inversion in the Convective Envelopes of Stars." In: Soviet Ast. 15, p. 51.

Fick, Adolf (Jan. 1855). "Ueber Diffusion". In: *Annalen der Physik* 170.1, pp. 59–86. DOI: 10.1002/andp.18551700105.

Foreman-Mackey, Daniel et al. (Mar. 2013). "emcee: The MCMC Hammer". In: PASP 125.925, p. 306. DOI: 10.1086/670067. arXiv: 1202.3665 [astro-ph.IM].

Fynbo, Hans O. U. et al. (Jan. 2005). "Revised rates for the stellar triple-α process from measurement of ^{12}C nuclear resonances". In: Nature 433.7022, pp. 136–139.

Gabriel, M. and R. Scuflaire (Jan. 1979). "Properties of non-radial stellar oscillations." In: Acta Astron. 29.1, pp. 135–149.

Gabriel, M. et al. (Sept. 2014). "Proper use of Schwarzschild Ledoux criteria in stellar evolution computations". In: A&A 569, A63, A63. DOI: 10.1051/0004-6361/201423442. arXiv: 1405.0128 [astro-ph.SR].

Gai, Ning et al. (Apr. 2011). "An In-depth Study of Grid-based Asteroseismic Analysis". In: ApJ 730.2, 63, p. 63. DOI: 10.1088/0004-637X/730/2/63. arXiv: 1009.3018 [astro-ph.SR].

Gaia Collaboration et al. (Nov. 2016). "The Gaia mission". In: A&A 595, A1, A1. DOI: 10.1051/0004-6361/201629272. arXiv: 1609.04153 [astro-ph.IM].

Gaia Collaboration et al. (June 2023). "Gaia Data Release 3. Summary of the content and survey properties". In: A&A 674, A1, A1. DOI: 10.1051/0004-6361/202243940. arXiv: 2208.00211 [astro-ph.GA].

García, Rafael A. and Jérôme Ballot (Sept. 2019). "Asteroseismology of solar-type stars". In: *Living Reviews in Solar Physics* 16.1, 4, p. 4. DOI: 10.1007/s41116-019-0020-1. arXiv: 1906.12262 [astro-ph.SR].

Girardi, Léo (Sept. 2016). "Red Clump Stars". In: ARA&A 54, pp. 95–133. DOI: 10.1146/annurev-astro-081915-023354.

Goldstein, J. and R. H. D. Townsend (Aug. 2020). "The Contour Method: a New Approach to Finding Modes of Nonadiabatic Stellar Pulsations". In: ApJ 899.2, 116, p. 116. DOI: 10.3847/1538-4357/aba748. arXiv: 2006.13223 [astro-ph.SR].

Gough, D. O. (Jan. 1993). "Linear adiabatic stellar pulsation." In: *Astrophysical Fluid Dynamics - Les Houches 1987*. Ed. by J. -P. Zahn and J. Zinn-Justin, pp. 399–560.

— (1996). "TESTING SOLAR MODELS: THE INVERSE PROBLEM". In: *The Structure of the Sun*. Ed. by T. Roca Cortes and FranciscoEditors Sanchez. Cambridge University Press, pp. 141–230.

— (Mar. 2007). "An elementary introduction to the JWKB approximation". In: *Astronomische Nachrichten* 328.3, p. 273. DOI: 10.1002/asna.200610730. arXiv: astro-ph/0702201 [astro-ph].

Gratton, R. G. et al. (July 2010). "The second and third parameters of the horizontal branch in globular clusters". In: A&A 517, A81, A81. DOI: 10.1051/0004-6361/200912572. arXiv: 1004.3862 [astro-ph.SR].

Green, Gregory M. et al. (Dec. 2019). "A 3D Dust Map Based on Gaia, Pan-STARRS 1, and 2MASS". In: ApJ 887.1, 93, p. 93. DOI: 10.3847/1538-4357/ab5362. arXiv: 1905.02734 [astro-ph.GA].

Grevesse, N. and A. Noels (Jan. 1993). "Cosmic abundances of the elements." In: *Origin and Evolution of the Elements*. Ed. by N. Prantzos, E. Vangioni-Flam, and M. Casse, pp. 15–25.

Grevesse, Nicolas and Edward Anders (Jan. 1989). "Solar-system abundances of the elements: A new table". In: *Cosmic Abundances of Matter*. Ed. by C. Jake Waddington. Vol. 183. American Institute of Physics Conference Series, pp. 1–8. DOI: 10.1063/1.38013.

Grisoni, V. et al. (Mar. 2024). "K2 results for "young" α-rich stars in the Galaxy". In: A&A 683, A111, A111. DOI: 10.1051/0004-6361/202347440. arXiv: 2312.07091 [astro-ph.GA].

Guandalini, R. et al. (Sept. 2009). "Extra-Mixing in Luminous Cool Red Giants: Hints from Evolved Stars With and Without Li". In: PASA 26.3, pp. 168–175. DOI: 10.1071/AS08063. arXiv: 0905.4458 [astro-ph.SR].

Gustafsson, B. et al. (Aug. 2008). "A grid of MARCS model atmospheres for late-type stars. I. Methods and general properties". In: A&A 486.3, pp. 951–970. DOI: 10.1051/0004-6361:200809724. arXiv: 0805.0554 [astro-ph].

Hagihara, Yusuke (1970). *Celestial mechanics. Vol.1: Dynamical principles and transformation theory.*

Halbwachs, Jean-Louis et al. (June 2023). "Gaia Data Release 3. Astrometric binary star processing". In: A&A 674, A9, A9. DOI: 10.1051/0004-6361/202243969. arXiv: 2206.05726 [astro-ph.SR].

Hammer, J. W. et al. (Apr. 2005). "New determination of the ^{12}C(α, γ) ^{16}O reaction rate from γ-ray angular distribution measurements". In: Nucl. Phys. A 752, pp. 514–521. DOI: 10.1016/j.nuclphysa.2005.02.056.

Han, Z., P. Podsiadlowski, and P. P. Eggleton (Sept. 1994). "A possible criterion for envelope ejection in asymptotic giant branch or first giant branch stars." In: MNRAS 270, pp. 121–130. DOI: 10.1093/mnras/270.1.121.

Handberg, R. et al. (Nov. 2017). "NGC 6819: testing the asteroseismic mass scale, mass loss and evidence for products of non-standard evolution". In: MNRAS 472.1, pp. 979–997. DOI: 10.1093/mnras/stx1929. arXiv: 1707.08223 [astro-ph.SR].

Harpaz, A. (Oct. 1984). "Density inversion in a red giant envelope". In: MNRAS 210, pp. 633–639. DOI: 10.1093/mnras/210.3.633.

Hatta, Yoshiki (June 2023). "Semi-analytical Expression of G-mode Period Spacing: The Case of Brunt-Väisälä Frequency with Not a Jump but a Ramp". In: ApJ 950.2, 165, p. 165. DOI: 10.3847/1538-4357/acd4b9. arXiv: 2305.06840 [astro-ph.SR].

Hekker, S. et al. (Jan. 2011). "Solar-like oscillations in red giants observed with Kepler: comparison of global oscillation parameters from different methods". In: A&A 525, A131, A131. DOI: 10.1051/0004-6361/201015185. arXiv: 1008.2959 [astro-ph.SR].

Hekker, Saskia and Jennifer A. Johnson (Aug. 2019). "Origin of α-rich young stars: clues from C, N, and O". In: MNRAS 487.3, pp. 4343–4354. DOI: 10.1093/mnras/stz1554. arXiv: 1906.10830 [astro-ph.SR].

Hendriks, D. D. and R. G. Izzard (2023). "binary_c-python: A Python-based stellar population synthesis tool and interface to binary_c". In: *Journal of Open Source Software* 8.85, p. 4642. DOI: 10.21105/joss.04642. URL: https://doi.org/10.21105/joss.04642.

Herwig, F. (Aug. 2000). "The evolution of AGB stars with convective overshoot". In: A&A 360, pp. 952–968. DOI: 10.48550/arXiv.astro-ph/0007139. arXiv: astro-ph/0007139 [astro-ph].

Hidalgo, Sebastian L. et al. (Apr. 2018). "The Updated BaSTI Stellar Evolution Models and Isochrones. I. Solar-scaled Calculations". In: ApJ 856.2, 125, p. 125. DOI: 10.3847/1538-4357/aab158. arXiv: 1802.07319 [astro-ph.GA].

Hole, K. Tabetha et al. (July 2009). "WIYN Open Cluster Study. XXIV. Stellar Radial-Velocity Measurements in NGC 6819". In: AJ 138.1, pp. 159–168. DOI: 10.1088/0004-6256/138/1/159. arXiv: 0902.4040 [astro-ph.SR].

Houdek, Günter and Marc-Antoine Dupret (Dec. 2015). "Interaction Between Convection and Pulsation". In: *Living Reviews in Solar Physics* 12.1, 8, p. 8. DOI: 10.1007/lrsp-2015-8. arXiv: 1601.03913 [astro-ph.SR].

Howell, Madeline et al. (Sept. 2022). "Integrated mass-loss of evolved stars in M4 using asteroseismology". In: MNRAS 515.3, pp. 3184–3198. DOI: 10.1093/mnras/stac1918. arXiv: 2207.02406 [astro-ph.SR].

— (Jan. 2024). "First asteroseismic analysis of the globular cluster M80: multiple populations and stellar mass-loss". In: MNRAS 527.3, pp. 7974–7993. DOI: 10.1093/mnras/stad3565. arXiv: 2307.07158 [astro-ph.SR].

Howell, Steve B. et al. (Apr. 2014). "The K2 Mission: Characterization and Early Results". In: PASP 126.938, p. 398. DOI: 10.1086/676406. arXiv: 1402.5163 [astro-ph.IM].

Huber, D. et al. (Dec. 2011). "Testing Scaling Relations for Solar-like Oscillations from the Main Sequence to Red Giants Using Kepler Data". In: ApJ 743.2, 143, p. 143. DOI: 10.1088/0004-637X/743/2/143. arXiv: 1109.3460 [astro-ph.SR].

Hurley, Jarrod R., Onno R. Pols, and Christopher A. Tout (July 2000). "Comprehensive analytic formulae for stellar evolution as a function of mass and metallicity". In: MNRAS 315.3, pp. 543–569. DOI: 10.1046/j.1365-8711.2000.03426.x.

Hurley, Jarrod R., Christopher A. Tout, and Onno R. Pols (Feb. 2002). "Evolution of binary stars and the effect of tides on binary populations". In: MNRAS 329.4, pp. 897–928. DOI: 10.1046/j.1365-8711.2002.05038.x. arXiv: astro-ph/0201220 [astro-ph].

Iaconi, Roberto and Orsola De Marco (Dec. 2019). "Speaking with one voice: simulations and observations discuss the common envelope α parameter". In: MNRAS 490.2, pp. 2550–2566. DOI: 10.1093/mnras/stz2756. arXiv: 1902.02039 [astro-ph.SR].

Iglesias, Carlos A. and Forrest J. Rogers (June 1996). "Updated Opal Opacities". In: ApJ 464, p. 943. DOI: 10.1086/177381.

Ivanova, N. and S. Chaichenets (Apr. 2011). "Common Envelope: Enthalpy Consideration". In: ApJ 731.2, L36, p. L36. DOI: 10.1088/2041-8205/731/2/L36. arXiv: 1103.2790 [astro-ph.SR].

Ivanova, N. et al. (Feb. 2013). "Common envelope evolution: where we stand and how we can move forward". In: A&A Rev. 21, 59, p. 59. DOI: 10.1007/s00159-013-0059-2. arXiv: 1209.4302 [astro-ph.HE].

Izzard, Robert G. and Adam S. Jermyn (May 2023). "Circumbinary discs for stellar population models". In: MNRAS 521.1, pp. 35–50. DOI: 10.1093/mnras/stac2899.

Izzard, Robert G. et al. (May 2004). "A new synthetic model for asymptotic giant branch stars". In: MNRAS 350.2, pp. 407–426. DOI: 10.1111/j.1365-2966.2004.07446.x. arXiv: astro-ph/0402403 [astro-ph].

Izzard, Robert G. et al. (Dec. 2006). "Population nucleosynthesis in single and binary stars. I. Model". In: A&A 460.2, pp. 565–572. DOI: 10.1051/0004-6361:20066129.

Izzard, Robert G. et al. (Dec. 2009). "Population synthesis of binary carbon-enhanced metal-poor stars". In: A&A 508.3, pp. 1359–1374. DOI: 10.1051/0004-6361/200912827. arXiv: 0910.2158 [astro-ph.SR].

Izzard, Robert G. et al. (Jan. 2018). "Binary stars in the Galactic thick disc". In: MNRAS 473.3, pp. 2984–2999. DOI: 10.1093/mnras/stx2355. arXiv: 1709.05237 [astro-ph.SR].

Jeffries Mark W., Jr. et al. (Sept. 2013). "WOCS 40007: A Detached Eclipsing Binary near the Turnoff of the Open Cluster NGC 6819". In: AJ 146.3, 58, p. 58. DOI: 10.1088/0004-6256/146/3/58. arXiv: 1307.0442 [astro-ph.SR].

Jiang, C. et al. (June 2020). "Variations of the mixing character of dipolar mixed modes in red giant stars". In: MNRAS 495.1, pp. 621–636. DOI: 10.1093/mnras/staa1285. arXiv: 2005.01464 [astro-ph.SR].

José, Jordi and Margarita Hernanz (Feb. 1998). "Nucleosynthesis in Classical Novae: CO versus ONe White Dwarfs". In: ApJ 494.2, pp. 680–690. DOI: 10.1086/305244. arXiv: astro-ph/9709153 [astro-ph].

Kaempf, T. A., K. S. de Boer, and M. Altmann (Mar. 2005). "Kinematics of RHB stars to trace the structure of the Galaxy". In: A&A 432.3, pp. 879–888. DOI: 10.1051/0004-6361:20041793. arXiv: astro-ph/0412428 [astro-ph].

Kalirai, Jasonjot Singh et al. (July 2001). "The CFHT Open Star Cluster Survey. II. Deep CCD Photometry of the Old Open Star Cluster NGC 6819". In: AJ 122.1, pp. 266–282. DOI: 10.1086/321141. arXiv: astro-ph/0104164 [astro-ph].

Kallinger, T. (June 2019). "Release note: Massive peak bagging of red giants in the Kepler field". In: *arXiv e-prints*, arXiv:1906.09428, arXiv:1906.09428. arXiv: 1906.09428 [astro-ph.SR].

Kamiński, Tomek et al. (Apr. 2023). "Lithium in red novae and their remnants". In: A&A 672, A196, A196. DOI: 10.1051/0004-6361/202244497.

Karakas, A. I., J. C. Lattanzio, and O. R. Pols (Jan. 2002). "Parameterising the Third Dredge-up in Asymptotic Giant Branch Stars". In: PASA 19.4, pp. 515–526. DOI: 10.1071/AS02013. arXiv: astro-ph/0210058 [astro-ph].

Khan, Saniya et al. (June 2018). "The Red-giant Branch Bump Revisited: Constraints on Envelope Overshooting in a Wide Range of Masses and Metallicities". In: ApJ 859.2, 156, p. 156. DOI: 10.3847/1538-4357/aabf90. arXiv: 1804.06669 [astro-ph.SR].

Kibédi, T. et al. (Oct. 2020). "Radiative Width of the Hoyle State from γ -Ray Spectroscopy". In: Phys. Rev. Lett. 125.18, 182701, p. 182701. DOI: 10.1103/PhysRevLett.125.182701. arXiv: 2009.10915 [nucl-ex].

Kim, Woong-Tae (Dec. 2010). "Nonlinear Dynamical Friction of a Circular-orbit Perturber in a Gaseous Medium". In: ApJ 725.1, pp. 1069–1081. DOI: 10.1088/0004-637X/725/1/1069. arXiv: 1010.1995 [astro-ph.GA].

Kippenhahn, Rudolf, Alfred Weigert, and Achim Weiss (2012). *Stellar Structure and Evolution*. Springer. ISBN: 978-3-642-30255-8. DOI: 10.1007/978-3-642-30304-3.

Kjeldsen, H. and T. R. Bedding (Jan. 1995). "Amplitudes of stellar oscillations: the implications for asteroseismology." In: A&A 293, pp. 87–106. arXiv: astro-ph/9403015 [astro-ph].

Kudritzki, R. P. and D. Reimers (Nov. 1978). "On the absolute scale of mass-loss in red giants. II. Circumstellar absorption lines in the spectrum of alpha Sco B and mass-loss of alpha Sco A." In: A&A 70, pp. 227–239.

Kunz, R. et al. (Mar. 2002). "Astrophysical Reaction Rate of $^{12}C(\alpha, \gamma)^{16}O$". In: ApJ 567.1, pp. 643–650. DOI: 10.1086/338384.

Kupka, Friedrich and Herbert J. Muthsam (July 2017). "Modelling of stellar convection". In: *Living Reviews in Computational Astrophysics* 3.1, 1, p. 1. DOI: 10.1007/s41115-017-0001-9.

Lamb, Horace (Jan. 1909). "On the Theory of Waves Propagated Vertically in the Atmosphere". In: *Proceedings of the London Mathematical Society* s2-7.1, pp. 122–141. ISSN: 0024-6115. DOI: 10.1112/plms/s2-7.1.122. eprint: https://academic.oup.com/plms/article-pdf/s2-7/1/122/4311000/s2-7-1-122.pdf. URL: https://doi.org/10.1112/plms/s2-7.1.122.

Landau, L. D. and E. M. Lifshitz (Jan. 1987). *Fluid Mechanics, Second Edition: Volume 6 (Course of Theoretical Physics)*. 2nd ed. Course of theoretical physics / by L. D. Landau and E. M. Lifshitz, Vol. 6. Butterworth-Heinemann. ISBN: 0750627670. URL: http://www.worldcat.org/isbn/0750627670.

Ledoux, P. (Mar. 1947). "Stellar Models with Convection and with Discontinuity of the Mean Molecular Weight". In: ApJ 105, p. 305. DOI: 10.1086/144905.

Lee-Brown, Donald B. et al. (Apr. 2015). "Spectroscopic Abundances in the Open Cluster NGC 6819". In: AJ 149.4, 121, p. 121. DOI: 10.1088/0004-6256/149/4/121. arXiv: 1501.04973 [astro-ph.SR].

Li, Yaguang et al. (Apr. 2022). "Discovery of post-mass-transfer helium-burning red giants using asteroseismology". In: *Nature Astronomy* 6, pp. 673–680. DOI: 10.1038/s41550-022-01648-5. arXiv: 2204.06203 [astro-ph.SR].

Lindegren, L. et al. (May 2021). "Gaia Early Data Release 3. Parallax bias versus magnitude, colour, and position". In: A&A 649, A4, A4. DOI: 10.1051/0004-6361/202039653. arXiv: 2012.01742 [astro-ph.IM].

Lindoff, U. (Dec. 1972). "The old open cluster NGC 6819." In: A&AS 7, p. 497.

Livio, Mario and Noam Soker (June 1988). "The Common Envelope Phase in the Evolution of Binary Stars". In: ApJ 329, p. 764. DOI: 10.1086/166419.

MacLeod, Morgan and Enrico Ramirez-Ruiz (Apr. 2015). "Asymmetric Accretion Flows within a Common Envelope". In: ApJ 803.1, 41, p. 41. DOI: 10.1088/0004-637X/803/1/41. arXiv: 1410.3823 [astro-ph.SR].

Maeder, A. (May 1975). "Stellar evolution III: the overshooting from convective cores." In: A&A 40.3, pp. 303–310.

Mallick, Anohita, Bacham E. Reddy, and C. Muthumariappan (Apr. 2022). "Probing infrared excess connection with Li enhancement among red clump giants". In: MNRAS 511.3, pp. 3741–3750. DOI: 10.1093/mnras/stac224. arXiv: 2201.09643 [astro-ph.SR].

Marconi, M. et al. (July 2015). "On a New Theoretical Framework for RR Lyrae Stars. I. The Metallicity Dependence". In: ApJ 808.1, 50, p. 50. DOI: 10.1088/0004-637X/808/1/50. arXiv: 1505.02531 [astro-ph.SR].

Martig, Marie et al. (Aug. 2015). "Young α-enriched giant stars in the solar neighbourhood". In: MNRAS 451.2, pp. 2230–2243. DOI: 10.1093/mnras/stv1071. arXiv: 1412.3453 [astro-ph.GA].

Matteuzzi, Massimiliano et al. (Mar. 2023). "Red horizontal branch stars: An asteroseismic perspective". In: A&A 671, A53, A53. DOI: 10.1051/0004-6361/202245746. arXiv: 2301.08761 [astro-ph.SR].

Matteuzzi, Massimiliano et al. (2024). "Anomalously low-mass core-He-burning star in NGC 6819 as a post-common-envelope phase product". In: å 691.A17. DOI: 10.1051/0004-6361/202451092. arXiv: 2408.11095 [astro-ph.SR].

McDermott, P. N. (July 1990). "Density Discontinuity G-Modes". In: MNRAS 245, p. 508.

Metcalfe, T. S., M. Salaris, and D. E. Winget (July 2002). "Measuring $^{12}C(\alpha, \gamma)^{16}O$ from White Dwarf Asteroseismology". In: ApJ 573.2, pp. 803–811. DOI: 10.1086/340796. arXiv: astro-ph/0203347 [astro-ph].

Michaud, G., G. Fontaine, and G. Beaudet (July 1984). "The lithium abundance - Constraints on stellar evolution". In: ApJ 282, pp. 206–213. DOI: 10.1086/162193.

Michaud, G., J. Richer, and O. Richard (Feb. 2010). "Atomic diffusion during red giant evolution". In: A&A 510, A104, A104. DOI: 10.1051/0004-6361/200912328.

Miglio, A. et al. (Sept. 2009). "Probing populations of red giants in the galactic disk with CoRoT". In: A&A 503.3, pp. L21–L24. DOI: 10.1051/0004-6361/200912822. arXiv: 0908.0210 [astro-ph.SR].

Miglio, A. et al. (Jan. 2012). "Asteroseismology of old open clusters with Kepler: direct estimate of the integrated red giant branch mass-loss in NGC 6791 and 6819". In: MNRAS 419.3, pp. 2077–2088. DOI: 10.1111/j.1365-2966.2011.19859.x. arXiv: 1109.4376 [astro-ph.SR].

Miglio, A. et al. (Feb. 2013). "Galactic archaeology: mapping and dating stellar populations with asteroseismology of red-giant stars". In: MNRAS 429.1, pp. 423–428. DOI: 10.1093/mnras/sts345. arXiv: 1211.0146 [astro-ph.GA].

Miglio, A. et al. (Jan. 2021). "Age dissection of the Milky Way discs: Red giants in the Kepler field". In: A&A 645, A85, A85. DOI: 10.1051/0004-6361/202038307. arXiv: 2004.14806 [astro-ph.GA].

Miglio, Andrea et al. (May 2008). "Probing the properties of convective cores through g modes: high-order g modes in SPB and γ Doradus stars". In: MNRAS 386.3, pp. 1487–1502. DOI: 10.1111/j.1365-2966.2008.13112.x. arXiv: 0802.2057 [astro-ph].

Mocák, M., L. Siess, and E. Müller (Sept. 2011). "Multidimensional hydrodynamic simulations of the hydrogen injection flash". In: A&A 533, A53, A53. DOI: 10.1051/0004-6361/201116940. arXiv: 1106.3260 [astro-ph.SR].

Montalbán, Josefina et al. (Oct. 2010). "Seismic Diagnostics of Red Giants: First Comparison with Stellar Models". In: ApJ 721.2, pp. L182–L188. DOI: 10.1088/2041-8205/721/2/L182. arXiv: 1009.1754 [astro-ph.SR].

Montalbán, Josefina et al. (Apr. 2013). "Testing Convective-core Overshooting Using Period Spacings of Dipole Modes in Red Giants". In: ApJ 766.2, 118, p. 118. DOI: 10.1088/0004-637X/766/2/118. arXiv: 1302.3173 [astro-ph.SR].

Montalbán, Josefina et al. (Jan. 2021). "Chronologically dating the early assembly of the Milky Way". In: *Nature Astronomy* 5, pp. 640–647. DOI: 10.1038/s41550-021-01347-7. arXiv: 2006.01783 [astro-ph.GA].

Montgomery, M. H., T. S. Metcalfe, and D. E. Winget (Sept. 2003). "The core/envelope symmetry in pulsating stars". In: MNRAS 344.2, pp. 657–664. DOI: 10.1046/j.1365-8711.2003.06853.x. arXiv: astro-ph/0305601 [astro-ph].

Mosser, B. et al. (Aug. 2011a). "Mixed modes in red-giant stars observed with CoRoT". In: A&A 532, A86, A86. DOI: 10.1051/0004-6361/201116825. arXiv: 1105.6113 [astro-ph.SR].

Mosser, B. et al. (Jan. 2011b). "The universal red-giant oscillation pattern. An automated determination with CoRoT data". In: A&A 525, L9, p. L9. DOI: 10.1051/0004-6361/201015440. arXiv: 1011.1928 [astro-ph.SR].

Mosser, B. et al. (Apr. 2012a). "Probing the core structure and evolution of red giants using gravity-dominated mixed modes observed with Kepler". In: A&A 540, A143, A143. DOI: 10.1051/0004-6361/201118519. arXiv: 1203.0689 [astro-ph.SR].

Mosser, B. et al. (Dec. 2012b). "Spin down of the core rotation in red giants". In: A&A 548, A10, A10. DOI: 10.1051/0004-6361/201220106. arXiv: 1209.3336 [astro-ph.SR].

Mosser, B. et al. (Dec. 2014). "Mixed modes in red giants: a window on stellar evolution". In: A&A 572, L5, p. L5. DOI: 10.1051/0004-6361/201425039. arXiv: 1411.1082 [astro-ph.SR].

Mosser, B. et al. (Apr. 2017). "Period spacings in red giants. III. Coupling factors of mixed modes". In: A&A 600, A1, A1. DOI: 10.1051/0004-6361/201630053. arXiv: 1612.08453 [astro-ph.SR].

Mosser, B. et al. (Oct. 2018). "Period spacings in red giants. IV. Toward a complete description of the mixed-mode pattern". In: A&A 618, A109, A109. DOI: 10.1051/0004-6361/201832777.

Nelemans, G. et al. (Jan. 2016). "The Formation of Cataclysmic Variables: The Influence of Nova Eruptions". In: ApJ 817.1, 69, p. 69. DOI: 10.3847/0004-637X/817/1/69.

Noether, E. (1918). "Invariante Variationsprobleme". ger. In: *Nachrichten von der Gesellschaft der Wissenschaften zu Göttingen, Mathematisch-Physikalische Klasse* 1918, pp. 235–257. URL: http://eudml.org/doc/59024.

Noll, Anthony, Sarbani Basu, and Saskia Hekker (Mar. 2024). "Effect of nuclear reactions rates and core boundary mixing on the seismology of red clump stars". In: A&A 683, A189, A189. DOI: 10.1051/0004-6361/202348276. arXiv: 2401.05519 [astro-ph.SR].

Ohlmann, Sebastian T. et al. (Jan. 2016). "Hydrodynamic Moving-mesh Simulations of the Common Envelope Phase in Binary Stellar Systems". In: ApJ 816.1, L9, p. L9. DOI: 10.3847/2041-8205/816/1/L9. arXiv: 1512.04529 [astro-ph.SR].

Ong, J. M. Joel and Sarbani Basu (Aug. 2020). "Semianalytic Expressions for the Isolation and Coupling of Mixed Modes". In: ApJ 898.2, 127, p. 127. DOI: 10.3847/1538-4357/ab9ffb. arXiv: 2006.13313 [astro-ph.SR].

Osaki, Yoji (Jan. 1975). "Nonradial oscillations of a 10 solar mass star in the main-sequence stage." In: PASJ 27.2, pp. 237–258.

Paczyński, B. (Jan. 1976). "Common Envelope Binaries". In: *Structure and Evolution of Close Binary Systems*. Ed. by Peter Eggleton, Simon Mitton, and John Whelan. Vol. 73. Symposium - International Astronomical Union, p. 75.

Pastorello, A. et al. (Oct. 2019). "Luminous red novae: Stellar mergers or giant eruptions?" In: A&A 630, A75, A75. DOI: 10.1051/0004-6361/201935999. arXiv: 1906.00812 [astro-ph.SR].

Paxton, Bill et al. (Jan. 2011). "Modules for Experiments in Stellar Astrophysics (MESA)". In: ApJS 192.1, 3, p. 3. DOI: 10.1088/0067-0049/192/1/3. arXiv: 1009.1622 [astro-ph.SR].

Paxton, Bill et al. (Sept. 2013). "Modules for Experiments in Stellar Astrophysics (MESA): Planets, Oscillations, Rotation, and Massive Stars". In: ApJS 208.1, 4, p. 4. DOI: 10.1088/0067-0049/208/1/4. arXiv: 1301.0319 [astro-ph.SR].

Paxton, Bill et al. (Sept. 2015). "Modules for Experiments in Stellar Astrophysics (MESA): Binaries, Pulsations, and Explosions". In: ApJS 220.1, 15, p. 15. DOI: 10.1088/0067-0049/220/1/15. arXiv: 1506.03146 [astro-ph.SR].

— (Mar. 2016). "Erratum: "Modules for Experiments in Stellar Astrophysics (MESA): Binaries, Pulsations, and Explosions" (2015, ApJS, 220, 15) ". In: ApJS 223.1, 18, p. 18. DOI: 10.3847/0067-0049/223/1/18.

Paxton, Bill et al. (Feb. 2018). "Modules for Experiments in Stellar Astrophysics (MESA): Convective Boundaries, Element Diffusion, and Massive Star Explosions". In: ApJS 234.2, 34, p. 34. DOI: 10.3847/1538-4365/aaa5a8. arXiv: 1710.08424 [astro-ph.SR].

Paxton, Bill et al. (July 2019). "Modules for Experiments in Stellar Astrophysics (MESA): Pulsating Variable Stars, Rotation, Convective Boundaries, and Energy Conservation". In: ApJS 243.1, 10, p. 10. DOI: 10.3847/1538-4365/ab2241. arXiv: 1903.01426 [astro-ph.SR].

Pinçon, C., M. J. Goupil, and K. Belkacem (Feb. 2020). "Probing the mid-layer structure of red giants. I. Mixed-mode coupling factor as a seismic diagnosis". In: A&A 634, A68, A68. DOI: 10.1051/0004-6361/201936864. arXiv: 1912.06008 [astro-ph.SR].

Pinçon, C. and M. Takata (May 2022). "Multi-cavity gravito-acoustic oscillation modes in stars. A general analytical resonance condition". In: A&A 661, A139, A139. DOI: 10.1051/0004-6361/202243157. arXiv: 2203.03402 [astro-ph.SR].

Pinsonneault, Marc H. et al. (Dec. 2018). "The Second APOKASC Catalog: The Empirical Approach". In: ApJS 239.2, 32, p. 32. DOI: 10.3847/1538-4365/aaebfd. arXiv: 1804.09983 [astro-ph.SR].

Podsiadlowski, Ph., S. Rappaport, and Z. Han (May 2003). "On the formation and evolution of black hole binaries". In: MNRAS 341.2, pp. 385–404. DOI: 10.1046/j.1365-8711.2003.06464.x. arXiv: astro-ph/0207153 [astro-ph].

Politano, Michael (Apr. 2004). "The Formation of Cataclysmic Variables with Brown Dwarf Secondaries". In: ApJ 604.2, pp. 817–826. DOI: 10.1086/381958. arXiv: astro-ph/0401224 [astro-ph].

Pols, Onno R. et al. (Aug. 1998). "Stellar evolution models for Z = 0.0001 to 0.03". In: MNRAS 298.2, pp. 525–536. DOI: 10.1046/j.1365-8711.1998.01658.x.

Pyrzas, S. et al. (Jan. 2012). "Post-common envelope binaries from SDSS - XV. Accurate stellar parameters for a cool 0.4 $M_{\odot}$ white dwarf and a 0.16 $M_{\odot}$ M dwarf in a 3 h eclipsing binary". In: MNRAS 419.1, pp. 817–826. DOI: 10.1111/j.1365-2966.2011.19746.x.

Rebull, Luisa M. et al. (Oct. 2015). "On Infrared Excesses Associated with Li-rich K Giants". In: AJ 150.4, 123, p. 123. DOI: 10.1088/0004-6256/150/4/123. arXiv: 1507.00708 [astro-ph.SR].

Reichardt, Thomas A. et al. (Mar. 2019). "Extending common envelope simulations from Roche lobe overflow to the nebular phase". In: MNRAS 484.1, pp. 631–647. DOI: 10.1093/mnras/sty3485. arXiv: 1809.02297 [astro-ph.SR].

Reimers, D (1975). "Mem. Soc. R. Sci. Liège". In: *Ser. 6* 8, p. 369.

Robe, H. (Feb. 1968). "Les oscillations non radiales des polytropes". In: *Annales d'Astrophysique* 31, p. 475.

Rodrigues, Thaíse S. et al. (May 2017). "Determining stellar parameters of asteroseismic targets: going beyond the use of scaling relations". In: MNRAS 467.2, pp. 1433–1448. DOI: 10.1093/mnras/stx120. arXiv: 1701.04791 [astro-ph.SR].

Rood, R. T. and D. A. Crocker (Jan. 1989). "Horizontal Branch Evolution". In: *IAU Colloq. 111: The Use of pulsating stars in fundamental problems of astronomy*. Ed. by Edward G. Schmidt, p. 103.

Röpke, Friedrich K. and Orsola De Marco (Dec. 2023). "Simulations of common-envelope evolution in binary stellar systems: physical models and numerical techniques". In: *Living Reviews in Computational Astrophysics* 9.1, 2, p. 2. DOI: 10.1007/s41115-023-00017-x. arXiv: 2212.07308 [astro-ph.SR].

Rosvick, Joanne M. and Don A. Vandenberg (Apr. 1998). "BV Photometry for the ~2.5 Gyr Open Cluster NGC 6819: More Evidence for Convective Core Overshooting on the Main Sequence". In: AJ 115.4, pp. 1516–1523. DOI: 10.1086/300304.

Roxburgh, I. W. and S. V. Vorontsov (Mar. 2001). "Semiclassical approximation for low-degree stellar p modes - III. Acoustic resonances and diagnostic properties of the oscillation frequencies". In: MNRAS 322.1, pp. 85–96. DOI: 10.1046/j.1365-8711.2001.04053.x.

Rui, Nicholas Z. and Jim Fuller (Apr. 2024). "Finding the unusual red giant remnants of cataclysmic variable mergers". In: *arXiv e-prints*, arXiv:2404.14474, arXiv:2404.14474. DOI: 10.48550/arXiv.2404.14474. arXiv: 2404.14474 [astro-ph.SR].

Rybizki, Jan et al. (Feb. 2022). "A classifier for spurious astrometric solutions in Gaia eDR3". In: MNRAS 510.2, pp. 2597–2616. DOI: 10.1093/mnras/stab3588. arXiv: 2101.11641 [astro-ph.IM].

Salaris, Maurizio and Santi Cassisi (2006). *Evolution of Stars and Stellar Populations*.

— (Aug. 2017). "Chemical element transport in stellar evolution models". In: *Royal Society Open Science* 4.8, 170192, p. 170192. DOI: 10.1098/rsos.170192. arXiv: 1707.07454 [astro-ph.SR].

Salaris, Maurizio et al. (Nov. 2015). "Post first dredge-up [C/N] ratio as age indicator. Theoretical calibration". In: A&A 583, A87, A87. DOI: 10.1051/0004-6361/201526951. arXiv: 1509.06904 [astro-ph.SR].

Sand, Christian et al. (Dec. 2020). "Common-envelope evolution with an asymptotic giant branch star". In: A&A 644, A60, A60. DOI: 10.1051/0004-6361/202038992. arXiv: 2007.11000 [astro-ph.SR].

Schneider, F. R. N. et al. (Jan. 2014). "Ages of Young Star Clusters, Massive Blue Stragglers, and the Upper Mass Limit of Stars: Analyzing Age-dependent Stellar Mass Functions". In: ApJ 780.2, 117, p. 117. DOI: 10.1088/0004-637X/780/2/117. arXiv: 1312.0607 [astro-ph.SR].

Schwarzschild, Martin (1958). *Structure and evolution of the stars.*

Scuflaire, R. (Nov. 1974). "The Non Radial Oscillations of Condensed Polytropes". In: A&A 36, p. 107.

Scuflaire, R. et al. (Aug. 2008a). "CLÉS, Code Liégeois d'Évolution Stellaire". In: Ap&SS 316.1-4, pp. 83–91. DOI: 10.1007/s10509-007-9650-1. arXiv: 0712.3471 [astro-ph].

Scuflaire, R. et al. (Aug. 2008b). "The Liège Oscillation code". In: Ap&SS 316.1-4, pp. 149–154. DOI: 10.1007/s10509-007-9577-6. arXiv: 0712.3474 [astro-ph].

Seaton, M. J. et al. (Feb. 1994). "Opacities for stellar envelopes". In: MNRAS 266, p. 805. DOI: 10.1093/mnras/266.4.805.

Shapley, Harlow (Dec. 1914). "On the Nature and Cause of Cepheid Variation". In: ApJ 40, p. 448. DOI: 10.1086/142137.

Shen, Ken J., Irit Idan, and Lars Bildsten (Nov. 2009). "Helium Core White Dwarfs in Cataclysmic Variables". In: ApJ 705.1, pp. 693–703. DOI: 10.1088/0004-637X/705/1/693.

Shetrone, M. et al. (Dec. 2015). "The SDSS-III APOGEE Spectral Line List for H-band Spectroscopy". In: ApJS 221.2, 24, p. 24. DOI: 10.1088/0067-0049/221/2/24. arXiv: 1502.04080 [astro-ph.IM].

Shibahashi, H. (Jan. 1979). "Modal Analysis of Stellar Nonradial Oscillations by an Asymptotic Method". In: PASJ 31, pp. 87–104.

Shima, E. et al. (Nov. 1985). "Hydrodynamic calculations of axisymmetric accretion flow". In: MNRAS 217, pp. 367–386. DOI: 10.1093/mnras/217.2.367.

Siess, L. et al. (Feb. 2013). "BINSTAR: a new binary stellar evolution code. Tidal interactions". In: A&A 550, A100, A100. DOI: 10.1051/0004-6361/201220327.

Silva Aguirre, V. et al. (Apr. 2018). "Confirming chemical clocks: asteroseismic age dissection of the Milky Way disc(s)". In: MNRAS 475.4, pp. 5487–5500. DOI: 10.1093/mnras/sty150. arXiv: 1710.09847 [astro-ph.GA].

Skrutskie, M. F. et al. (Feb. 2006). "The Two Micron All Sky Survey (2MASS)". In: AJ 131.2, pp. 1163–1183. DOI: 10.1086/498708.

Slumstrup, D. et al. (Feb. 2019). "Systematic differences in the spectroscopic analysis of red giants". In: A&A 622, A111, A111. DOI: 10.1051/0004-6361/201833739. arXiv: 1812.05630 [astro-ph.SR].

Smith, Verne V. et al. (June 2021). "The APOGEE Data Release 16 Spectral Line List". In: AJ 161.6, 254, p. 254. DOI: 10.3847/1538-3881/abefdc. arXiv: 2103.10112 [astro-ph.SR].

Sneden, Christopher et al. (Nov. 2022). "The Active Chromospheres of Lithium-rich Red Giant Stars". In: ApJ 940.1, 12, p. 12. DOI: 10.3847/1538-4357/ac922e. arXiv: 2209.05941 [astro-ph.SR].

Speagle, Joshua S. (Apr. 2020). "DYNESTY: a dynamic nested sampling package for estimating Bayesian posteriors and evidences". In: MNRAS 493.3, pp. 3132–3158. DOI: 10.1093/mnras/staa278. arXiv: 1904.02180 [astro-ph.IM].

Stancliffe, R. J. et al. (Mar. 2007). "Carbon-enhanced metal-poor stars and thermohaline mixing". In: A&A 464.3, pp. L57–L60. DOI: 10.1051/0004-6361:20066891.

Stello, Dennis et al. (Mar. 2013). "Asteroseismic Classification of Stellar Populations among 13,000 Red Giants Observed by Kepler". In: ApJ 765.2, L41, p. L41. DOI: 10.1088/2041-8205/765/2/L41. arXiv: 1302.0858 [astro-ph.SR].

Stello, Dennis et al. (Dec. 2016). "The K2 M67 Study: Revisiting Old Friends with K2 Reveals Oscillating Red Giants in the Open Cluster M67". In: ApJ 832.2, 133, p. 133. DOI: 10.3847/0004-637X/832/2/133. arXiv: 1610.03060 [astro-ph.SR].

Stetson, Peter B. et al. (May 1989). "CCD Photometry of the Anomalous Globular Cluster Palomar 12". In: AJ 97, p. 1360. DOI: 10.1086/115079.

Straniero, Oscar et al. (Feb. 2003). "The Chemical Composition of White Dwarfs as a Test of Convective Efficiency during Core Helium Burning". In: ApJ 583.2, pp. 878–884. DOI: 10.1086/345427. arXiv: astro-ph/0210191 [astro-ph].

Taam, Ronald E. and Eric L. Sandquist (Jan. 2000). "Common Envelope Evolution of Massive Binary Stars". In: ARA&A 38, pp. 113–141. DOI: 10.1146/annurev.astro.38.1.113.

Tailo, M. et al. (Nov. 2020). "Mass-loss along the red giant branch in 46 globular clusters and their multiple populations". In: MNRAS 498.4, pp. 5745–5771. DOI: 10.1093/mnras/staa2639. arXiv: 2009.01080 [astro-ph.SR].

Tailo, M. et al. (June 2022). "Asteroseismology of the multiple stellar populations in the globular cluster M4". In: A&A 662, L7, p. L7. DOI: 10.1051/0004-6361/202243721. arXiv: 2205.06645 [astro-ph.SR].

Takata, Masao (Apr. 2005). "Momentum Conservation and Mode Classification of the Dipolar Oscillations of Stars". In: PASJ 57, pp. 375–389. DOI: 10.1093/pasj/57.2.375.

— (Oct. 2006a). "Analysis of Adiabatic Dipolar Oscillations of Stars". In: PASJ 58, pp. 893–908. DOI: 10.1093/pasj/58.5.893.

— (Aug. 2006b). "First Integrals of Adiabatic Stellar Oscillations". In: PASJ 58, pp. 759–775. DOI: 10.1093/pasj/58.4.759.

— (Dec. 2016a). "Asymptotic analysis of dipolar mixed modes of oscillations in red giant stars". In: PASJ 68.6, 109, p. 109. DOI: 10.1093/pasj/psw104.

— (Dec. 2016b). "Physical formulation of mixed modes of stellar oscillations". In: PASJ 68.6, 91, p. 91. DOI: 10.1093/pasj/psw093.

Tassoul, M. (Aug. 1980). "Asymptotic approximations for stellar nonradial pulsations." In: ApJS 43, pp. 469–490. DOI: 10.1086/190678.

Tayar, Jamie et al. (Aug. 2023). "Lithium in Kepler Red Giants: Defining Normal and Anomalous". In: AJ 166.2, 60, p. 60. DOI: 10.3847/1538-3881/ace25d. arXiv: 2306.16465 [astro-ph.SR].

Tognini, F. et al. (Nov. 2023). "Impact of the uncertainties of 3α and $^{12}C(\alpha, \gamma)^{16}O$ reactions on the He-burning phases of low- and intermediate-mass stars". In: A&A 679, A75, A75. DOI: 10.1051/0004-6361/202346382. arXiv: 2310.05745 [astro-ph.SR].

Townsend, R. H. D., J. Goldstein, and E. G. Zweibel (Mar. 2018). "Angular momentum transport by heat-driven g-modes in slowly pulsating B stars". In: MNRAS 475.1, pp. 879–893. DOI: 10.1093/mnras/stx3142. arXiv: 1712.02420 [astro-ph.SR].

Townsend, R. H. D. and S. A. Teitler (Nov. 2013). "GYRE: an open-source stellar oscillation code based on a new Magnus Multiple Shooting scheme". In: MNRAS 435.4, pp. 3406–3418. DOI: 10.1093/mnras/stt1533. arXiv: 1308.2965 [astro-ph.SR].

Tylenda, R. and N. Soker (May 2006). "Eruptions of the V838 Mon type: stellar merger versus nuclear outburst models". In: A&A 451.1, pp. 223–236. DOI: 10.1051/0004-6361:20054201. arXiv: astro-ph/0509379 [astro-ph].

Ulrich, R. K. (July 1986). "Determination of Stellar Ages from Asteroseismology". In: ApJ 306, p. L37. DOI: 10.1086/184700.

Unno, Wasaburo et al. (1989). *Nonradial oscillations of stars*.

Valcarce, A. A. R. and M. Catelan (Aug. 2008). "A semi-empirical study of the mass distribution of horizontal branch stars in M 3 (NGC 5272)". In: A&A 487.1, pp. 185–195. DOI: 10.1051/0004-6361:20078231. arXiv: 0805.3161 [astro-ph].

Valentini, M. et al. (July 2019). "Masses and ages for metal-poor stars. A pilot programme combining asteroseismology and high-resolution spectroscopic follow-up of RAVE halo stars". In: A&A 627, A173, A173. DOI: 10.1051/0004-6361/201834081. arXiv: 1808.08569 [astro-ph.SR].

van den Heuvel, E. P. J. (Jan. 1976). "Late Stages of Close Binary Systems". In: *Structure and Evolution of Close Binary Systems*. Ed. by Peter Eggleton, Simon Mitton, and John Whelan. Vol. 73. Symposium - International Astronomical Union, p. 35.

van Rossem, Walter, Andrea Miglio, and Josefina Montalbán (Aug. 2024). "Mixed-mode coupling in the red clump. I. Standard single-star models". In: *8th TESS/15th Kepler Asteroseismic Science Consortium Workshop*, 42, p. 42. DOI: 10.5281/zenodo.12819078. arXiv: 2410.02865 [astro-ph.SR].

Vrard, M., B. Mosser, and R. Samadi (Apr. 2016). "Period spacings in red giants. II. Automated measurement". In: A&A 588, A87, A87. DOI: 10.1051/0004-6361/201527259. arXiv: 1602.04940 [astro-ph.SR].

Vrard, M. et al. (Aug. 2018). "Amplitude and lifetime of radial modes in red giant star spectra observed by Kepler". In: A&A 616, A94, A94. DOI: 10.1051/0004-6361/201732477. arXiv: 1805.03690 [astro-ph.SR].

Vrard, Mathieu et al. (Dec. 2022). "Evidence of structural discontinuities in the inner core of red-giant stars". In: *Nature Communications* 13, 7553, p. 7553. DOI: 10.1038/s41467-022-34986-z. arXiv: 2212.11393 [astro-ph.SR].

Wallace, Joshua J. et al. (Sept. 2019). "A Search for Variable Stars in the Globular Cluster M4 with K2". In: ApJS 244.1, 12, p. 12. DOI: 10.3847/1538-4365/ab3849. arXiv: 1908.02373 [astro-ph.SR].

Wang, Chen, Kun Jia, and Xiang-Dong Li (Aug. 2016). "The binding energy parameter for common envelope evolution". In: *Research in Astronomy and Astrophysics* 16.8, 126, p. 126. DOI: 10.1088/1674-4527/16/8/126. arXiv: 1605.03668 [astro-ph.SR].

Webbink, R. F. (Feb. 1984). "Double white dwarfs as progenitors of R Coronae Borealis stars and type I supernovae." In: ApJ 277, pp. 355–360. DOI: 10.1086/161701.

Webbink, Ronald F. (Jan. 2008). "Common Envelope Evolution Redux". In: *Astrophysics and Space Science Library*. Ed. by Eugene F. Milone, Denis A. Leahy, and David W. Hobill. Vol. 352. Astrophysics and Space Science Library, p. 233. DOI: 10.1007/978-1-4020-6544-6_13. arXiv: 0704.0280 [astro-ph].

White, Timothy R. et al. (Dec. 2011). "Calculating Asteroseismic Diagrams for Solar-like Oscillations". In: ApJ 743.2, 161, p. 161. DOI: 10.1088/0004-637X/743/2/161. arXiv: 1109.3455 [astro-ph.SR].

Wong, Tsing-Wai et al. (Aug. 2014). "Understanding Compact Object Formation and Natal Kicks. IV. The Case of IC 10 X-1". In: ApJ 790.2, 119, p. 119. DOI: 10.1088/0004-637X/790/2/119. arXiv: 1304.3756 [astro-ph.HE].

Woosley, S. E. and Thomas A. Weaver (Nov. 1995). "The Evolution and Explosion of Massive Stars. II. Explosive Hydrodynamics and Nucleosynthesis". In: ApJS 101, p. 181. DOI: 10.1086/192237.

Xu, Xiao-Jie and Xiang-Dong Li (Oct. 2010a). "ERRATUM: "On the Binding Energy Parameter λ of Common Envelope Evolution" (2010, ApJ, 716, 114) ". In: ApJ 722.2, pp. 1985–1988. DOI: 10.1088/0004-637X/722/2/1985.

— (June 2010b). "On the Binding Energy Parameter λ of Common Envelope Evolution". In: ApJ 716.1, pp. 114–121. DOI: 10.1088/0004-637X/716/1/114. arXiv: 1004.4957 [astro-ph.SR].

Yang, Soung-Chul et al. (Jan. 2013). "WIYN Open Cluster Study LII: Wide-field CCD Photometry of the Old Open Cluster NGC 6819". In: ApJ 762.1, 3, p. 3. DOI: 10.1088/0004-637X/762/1/3. arXiv: 1211.0077 [astro-ph.SR].

Yates, Robert M. et al. (Jan. 2024). "The impact of binary stars on the dust and metal evolution of galaxies". In: MNRAS 527.3, pp. 6292–6311. DOI: 10.1093/mnras/stad3419. arXiv: 2310.15218 [astro-ph.GA].

Yu, Jie et al. (June 2018). "Asteroseismology of 16,000 Kepler Red Giants: Global Oscillation Parameters, Masses, and Radii". In: ApJS 236.2, 42, p. 42. DOI: 10.3847/1538-4365/aaaf74. arXiv: 1802.04455 [astro-ph.SR].

Zahn, J. -P. (Dec. 1991). "Convective penetration in stellar interiors." In: A&A 252, pp. 179–188.

Zamora, O. et al. (Jan. 2006). "The chemical composition of R-stars". In: Mem. Soc. Astron. Italiana 77, p. 973.

Zhang, Xianfei et al. (Feb. 2017). "Evolution Models of Helium White Dwarf-Main-sequence Star Merger Remnants". In: ApJ 835.2, 242, p. 242. DOI: 10.3847/1538-4357/835/2/242.

Zhang, Xianfei et al. (Jan. 2020). "Population Synthesis of Helium White Dwarf-Red Giant Star Mergers and the Formation of Lithium-rich Giants and Carbon Stars". In: ApJ 889.1, 33, p. 33. DOI: 10.3847/1538-4357/ab5e89. arXiv: 2001.05600 [astro-ph.SR].